INFORMATION TO USERS

This manuscript has been reproduced from the microfilm master. UMI films the text directly from the original or copy submitted. Thus, some thesis and dissertation copies are in typewriter face, while others may be from any type of computer printer.

The quality of this reproduction is dependent upon the quality of the copy submitted. Broken or indistinct print, colored or poor quality illustrations and photographs, print bleedthrough, substandard margins, and improper alignment can adversely affect reproduction.

In the unlikely event that the author did not send UMI a complete manuscript and there are missing pages, these will be noted. Also, if unauthorized copyright material had to be removed, a note will indicate the deletion.

Oversize materials (e.g., maps, drawings, charts) are reproduced by sectioning the original, beginning at the upper left-hand corner and continuing from left to right in equal sections with small overlaps.

Photographs included in the original manuscript have been reproduced xerographically in this copy. Higher quality 6" x 9" black and white photographic prints are available for any photographs or illustrations appearing in this copy for an additional charge. Contact UMI directly to order.

Bell & Howell Information and Learning
300 North Zeeb Road, Ann Arbor, MI 48106-1346 USA
800-521-0600

APPLICATION OF ULTRAFAST OPTICAL TECHNIQUES TO THE CHARACTERIZATION OF MM-WAVE INTEGRATED CIRCUITS AND RADIATING STRUCTURES

by

Kyoung Yang

A dissertation submitted in partial fulfillment
of the requirements for the degree of
Doctor of Philosophy
(Electrical Engineering)
in The University of Michigan
2001

Doctoral Committee:

Professor Linda P. B. Katehi, Co-Chair
Research scientist John F. Whitaker, Co-Chair
Professor Philip Bucksbaum
Research Scientist Jack R. East
Professor Gerard A. Mourou

UMI Number: 3001072

UMI Microform 3001072

Bell & Howell Information and Learning Company
300 North Zeeb Road
P.O. Box 1346
Ann Arbor, MI 48106-1346

To my father and mother

ACKNOWLEDGMENTS

An ancient wise man said that the life of man is enriched in the course of endless encounters with many people. While writing this dissertation as a result of my Ph.D. course, I realized this piece of work would not been possible without the help of many people I encountered throughout the years.

First and foremost, I would like to thank Dr. John Whitaker, one of my co-advisors. Without his understanding, encouragement, and support, this research would have been a more difficult and rough journey. Also, I cannot thank too much Professor Linda Katehi, my co-advisor, for her endless encouragement. Her thoughtful advice gave me strength to overcome many obstacles during this research. I would also like to thank my committee members for their support: Professor Gerard Morou, Dr. Jack East, and Professor Philip Bucksbaum.

I thank Dr. Gerhard David, who spent tremendous time and effort with me in establishing the early measurement setup that became the foundation of this research. I also thank Professor Jong-Gwan Yook who always provided me not only technical support but also a close friendship.

Thank you to my colleagues Dr. Katherine Herrick, Dr. J.D. Shumpert, Dr. Dong-Hoon Chen, Sergio Pacheco, Kevin Lu, and James Becker. I would also like to thank Richard Lai, Boh Ruffin, and Jason Deible. I would like to acknowledge Jea-Sung Rhie and Uk-Song Kang for their warm friendship.

My research has been supported by the MURI project, and I would like to thank the members of the MURI project for their support: Dr. Jim Harvey, Professor Wilson Pearson, Professor Amir Mortazawi. Also, I should thank Professor Zoya Popović, Todd

Marshall, John Hubert, and Lee Mirth for providing state of the art arrays for measurements.

I also express my sincere gratitude to Professor Min-Koo Han and Professor Yearn-Ik Choi. They showed me the way of the engineer. Enthusiasm for the knowledge I learned from them has been a foundation of my research.

Most importantly, I would like to express my deep gratitude to my family. Throughout my life, my father's encouragement and my mother's selfless love and prayer have been a guiding light to me. I also thank my sister and brother, who have always believed in and supported me.

PREFACE

This dissertation presents new characterization methods for high-frequency circuits and devices utilizing optical techniques. Due to its low invasiveness, broad bandwidth, and high-resolution, an electro-optic near-field mapping system makes it possible to obtain the detailed three orthogonal near-field components of various microwave and millimeter wave structures, which cannot be obtained by any other measurement methods. The electro-optic field mapping method has demonstrated its unique usefulness as an independent characterization method for guided and radiating devices by providing accurate fault isolations and performance verifications. Furthermore, the most recent development in electro-optic field mapping techniques, a fiber-based electro-optic field mapping system, provides maximum measurement flexibility. In addition, the high-resolution near-field data obtained this technique lead to new radiation wave analysis methods such as accurate near- to far-field transformation associated with various filtering processes and near-field wave front reconstruction. Also, a photoconductive absolute potential measurement method is discussed as an alternative high-frequency measurement technique.

TABLE OF CONTENTS

LIST OF TABLES

Table

LIST OF FIGURES

Figures

LIST OF APPENDICES

Appendix

CHAPTER 1
INTRODUCTION

1.1 Foreword

After the industrial revolution that was invoked by rapid development of mechanical engineering based on Newtonian mechanics, the rapid development of high-speed, high-frequency electrical engineering has stimulated an information revolution. Due to the benefit of the information revolution, it is possible to communicate over immense distances and to obtain valuable information from anywhere in the world. Wireless communication technology occupies the center of attention as one of fastest growing areas in electrical engineering. For example, the recent advancement of satellite and mobile communication systems make it possible for every individual to have their own personal wireless communication devices. In past, such systems were used only for very limited special purpose. Also, the improvement of military and commercial radar systems and remote sensing technologies have provided more information than ever.

This explosive increase of information is requiring even more rapid development of high-speed electrical engineering that made the information revolution possible. Confronted with the task to develop high-speed electrical systems, electrical engineers have been asked to overcome barriers between different areas in engineering. Nowadays, it is not difficult to find high-frequency electrical systems that include various technologies from many different areas of engineering such as micromachined radio-frequency (RF) circuits and antenna arrays utilizing high-speed monolithic microwave

integrated circuits (MMICs). Such electrical systems as micro/millimeter wave integrated circuits or antenna arrays are more complicated, sophisticated, and faster than ever.

As microwave and millimeter wave circuits and antenna arrays are becoming faster and more complicated, the importance of accurate measurement methods is continuously increasing. However, unfortunately, conventional electrical measurement techniques can provide only a limited amount of information about modern sophisticated and complicated high-frequency systems. For example, traditional port-based characterization methods such as network analyzer measurements have been used to analyze high frequency systems. In those port-based measurement methods, a device under test (DUT) is usually considered as a single block structure. Such measurement methods only provide information about the characteristics of the DUT at their input and output ports. As a result, the conventional port-based measurements fail to explain detailed phenomena inside of the DUT. More importantly, for a DUT that is not functioning correctly, it is very difficult or even impossible to detect the reason of the malfunction.

Conventional far-field measurement of radiating structures can only provide far-field patterns and have shown limitation when applied to complicated arrays. In particular, as the number of the arrays associated with many solid state devices or circuits increases, near-field characterization becomes as important as the far-field measurements. In order to optimize the performance of such arrays, new accurate near-field measurement techniques must be developed. In addition, traditional theoretical analysis approaches for the high frequency circuits and antennas such as finite element method (FEM), method of moment (MOM), and finite difference time domain method (FDTD), have failed to provide sufficient information. Also, the merger of technologies from various areas of engineering requires totally new concepts of measurement that can provide new insight about modern high-frequency electrical systems. On the verge of the demand for new measurement methods that can provide profound information about

sophisticated high frequency circuits and antennas, a high-resolution near-field measurement method has been spotlighted as one of promising techniques that can overcome the limits of conventional high-frequency measurement methods.

In general, several fundamental characteristics of a desirable measurement technique should be contemplated before development of a new measurement system. The most important characteristic is the fidelity of a measurement system. In other words, a measurement system should provide correct information, revealing what the state of the measured quantity is. Also, most conventional measurement methods that rely on N-port measurements exhibit limitations on explaining phenomena inside of modern complicated systems. Thus, would be ideal to develop a measurement technique that can offer understanding of phenomena occurring inside of the systems.

High-frequency measurement techniques utilizing short-pulse, mode-locked lasers are one of the promising solutions that meet the measurement requirements of complicated high-speed systems. These systems can measure micro/millimeter-wave integrated circuits or radiating structures such as arrays associated with solid-state devices. The use of a laser to detect microwave or millimeter wave signals makes it possible to obtain a number of unique advantages that cannot be found among conventional measurement methods. Due to the short pulsewidth of the laser, the measurement bandwidth of this optical measurement technique is superior to any other measurement methods. Also, most electrical measurement techniques require a certain type of metal structures to detect the signal. However, the optical method usually does not require any metal structure near the signal sensor area. As a result, undesirable effects caused by introducing a metal structure around the DUTs such as distortion of the signal and disturbance in the operation of the DUTs can be significantly reduced. Among those techniques, electro-optic and photoconductive sampling have been studied intensively. These two techniques have very wide measurement bandwidth, covering even the fastest millimeter-wave circuits. Additionally, both techniques offer in-circuit measurement

results with very high spatial resolution, which is one of the desirable features of an ideal measurement technique.

1.2 Electro-Optic Field Mapping Method

In certain types of crystals, the application of an electric field causes a change in the crystal's refractive indices. This phenomenon is referred to as the electro-optic (EO) effect or Pockels effect, and such crystals are known as electro-optic crystals. Figure 1.1 shows conceptual schematic of the electro-optic effect.

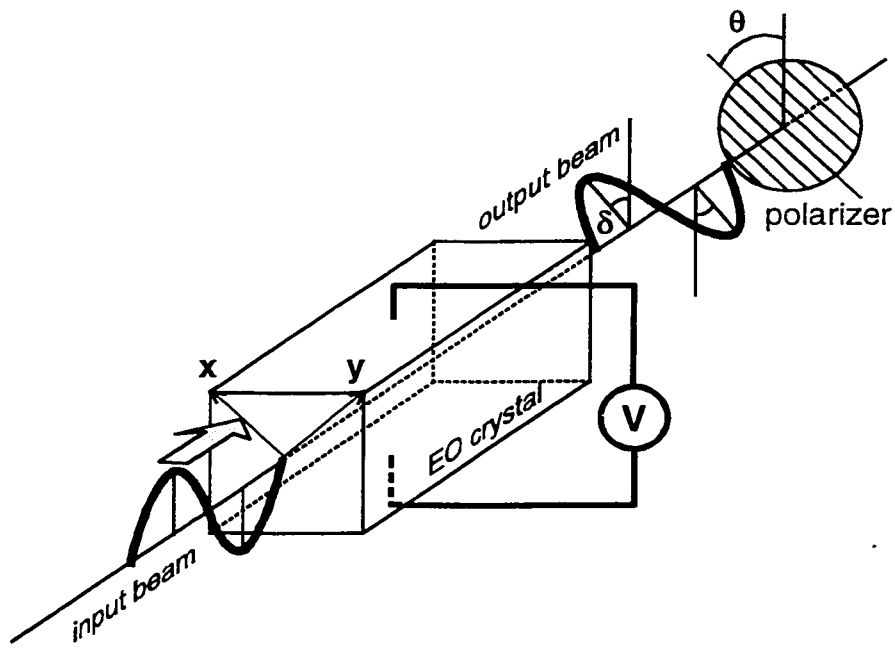

Figure 1.1: Electro-optic modulation

Two vectorial polarization components of the input optical beam (vertically polarized beam in Fig. 1.1) – x- and y-component – experience different retardation in the course of the traveling through the EO crystal due to the presence of the electric field and Pockels effect. As a result, the polarization axis of the output beam is modulated, and

the amount of the difference is shown as an angle δ in Fig. 1.1. The angle δ is determined by the length of the beam path in the EO crystal, the strength of the electric field in the crystal, and the EO coefficient of the crystal. Thus, for a given EO crystal that has fixed physical size with a certain EO coefficient, the angle δ reveals the strength of the electric field in the crystal (or bias voltage V across a distance). From this principle, if one places an optical polarizer in the output beam path with certain orientation, the output signal can be obtained as a form of power modulation. For example, once the polarizer is aligned to the polarization direction of the input beam (vertical direction, θ =0 in Fig. 1.1), the output (optical power) signal should be maximized if the external bias voltage equals 0 – or electric field does not exists in the crystal. Otherwise, if the polarizer is oriented to obtain maximum output power with maximum bias voltage (or maximum electric field in the crystal, $\theta = \delta$ in Fig. 1.1), the output power is reduced as the bias voltage (or electric field) decreases. Further detailed mathematical explanations can be found in ref. [1] and Chapter 4 of this thesis.

The electro-optic effect is a widely used method of controlling the phase or intensity of the optical radiation [1]. In another sense, this effect also makes it possible to detect the presence of an electric field in the crystal. Optical radiation (typically, a laser beam) travels through the crystal with a modulated index of refraction (due to an electric field) and exhibits a different state of polarization with respect to the laser that travels through the crystal without an applied electric field. Comparing the polarization states allows one to determine the amplitude and phase of the existing electric field. Since the electro-optic sensing procedure completely relies on the small displacement of the atomic crystal structure, the response time of the procedure is extremely short. This short response time makes it possible to measure high-frequency electric field up to the Terahertz regime [2][3]. Because the electro-optic field sensing technique is based on the optical modulation of the incident laser beam, its spatial resolution is determined by the

size of the focused laser beam. Thus, the limit of optical focusing capability can be referred as the limit of spatial resolution of a system [4].

Electro-optic (EO) field measurement techniques can be categorized into three generations with respect to their embodiments. Internal EO field mapping method can be considered as the first generation of EO sampling technique. The internal probing method utilizes the substrate of a DUT as the sensor crystal [5]-[10], and senses an electric field inside of the substrate. The internal EO method needs a relatively simple measurement setup with respect to other EO field mapping techniques because it does not require a separate crystal. As a result, a sophisticated fabrication process for the electro-optic crystals, which is crucial for other EO methods, can be avoided. The optical beam is directly focused into the substrate of the DUT, and the reflected or transmitted beam is detected in order to measure the electric field inside of the substrate. However, the significant drawback of this method is that it can be applied only to circuits fabricated on substrates that exhibit the electro-optic effect, such as GaAs or InP. Also, the detectable electric field component is determined by the relative orientation of the DUT structure and crystal axes of the substrate. The internal EO field sensing method shows its limit for the characterization of radiating structures since this method is only able to detect the field inside of the substrate. To overcome the limits of the internal EO sampling methods, external EO crystals with electrode structures were used as electric field sensors [11], and this method eventually led to the development of a free-space EO field mapping method.

A free-space external EO field mapping method, the second generation method, was developed to overcome the limits of the previous internal method [12]-[16]. In this method, the optical beam propagates through air, and the beam is then focused into an external electro-optic crystal. The reflected or transmitted beam from the EO crystal is then detected to measure the electric fields. When using reflected beam detection method, maximizing the reflected beam often leads to higher sensitivity of the system. In order to

do this, a high-reflection coating is often applied to enhance the sensitivity of the system. Also, the EO crystals can be polished to have a total internal reflection profile.

During the measurement process, there is no physical connection between the optical beam (typically a short-pulse laser) system and the external EO crystal. As a result, the free space EO field detection system requires a very sophisticated alignment procedure of the optical beam in order to optimize the sensitivity. By using an external EO crystal, the electric field can be measured regardless of the type of substrate. Furthermore, by selecting the appropriate EO crystal, complete three orthogonal electric field components have been successfully measured [4][17]. The external probing method can be used not only for guided wave structures, but also radiating structures [18][19]. Plane field mapping is accomplished via the two dimensional movement of the external probe. In addition, the probe also can be positioned at many different distances from the DUT. Because of the three-dimensional freedom of movement of the probe, a near- to far-field-transition measurement of a single antenna has been successfully performed. This 3-dimensional measurement capability provides a lot of information about radiating structures. In particular, it reveals critical information for the improvement of complicated radiating structures such as grid oscillators or amplifier arrays.

Finally, the most advanced third generation fiber-based EO field-mapping method utilizes single-mode optical fiber and micromachined gallium arsenide (GaAs) crystals has been recently developed [20][21]. The fiber-based electro-optic sampling method, in which a micromachined external EO crystal is mounted at the end of the optical fiber to detect the electric field from DUT, can be categorized an improved external EO field mapping technique. The fiber-based EO system has the same associated with the first (internal) and second (external free-space) generation EO methods. In addition, due to the flexibility and small diameter of the optical fiber, the fiber-based EO field mapping system demonstrates exceptional measurement versatility. As a result, the field-sensing probe can be freely placed with respect to the DUTs. For example, the fiber-based system

can detect electric fields inside partially closed microwave and millimeter wave structures such as those structures. This can include inside horn antennas or waveguides. In the case of complete closure such as packaged circuits, all that is needed is a small access opening for the probe tip to allow the accurate field measurement inside of the package. Since the optical beam is guided inside of the fiber, the alignment between the beam source and the EO crystal can be achieved in great convenience. Also, it is only the field-sensing tip that is placed near the DUTs, and thus, many metal components that are required in order to support various optical components near the DUTs for the internal and free-space external methods are no longer necessary in the fiber-based EO field mapping system. As a result, the interference from the fiber-based EO system can be expected to be lowest among all of the EO measurement methods.

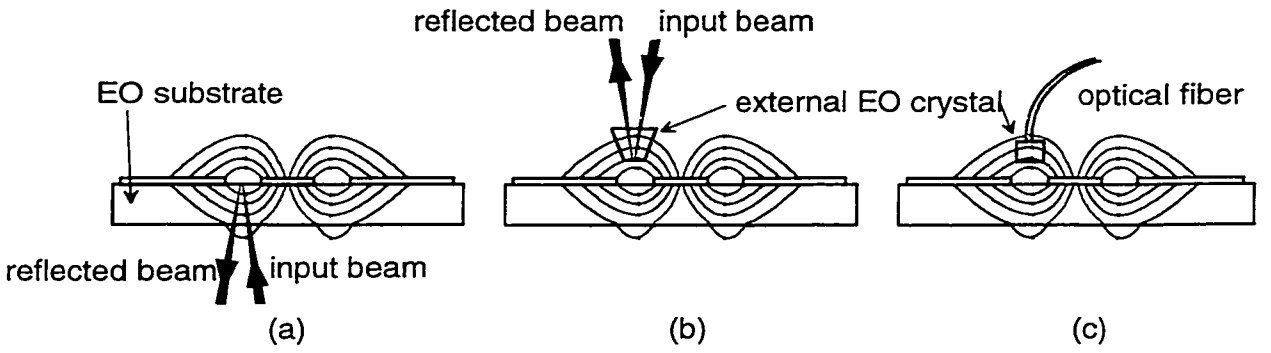

Figure 1.2: Three different EO field-mapping methods with CPW line as a DUT. (a) Internal, (b) free-space external, and (c) fiber-based EO field-mapping methods. The field lines are overlayed on the cross sectional view of a CPW.

Figure 1.2 shows the internal (Fig. 1.2(a)), free-space external (Fig. 1.2(b)), and fiber-based EO field mapping methods (Fig. 1.2(c)) with a cross sectional view of the coplanar waveguide (CPW) transmission line as a DUT. In the internal EO field probing, the EO signal is induced by the Pockels effect in the substrate, and thus it measures the electric field in the substrate. In comparison, the free-space external and fiber-based

methods are able to detect the electric field above the DUT structure. As a result, both free-space external and fiber-based methods have the capability of measurement in three-dimensional space.

EO field mapping (Generation)	Applicable structure	System complexity	Measurement flexibility
Internal EO method (first generation)	Guided wave structures fabricated on EO substrate	Complex	Limited 1-D or 2-D measurement
Free-space External EO method (second generation)	Guided and Radiating wave structure (insensitive to substrate; open structure)	Complex	1-D, 2-D, and 3-D measurements with limited maneuverability
Fiber-based EO method (third generation)	Guided and Radiating wave structure (insensitive to substrate; open and closed structures)	Simple	1-D, 2-D, and 3-D measurements with virtually unlimited maneuverability

Table 1.1: Comparison between three different EO field-mapping methods

Under certain circumstances, one may need to change the orientation of the EO crystal with respect to the geometry of a DUT. For example, the EO crystal may need to be aligned horizontally for certain geometries (figure 1.2 shows vertical alignments of the EO crystal.). This reconfiguration is basically impossible to achieve in the internal method since it utilizes the substrate as an EO sensor crystal. In the free-space external EO field probing, the EO crystal can be positioned into different directions. However, the orientation of the EO crystal cannot be changed without major manipulations of optical beam pathway. Unlike the internal and free-space external system, the probe crystal of the fiber-based EO system can be placed at any position with arbitrary direction due to the flexibility of the optical fiber. Furthermore, the probe is able to detect the electric field in the closure if there is a small access hole for the optical fiber.

The properties of the three different EO field-mapping methods are summarized in table 1.1.

CHARACTERISTIC	VALUE
Bandwidth	> 100 GHz (low limit : 40 MHz)
Spatial resolution	< 8 μm
Sensitivity	$< 40\ \mathrm{mV}/\sqrt{Hz}$
Cross polarization suppression	> 30 dB
Scanning elapse time	About 30 min. for 100 × 100 points scan

Table 1.2: Important features of fiber-based (free-space external) EO field mapping

Table 1.2 summarizes important characteristics of the fiber-based (free-space external) EO method. The EO field mapping method successfully extracted the electric field distribution in the output aperture of a 6× frequency multiplier with 16.7205 GHz input signal, and the resultant output signal frequency was 100.323 GHz at the output waveguide aperture. Currently, the upper boundary of the bandwidth is limited by the capability of the microwave source. Theoretically, the upper limit is expected to reach several THz, as determined by a combination of laser pulse width, EO crystal resonance characteristics, interaction length in the EO crystal, and phase-noise properties of the laser and the synthesizers. The lower boundary of the bandwidth is confined by the pulse repetition rate of the laser system used in the EO field mapping. The spatial resolution of the EO field mapping is determined by the focusing diameter of the optical beam in the EO crystal. As a result, the resolution can be reduced down to 1 ~ 2 μm range. However, the smallest structure used in actual measurements had 8-μm dimension. Thus, the resolution shown in table 1.2 is only a confirmed value and does not indicate the true limit of the EO field mapping.

One important feature of the EO field mapping is cross polarization suppression capability. This characteristic indicates the capability of the EO field mapping to separate one electric field component from others. Due to the excellent cross polarization

suppression of the EO field mapping (> 30 dB), an additional polarization grid is not required to separate each component during the EO field measurements.

1.3 Photoconductive Sampling

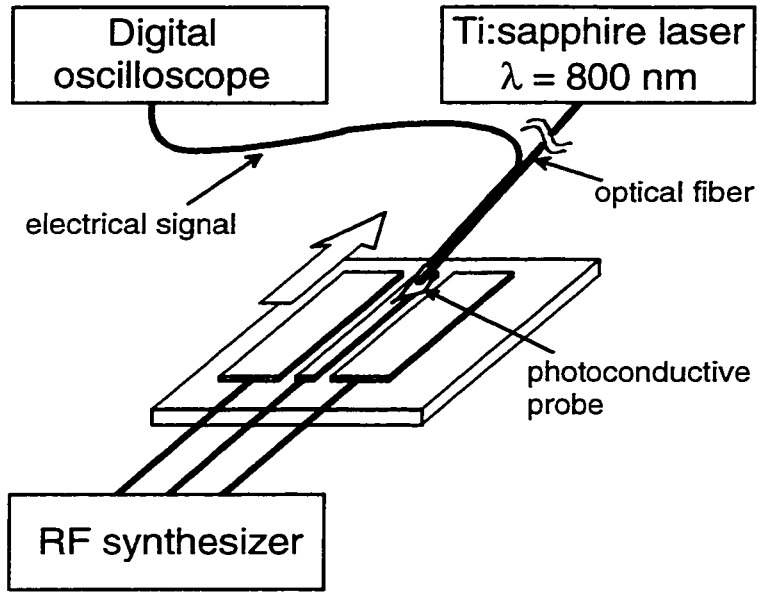

Figure 1.3: Photoconductive sampling schematic

Electro-optic (EO) field mapping techniques are able to provide high-resolution, broad bandwidth electric field distributions of various micro- and millimeter wave structures. However, for integrated circuits, potential distributions can be more helpful information than electric field distribution around the circuits. In particular, an absolute potential measurement inside of a circuit can provide crucial information about the operation of the circuit.

A photoconductive measurement technique, which is another application of short pulse lasers for high-frequency measurement, relies on a fast, laser driven photoconductive switch to transfer small amount of charge from a test point in a DUT to

an external source follower JFET buffer [22]. The photoconductive switch, fabricated on a fast-relaxation, low-temperature-grown GaAs, behaves as a sampling gate activated by ultrafast laser pulses. The small capacitance of the JFET source follower is charged up by the signal from the photoconductive switch and generates a voltage signal that is collected by external readout equipment. Unlike the electro-optic measurement technique that has sensitivity to the electric field, a photoconductive measurement technique has sensitivity to the potential. The photoconductive measurement can detect absolute voltages at test points by calibration of the output signal from the source follower amplifier. Especially, this method has its advantages for measurement of integrated digital circuits [23][24] or integrated analog circuits without confined ground planes. Also, this method has much better sensitivity than the electro-optic method due to the direct contact scheme.

Figure 1.3 shows the schematic of conventional photoconductive measurement setup. A CPW line is shown as a DUT. The optical signal from the Ti:sapphire laser propagates through an optical fiber and illuminates a metal-semiconductor-metal (MSM) interdigitated switch on the photoconductive probe. The electric signal detected from the probe travels through an electrical wire to the readout equipment. In Fig. 1.3, a digital oscilloscope is shown as the readout equipment. However, other equipment such as a Lock-in amplifier or spectrum analyzer can be used instead of the digital oscilloscope with respect to the measurement purpose. Also, Fig. 1.3 does not include the JFET amplifier after the MSM switch in order to display only basic components used in photoconductive measurement. A detailed description can be found in Chapter 7 of this thesis.

1.3 Scope and outline of this study

This dissertation consists of 8 chapters. In Chapter 1, the basic properties of electro-optic and photoconductive measurements are described. In addition, according to the their embodiments, three EO field mapping methods are categorized into three generations, and their advantages are compared.

In the beginning part of Chapter 2, the free-space electro-optic measurement system configuration is presented along with some detailed properties of the system. For the demonstration of high-resolution, near-field measurement capability for integrated circuits, a microwave distribution network circuit is fabricated and measured. Also, comparison results between functioning and malfunctioning parts are presented as a demonstration of fault isolation.

In Chapter 3, electro-optic mapping results of various radiating structures, including a microstrip patch antenna, a grid oscillator, and quasi-optic amplifier arrays are presented. Complete three-orthogonal-field-component measurement results of the patch antenna are described. Also, the near-field patterns obtained from finite element method (FEM) simulations are compared with the measured results for patch antennas. In order to explain an unusual phase distribution of the grid oscillator, an analytically calculated far-field pattern is presented along with electro-optic measurement results. For the quasi-optical amplifier arrays, the electro-optic measurement technique is used as a feedback measurement tool that provides valuable information to improve the performance of the arrays. Also, a substrate mode propagation wave is measured and 2 dimensionally mapped for the first time.

An electro-optic measurement system utilizing GaAs probes is described in Chapter 4. In the course of the chapter, comprehensive theoretical analysis of the electro-optic effect in GaAs is presented. The results with GaAs probes are compared with the

results obtained by other electro-optic crystals. Also, successful measurement of electric field at 100 GHz is demonstrated.

In Chapter 5, the detailed development of the third generation fiber-based EO field mapping system is explained along with operating principles of the system. For the demonstration of the capabilties of the system, three field components of a folded slot antenna were measured separately by the fiber-based EO field mapping system. Also, field distributions in the aperture and the inside plane of a Ka-band horn antenna including an electric field scattering metal structure inside were mapped. A successful field imaging inside of a shielded microstrip cavity highlighted the measurement versatility of the fiber-based EO field mapping system.

Based on the advantages obtained from the EO field mapping method, a new accurate near- to far-field transformation technique is developed, and detailed procedures are covered in Chapter 6. Also, a radiating wave front recovery technique based on the near-field data obtained from the EO field mapping method is discussed in Chapter 7.

As another high-frequency, high-resolution measurement technique, photoconductive sampling is discussed in Chapter 8. A 3-stage SiGe amplifier MMIC is selected and measured. The measured results obtained on internal points of the circuit are compared with LIBRA simulation results.

Finally, Chapter 9 finishes the thesis by providing a conclusion and proposals for future work.

CHAPTER 2

ELECTRO-OPTIC MAPPING OF NEAR-FIELD DISTRIBUTIONS IN INTEGRATED MICROWAVE CIRCUITS

2.1 Introduction

Electromagnetic field probes are used for a variety of applications in RF metrology where knowledge of electric field structure is required. These include such diverse areas as the characterization of near-field patterns of antennas and antenna arrays, verification of electromagnetic compatibility (EMC) of electronic equipment, and failure diagnosis of microelectronic integrated circuits. Mainly techniques using dipole- or monopole-type probes [25]-[27] have been pursued, although the optically based technique of electro-optic (EO) sampling [4][28] has also been investigated. The features that make the EO techniques very promising for near-field measurements are extremely broad bandwidth (into the THz regime for systems using ultrashort-pulse lasers as optical sources) and a spatial resolution on the order of the size of the laser beam diameter or even less. Furthermore EO sampling does not require electrodes or ground planes as a part of the field probe so that, compared with conventional probes, the invasiveness is minimized. Since the measurement height can be reduced to a several microns range above a device under test (DUT), the EO field mapping has a capability of measuring near-field distributions from the DUT.

Electro-optic measurements of field distributions of guided microwaves have been extensively demonstrated within monolithic microwave integrated circuits using the substrate of the circuits as the sensor element (internal EO sampling). These

measurements have revealed information for circuit characterization and failure detection [29]-[31] and could be used for verification of electromagnetic simulations. If the substrate does not exhibit the linear EO effect, and moreover when field patterns outside the substrate need to be known, external EO sampling has to be used. This technique uses an EO crystal as an electric field probe, which is inserted into the electric field to be characterized. Measurements of near field patterns of antennas and stray fields of simple waveguide structures [32]-[34] have been performed in this way. However, the potential of this technique with respect to the full characterization of the electric field inside integrated circuits, i.e., in terms of the different field components in amplitude and phase inside a microwave integrated circuit, has not been shown up to now.

In this chapter, the development of an EO field mapping system is described in detail including the optical and electrical configurations. Furthermore, as an example of the capability of the EO field mapping system, measurements of near-field distributions of guided waves above an integrated microwave circuit are demonstrated using a distribution network having structure sizes down to 20 μm as an example DUT. The measurements are carried out using two different miniaturized probes. The footprints of these probes are reduced by a factor of 5 to 10 compared with conventional EO probes that have been used, so that their size becomes equivalent to or even smaller than the investigated structures inside the DUT. The measurements reveal distinct field distributions of either the normal or the tangential field components in amplitude and phase. Using this information, the performance of circuit elements has been analyzed up to 20 GHz thus far. Moreover, fault isolation has been performed comparing results obtained in a functioning structure operated accordingly to its design and several non-functioning structures. This has demonstrated the ability of this mapping technique to locate malfunctioning devices by studying the electric field distribution of a circuit.

2.2 Measurement System Configuration

The measurement setup used is shown in Fig. 2.1. The whole setup is built on an optical bench. A phase-stabilized Ti:sapphire laser that has 100-fs pulse width and 80-MHz pulse repetition rate is used as source of optical beam. The laser system is equipped with a Lock-to-Clock system that provides phase-locked loop (PLL) stabilization of output pulses. This PLL allows precise synchronization of the output to the internal 80 MHz reference source. To stabilize the phase of the output pulse, the PLL control electronics unit adjusts the dimension of the cavity by controlling a servomotor and a piezo positioner. Another unique feature of the laser system is its adjustable output wavelength. The output wavelength can be adjusted between 690-nm to 1080-nm range. This feature allows one to utilize various EO crystals for the measurement.

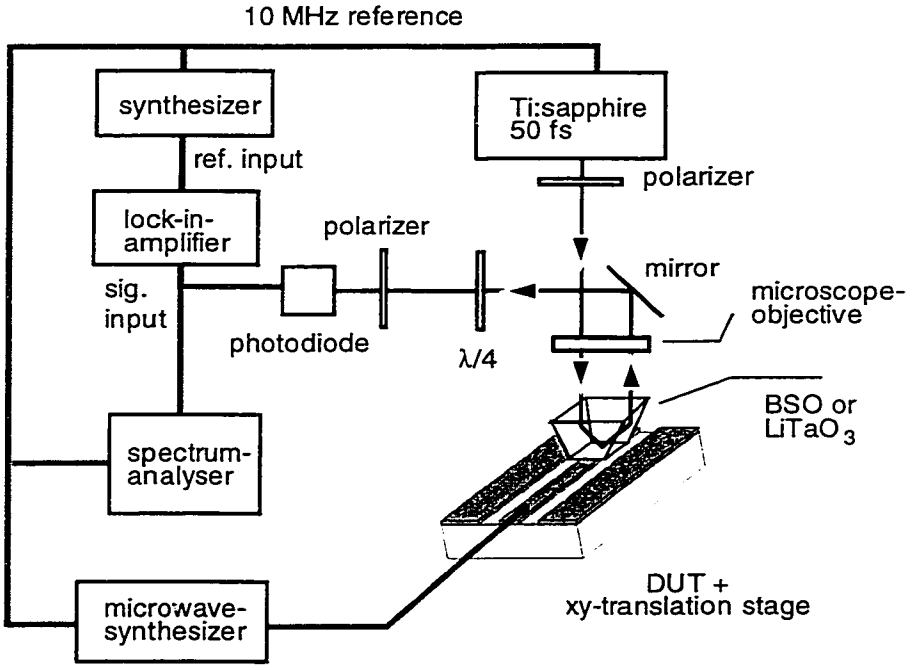

Figure 2.1: Electro-optic probe station schematic

The optical path from the laser to the photodiode can be divided into two sections; one is stationary and the other is maneuverable section mounted on a separate board. The stationary path consisting of a number of mirrors and a polarizer (in Fig. 2.1) defines the beam path from the laser system to a periscope mirror. In the stationary path, the traveling beam is parallel to the top of the optical bench. After illuminating on the periscope mirror, the beam changes its propagation into the vertical direction, and now the beam follows the maneuverable path. The board supporting optical components in the maneuverable path is perpendicularly aligned to the top of the optical table using vertically adjustable base. The maneuverable path is started with a periscope mirror that makes optical coupling to the periscope mirror at the end of the stationary path. Since the two periscope mirrors make vertical beam transition of the beam, the incident condition of the beam to the maneuverable path maintains same condition regardless of the distance change of the maneuverable board (path) to the optical table. The beam direction from the periscope mirror (in maneuverable path) is changed toward a focusing microscope objective by an infrared dichroic mirror that reflects only the light with infrared-range wavelength. As a result, one can observe the EO crystal through the dichroic mirror during the laser alignment process.

Eventually, the optical beam from the dichroic mirror is focused inside the EO probe crystal though a microscope objective, which is one of optical components in the maneuverable path. To enhance the sensitivity of the EO system, it is important to minimize the loss of the beam while it reflects from the EO crystal. In order to minimize the loss, the side facets of the EO crystal are polished to satisfy a total reflection condition. Thus, the incident beam is focused into one of the side facet instead of being directly focused in the bottom of the crystal (Fig. 2.1). The side facet is polished to be slanted about 40° from vertical direction. The beam reflected from the facet is then bounced from the bottom facet and reflected by the other side facet. The incident beam is totally reflected, so that no illumination of the circuit under test occurs. In the course of

traveling inside of crystal, the polarization of the beam is modified by the electric field inside of the crystal and Pockels effect. The reflected beam from the crystal is analyzed with respect to the change of the polarization state, which is sensitive to the circuit electric field reaching the probe. This is performed using a Pockels-cell arrangement consisting of a combination of polarizers and retardation plates. In orther words, the analyzer (polarizer and wave plate) transforms the EO signal in the form of polarization variation into the power variation of the beam. Then, the photodiode converts the intensity variation into the electrical signal. The EO signal is measured in a harmonic mixing scheme at an intermediate frequency of several MHz using an RF lock-in amplifier or a spectrum analyzer. Figure 2.2 shows the concept of the harmonic mixing technique used in the measurement.

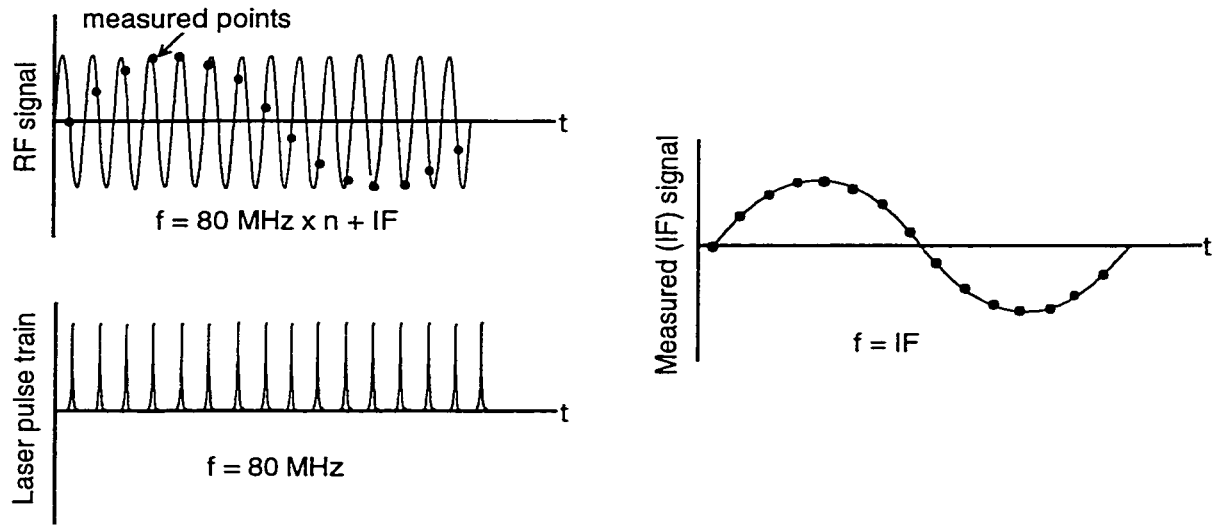

Figure 2.2: Concept of time-harmonic mixing scheme

Figure 2.2 displays the laser pulse train, the RF signal, and the measured IF signal as a function of the time, t. In the EO field mapping, the EO crystal detects the electric fields at the exactly same position with the laser pulses in the time domain. During the

measurement, the RF signal is the sum of an integer multiple (n) of the laser pulse frequency (80 MHz) and a small offset IF frequency. Since the pulse frequency of the laser is much smaller than the operating frequency of microwave or millimeter wave structures, the integer multiple of the pulse frequency can be selected very closely to the actual operating frequencies of the DUTs. The maximum difference between the actual operating frequency and the integer multiple of pulse repetition frequency can be 80 MHz. If one sets the RF frequency without an IF frequency, the positions of the laser pulses correspond exactly the same positions of the RF signal. As a result, the measured signal should show a uniform value with respect to time. However, by adding the IF and the RF frequency, now the laser pulses can detect slightly different positions in the RF signal. As a result, the measured EO signal has very low IF frequency as shown in Fig. 2.2. Thus, the electric network after the photodiode (Fig. 2.1) does not need to handle high-frequency signals. The IF frequency can be selected independently with the operating frequency of the DUT. For the actual measurement, the 3-MHz IF frequency is added to the 15.040 GHz (188×80 MHz). The odd number IF frequency is selected intentionally, because most electronic equipment is operated by even number frequency power source (60 Hz AC), and thus, the possibility of the noise from the AC power source can be minimized.

In addition, due to phase-locked-loop electronics in the laser system, it is possible to synchronize cw signals from a microwave synthesizer to the laser pulse train. As a result, the lock-in amplifier reads amplitude and phase simultaneously. This feature is very important to characterize any microwave and millimeter wave DUT, because the amplitude of near field often fails to provide sufficient information to analyze the DUT without phase information. Especially, accurate phase measurement has been one of the most difficult obstacles for traditional near-field measurement methods. However, by utilizing the EO field mapping method, accurate phase data can be obtained along with

the amplitude information without any post processing, and it emphasizes the superiority of the EO field mapping technique over other conventional near-field mapping methods.

In order to achieve the two-dimensional field mapping, the DUT is mounted on the computer controlled x-y translation stage that has the movement resolution of 0.1 μm. For the control of the translation stage and data acquisition, a PENTIUM-II level personal computer is used. A scanning control program has been developed using National Instrument LabVIEW software. The control program acquires amplitude and phase data from the Lock-in amplifier shown in Fig. 2.1 at every measurement point.

Complete three electric field components measurement can be achieved using only one type of EO crystal by reconfiguring the orientation of the crystal and direction of the detection beam. However, as mentioned in Chapter 1 of this thesis, it is very inconvenient to modify the direction of the detection beam to the EO crystal. Thus, it is more practical approach to use two different types of crystals in order to detect a normal (to the surface of DUT) field and two tangential fields. The two tangential field components can be easily separated by simply rotating the DUT (or crystal) by 90° with respect to the EO crystal (or DUT).

Two different types of EO probes employed in this work were fabricated from Bismuth Silicate (BSO) and Lithium Tantalate ($LiTaO_3$), which allow the determination of the normal and the tangential field components, respectively. The EO crystals have much smaller invasiveness than any conventional near-field probes utilizing metal structures such as open waveguides or small antennas. However, it is still desirable to miniaturize the EO crystal to minimize the invasiveness of the crystals. Also, during the miniaturizing process, the side facets of the crystal can be polished to achieve a total internal reflection condition. The polishing process starts with cutting the EO crystal slab into small crystal cubes that have about 1.0 mm × 1.0 mm top and bottom surface. Both BSO and $LiTaO_3$ have about 1.0-mm thickness. The crystal cube is then mounted at the end of the silica post that are used as sacrificial material for the polishing. During the

polishing process, the crystal is rotated by 90° to form four side facets, and the angle between the crystal and polishing wheel is adjusted to be 50° to achieve a total internal reflection condition. After finishing the polishing process, the crystals have a footprint of 40×40 μm for the BSO, and 20×10 μm for the $LiTaO_3$.

The distance between probe and DUT is adjusted to be 5-7 μm. This distance avoids capacitive loading of the circuit and therefore minimizes the invasiveness of the measurement technique [35]. The minimum detectable voltage is measured to be about 1 mV or -45 dBm for 50 Ω geometries, and the sensitivity is 40 $mV/\sqrt{Hz}$. The DUT is mounted on a computer-controlled x-y-translation stage, and the microwave signal is applied via on-wafer probes. Typical measurements including 6400 points were carried out in approximately 45 min. This duration was mainly limited by the speed of the translation stage and has been improved to about 20 min. by using an improved translation stage.

2.3 1×4 Power Distribution Network Fabrication

A power distribution network that has one input port and 4 output ports is designed to have operating frequency of 15 GHz. For 1 × 4-power dividing, one T-junction and two Wilkinson power dividers are utilized. Coplanar waveguide (CPW) transmission line is utilized as a basic structure of the network circuit. To achieve 50 Ω characteristic impedance, the dimensions of the widths of the center conductor, gap between the center conductor and the ground planes, and the ground plane are designed to be 40 μm, 24 μm, and 106 μm, respectively. The signal applied into the input port propagates through the 50 Ω CPW line. The T-junction network then divides the input signal into the two signals and delivers them to the two Wilkinson power dividers. Since the T-junction makes one-to-two transmission line transition, the modification of the CPW geometry is required to achieve impedance matching. For the impedance matching,

the CPWs in the T-junction should have 70.7 Ω characteristic impedance, which is $\sqrt{2}\times 50$ Ω. To make 70.7 Ω CPW line, the center conductor width is adjusted to 16 μm. Also, the size of the gap is modified to 35 μm. The signal from the T-junction is then divided into two again by the Wilkinson power divider. Since there are two Wilkinson power dividers, the original input signal that already divided into two by the T-junction is now divided into 4 signals. For the Wilkinson power dividers, CPW to coplanar strip (CPS) transitions are utilized. However, these unbalanced CPW to CPS are replaced with balanced CPW to CPW transitions for better performance. Finally, the signals from the two Wilkinson dividers are delivered into the four output ports via 50-Ω CPW lines. In order to investigate usefulness of the EO field mapping for the performance validation of the power distribution circuit, two different terminations are used for the four output ports. For the normal operation condition, the four ports are terminated by 50-Ω resistors. Also, open terminated circuits are fabricated at the same time to make the comparison with functional circuit. In addition, a distribution circuit that has intentionally designed short point is fabricated to demonstrate the fault isolation capability of the EO field mapping system.

The three different types of the power divider circuits – 50 Ω matched termination, open termination, and matched termination with short point – are fabricated high-resistance silicon wafer. For the 50 Ω termination, a NiCr alloy is used as thin filme resistor. Since the thin film resistor layer is very thin with respect to the metal transmission lines, the thin film resistors are deposited before the transmission line deposition in order to avoid contact failure between the resistor and metal line. A positive type photoresistor PR 1813 is spin coated and patterned by photolithography process. A NiCr alloy is then deposited by evaporation process. The sheet resistance of the NiCr is 50 Ω/□ with the thickness of 350 Å.

A positive type photoresistor PR 1827 is spin coated and patterned by lithography process. For the metalization of the circuit, Ti/Al/Ti/Au layers of 500/11000/500/5000-Å

thickness are deposited from the top of the silicon substrate, and lift-off process is used to form the circuit. The two Ti layers are deposited to enhance adhesions between metal-to-metal or metal-to-silicon interfaces. The thick Al layer is sued to reduce ohmic loss of the transmission line. The top Au layer protects the transmission line from the corrosion or oxidation, and as a result, maintains good electrical contact.

After finishing the transmission line fabrication, a number of air bridges are formed in order to suppress unbalanced higher-mode propagation of CPW lines. The detailed fabrication procedures for the power distribution circuits can be found in appendix A.1 of this thesis.

2.4 Experimental Results

2.4.1 Coplanar Waveguide

Figure 2.3(a) and (b) display typical EO field maps of the electric normal and tangential field components for an even mode on a coplanar waveguide in the transverse direction. Figure 2.3(a) shows one-dimensional mapping at 15 GHz using BSO, with a high EO signal on the center conductor and a low EO signal on the ground conductor corresponding to the strength of the normal field component. A phase change of 180° between the center conductor and the two ground planes is observed. The results indicate the high electric field concentration on the center conductor and relatively weak electric field on the ground planes, and the normal fields on the center conductor and on the ground planes are in opposite directions.

Figure 2.3(b) shows 1-D measurements of the tangential components at 15 GHz using the $LiTaO_3$ probe. Corresponding to the strength of the tangential field component in the x-direction (for coordinate system see Fig. 2.1), the maximum signal appears above

the spacings with a phase change of 180 degrees taking place over the center conductor. From the normal and tangential electric fields obtained by the EO field mapping, one can concludes that the electric field is initially generated at the center conductor in normal direction. As the field travels from the center conductor into air it changes its direction from normal to two opposite tangential directions. Then, eventually, the fields change their directions toward ground planes. Since the width of the ground plane is much bigger than that of center conductor, the electric field density is lower on the ground plane than on the center conductor. These 1D field maps demonstrate the excellent discrimination in electric field components available using external EO sampling.

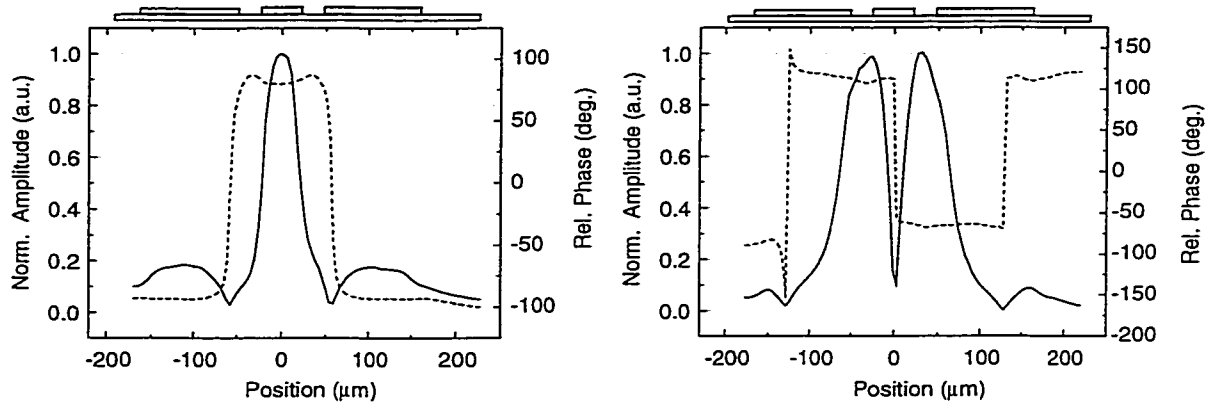

(a) (b)

Figure 2.3: Electro-optic mapping of the (a) normal field and (b) tangential field component of the even mode on a coplanar waveguide (transverse direction) measured by (a) BSO and (b) $LiTaO_3$ crystals at f = 15 GHz; solid line: normalized amplitude, dashed line: phase; (the center conductor has a width of 40 μm, with spacings of 24 μm).

2.4.2 Microwave Distribution Network

The examined distribution network circuit is a coplanar design (see Fig. 2.4) fabricated on high-resistivity silicon substrate as described in section 2.2. It is based on two Wilkinson power dividers, which distribute the input microwave signal to four output ports. The ports are terminated with 50 Ω thin film resistors, and this matched circuit is considered to be the correctly functioning circuit. The small lines crossing the coplanar structure at discontinuity points are air bridges, and impedance transformations appear at several places.

Two malfunctioning circuits of the same type were also examined. In the first circuit the termination resistors are missing so that the output ports are open terminated. The second circuit is fabricated with a short between the center and one ground conductor near the upper side output of one coplanar waveguide bend as indicated in Fig. 2.4.

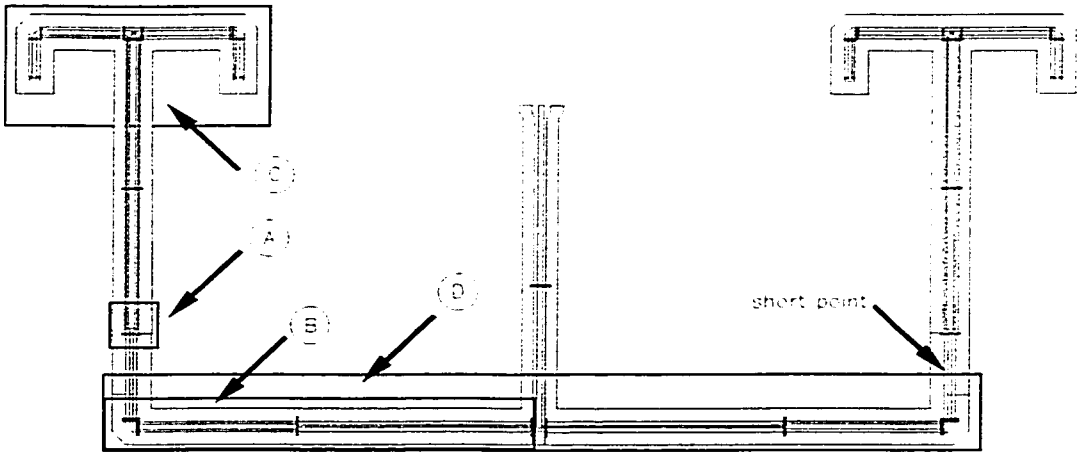

Figure 2.4: Distribution network circuit with investigated areas. Unit circuit size: 8.3 mm × 3.7 mm.

Figure 2.5 shows the results of one port s-parameter measurements of the examined circuits using a conventional microwave network analyzer (HP 8510B). The

three curves represent the forward reflection coefficients of the matched, the partially shorted, and the open-ended circuit, respectively. The matched circuit shows very low reflection in comparison with the two other circuits, revealing its functionality as a distribution network. These measurements clearly show the malfunction of the shorted and the open-ended circuit, but they can not deliver information about the concrete location of the faulty components inside the circuits.

In the rest of this section, examples of 2D field distributions inside the circuits measured using the EO probe station are presented. These measurements reveal additional information about the functioning and malfunctioning performance of the circuits that is not accessible using the external port s-parameter measurement technique.

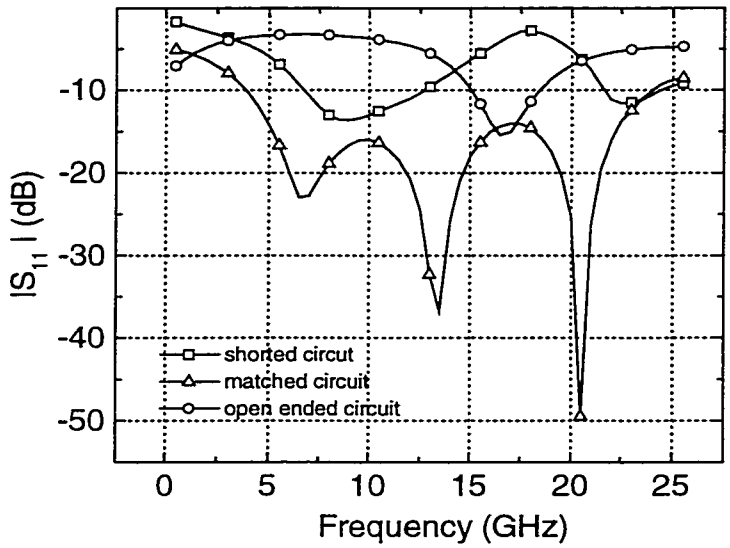

Figure 2.5: Magnitude of the forward reflection coefficient $|S_{11}|$ examined distributions networks

As an example of the vectorial measurement capabilities of the EO technique, Fig. 2.6 displays the normal and the tangential field distribution around the input of the Wilkinson power divider (pos. A in Fig. 2.4). Figure 2.6(a) and (b) show field

distributions that are in good agreement with the 1D field maps in Fig. 2.3 and Fig. 2.4 that have already displayed transverse distributions of the even mode. That is, we can see how the high normal fields are present above the center conductors of the coplanar waveguides for the normal-field probe, and how the tangential-field probe senses a high signal in the spacings of the waveguide. Additionally, the 2D measurements now reveal that a small asymmetric coupling into both signal lines of the Wilkinson divider occurs. Another interesting fact is that the two center conductors in the Wilkinson divider act like single center conductor of CWP line.

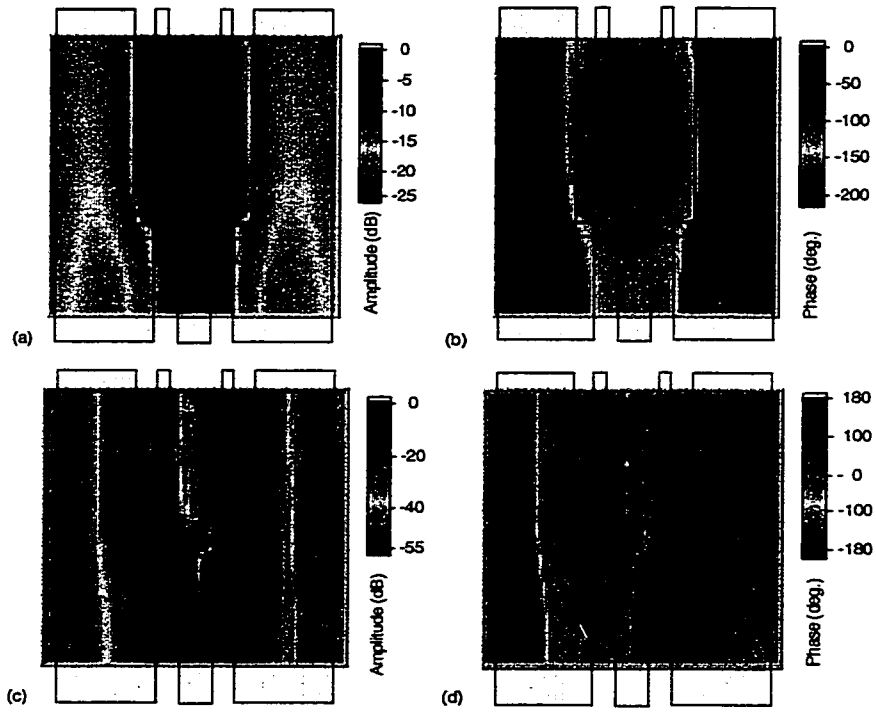

Figure 2.6: Electro-optic field mapping at the input of the Wilkinson power divider at pos. A in Fig. 2.5. f = 15 GHz (scanned area: 375 μm x 400 μm for (a) and (b) and 400 μm x 400 μm for (c) and (d)). (a) normalized amplitude of normal component in dB, (b) relative phase of the normal component in deg., (c) normalized amplitude of tangential component in dB, (d) relative phase of the tangential component in deg.

From Fig. 2.6 (c) and (d) it can also be concluded that at this frequency no significant coupling between the lines is present, since only small tangential field components can be measured in the spacing between them. Note also in all figures that the air bridges screen the electric field of the underlying waveguide from the probe.

Figure 2.7 shows measurements in section B of the network where the length of the transmission line is comparable with the wavelength for the 15 GHz input signal. Figure 2.7(a) and (b) display the result for the functioning circuit and reveal a propagating microwave signal. The phase along the center conductor is changing 140 degrees, which is in good agreement with the expected wavelength of 7.9 mm of the 15 GHz microwave signal on the transmission line. The field amplitude is also consistent across the length of the line, although an impedance transformation from 70 to 50 Ω in the middle of the line changes the CPW dimensions and thus also the field strength that the probe is sensing on either side of the discontinuity. In contrast to this result, the field distribution in the same area for the structure with the open termination at its four outputs reveals a standing wave pattern (Fig. 2.7 (c) and (d)). Field minima and maxima are observed in the amplitude of the open circuit pattern with a phase shift of 180° between the maxima. These malfunctioning circuit measurement results demonstrate how the EO near-field mapping method can be utilized to isolate exact failure positions in integrated circuits. As shown in Fig. 2.5, a malfunctioning circuit can be separated from normal operating circuits by using conventional measurement methods – in this case vector network analyzer measurement. However, the network analyzer fails to provide sufficient information about the cause or position of the fault. In contrast, the EO near-field mapping is able to isolate fault position and also provides the detail information about the effects of the fault inside of the circuit. As a result, the EO near-field mapping can be one of the most effective diagnostic tools for the integrated circuits, and furthermore, it can be used as a validation tool for various circuits. In particular, the detailed information

obtained by the EO field mapping can be fed back to the design process of the circuit to improve the performance of the circuit.

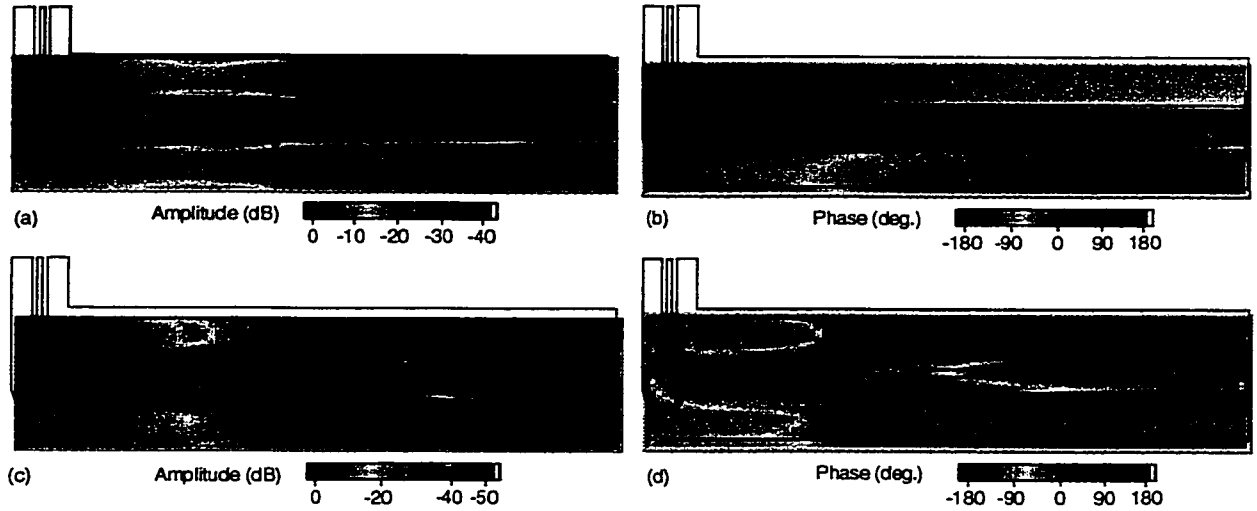

Figure 2.7. Electro-optic field mapping of the transmission line at pos. B in Fig. 2.5. f = 15 GHz, scanned area: 3400 μm x 400 μm. (a) normalized amplitude of normal component in dB (functioning circuit), (b) relative phase of the normal component in deg. (matched circuit), (c) normalized amplitude of normal component in dB (open ended circuit), (d) relative phase of the normal component in deg (open ended circuit).

Figure 2.8 shows the 2-D normal field distribution of the output of the Wilkinson power divider feeding the two output ports (pos. C in Fig. 4). Figure 2.8(a) again displays a propagating microwave signal with uniform field amplitude on the individual divider elements, while this effect cannot be seen in Fig. 2.8 (b). Here the effect of a standing wave with maxima at the terminations is observed, indicating a mismatch of the termination thin film resistors. For Fig. 2.8(a), the EO signals from the vertical and horizontal parts of the structure are not the same because, as for the impedance transformer, different line dimensions yield different field strengths.

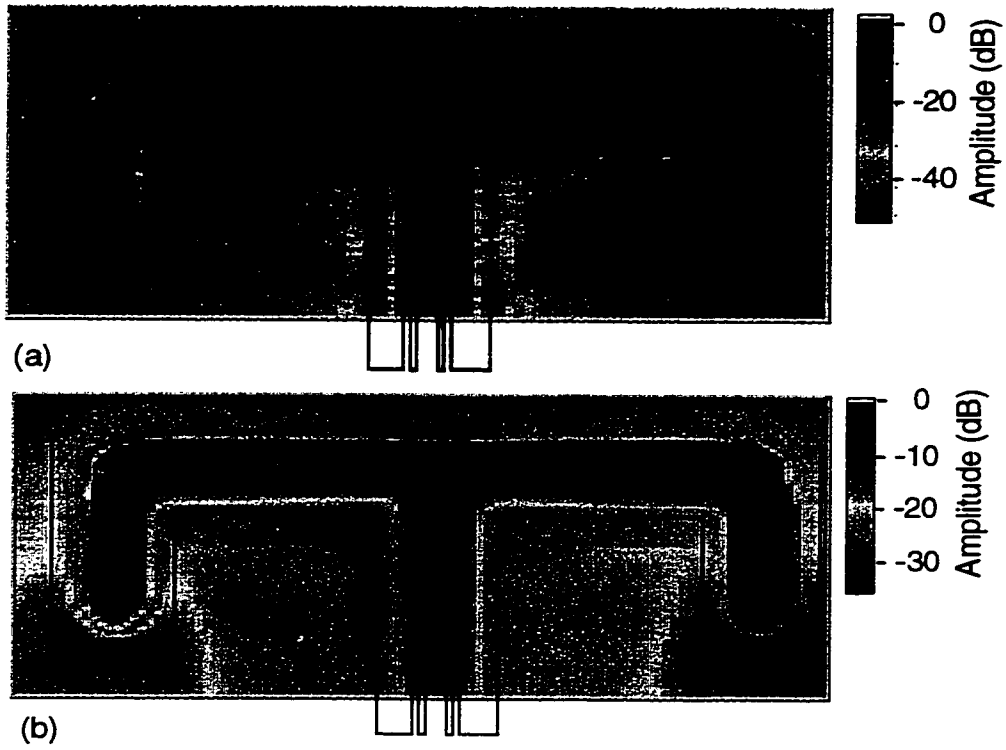

Figure 2.8: Electro-optic mapping of the normal field component of the output of the Wilkinson divider including termination at pos. D in Fig. 2.5. f = 15 GHz, scanned areae: 3200 µm x 940 µm). (a) normalized amplitude in dB (matched circuit), (b) normalized amplitude in dB (open ended circuit)

Fig. 2.9 shows 2D- measurements of the normal field components in section D of the matched and the shorted circuit. The short point is intentionally fabricated approximately 200 µm above the upper output of one of the coplanar waveguide bends (position marked in Fig. 2.4). The matched circuit shows a symmetric field distribution along the transmission lines (Fig. 2.9 (a)), revealing a propagating microwave signal, as well as equal field strengths along the right and left side vertical lines. In contrast, the shorted circuit shows an asymmetric distribution, with a complete absence of normal electric field on the right-hand side vertical structure. As can be seen from Fig. 2.9 (b) in

the amplitude, and additionally from the corresponding phase measurement (not shown here), a standing wave pattern is present in front of the short point, while the microwave signal can not be detected passing the short point.

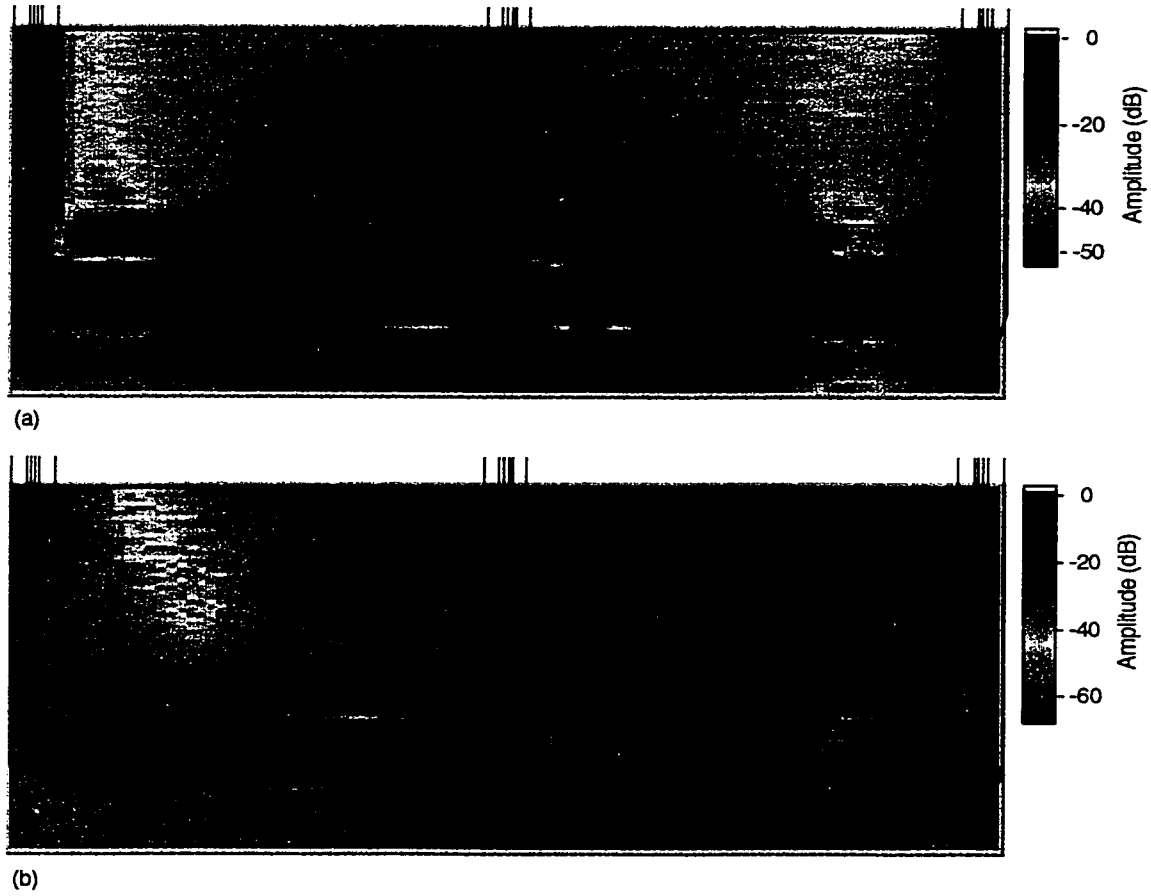

Figure 2.9: Electro-optic field mapping of the transmission line at section C in Fig. 2.5. Operating frequency, f = 15 GHz. normalized amplitude of normal component in dB, (a) matched circuit, (b) partially shorted circuit

2.6 Summary

A free-space electro-optic (EO) near-field mapping system utilizing two different miniaturized EO crystals has been developed. By utilizing the two EO crystals, complete

three-orthogonal field components were measured. The EO field-mapping system was demonstrated its broad bandwidth and high-resolution measurement capability. Also, the EO system does not require any electrodes or ground planes as a part of the field probe. As a result, the invasiveness of the probe to the device under test (DUT), can be minimized with respect to other conventional near-field measurement methods in which metal structures are utilized as field sensors. Furthermore, by using common reference signal configuration, the EO system has the capability of measuring accurate phase and amplitude data simultaneously.

To demonstrate the capability of the EO field-mapping system, two-dimensional near-field mapping of a microwave distribution network is performed, revealing insight into the normal and tangential field components inside the circuit. The technique makes it possible to investigate the microwave performance of single components within a circuit. An analysis of effects due to electrical short and open termination of the output ports has provided information on how such faults affect the internal operation of the circuit.

In conclusion, the results demonstrated that the external EO field mapping technique is a powerful tool for accurate fault isolation and performance verification of various microwave and millimeter wave integrated circuits.

CHAPTER 3

ELECTRO-OPTIC MAPPING OF RADIATING STRUCTURES

3.1 Introduction

The expanding use of microwaves in areas such as satellite communications, wireless and mobile communications, navigation, remote sensing, etc. has fueled an increasing demand for accurate characterization of microwave antennas. In particular, antenna arrays, such as those found in quasi-optic power combining systems, would benefit from a diagnostic technique that could determine the amplitude and phase of the electric field radiated from the individual elements. This has prompted the development of the electro-optic measurement system – one that provides high spatial resolution and high measurement bandwidth in order to evaluate the near-field pattern of radiating structures within an extremely close range from an antenna under test.

A number of electro-optic measurements of the near-field radiation patterns of antennas have been reported [36] [37]. However, previous work has mainly concentrated on one-dimensional scans or the acquisition of only two field components in the near-field pattern. Any determination of the S-parameters of the antennas has also relied upon additional characterization using a conventional network analyzer.

In this chapter, measurements of all three orthogonal electric field components are demonstrated for a variety of radiating structures. The first is a microstrip patch antenna that is designed to have a 4-GHz resonance frequency. Measurements include a near- to far-field transition, as well as near-field amplitude and phase measurements of the complete patch antenna radiation pattern. For comparison, a three-dimensional Finite

Element Method (FEM) simulation has been performed for the investigated antenna structure. Even though electro-optic measurement results are found to be superior to the FEM simulation results in terms of spatial resolution and data acquisition time, the measurement and simulation show good agreement. In addition, the scattering parameter S_{11} of the antenna is calculated from the electro-optic field map data, revealing the standing wave characteristics of the structure at different frequencies. Finally, these results extracted from the electro-optic field measurements are compared with the S_{11} from a conventional network analyzer.

Also, experimental results for a grid oscillator consisting of 16 radiating elements [38] are presented to illustrate the capabilities of the measurement technique. 2D scans of the amplitude and phase of each of the orthogonal field components (typically two tangential as well as the normal field component) have been made in different planes of the radiation pattern above the grid. The results demonstrate the usefulness of this scheme especially for the characterization of arrays of passive or active radiators. An analytical calculation of the far-field pattern is carried out and the results are compared with measured results.

Finally, measurements of quasi-optical amplifier arrays are performed. The electro-optic measurement presented demonstrates its usefulness to improve the performance of those structures providing detailed information that cannot be obtained by conventional measurement techniques. Furthermore, a substrate mode propagation wave is detected experimentally for the first time.

3.2 Measurement System Configuration

The overall system configuration of the EO system has similar structure as the EO system described in Chapter 2. However, the EO system described in Chapter 2 was developed to measure integrated circuitry. Thus a high-power microscope was utilized to

obtain tight beam focus in the EO crystals, and as a result extremely high-resolution field mapping was possible. However, the presence of the microscope objective within a compact range to the radiating structures can cause undesirable reflections, and as a result, an accurate measurement can be interfered. Thus, the microscope objective is replaced by a single focusing lens in order to minimize the field reflection. Also, in addition to the two-dimensional movement of the translation stage, the distance of the EO crystal to the device under test (DUT) can be adjusted. This vertical freedom of movement makes it possible to measure the near- to far-field transition as well as near field on the DUT.

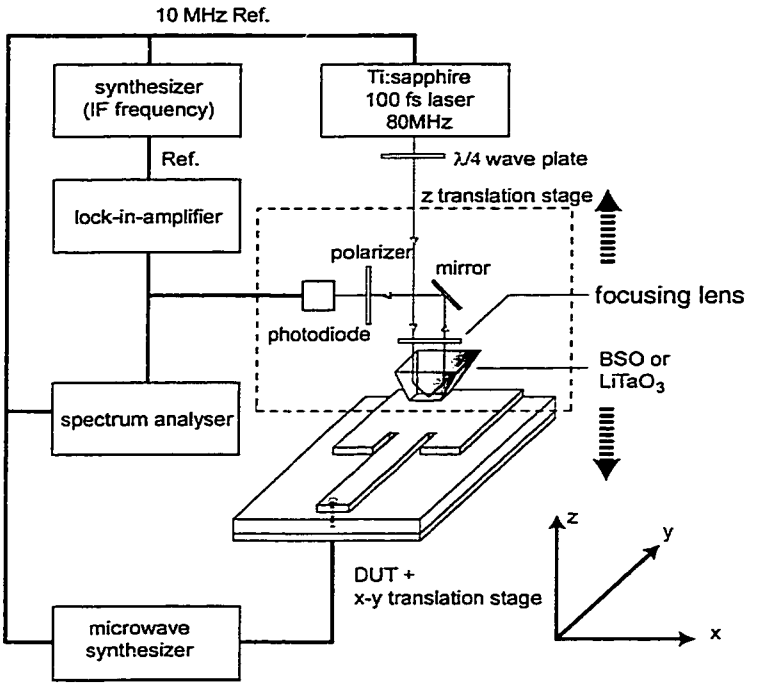

Figure 3.1: Electro-optic measurement schematic for a microstrip patch antenna.

The EO system used for the measurements of radiating structures is shown in Fig. 3.1. The optical beam from a phase-stabilized Ti:Sapphire laser, which has 100-fs duration pulse output at an 80-MHz pulse repetition rate, is focused inside of the electro-

optic probe crystal. The faces of the probe crystal are polished in order to achieve total internal reflection of the incident beam, which is detected by a photodiode. The reflected beam is analyzed to determine the change of its polarization state, which is sensitive to the RF electric field that extends into the probe crystal.

The electrical signal from the photodiode, which is then proportional to the optical signal modulated by the RF electric field in the electro-optic crystal, is measured in a harmonic mixing scheme at an intermediate frequency of several MHz using an RF lock-in amplifier or a spectrum analyzer. The IF signal is derived from the difference between the input signal frequency and an integer harmonic of the 80-MHz repetition rate. In actual measurements, the 3-MHz IF signal is utilized. For example, the patch antenna shown in Fig. 3.1 as a DUT has operating frequency of 4 GHz. During the measurement, the synthesizer provides 4.003 GHz signal to the patch, which is sum of 4-GHz RF and 3-MHz IF signal. By using the harmonic mixing scheme, the measurement equipment measures low frequency IF signals regardless of the operating frequency of a DUT. As a result, the EO system does not require any high-frequency readout equipment, which is advantageous in terms of cost and ease of signal connections. The detailed harmonic mixing scheme can be found in Chapter 2 of this thesis.

Using phase-locked-loop electronics in the stabilized laser system, one is able to synchronize the cw signal from a microwave synthesizer to the laser pulse train, with the small offset frequency providing the time delay for the sampling gate. Measurements in amplitude and phase are then performed simultaneously as the computer reads the output of the two channels of the lock-in amplifier, which uses the output of a low-frequency synthesizer, also synchronized to the laser electronics, to maintain a phase reference.

The two types of electro-optic probes utilized in this work are fabricated from Bismuth Silicate (BSO) and Lithium Tantalate ($LiTaO_3$). The side facets of the crystals are polished to be 50° tilted from the vertical direction in order to achieve a total internal reflection condition. The incident beam into the crystal is focused on one of the tilted side

facet (incident facet) and changes its direction to the bottom of the crystal. The beam reflected from the bottom facet propagates onto the opposite side facet, and reflected into air through the top facet of the crystal. In the course of the propagation, the beam maintains total internal reflection angle to all reflection facets – incident side facet, bottom, and opposite side facets. Thus, a loss of the beam power can be minimized, and as a result, the sensitivity of can be maximized. The polarization of the incident beam is modulated by the electric field inside of the EO crystal (Pockels effect), and this polarization difference is converted into the modulation of beam power by a polarizer in front of the photodiode. More detailed theory of the polarization modulation of the EO crystal can be found in Chapter 4 of this thesis.

The BSO and $LiTaO_3$ crystals allow the determination of the normal and tangential electric field components above the antenna under test, respectively. The crystals have a tip area of 40×40 μm for the BSO and 20×10 μm for the $LiTaO_3$. The antenna is mounted on a computer-controlled x-y translation stage. In addition to the two-dimensional movement of the DUT, several optical components have freedom of movement in the vertical direction (area shown in the dashed box in Fig. 3.1), in order to achieve three-dimensional field mapping capability. The minimum detectable voltage is measured to be about 1 mV, or –45 dBm, and the sensitivity is 40 mV/$\sqrt{Hz}$.

3.3 Results I – Microstrip Patch Antenna

The microstrip patch antenna that served as the DUT was designed for a resonance frequency of 4 GHz. The antenna has 15-μm-thick Cu metallization on both sides of a 2.55-mm-thick Duroid substrate that has a dielectric constant of 10.3. The dimensions of the antenna are 8 mm along the x-direction and 11.18 mm in the y-direction (Fig. 3.1). Also, impedance matching insets, which have 0.5-mm width and 6.1-mm length are fabricated along the feed line. The back-side coaxial feeding method is

employed for the antenna as depicted in Fig, 3.1. The center conductor of the feeding coaxial cable is connected to the antenna through the 2.2-mm-wide and 34-mm-long microstrip line. During the two-dimensional field mapping, the unit step size of the scanning was 200 μm × 250 μm along the x- and y-axes, and 80 × 80 points were taken. The total elapsed time for the scanning was about 30 minutes.

3.3.1 Three-Dimensional Electro-Optic Field Mapping

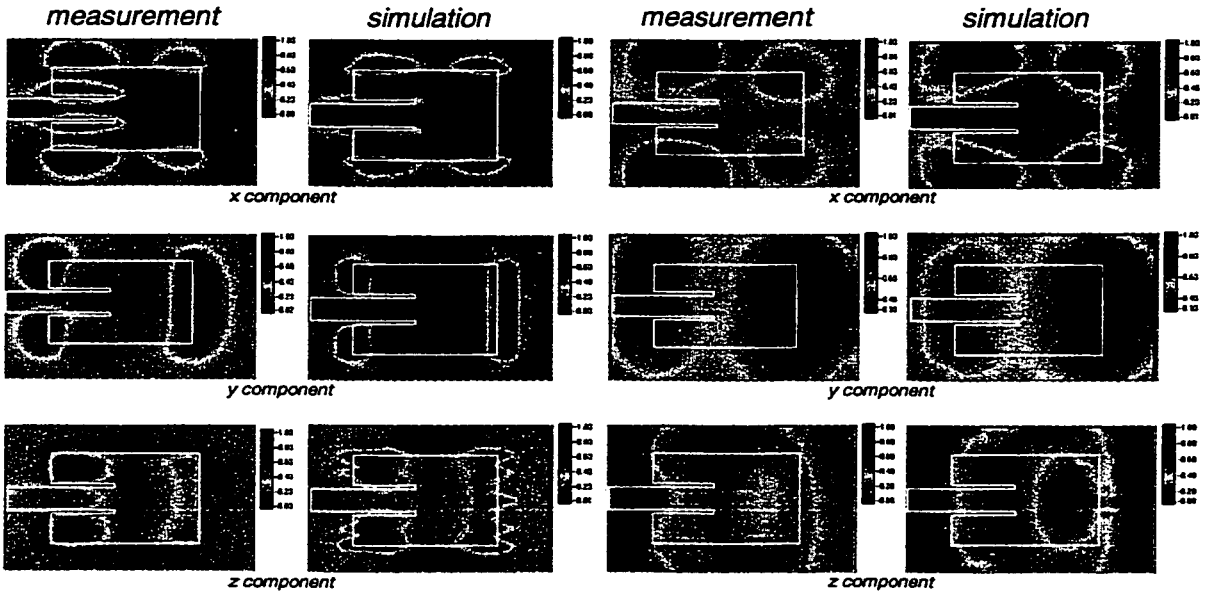

Figure 3.2: Measured and simulated amplitude field pattern for three orthogonal components of patch antenna at 4.003 GHz. All values are normalized. The perimeter of the antenna is indicated by the solid white line. (a) measurement height: 0 mm (~100 μm); (b) measurement height: 5.0 mm.

Figure 3.2 shows the amplitude of three orthogonal electric field components at two different detection heights, with the perimeter of the antenna superimposed to

indicate the position of the metal patch. The direction of each component corresponds to the axes shown in Fig. 3.1. Each component is normalized to its maximum value. The left-hand column of Fig. 3.2(a) depicts the measured amplitudes at a reference level of 0 mm, approximately 100 μm away from being in contact with the patch antenna. Because the length of the antenna (along the y-direction) is designed to be a half wavelength at the resonance frequency, the potential reaches its maximum value at the edges of the patch close to the feed line and at the farthest extent from the feed. Following the potential distribution, the maximum electric field in both the x and y tangential directions can be observed around the edges of the patch and near the ends of the long dimension.

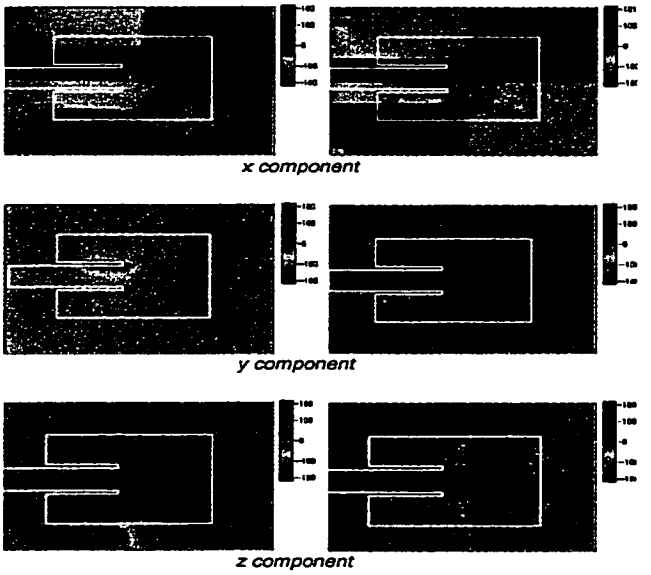

Figure 3.3: Measured (left) and simulated (right) phase for three orthogonal field components of the patch antenna at 4.003 GHz and 0 mm height. The scale is in degrees.

For the measurement of the normal electric field component (z-component), the BSO crystal probe is used. The z-component measurement result clearly displays the peak electric field around both near- and far-edges of the antenna (relative to the feed

end). Because the z-component represents the normal field, the peak amplitude appears primarily over the metal of the antenna and near the edges. The x- and y-components (tangential fields), on the other hand, have their peak amplitudes outside the antenna pattern around the edges, where the probe captures the electric field as it becomes parallel to the plane of the patch. For the measurement of the tangential components, a $LiTaO_3$ crystal probe is employed. The two-directional sensitivity has been obtained in separate scans after rotating either the DUT or the probe by 90°.

For the electric field x-component, the peak amplitudes are observed along the corners of the long side edges of the antenna and between the patch and the matching-section insets. The four peaks around the corners of the antenna are explained by the potential distribution on the antenna, which is described at the beginning of this section. Due to the phase difference of the voltage between the feed line and the near-side edge of the antenna (as seen in Fig. 3.3), two peak amplitudes also occur at the impedance matching insets. For the y-component, the electro-optic field map measurement shows peak amplitudes on both the near- and far-side edges of the patch. These two y-component peak amplitudes also correspond well to the expected potential distribution on the antenna.

In order to verify the trends of the electro-optic measurements, a three-dimensional FEM simulation of the patch has been performed. The right-hand column of Fig. 3.2(a) shows the FEM simulation results at 0-mm height, right at the surface of the patch. For this FEM simulation, 183,816 mesh elements were used, and a calculation time of approximately 1.5 hours with a SUN ULTRA SPARC-2 workstation was necessary to produce one field map for the patch structure. All three field components show very good agreement between the simulation and the measurement results. Because of the limited memory capacity of the computer and the long processing time for the simulation, each tetrahedral mesh used in the simulation has a certain low-size limit. This limitation of the mesh size causes sampling errors. For instance, the simulation result for

the z-component shows a relatively coarse field pattern due to the sampling error in the simulation. In comparison, the measurement field pattern from the electro-optic probe indicates a much smoother, more physically intuitive field pattern than the simulation. In overall, the EO field mapping provides better field maps than the FEM simulation. This comparison between the EO field mapping versus FEM simulation strongly suggests that the EO field mapping can be useful tool for the verification of new simulation methods.

3.3.2 Near-Field to Far-Field Transition Measurement

Figure 3.2(b) shows the measurement and simulation results at a height of 5 mm from the patch surface. The measurement result for the x-component shows a more broadened peak pattern than in Fig. 3.2(a) for 0-mm height. Due to the proximity of the two impedance matching insets to each other, the peaks observed on the insets at 0-mm height, which are 180 degree out of phase as seen in the phase maps of Fig. 3.3, rapidly cancel each other as the measurement height increases. As a result, the peaks on the insets can not be observed at 5-mm height, while the other four peaks around the corners are still detectable. For the y-component, Fig. 3.2(a) shows equal peak amplitude on both the near- and far-side edges. However, as the measurement height increases the peak located on the near-side edge decreases more rapidly than the peak on the far-side edge as shown in Fig. 3.2(b). The y-component measurement result is thus illustrating the transient state from the near- to far-field stage. Also, Fig. 3.2(b) shows a very uniform z-component field pattern at 5-mm height. Thus we can conclude that the z-component has far less contribution than the x- or y-components as the measurement height increases. Both of the measurement and simulation results show excellent agreement for all three components. From Figs. 3.2 and 3.3, each peak of the electric field in the x- and z-directions has a 180 degree phase difference with respect to its neighbors. Due to these phase characteristics, the peak fields for the x- and z-components cancel each other at a

relatively long distance from the antenna (i.e., the far field). As a consequence of the rapid field cancellations with height, the x- and z-components show a much quicker decrease than the y-component as the measurement height increases. In contrast, the two peaks of the electric field y- component are essentially in phase with each other. Thus, we can conclude that the y-component is the dominant field component for the patch antenna in the far-field condition.

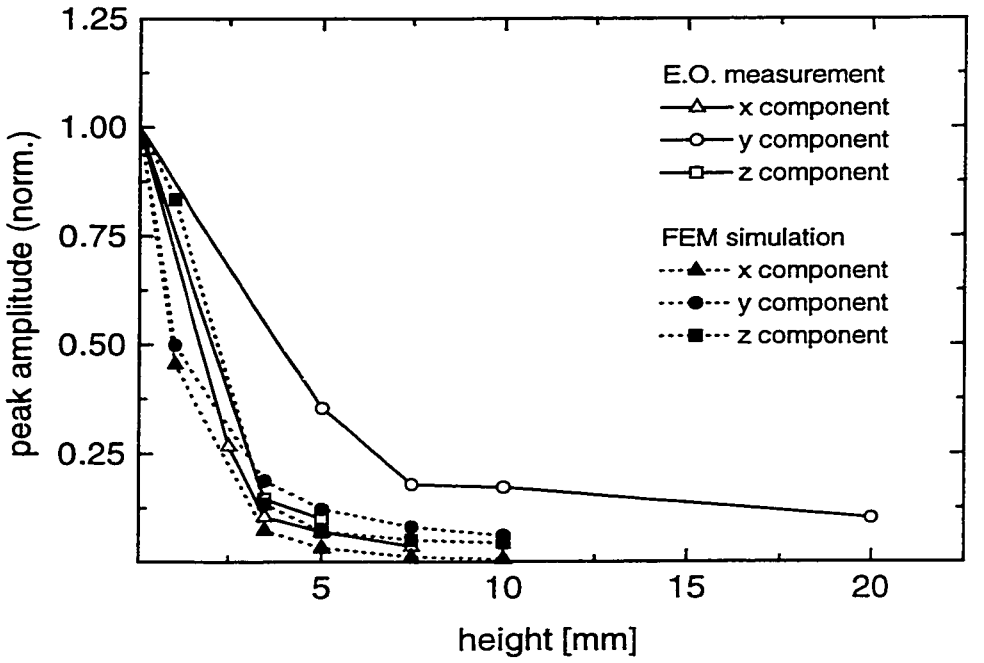

Figure 3.4: Variation in peak electric field with respect to measurement height at 4.003 GHz. Each result is normalized to the maximum value at 0 mm.

To investigate the peak-value variation with height for each electric field component, the field maxima are extracted from each of the 2-dimensional mapping results and normalized to the maximum amplitude at 0-mm height. Figure 3.4 shows the variation of the normalized peak electric field values with respect to the measurement height. All three components show a monotonic decrease as the measurement height

increases. However, the y-component exhibits a slower decrease up to the 5-mm height compared with the x- and z-components. Also, the y-component has a larger peak value compared with the x- and z-components beyond a height of 5 mm. The peak field variations from the 3-dimensional FEM simulation results are presented along with those from the measurements in Fig. 3.4.

Both the x- and z-components show very good agreement between the measurement and the simulation results. However, the y-component shows a noticeable discrepancy between the simulation and measurement results. The discrepancy can be explained by the imperfect absorbing boundary conditions during the simulation. Practically, it is impossible to handle infinite space in the simulation, so an absorbing boundary condition is employed to confine the simulation space. The ideal absorbing boundary condition can not be obtained without knowing the exact field profile. Thus we have to assume the resultant field profile before the simulation to set the absorbing boundary condition. However, the exact field profile can be acquired by the results of the simulation, given the ideal boundary conditions. This imperfection of the absorbing boundary condition causes errors between the real and calculated fields. In particular, the top boundary is more important than the other boundaries in the case of radiating structures (e.g. antennas). In the case of our 4-GHz patch, the x- and z-components decrease very rapidly as the height increases, while the y-component decreases more slowly. Thus, the imperfect absorbing boundary condition has more effect on the y-component than on the two other components. As a result, the y-component simulation result is inconsistent with the result from the measurement.

Figure 3.5 shows the transition of the dominant field component (y-component) from the near field to the far field. The field maps are obtained at heights of 0.1, 1.0, 5.0, 7.5, and 10 mm. The measurement result at 1.0-mm height shows a very similar pattern as that at 0.1-mm height.

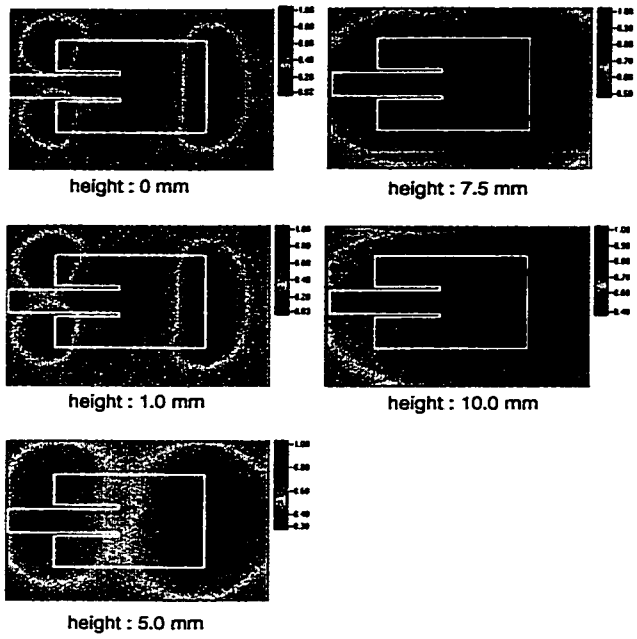

Figure 3.5: Normalized measured amplitude variation from field maps, showing near-field to far-field transition for dominant field component (y-component). Measurement plane height: 0, 1.0, 5.0, 7.5, and 10.0 mm.

However, the peak field at the edge opposite the feed end becomes dominant beyond 5-mm height. Also, the measurement results beyond 5-mm height show a more circularly shaped peak at the far-side edge. The transient patterns shown in Fig. 3.5 reveal that the peak electric field from the far-side edge of the patch provides the dominant contribution to the far field radiation pattern. Theoretically, the two radiating edges of the patch antenna should show identical radiation patterns regardless of the measurement height. However, about 1/3 of the feed-side radiating edge is sacrificed for the feed microstrip line. As a result, significant radiating power reduction occurs at the feed-side edge, and eventually, the radiation from the far-side edge becomes dominant as the distance from the patch increases. This suggests that other feeding method such as backside coaxial feeding may be advantageous in terms of optimization of radiating power of the patch.

3.3.3 S-Parameter Measurement

The electro-optic measurement technique has also been employed for the extraction of the scattering parameters of the microstrip patch antenna in an application that provides an alternative to conventional network analysis. This is potentially of great interest because the terahertz-bandwidth measurement capabilities of ultrafast-laser-based electro-optic sampling can lead to very high frequency, optically-based network analysis. In addition to the broad bandwidth capability of the electro-optic technique, the ability to measure directly on the DUT allows one to exclude the undesirable effects that occur between the RF source and the DUT, such as the attenuation of the microwave cable and the imperfect termination of the connectors. Because the microstrip antenna has only one port (input port), S_{11} is the sole relevant S parameter. The S_{11} has thus been measured and also compared with the result obtained using the HP 8510B network analyzer.

To obtain the S_{11} of the microstrip patch, the relationship between the reflection coefficient and the standing wave characteristic is used. A transmission line which has an impedance discontinuity generates a standing wave on it, with the voltage standing wave ratio (VSWR) being one of the important parameters used to explain standing wave phenomena on a transmission line. The VSWR is defined as

$$VSWR = \frac{V_{min}}{V_{max}} \tag{3.1}$$

where V_{min} is the minimum voltage value and V_{max} is the maximum voltage value in the standing wave. Also, this VSWR has the specific relation with the reflection coefficient, Γ, of [39]

$$VSWR = \frac{1+|\Gamma|}{1-|\Gamma|} \tag{3.2}$$

From Eq. 3.1 and 3.2, the relation between the measured minimum and maximum voltage values versus the reflection coefficient is obtained as

$$|\Gamma| = \frac{VSWR + 1}{VSWR - 1} \tag{3.3}$$

It is well known that the reflection coefficient Γ is identical to the S_{11} if the system has a single port. One of the important characteristics of a transmission line is that the voltage and the electric field relation are not changed unless the geometrical and electrical properties of the line are modified. Thus, along the microstrip feed line for our antenna, the field measured by the electro-optic probe has a direct correspondence to the voltage.

The electro-optic measurement technique has the capability to measure all three orthogonal electric field components, as described above. Also the patch antenna used in the measurement has a 50-Ω microstrip feed line as shown in Fig. 3.1. By measuring one of the field components, we can calculate the VSWR on the feed line. However, due to the alignment of the antenna, the y-component is not detectable on the feed line (Fig. 3.2(a)). The normal electric field (z-component) has better uniformity across the feeding (x direction) transmission line than the x-component, as observed in Fig. 3.2(a), and thus the z-component is used for the S-parameter measurement.

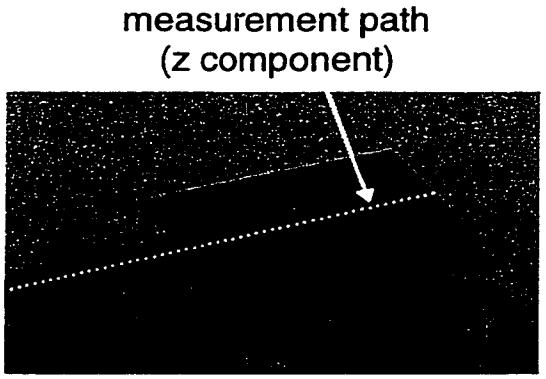

Figure 3.6: One-dimensional field scanning path for the S-parameter measurement

One-dimensional electro-optic scanning is performed along the center of the feed line from the feeding point to the edge of the antenna using the BSO crystal probe. The measurement height is 200 μm. Figure 3.6 shows the magnified photograph of the patch antenna with the one-dimensional EO field-scanning path for the S-parameter measurement.

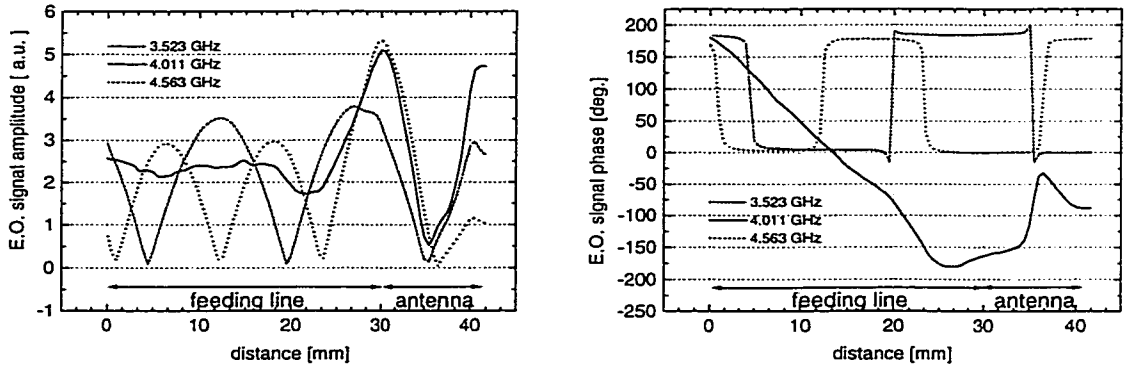

Figure 3.7: Standing-wave (a) amplitude and (b) phase measurement on the feed line and patch antenna at various operating frequencies at a measurement height of 200 μm. Dashed line: f=3.523 GHz; solid line: f=4.011 GHz (resonance frequency); dotted line: f=4.563 GHz. The x-axis origin is where the center conductor of the coaxial cable meets the microstrip line. The lengths of the feeding line and antenna are indicated above the x-axis.

Figure 3.7(a) shows measured standing wave amplitude patterns at three different frequencies. At 3.523 GHz, the frequency is not sufficiently high for the resonance to exist. On the other hand, 4.563 GHz is beyond the resonance frequency. In both cases the measurement results show a distinct standing wave pattern on the feeding line. Two asymmetry peaks can also be observed at each edge of the antenna. At the resonance frequency (4.011 GHz), the measurement result shows that the standing wave patterns on the feed line are vanishing, and the two symmetry peaks occur on both edges of the antenna.

Figure 3.7(b) depicts the measured phase pattern on the feed line and the patch antenna. The measurement results show typical standing-wave phase characteristics for both 3.523 and 4.563 GHz frequencies. Each point where the phase changes by 180 degree in Fig. 3.7(b) is coincident with a minimum amplitude point in Fig. 3.7(a). However, the phase appears to have the property of a traveling wave when the antenna is operated at its resonance frequency. The results show that most of the input signal is reflected back from the antenna when the antenna is operated under the off-resonance conditions. On the contrary, good signal propagation is observed on the feed line at the resonance frequency. From the result, we can conclude that most of the input signal is radiated from the antenna under the resonance frequency condition. Finally, $|S_{11}|$ of the antenna can be obtained by applying Eq. 3.3 to the measured data under the assumption that the feed line has very small loss. Figure 3.7(b) shows the resultant $|S_{11}|$ along with the result obtained using the HP 8510 network analyzer. The results show excellent agreement with each other.

During conventional network analyzer measurements, it is almost impossible to calibrate out certain factors such as the imperfect connection between the center conductor of the coaxial cable and the microstrip line. Herein lies a tremendous advantage for the use of electro-optic sampling for network analysis. That is, the electro-

optic technique allows one to determine the pure electric field that exists on the feed line and antenna, in this case, without worrying about the mismatch or loss of external cables and connectors. This difference between the two methods likely explains the slight disagreement in the two resonance frequencies presented in Fig. 3.8.

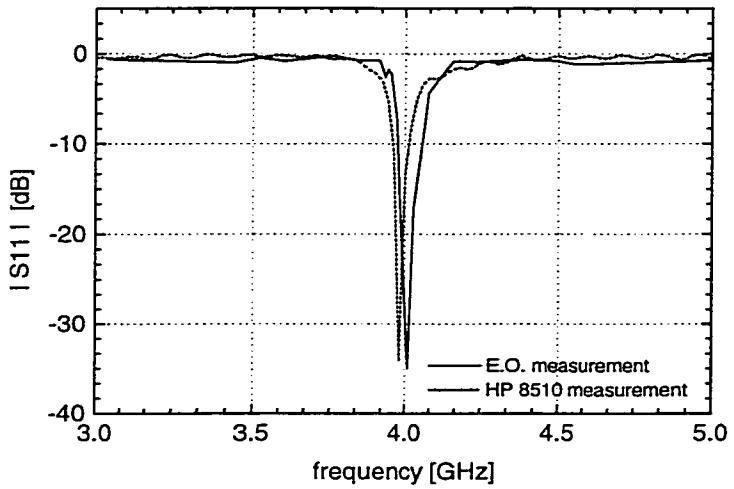

Figure 3.8: Magnitude of S_{11} parameters of the microstrip patch antenna in dB. Dashed line: HP 8510 network analyzer result; solid line: electro-optic measurement result.

3.4 Results II – 4×4 Grid Oscillator

A spatial power combing technique has been noticed as one of promising methods that can be used to produce high-power microwaves. One approach of the spatial power combining system is generating high-power microwaves by using grid type oscillator, and the other is to amplify a small signal by employing an amplifier array, which is known quasi-optical amplifier array.

Figure 3.9 shows a schematic diagram of the grid oscillator measurement setup. Figure 3.10 shows the layout of the 16-element voltage-controlled grid oscillator array fabricated on a 0.01-inch thick RT/Duroid 5880 substrate.

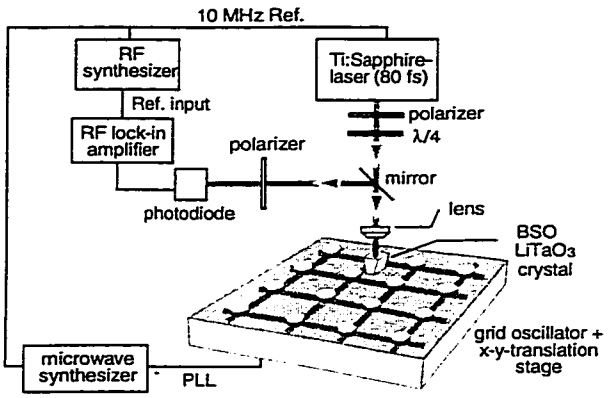

Figure 3.9: Schematic of the electro-optic near-field measurement setup

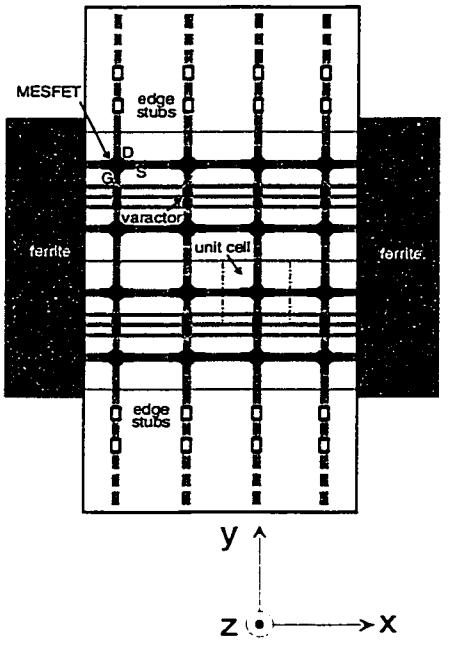

Figure 3.10: The grid oscillator used as a DUT

The transistors and varactor chips are attached to the metal grids with silver epoxy and wire bonds. The size of each unit cell is 8×8 mm. The transistors used here are Fujitsu GaAs MESFETs (FHC30LG) and the varactor diodes are Metelics MSV-34. The grid oscillator has a center frequency of 4.7 GHz and is locked to a frequency synthesizer by way of a phase-locked loop (PLL). The effective isotropic radiated power is about 1W.

The DUT is mounted on a computer-controlled x-y-translation stage. The 2D scans are made immediately above the grid oscillator transistors (8 mm to 20 mm above the substrate). The measured results shown include 3600 points and are obtained in approximately 60 min. This duration was mainly determined by the speed of the translation stage and therefore could be further improved.

3.4.1 Near-field mapping

Figures 3.11 and 3.12 show the distribution of the principally polarized field component—*i.e.*, the y component measured at heights of 10 and 20 mm. Figure 3.11 resolves an inhomogeneous field distribution which is associated with the single devices in the grid. These results are in all rather surprising. The field concentrations around the active devices are discernable, but it is clear that the field strengths vary from device to device. More surprisingly, the phase distribution exhibits virtually a full 360 degree phase across the aperture (Fig. 3.11(b)). This phase distribution explains why the beam that is evidenced in Fig. 3.12 is off-center. Indeed, far field measurements of the radiation field from this aperture, and field calculations based on the phase progression observed from Fig. 3.11, both exhibit a shift in the main beam approximately 15 degrees off normal. In Fig. 3.12, the distribution of the principal polarization is given for a distance of 20 mm. At this distance, the formation of the far-field pattern is evident, and the beam shift is observable here.

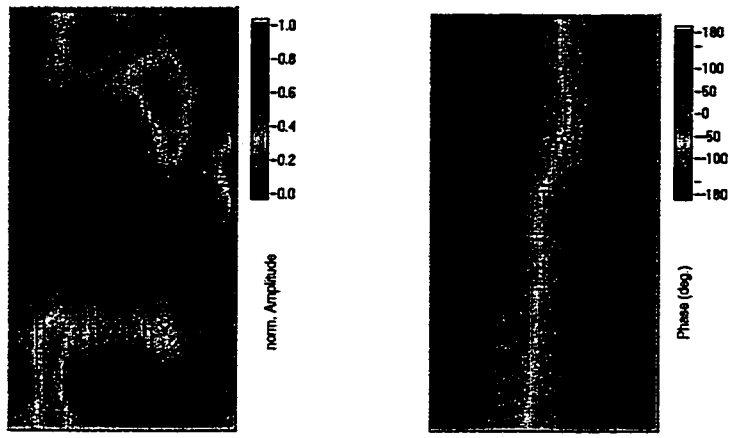

(a) (b)

Figure 3.11: Two-dimensional map of the field component in the y-direction of the grid oscillator at f= 4.7 GHz, 10 mm above the array. (a) normalized amplitude, (b) relative phase; scan-area: 6.5 cm × 3.3 cm. The outline of the grid is superimposed on the field maps.

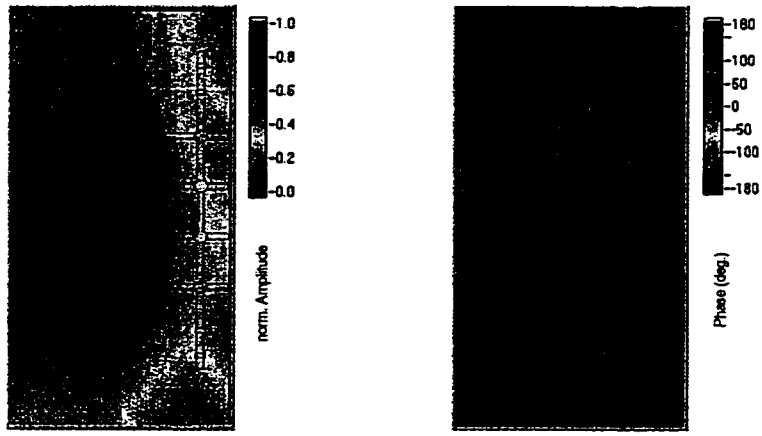

(a) (b)

Figure 3.12: Two-dimensional map of the field component in the y-direction of the grid oscillator at f= 4.7 GHz, 20 mm above the array. (a) normalized amplitude, (b) relative phase; scan-area: 6.5 cm × 3.3 cm.

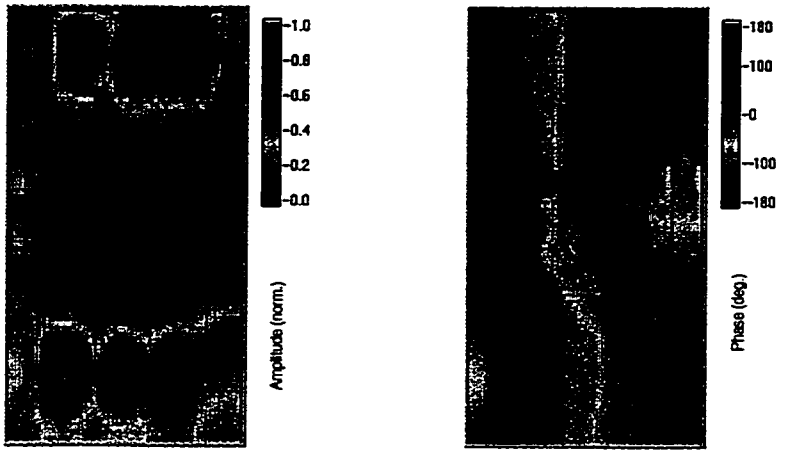

(a) (b)

Figure 3.13. Two-dimensional map of the field component in the x-direction of the grid oscillator at f= 4.7 GHz, 8 mm above the array. (a) normalized amplitude, (b) relative phase, scan-area: 6.5 cm x 3.3 cm.

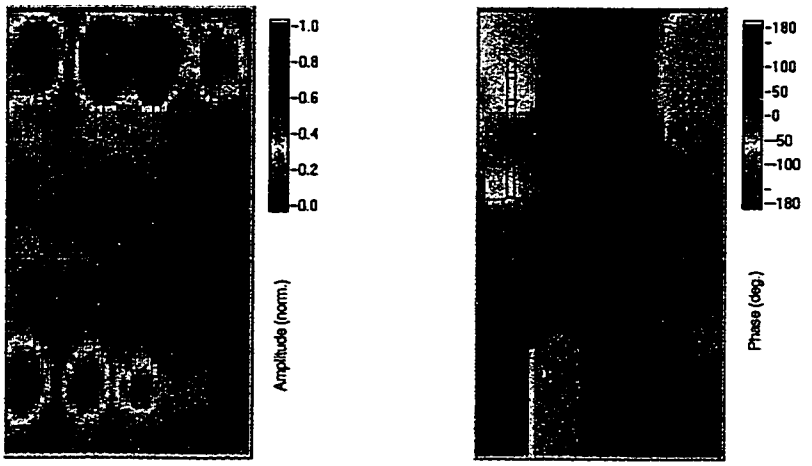

(a) (b)

Figure 3.14: Two-dimensional map of the field component in the z-direction of the grid oscillator at f= 4.7 GHz, 8 mm above the array. (a) normalized amplitude, (b) relative phase; scan-area: 6.5 cm x 3.3 cm.

Figure 3.13 and 3.14 show the distributions of the cross-polarized (x) component

and of the normal (z-directed) electric field pattern at an height of 8 mm. The distributions exhibit the principal feature of field concentration at the ends of the radiating (vertical) circuit traces. One would expect such field concentration associated with the high charge densities that are present at the ends of open-ended linear radiators. It should also be noted that adjacent high-field regions are 180 degrees out of phase with each other, so they consequently cancel themselves in the far field.

3.4.2 Far-Field Calculation Based on the Near-Field Measurement Results

The near-field measurement result for the dominant component (y-component, Fig. 3.11) shows a 360-degree phase variation across the grid oscillator. A far-field pattern is calculated from the near-field result and compared with the far-field pattern obtained by conventional far-field measurement techniques to prove the validity of the electro-optic measurement result. For the simplification of the problem during the far-field calculation, each unit oscillator is assumed to be an isotropic radiator, which is reasonable because the unit element has no specific radiation direction. Therefore, all unit cells are assumed to have the same amplitude. All 4 elements on the same column have uniform phase. On the contrary, a 360-degree phase variation is applied across the array along the x-direction (Fig. 3.11(b)). Because each individual element is assumed to be an isotropic radiator, the far-field radiation pattern is decided by the array factor (AF) [40]. For 2-dimensional planar arrays, AF can be expressed as

$$AF(\theta,\phi)=\left\{\frac{1}{M}\frac{\sin\left(\frac{M}{2}\psi_x\right)}{\sin\left(\frac{\psi_x}{2}\right)}\right\}\left\{\frac{1}{N}\frac{\sin\left(\frac{M}{2}\psi_y\right)}{\sin\left(\frac{\psi_y}{2}\right)}\right\} \tag{3.4}$$

where

$$\psi_x = k\ d_x \sin\theta\cos\phi + \beta_x$$

$$\psi_y = k\ d_y \sin\theta\cos\phi + \beta_y$$

where M and N represent the number of the elements along the x and y directions, respectively. In this case, the number of elements is 4 for both the x and y directions. Also, d_x, d_y, β_x, and β_y represent spacing and phase difference between each element along the x and y direction, respectively. Figure 3.15 shows the calculated far-field patterns of the 4×4 grid oscillator with uniform phase distribution and 360-degree phase variation across the grid oscillator (along x direction). Figure 3.15(a) shows that a single main lobe occurs at the center of the grid oscillator with a uniform phase distribution. On the contrary, the main beam is slightly off from the center of the oscillator and a side lobe can be observed under the 360-degree phase variation condition (Fig. 3.15(b)). For accurate analysis, 1-dimensional polar plots are compared in Fig. 3.15(c) and (d). Figure 3.15(d) shows one side lobe and a main lobe that is 15 degree off from the center. The calculation result shows excellent agreement with conventional far-field measurement in which the main lobe is observed 12° off from the center. Also, the calculation result shows good agreement with the electro-optic far-field transition measurement (Fig. 3.12(a)).

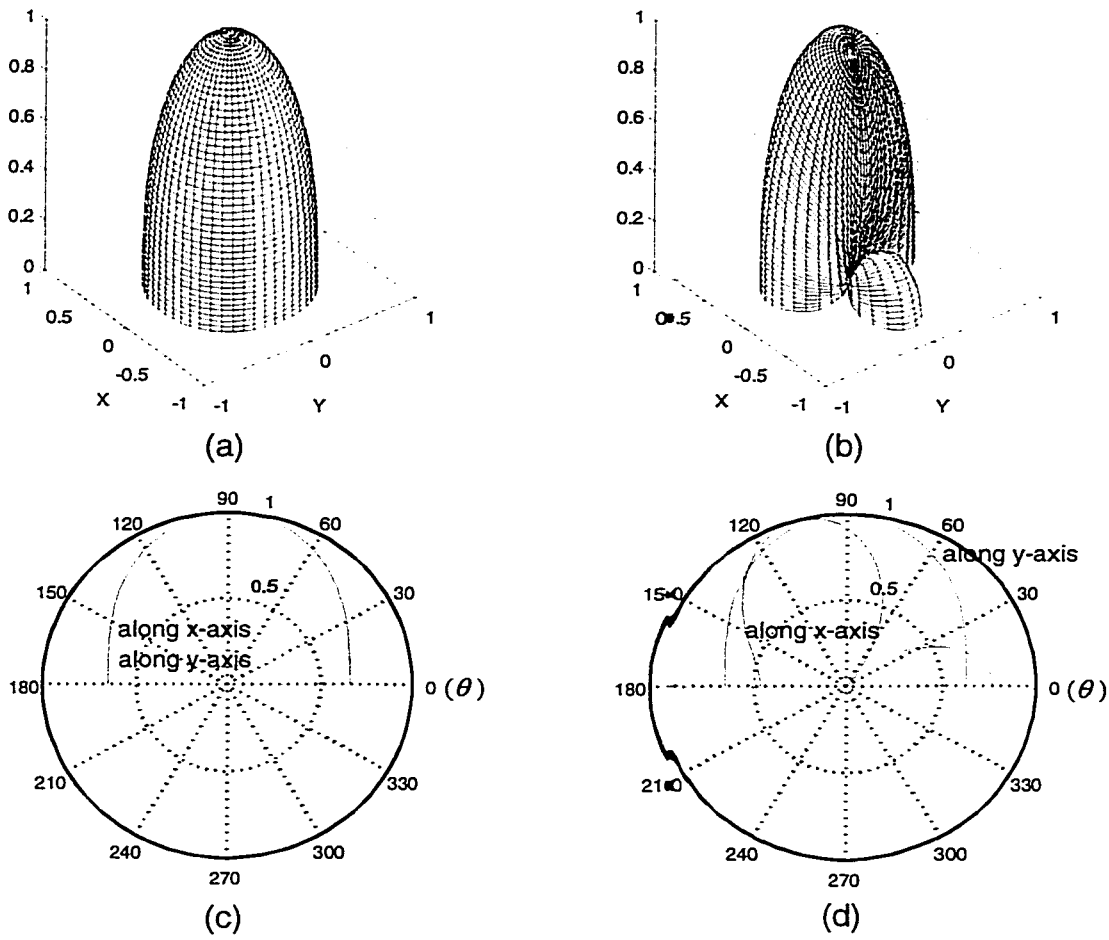

Figure 3.15: Far-field calculation results obtained by classical 2-dimensional array analysis technique. (a) normalized amplitude with uniform phase distribution condition; (b) normalized amplitude with 360 degree phase variation along x axis (y=0); (c) two cross sectional polar plot of far-field pattern (along x-axis and y-axis) with uniform phase distribution; (d) two cross sectional polar plot of far-field pattern (along x-axis and y-axis) with 360 degree phase variation.

3.5 Results III – Ka-Band Quasi-Optical Amplifier Arrays

Near-field measurements based on the electo-optic sampling technique have been performed for two different types of Ka-band quasi-optical amplifier arrays in order to evaluate the performance of the arrays and identify important design issues. In the process of conducting the measurements, three different types of horn antenna feeds, which are integral parts of the QO amplifier arrays, have also been characterized. The high resolution and accuracy of the electro-optic field mapping technique has proved to be advantageous in the design cycle of amplifier arrays, and has diagnosed problems such as nonuniform bias, nonuniform feed amplitude, and malfunctioning MMICs.

3.5.1 Feeding Horn Measurements

Before testing arrays, it is very important to measure the output field pattern of the feeding horns, because the output near-field pattern of the array depends strongly on the input field pattern (output of feeding horn). A standard WR-28 tapered horn and two different types of hard horns are used to feed various arrays. One of the hard horns (type A) utilizes a WR-28 standard horn. Hard horn type B uses a customized horn body. Dielectric layers and lenses are used for both hard horns to achieve plane wave outputs at a short distance from the opening of the horn [41]. Figure 3.16 shows electro-optic measurement results for the dominant electric field component (y-component) of all three horns. Each horn is operated at a frequency of 31.043 GHz, which is a combination of a 31.04 GHz RF signal (388×80 MHz, the closest integer-multiple frequency of 80 MHz to the operating frequency of the horn antenna) and a 3 MHz IF signal. Due to the limit of the RF synthesizer used in the measurement, a frequency doubler is used between the RF synthesizer output port and the input port of the horn antennas. The frequency doubler generates 31.043 GHz output with 15.5215 GHz input. Figure 3.16(a) and (b) show the

normalized amplitude and phase of the dominant electric field component for the standard WR-28 horn.

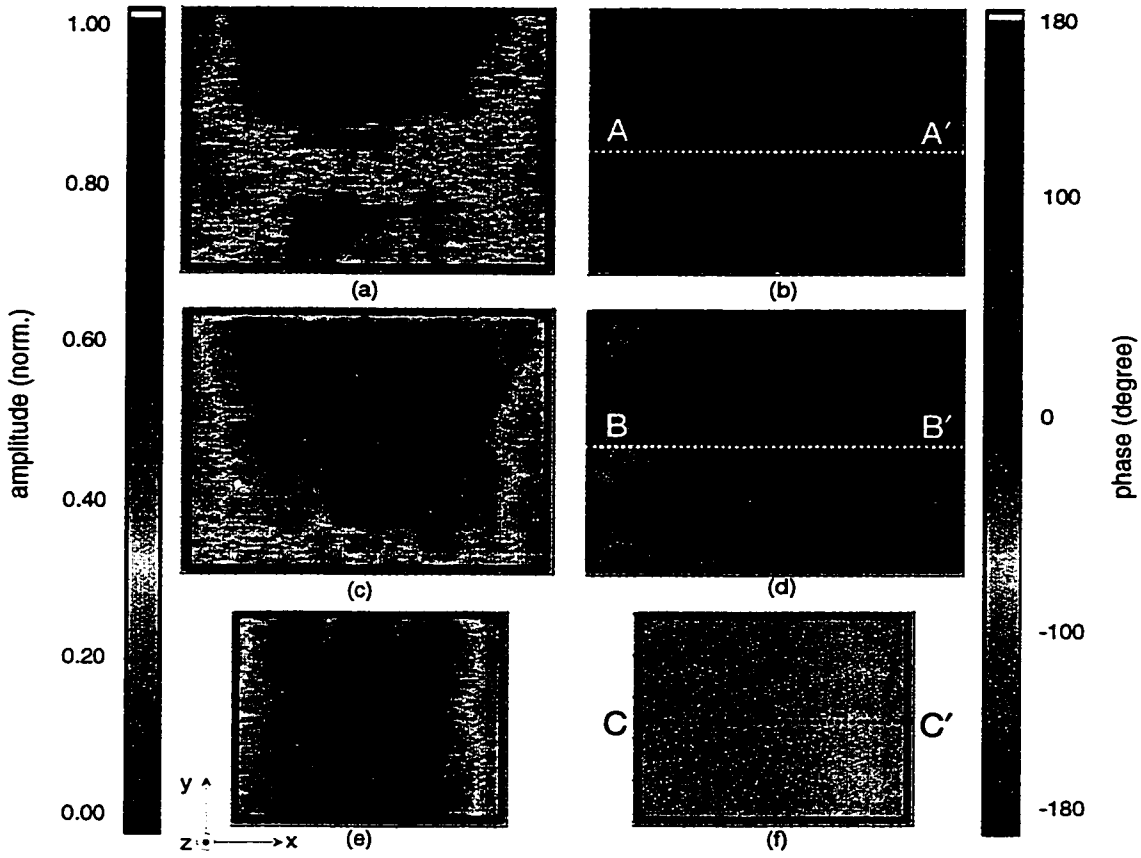

Figure 3.16: Electro-optic measurement results for various horn antennas at f_{in} = 31 GHz. (a) normalized amplitude for standard WR-28 horn and (b) phase in degrees; (c) normalized amplitude and (d) phase in degrees for hard horn type A; (e) normalized amplitude and (f) phase in degrees for hard horn type B. The metal boundaries of the horn apertures are overlayed with a bold blue line.

The phase measurement result displays a 180° phase variation from the center to the edge of the aperture, which agrees well with theoretical predictions for this horn

output. Figure 3.16(c) and (d) display the normalized amplitude and phase of hard horn type A. In comparison with a standard horn, the results show significant improvement of the uniformity of phase (Fig. 3.16(d)). The phase variation of hard horn type A is around 50 degree. The hard horn type B shows the best results for both amplitude and phase distribution (Fig. 3.16(e) and (f)). It shows an excellent 20 degree phase variation and the most uniform amplitude distribution among the three horn antennas.

From the results of three different types of horn antenna measurements, it is clear that the two hard horns have superior characteristics in terms of uniformity of phase, which is a critical factor for generating a plane wave.

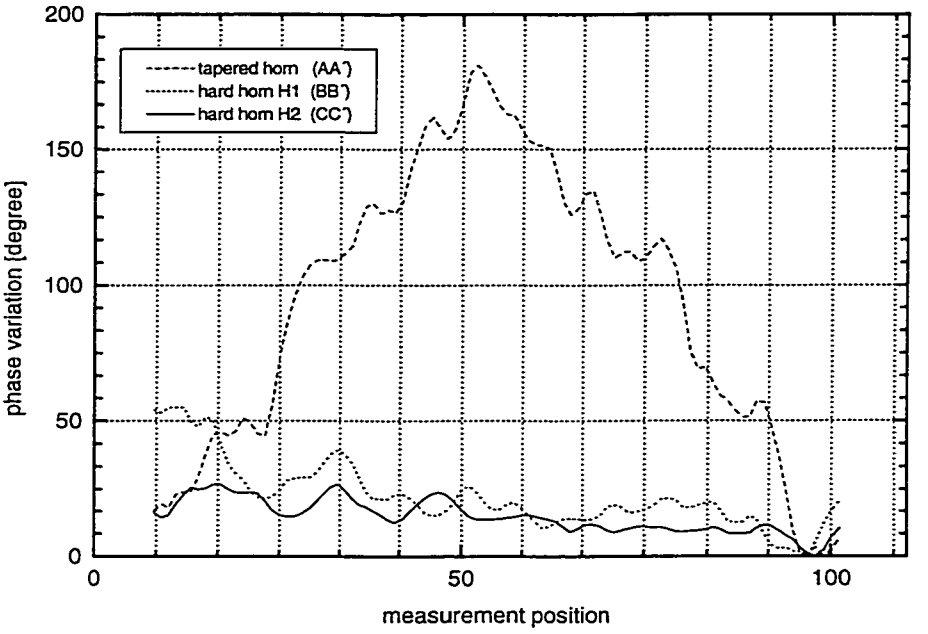

Figure 3.17: One dimensional phase variations for three horn antennas along the dotted lines shown in the phase plots in Fig. 3. The phase variations are extracted along $\overline{AA'}$ for the standard WR-28 horn, $\overline{BB'}$ for hard horn H1, and $\overline{CC'}$ for hard horn H2. Measurement position 50 is the center of the aperture.

3.5.2 Slot Antenna Array, Type 1: Improper DC bias network

A picture of a 6×6 quasi-optical amplifier mounted as the DUT is shown in Fig. 3.18. The array was developed from University of the Colorado at Boulder as a prototype array. For the detailed performance verification and design validation, near-field distributions were extracted by using the EO field mapping system.

Each input slot antenna receives power from the horn feed antenna. The received power is coupled onto a 50-Ω coplanar waveguide (CPW) transmission line and is then amplified by an Alpha AA0028P3-00 MMIC amplifier. The amplified power is re-radiated after 90-degree polarization rotation with respect to the input field. Isolation and stability is provided by orthogonal input and output antennas [42].

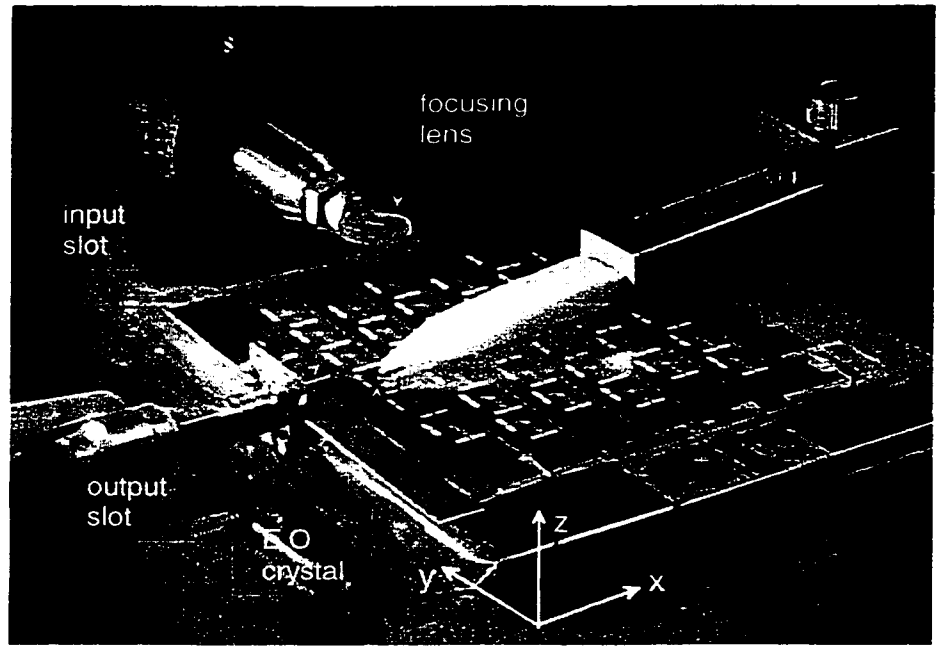

Figure 3.18: Picture of 6×6 quasi-optical amplifier array type A as DUT. The input slots are aligned along the x-direction (y-direction polarization), while output slots are aligned along the y-direction (x-direction polarization). $LiTaO_3$ is mounted at the end of styrofoam arm as electro-optic crystal.

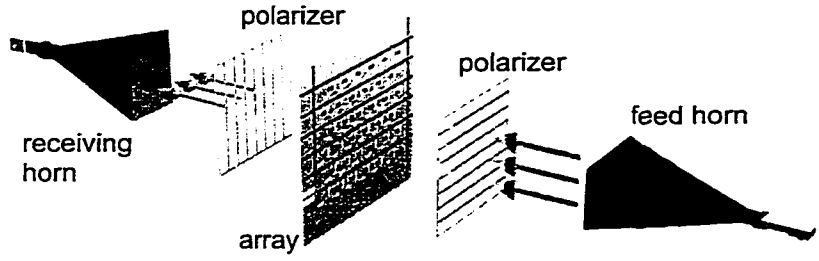

Figure 3.19: Operational schematic of a planar quasi-optical amplifier.

Figure 3.19 shows general operation schematic of planar quasi-optical amplifier array. In order to isolate the input and output radiation, two polarizers are used with orthogonal configuration.

Figure 3.20 shows the electro-optic measurement setup used for quasi-optical amplifier arrays.

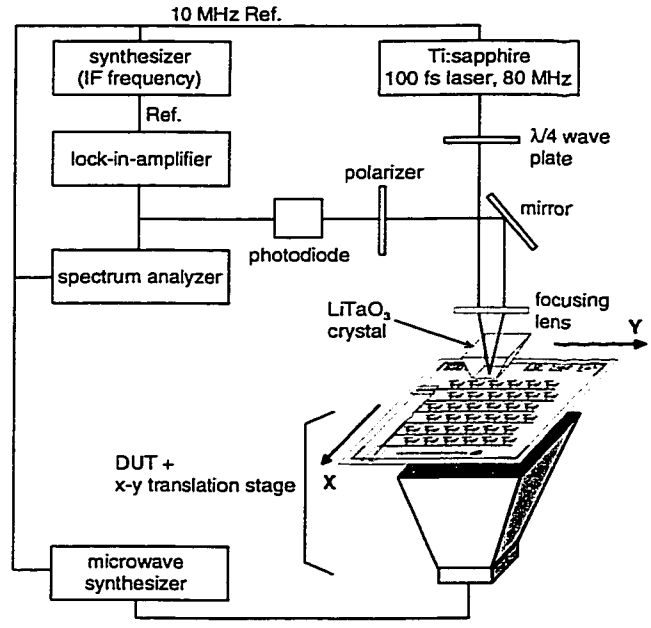

Figure 3.20: Electro-optic measurement schematic for near-field mapping of quasi-optical amplifier arrays.

The overall setup configuration is quite similar to the patch antenna measurement, except that the microwave synthesizer feeds the horn antenna to activate the array. Thus, both the feed horn and array are mounted on the x-y translation stage for the complete two-dimensional field mapping.

Figure 3.21 shows the electro-optic field mapping results for the type 1 array. The unit step size for the scanning is 500 μm × 450 μm and the total scanning area is 6.25 cm × 4.8 cm. Total elapsed time for the scanning is around 1 hour and 10 minute.

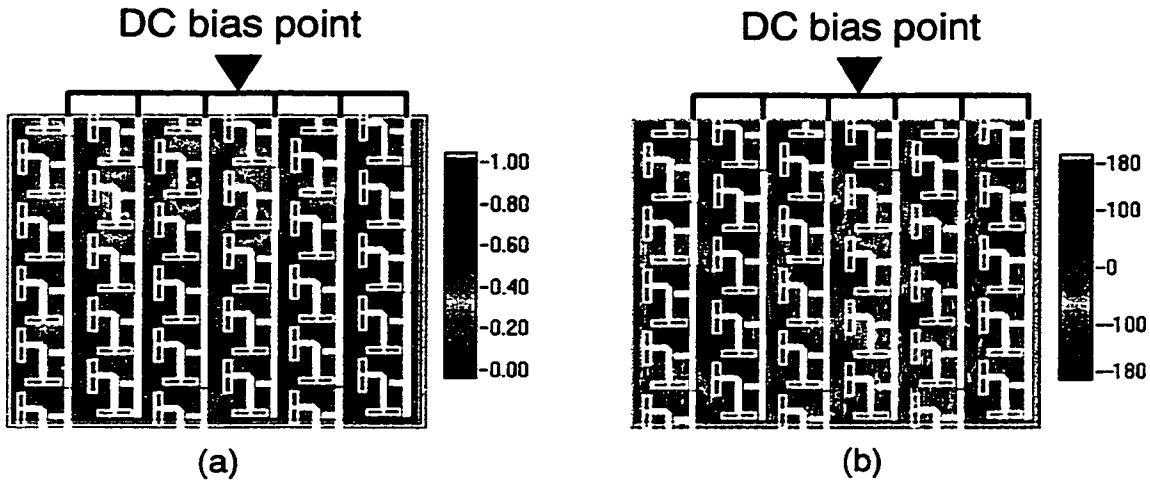

Figure 3.21: Electro-optic field mapping of the quasi-optical array with improper dc bias network. (a) normalized amplitude and (b) phase in degrees. Circuit outline is overlayed.

Figure 3.21(a) clearly shows that most of the functioning elements are concentrated around the dc bias point. From the results, several possible diagnoses can be suggested. The first possibility is that most of the amplifier MMICs are malfunctioning, except in an area close to the dc bias point. However, this analysis is not reasonable because the MMICs around the dc bias point are more vulnerable than those are far away

from the dc bias point to external disturbances such as static charges or abrupt bias changes. The second possibility is an improper dc bias network. In other words, the bias lines fail to supply a uniform bias across the whole array area due to the distributed ohmic loss. The latter explanation agrees well with the measurement results. Also, an accurate voltage distribution calculation reveals that array type 1 has a noticeable dc voltage variation along the bias network [43]. To reduce the ohmic loss of the dc network, which is critical for the uniform bias of a large number of MMICs, an improved array that utilizes thicker metal line in its dc bias network has been developed.

3.5.3 Slot Antenna Array, Type 2: Improved DC Bias Network

Two different arrays have been developed that have improved dc bias networks (array type 2A and type 2B, provided by University of Colorado at Boulder) [43]. Two Ka-band slot antenna amplifier arrays with 36 elements each were fabricated on aluminum nitride substrates with commercial low-power MMIC amplifiers in CPW circuits as described in detail in [43]. The two arrays differ in the biasing network only; the RF parts of the arrays are identical. For completeness, we list the microwave measurement results on these two arrays. The saturated output powers at 31 GHz were 0.3 W and 0.5 W, with each MMIC contributing on average between 8.3 and 14 mW – this is 7 dB lower than the power specified by the manufacturer for a higher bias point. No liquid cooling was needed, and the AlN substrate reached a peak temperature of 40 °C. The average small signal gain contributed by the MMICs was 10 and 14 dB, respectively, and was measured relative to a passive array. The measured far-field radiation patterns had bias on/off ratios of over 34 and 38 dB, and 3-dB beamwidths of about 10 degree.

The two different biasing schemes investigated were implemented as a direct result of an initial electro-optic-field-mapping diagnostic measurement on a previous

embodiment of these arrays. Both arrays share the same physical design as array type 1. Array type 2A has an improved bias network utilizing thick copper tape for the main bias line and type 2B array utilizes a thick metal plating process to reduce the ohmic loss. Also, many capacitors are mounted along the bias line to block the RF cross talk between each element throughout the bias network. For the measurement, both the type 2A and type 2B arrays are mounted face-down toward the feeding horn to improve the accessibility of the electro-optic probe to the slot antennas (Fig. 3.22).

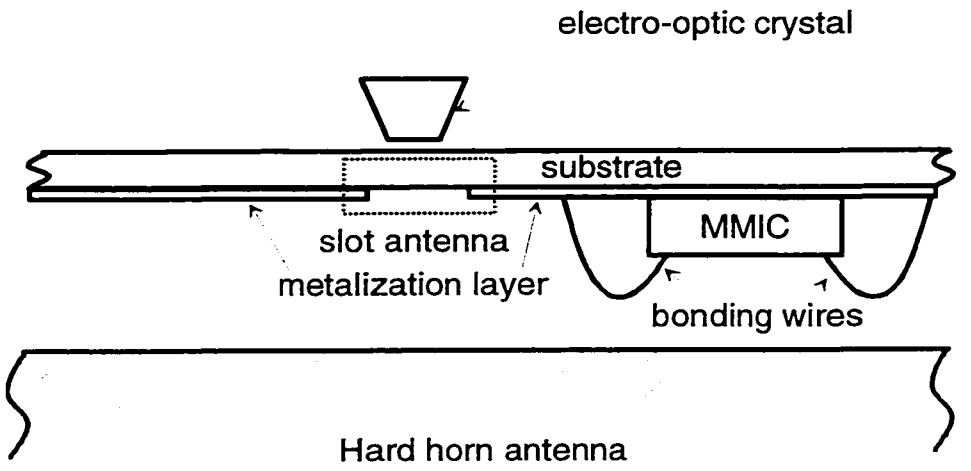

Figure 3.22: Schematic of type 2A and type 2B array measurement; $LiTaO_3$ is used as electro-optic crystal.

Furthermore, this setup makes it possible to measure the propagation wave through the substrate (substrate propagation mode), due to the proximity of the electro-optic crystal to the substrate. The individual scanning step size is 500 μm × 450 μm and the total scanning area covers 63 mm × 54 mm. The total scanning time is around 1 hour 10 minute. The hard horn type B (Fig. 3.16(e), (f)) is used as the feeding horn antenna because it shows superior performance to the standard horn or type A hard horn.

Figure 3.23 shows electro-mapping results for both the type 2A and type 2B arrays. The normalized amplitude of the type 2A array shows an uneven distribution (Fig.

3.23(a)), even though it exhibits an improved pattern with respect to the array type 1 (Fig. 3.21(a)). The electro-optic mapping results of array type 2B display significant improvement of output field distribution both of amplitude and phase (Fig. 3.23(c) and (d)).

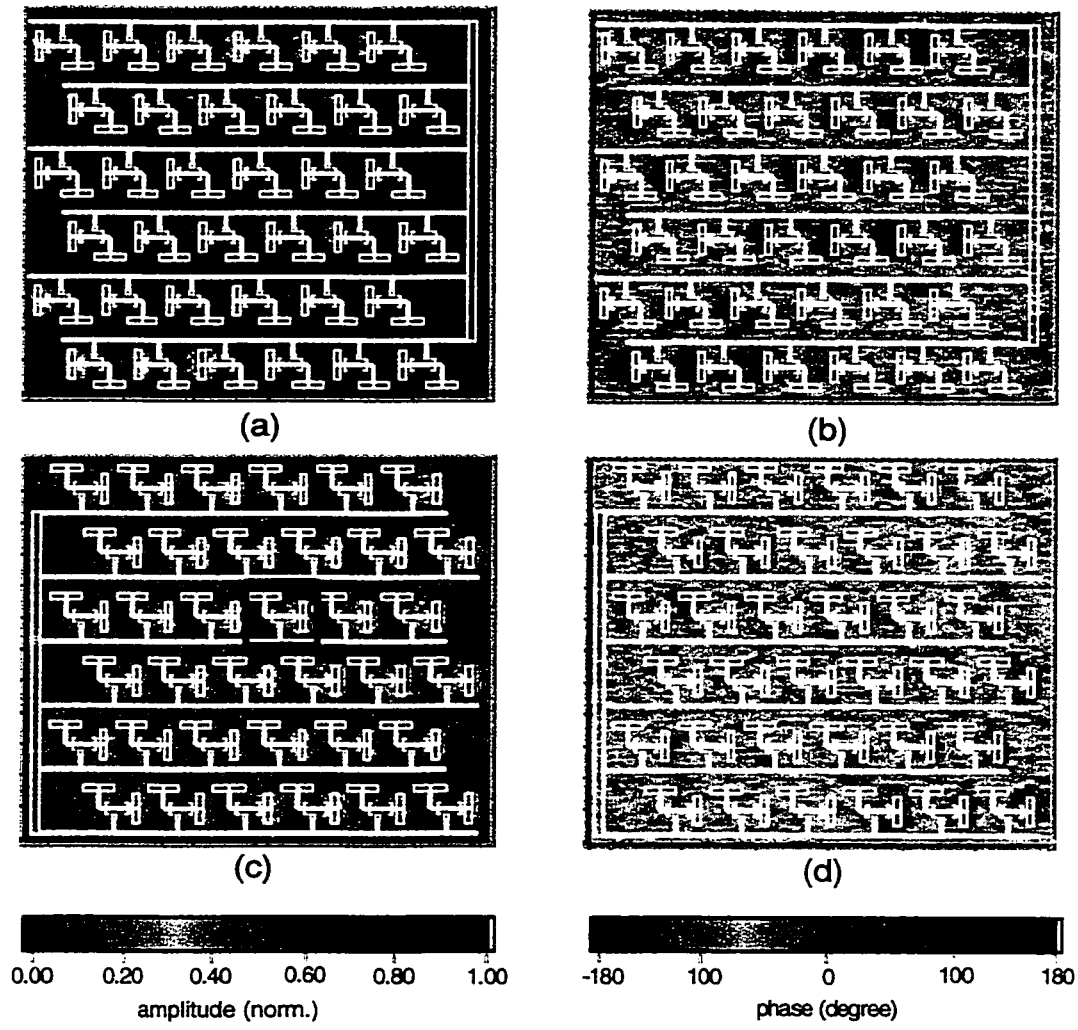

Figure 3.23: Electro-optic field mapping of array type 2A and type 2B. (a) normalized amplitude and (b) phase in degrees of array type 2A; (c) normalized amplitude and (d) phase in degrees of array type 2B. Square box in (c) shows position of the cell used for unit cell measurement. Circuit outline is overlayed. The bias ports are indicated with additional rectangles.

Since array type 2A and type 2B share the same layout design, the discrepancy of the performance between the two arrays can best be explained as RF cross talk between individual elements. As mentioned above, both arrays type 2A and type 2B utilize improved bias networks. However, only the type 2B array has RF blocking capacitors on the bias line. The results show that suppressing cross talk between each element is another important factor to enhance the performance of amplifier arrays along with achieving uniform dc bias distribution.

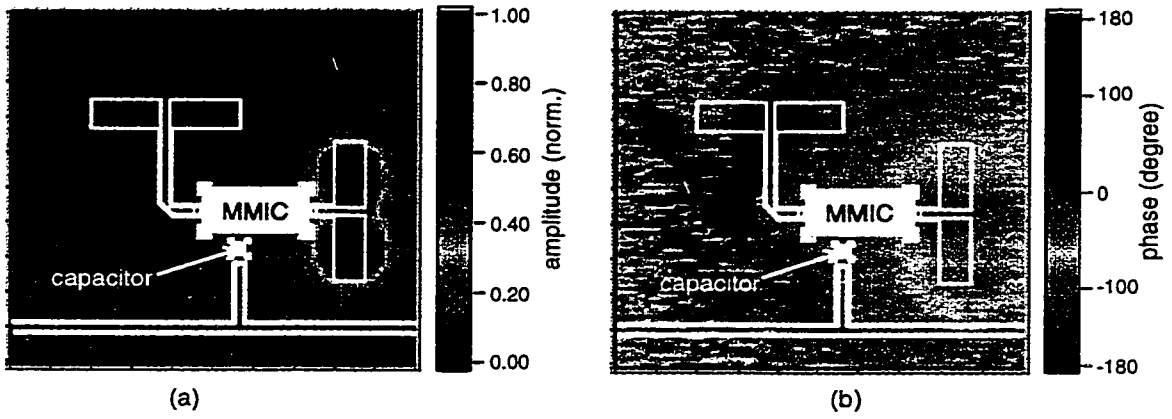

Figure 3.24: Electro-optic mapping result of a unit cell (square box shown in Fig. 3.23 (c)). (a) normalized amplitude and (b) phase in degrees.

To examine detailed information on the array, a unit cell is selected (shown in the box in Fig. 3.23(c)) and measured. The normalized amplitude and phase are shown in Fig. 3.24(a) and (b). Figure 3.24(a) displays an excellent symmetry in the amplitude in the output slot antenna. Also, the measured phase in the output slot antenna shows very uniform distribution, which is desirable. To obtain a higher resolution result for the unit cell mapping, the scanning step size is reduced to 93 μm × 100 μm and the total scanning area covers 9.3 mm × 10 mm.

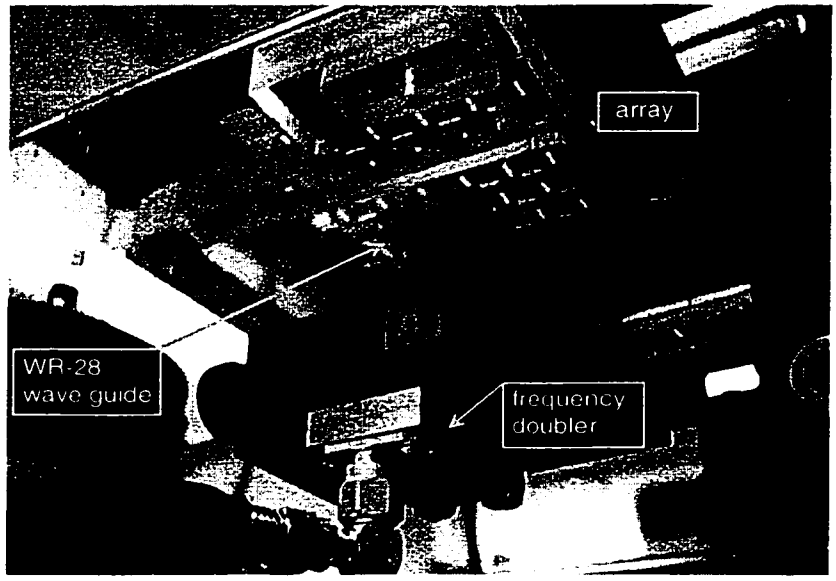

Figure 3.25: Isolation measurement setup picture for array type 2A and 2B. WR-28 waveguide is used to feed one element in the arrays. The frequency doubler generates 31.003 GHz output signal from a 15.5215 GHz input.

Another important performance characteristic of the array is its RF isolation properties. As shown in Fig. 3.23(a), poor RF isolation between the unit cells can degrade the performance of the array significantly. It is impossible to feed a single element with the hard horn due to its large aperture. Thus, WR-28 waveguide was used to feed a single element. Also, to examine the position dependence of the isolation performance, unit cells around both the center and the corner of the arrays are selected and fed separately. Figure 3.25 shows the setup for isolation measurement, including an L-bend connector, the frequency doubler, and WR-28 waveguide. To confine the output field of the waveguide into one cell, the waveguide is placed right below the desired unit cell of an array.

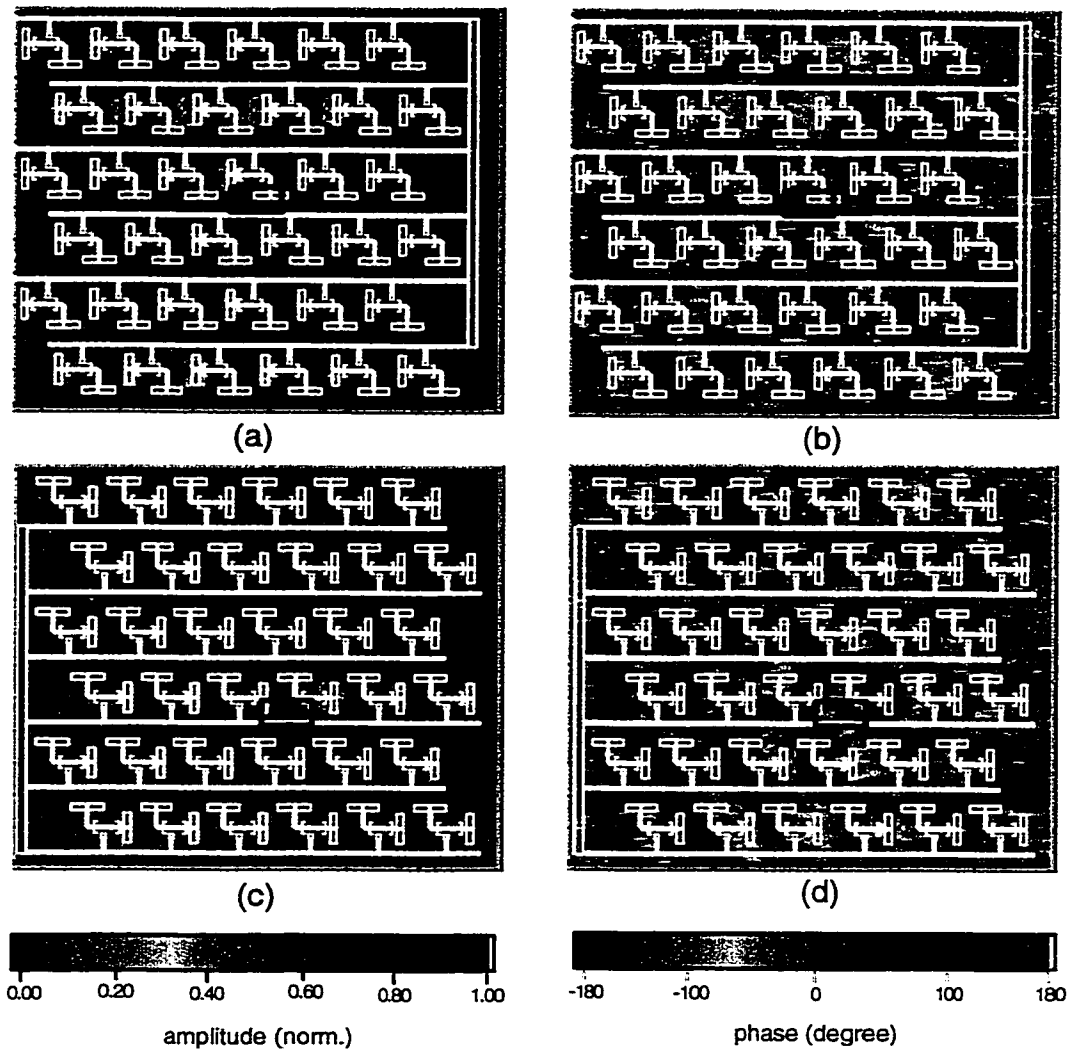

Figure 3.26: Isolation measurement results of array type 2A and 2B. (a) normalized amplitude and (b) phase (in degrees) of array type 2A; (c) normalized amplitude and (d) phase (in degrees) of array type 2B; The blue rectangle represents the position and relative size of feeding waveguide.

To examine the isolation properties, our scanning covers the full array area, even though only one cell is fed as shown in Fig. 3.25. Figure 3.26 shows the measured amplitude and phase results of array type 2A and 2B when the waveguide is placed under a unit cell in the center of the array. The blue rectangle in the figure represents the position and size of the aperture of the feeding waveguide.

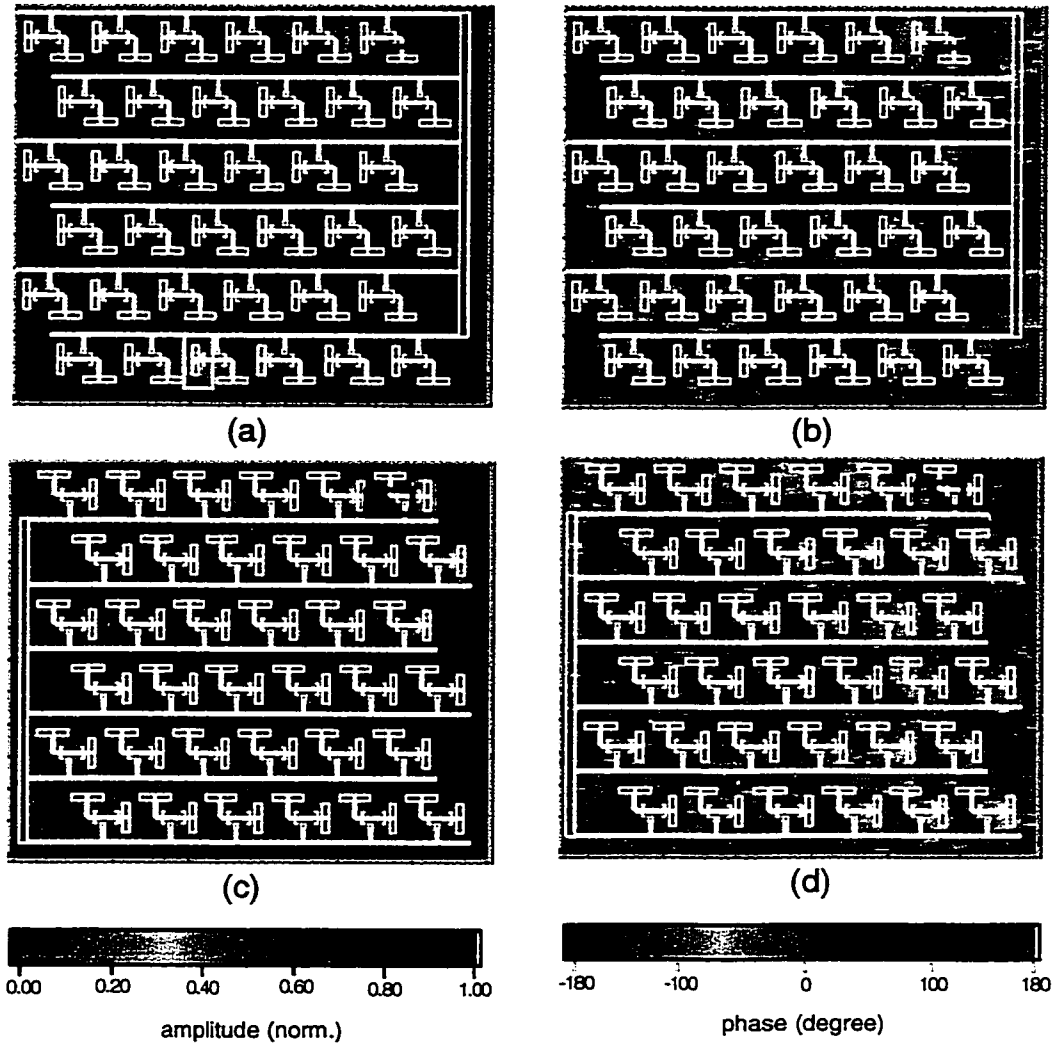

Figure 3.27: Isolation measurement results of array type 2A and 2B. (a) normalized amplitude and (b) phase (in degrees) of array type 2A; (c) normalized amplitude and (d) phase (in degrees) of array type 2B; The blue rectangle represents the position and relative size of feeding waveguide.

As shown in Fig. 3.26(a), the type 2A array shows a stronger signal in some elements that are far away from the feeding point. One of the possible explanations about this strong cross talk is that the dc bias line behaves as an RF signal wave guide. In other words, the output signal generated by the element fed by the waveguide is transmitted to

other elements through the dc bias lines. This transmitted signal acts like an input signal for elements that are isolated from the waveguide feeding. Because the transmitted signal is already amplified by the MMIC of the element that is fed, the outputs of elements activated by cross talk can be even stronger than the output of the excited element. In Fig. 3.26(a), several elements show much stronger output signals than the element that is directly fed from the waveguide. Array type 2B (Fig. 3.26(c) and (d)) shows superior characteristics in terms of RF cross talk suppression. As expected, capacitors mounted along the dc bias lines show excellent performance for suppressing cross talk between individual cells.

To examine the position dependence of the cross talk property, the feeding point is also positioned around one of the corner unit cell (Fig. 3.27). As shown in Fig. 3.27(a), the type 2A array measurement result shows better isolation characteristics when it is fed near its corner. However, Fig. 3.27(a) shows strong output from one element in the bottom row. On the contrary, the measurement result of array type 2B shows gradual decreasing output signal as the distance from the feeding point increases.

One of the distinct advantages of the electro-optic measurement with respect to conventional field measurement techniques is the capability to capture substrate propagation mode waves. Due to the proximity of the electro-optic crystal to the substrate and its high sensitivity, it is possible to detect an electric field traveling through the substrate. Figure 3.28 shows a magnified 2-dimensional amplitude mapping result obtained from the center-feed measurement of array type 2B (Fig. 3.26(c)). The picture is captured from a real-time animation of the time-varying electric field at one point in space. Also, the amplitude scale is adjusted to enhance the substrate mode wave visibility.

The element that is directly fed from the waveguide is inscribed within the dotted box. The result clearly displays the existence of substrate-mode propagation by concentric peak wave fronts that are displayed in the periodic green areas. This result

suggests that the electro-optic measurement system can be a powerful tool for observing real substrate propagation waves, which are very difficult to detect by other conventional measurement techniques.

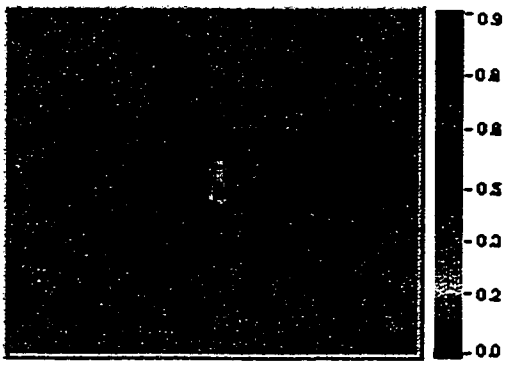

Figure 3.28: Substrate propagation mode wave measurement result (amplitude, in linear scale) of type 2B array for center feeding; The picture is captured during real-time animation as a results of the amplitude associated with the phase condition. The element that is fed directly by waveguide is shown in the dotted box.

3.5.4 Amplifier Array utilizing Patch Antennas

Another type of amplifier array, using microstrip patch antenna structures for input and output antennas, has also been measured by the electro-optic setup to examine the characteristics and performance of the array. Figure 3.29 shows the measurement scheme picture for the array. This array has five columns of active cells, and three of those columns have four elements while the other two columns have three elements. The array has two amplifier MMICs per unit cell, one to amplify the input signal before its coupling through the substrate and the other one mounted right before the output patch antenna. Because the main purpose of the measurement is to examine the active cells,

scanning has been performed over the active area. The actual scanning area is enclosed by the dotted line.

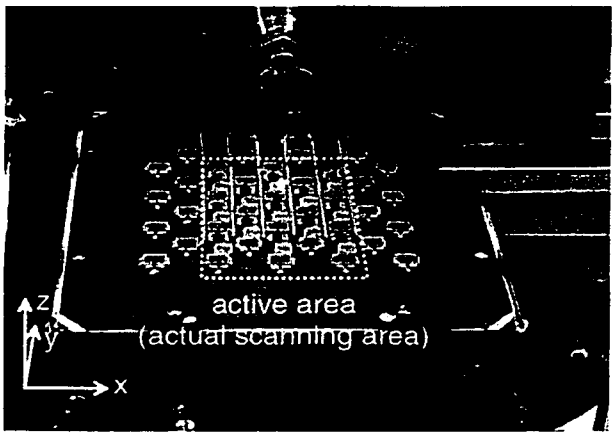

Figure 3.29: Measurement setup for the array utilizing patch antennas; The active area (actual scanning area) is enclosed by dotted line.

For the measurement, hard horn type B is used as the feeding antenna (see Fig. 3.16(c) and (d)). The unit step size for the scanning was 284 μm × 341 μm, and 100 steps are taken for both the x- and y-directions. Thus the total scanning covers 28.4 mm × 34.1 mm (x × y, area enclosed by dotted box in Fig. 3.29). Total scanning time is around 45 minutes for one complete field mapping. Two different types of crystals - BSO for z component and $LiTaO_3$ for the x and y components - are used to detect the three orthogonal field components.

Figure 3.30 shows one of the measurement results obtained by electro-optic mapping. Figure 3.30(a) and (b) display normalized amplitude and phase (in degrees) of the y component, which is the dominant field component. Due to the high-resolution property of the electro-optic measurement technique, two radiating edges of individual patch antenna are easily distinguished in Fig. 3.30(a). Also the results show good

agreement with the single patch antenna measurement that is discussed in the previous sections of Chapter 3.

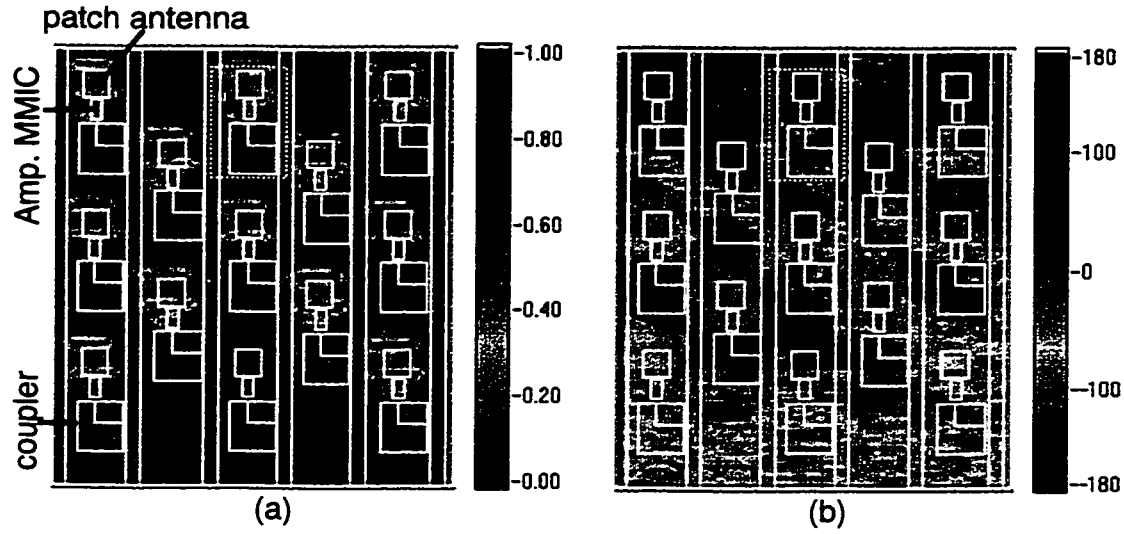

Figure 3.30: Electro-optic mapping result for the array. (a) normalized amplitude and (b) phase (in degrees) of the array for the y component.

It is quite noticeable that one element at the bottom of the middle column is malfunctioning. Also, this malfunctioning element disturbs the phase distribution significantly (Fig. 3.30(b)). However, most of the patch antennas show quite uniform phase distribution. The measurement results demonstrate the usefulness of the electro-optic field mapping technique for the diagnosis and fault isolation of array structures. The technique was quickly and easily able to demonstrate failure associated with an MMIC or a wire-bond connection.

Figure 3.31(a) displays how the peak amplitude distributes uniformly over the entire patch structure. At this distance above the array ($\lambda/8$), the electric field generated from the two radiating edges (Fig. 3.30(a)) is broadened enough to cover the whole antenna structure. Also, the effect of the malfunctioning element on the phase disturbance

in areas extending away from the "off" element decreases significantly (Fig. 3.31(b)). As the distance from the array increases, the output electric field of the surrounding elements around the malfunctioning element stretches over the malfunctioning element.

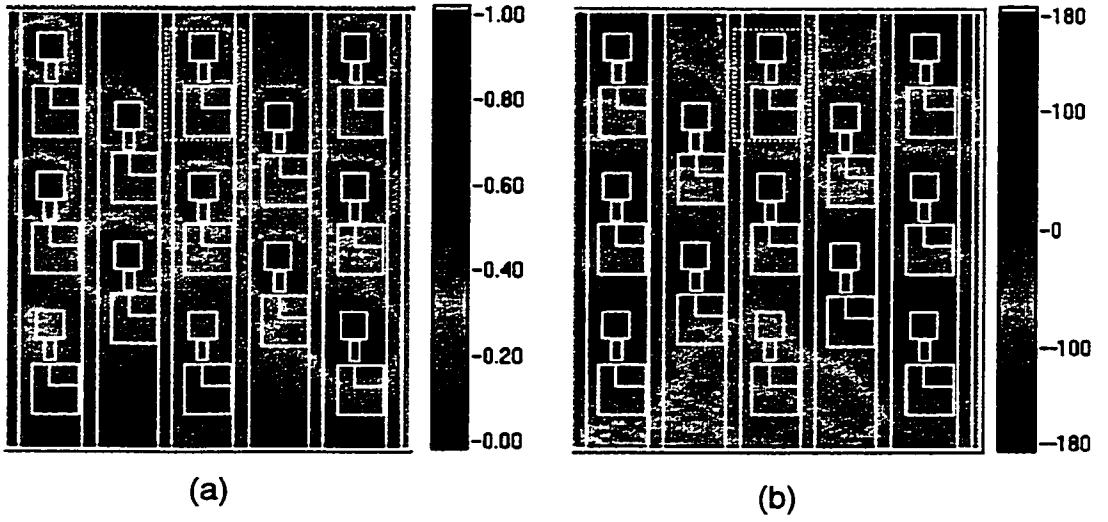

Figure 3.31: Electro-optic mapping result for the array. (a) normalized amplitude and (b) phase (in degrees) of the array for the y component at measurement height of 1.2 mm ($\lambda/8$).

As a result, the absence of electric field above the malfunctioning element becomes less significant as the distance increases. Thus, we can predict that it is very difficult or even impossible to detect malfunctioning elements above a certain distance from the array. This phenomenon emphasizes the importance of accurate near-field measurements for validating the integrity of QO power-combining array structures. In other words, neither conventional far-field measurements nor low-resolution near-field measurement techniques are sufficient to isolate a problem *within* a unit cell of an array. In fact, for the system described in this section, verification of the unit cell design

through detailed electro-optic field mapping encouraged the successful expansion of the array to one that has been demonstrated to radiate 25 W at Ka-band [44].

3.6 Summary

Three-dimensional electro-optic field mapping of a microstrip patch antenna structure is performed for a complete set of three orthogonal electric field components. The technique makes it possible to accurately determine the near-field radiation pattern of an antenna array, as well as the dominant field component of the patch antenna structure. Also, the capability for detecting the near-field to far-field transition is demonstrated. The 3-dimensional measurement results are compared with FEM simulation results, making clear that the electro-optic measurement can provide superior results to the simulation. Also, the forward scattering parameter S_{11} is calculated from the electro-optic measurement of the standing wave pattern on the feed line and antenna based on the normal-field measurement result. The result obtained from the electronic network analyzer shows an almost identical S_{11} pattern. Due to the capability of measuring electric fields directly on a microwave structure, the demonstrated electro-optic method can minimize effects that are otherwise very difficult to calibrate out during network analyzer measurements, including imperfect feeding and electrical contact. In conclusion, electro-optic field mapping is a very powerful tool for the analysis and design of microwave radiating structures, such as single antenna elements or radiating arrays.

Near-field images of the full set of orthogonal field components obtained by an electro-optic measurement system have given a profound insight into the radiation properties of a grid oscillator. The measurements are performed at different distances from the sample revealing the conversion of the radiation pattern from the near field of the single radiator elements to the superimposed field at the onset of the far field. As a result, an unexpected phase variation is detected by the near-field measurement. To verify

the measurement results, far-field calculations that are based on the near-field measurement result were performed. The calculated far-field shows excellent agreement with conventional far-field and electro-optic far-field transition measurement results. The measurements can be used to locate existing defects or to determine discrepancies between the intended and the actual operation of the device.

Also, the electro-optic field mapping technique is applied extensively to three different types of horn antennas to examine their performance. Through the electro-optic measurement, the hard horns show superior performance to the conventional WR-28 horn antenna in terms of plane wave generation. For the quasi-optical amplifier arrays, three orthogonal electric field components are measured successfully by utilizing two different types of crystals. The measurement displays a number of important characteristics of the arrays such as an improper dc bias network design, RF isolation performance, etc. Also, the high sensitivity and ability to probe very close to the arrays make possible the measurement of substrate propagation waves, which provides very crucial information for the analysis and design of periodic structures. Also, the isolation of malfunctioning elements in the arrays is demonstrated. In conclusion, the electro-optic measurement technique brings a very powerful analysis and design tool for of array structures by providing profound physical insight of them.

CHAPTER 4

FREE-SPACE EXTERNAL ELECTRO-OPTIC MAPPING SYSTEM UTILIZING GALLIUM ARSENIDE PROBES

4.1 Introduction

As discussed in previous chapters, the electro-optical measurement system utilizing Bismuth Silicate (BSO) and Lithium Tantalate ($LiTaO_3$) demonstrates excellent capability to provide a great deal of important information for many different types of microwave and millimeter wave structures, including integrated circuits, antennas, and arrays. The system can provide high-sensitivity, high-resolution 2-dimensional or even 3-dimensional field mapping results, which are very difficult to obtain via conventional measurement techniques such as open waveguide near-field measurements or far-field measurements. The information obtained by the electro-optic system is crucial to the understanding, design, and analysis of microwave or millimeter wave circuits, antennas, and arrays.

However, in spite of the many advantageous features, the system requires improvements, too. The first controversial issue about the system is the invasiveness of the electro-optic crystals to the device under test (DUT). To minimize the invasiveness, the crystals are polished to have very small size. The smallest crystal has 20 μm × 10 μm footprint area. Even though miniaturization of the crystal is possible, however, there are certain limits on the size because of the fact that the polishing process relies totally on mechanical processes. Furthermore, the dielectric constants of conventional electro-optic crystals are usually very large (e.g., $LiTaO_3$:44), which can cause distortion of the local

electric field distribution. Thus, desirable electro-optic crystals that can replace BSO or $LiTaO_3$ should possess several properties, such as ease of miniaturization and small dielectric constant.

Gallium Arsenide (GaAs) is one of the crystals that can be used as an electro-optic probe material [1]. GaAs has several advantages to BSO or $LiTaO_3$. First of all, it is more convenient to miniaturize GaAs than BSO or $LiTaO_3$, because standard solid state fabrication processes such as photolithography and various etching technique can be used for GaAs [45]. Also, GaAs has a relatively small dielectric constant (around 12) as compared to BSO or $LiTaO_3$, which is an important factor for reducing the invasiveness of the system. A number of groups have reported the use of GaAs as an electro-optic sensor crystal [46]-[48]. However, usage of GaAs as an electro-optic crystal has been limited to normal-field-component detection up to now.

In this chapter, field mapping of three complete orthogonal field components obtained using GaAs electro-optic probes is demonstrated with microwave integrated circuits and a patch antenna. Furthermore, successful W-band measurement results obtained by GaAs probes are presented.

4.2 Theory

The electro-optic field measurement technique is a practical application of the characteristic of crystal structures that change optical properties in the presence of electric fields. Thus, the sensitivity of the electro-optic crystal strongly relies on the crystal structure. It is very well known that (100) orientated GaAs has sensitivity to the normal field component (perpendicular direction to the (100) surface), and many works have been reported [47][48]. However, in spite of its advantages mentioned above, it is not sufficient to replace conventional electro-optic crystals that can detect three orthogonal field components. Thus, it is very important to achieve tangential field

sensitivity with GaAs for the implementation of a GaAs probe in an electro-optic measurement system.

It is very well known that GaAs has a zincblend lattice crystal structure [49]. In other words, GaAs has identical crystal structure for (100), (010), and (001) direction. All these three directions can be categorized as <100> by using Miller indices [49]. Thus, it can be concluded that all three orientations belonging to <100> have normal field sensitivity (field component that is perpendicular to the plane).

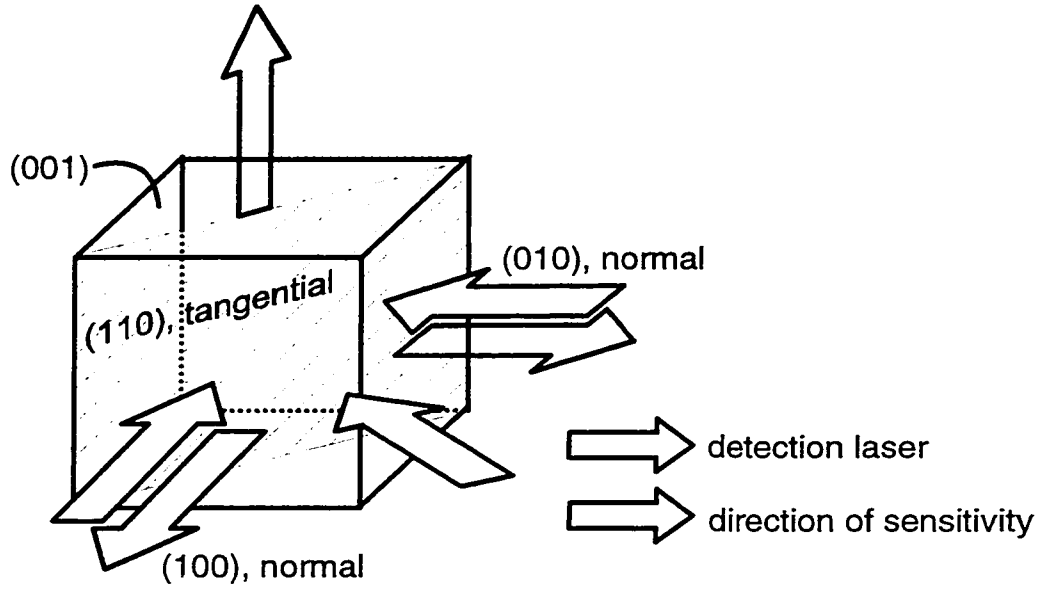

Figure 4.1: Description of sensitivity directions of GaAs crystal; White and gray arrows represent detection laser inputs and direction of sensitivities respectively. The detection laser beams are perpendicular to (100), (010), and (110) planes.

Figure 4.1 displays the relation of the sensitive direction with respect to the detection laser-beam direction and the orientation of the GaAs crystal. All incident laser beams are perpendicular to the faces. For (100) and (010) orientation, both the incident laser beam and sensitivity direction are normal to each plane. These characteristics can be

used for normal field component detection. On the other hand, when an incident laser beam is aligned normal to the (110) plane, the GaAs crystal shows sensitivity to the field component that is parallel to the plane. This is a very important characteristic of GaAs crystal for the detection of tangential field components.

In this section, a theoretical analysis of the EO effect in a GaAs crystal will be discussed. Since the theoretical approach to the EO effect in the (110) oriented GaAs crystal can be applied to (100) oriented GaAs, (110) oriented GaAs is chosen as an example.

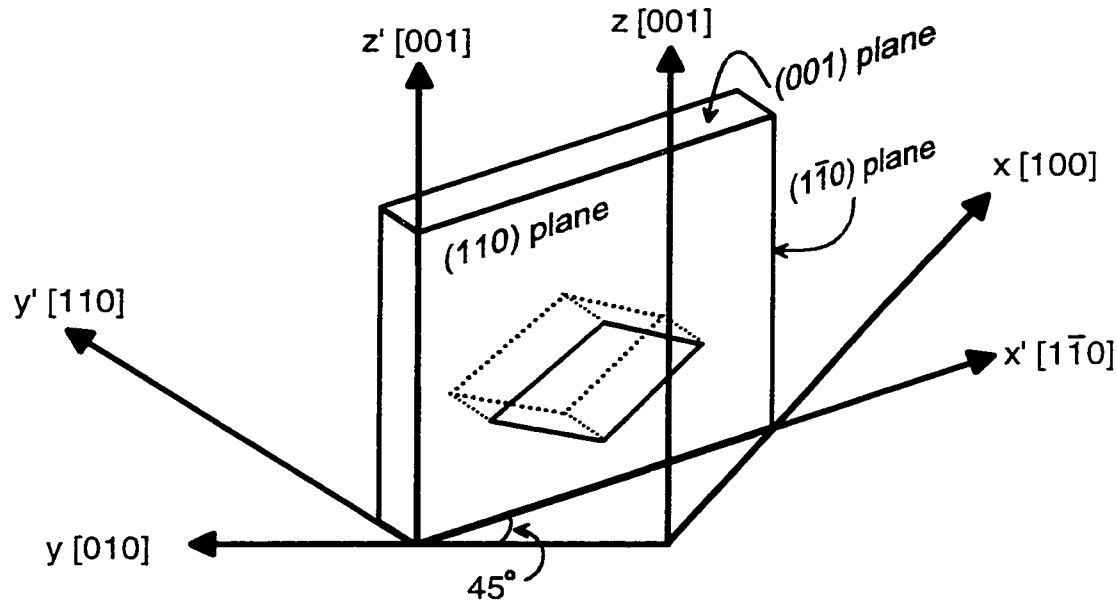

Figure 4.2: Principal axes (x, y, z) and crystal orientation for (110) GaAs crystal.

Figure 4.2 shows the axes system used in the analysis with a (110) oriented GaAs crystal. The principal axes are parallel to the [100]-[010]-[001] crystal orientations while the secondary (local) axes x′-y′-z′ are set to be parallel to the [1$\bar{1}$0]–[110]–[001] orientations of the crystal. The diamond pattern in the middle of the crystal represents the resultant etching pattern of the (110) crystal after the anisotropic wet etching process. The

detailed etching procedure will be explained in Chapter 5 of this thesis.

The propagation of an optical beam in the crystal can be expressed in terms of the impermeability tensor $\eta_{i,j}$ [1], and principal values of the tensor have the relationship with the principal axes as follows

$$\frac{x^2}{n_x^2}+\frac{y^2}{n_y^2}+\frac{z^2}{n_z^2}=1, \tag{4.1}$$

where x, y, and z represent the directions of the principal axes shown in Fig. 4.2. Also, n_x, n_y, and n_z are principal refractive indices, and $1/n_x^2$, $1/n_y^2$, and $1/n_z^2$ are the principal values of the impermeability tensor. Equation 4.1 is known as the index ellipsoid, and it is used for the explanation of the optical polarization states in a crystal.

The optical dielectric impermeability is determined by the charge distribution in the atomic lattice of the crystal. Once the electric field is applied in the crystal, it causes a slight deformation of ionic distributions in the atomic lattices. As a result, the impermeability in the crystal is modulated by the presence of the electric field. This phenomenon is known as the electro-optic effect and the electro-optic coefficients are defined as

$$\eta_{ij}(\mathbf{E})-\eta_{ij}(0)\equiv\Delta\eta_{ij}=r_{ijk}E_k+s_{ijkl}E_l, \tag{4.2}$$

where $\mathbf{E}$ is applied electric field. Also, r_{ijk} is the linear electro-optic coefficient (Pockels coefficient, F. Pockel, 1893), and s_{ijkl} is the quadratic electro-optic coefficient typically found in media that are optically isotropic such as liquids and glass (J. Kerr, 1875). Since GaAs is a solid crystal structure, we can ignore the second term (Kerr effect) in the right hand side of Eq. 4.2.

From Eq. 4.1 and 4.2, a generalized expression of the index ellipsoid in a crystal in the presence of an electric field can be obtained as

$$\sum_{i,j}\eta_{ij}(\mathbf{E})x_i x_j=1, \tag{4.3}$$

where $i, j = 1,2,3$. Also, Eq. 4.3 can be rewritten as

$$\begin{aligned}&\eta_{11}(\mathbf{E})x_1x_1+\eta_{22}(\mathbf{E})x_2x_2+\eta_{33}(\mathbf{E})x_3x_3+\\&\eta_{12}(\mathbf{E})x_1x_2+\eta_{21}(\mathbf{E})x_2x_1+\eta_{13}(\mathbf{E})x_1x_3+\\&\eta_{31}(\mathbf{E})x_3x_1+\eta_{23}(\mathbf{E})x_2x_3+\eta_{32}(\mathbf{E})x_3x_2=1\end{aligned} \tag{4.4}$$

where x_1, x_2, and x_3 are identical to the principal axes x, y, and z in Fig. 4.2.

By using the permutation symmetries such as

$$\begin{aligned}&(11)=1,\ (22)=2,\ (33)=3,\\&(23)=(32)=4,\ (13)=(31)=5,\ (12)=(21)=6\end{aligned} \tag{4.5}$$

equation 4.4 can be simplified as

$$\begin{aligned}&\eta_1(\mathbf{E})x^2+\eta_2(\mathbf{E})y^2+\eta_3(\mathbf{E})z^2+\\&2\eta_4(\mathbf{E})yz+2\eta_5(\mathbf{E})xz+2\eta_4(\mathbf{E})xy=1.\end{aligned} \tag{4.6}$$

Using Eq. 4.1 and 4.2, equation 4.6 can be expressed as

$$\begin{aligned}&\left(r_{1k}E_k+\frac{1}{n_x^2}\right)x^2+\left(r_{2k}E_k+\frac{1}{n_y^2}\right)y^2+\left(r_{3k}E_k+\frac{1}{n_z^2}\right)z^2+\\&2r_{4k}E_kyz+2r_{5k}E_kyz+2r_{6k}E_kyz=1\end{aligned} \tag{4.7}$$

with k = 1, 2, and 3 corresponding to the axes x, y, and z. Equation 4.7 shows the generalized index ellipsoid including the effect of the electric field in the crystal. Equation 4.7 can be applied to both (100) and (110) oriented GaAs crystals. Once the effect of the electric field is eliminated (*i.e.*, $E_k = 0$), equation 4.7 becomes an identical formula with Eq. 4.1.

The resultant Eq. 4.7 is derived based on the principal axes system. In order to use the equation for (110) oriented GaAs, an axes transformation procedure is required. The relationship between the principal axes and the secondary axes x′-y′-z′ system can be expressed as

$$\begin{aligned} x &= x'\cos\left(\frac{\pi}{4}\right) + y'\sin\left(\frac{\pi}{4}\right) = \frac{1}{\sqrt{2}}(x' + y') \\ y &= -x'\cos\left(\frac{\pi}{4}\right) + y'\sin\left(\frac{\pi}{4}\right) = \frac{1}{\sqrt{2}}(-x' + y') \\ z &= z' \end{aligned} \tag{4.8}$$

Since GaAs is one of the cubic crystal structure family, the electro-optic coefficient can be expressed as

$$\begin{bmatrix} 0 & 0 & 0 \\ 0 & 0 & 0 \\ 0 & 0 & 0 \\ r_{41} & 0 & 0 \\ 0 & r_{41} & 0 \\ 0 & 0 & r_{41} \end{bmatrix} \tag{4.9}$$

The coefficient matrix of the GaAs shows that the electro-optic coefficients r_{1k}, r_{2k}, and r_{3k} in Eq. 4.7 are 0, and r_{4k}, r_{5k}, and r_{6k} are equal to r_{41}. The coefficient r_{41} is determined

by the wavelength of the optical beam and the frequency of the electric field. For example, $r_{41} = 1.1 \times 10^{-12}$ m/V for an optical beam with a wavelength of 900 nm [1]. Also, the refractive indices in the Eq. 4.7, n_x, n_y, and n_z have identical value n_0, which is the refractive index of GaAs.

Using Eq. 4.8 and 4.9, equation 4.7 can be modified as

$$\frac{1}{2n_0^2}\left(x'^2+2x'y'+y'^2\right)+\frac{1}{2n_0^2}\left(x'^2-2x'y'+y'^2\right)+\frac{1}{n_0^2}z'^2+$$
$$2r_{41}E_x\frac{1}{\sqrt{2}}(x'+y')z'+2r_{41}E_y\frac{1}{\sqrt{2}}(-x'+y')z'+2r_{41}E_z\frac{1}{\sqrt{2}}\left(y'^2-x'^2\right)z'=1 \qquad (4.10)$$

or

$$\frac{x'^2}{n_0^2}+\frac{y'^2}{n_0^2}+\frac{z'^2}{n_0^2}+\sqrt{2}r_{41}E_x(x'y'+y'z')+\sqrt{2}r_{41}E_y(-x'z'+y'z')+r_{41}E_z\left(y'^2-x'^2\right)=1$$

Also, equation 4.10 can be organized with respect to the x', y' and z' as follows

$$\left(\frac{1}{n_0^2}-r_{41}E_z\right)x'^2+\left(\frac{1}{n_0^2}-r_{41}E_z\right)x'^2+\sqrt{2}r_{41}\left\{E_x(x'+y')+E_y(-x'+y')\right\}z'=1. \qquad (4.11)$$

Equation 4.11 shows a generalized index ellipsoid of the (110) GaAs in the presence of electric fields.

Equation 4.11 includes effects of three orthogonal electric fields E_x, E_y and E_z. However, for the practical usage of the GaAs crystal as an electro-optic field sensor, one needs to specify only one electric field component. In other words, it may be more reasonable to use the GaAs as an electric-field sensor to detect one field component rather than detecting multiple field components at the same time. From Eq. 4.11, it is obvious that z-component (E_z) detection is a rational choice due to the mathematical simplicity.

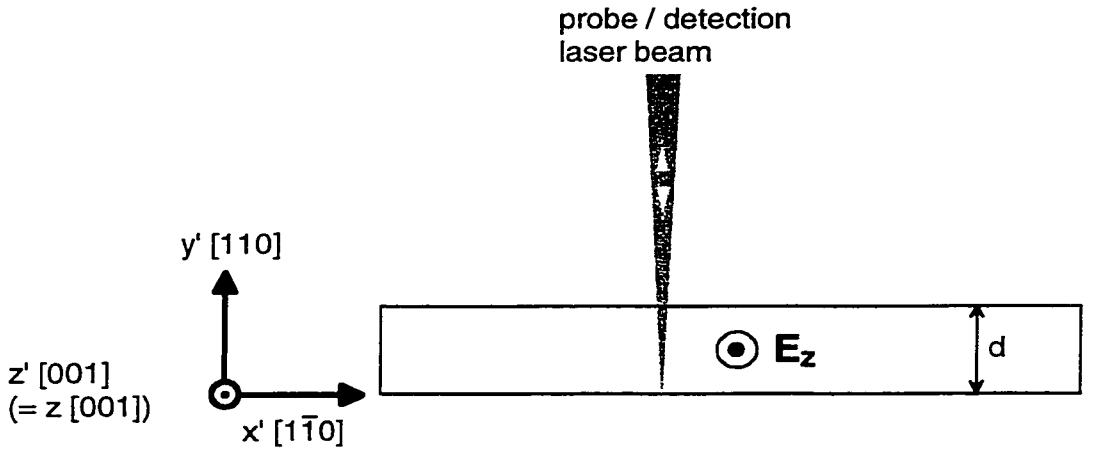

Figure 4.3: Cross sectional view of GaAs crystal with electric field E_z and laser beam (Top view of Fig. 4.1).

Figure 4.3 displays the cross sectional view of a (110) oriented GaAs crystal (top view of Fig. 4.1) with thickness d. The laser beam is aligned in the direction of the y′ axis to detect the electric field that is parallel to z′ (or z, Fig. 4.1). Since we assume that the electric field has only z-component (*i.e.*, $E_x = E_y = 0$), Eq. 4.11 can be simplified as

$$\left(\frac{1}{n_0^2} - r_{41}E_z\right)x'^2 + \left(\frac{1}{n_0^2} - r_{41}E_z\right)x'^2 = 1 . \tag{4.12}$$

Since the modulation due to the electric field is usually very small, we can assume that

$r_{41}E_z << \frac{1}{n_0^2}$, and as a result

$$n_x' \cong n_0 + \frac{1}{2} n_0^2 r_{41} E_z \tag{4.13}$$

$$n_y' \cong n_0 - \frac{1}{2} n_0^2 r_{41} E_z$$

The electro-optic modulation can be expressed

$$n_x' - n_y' = n_0^3 r_{41} E_z . \tag{4.14}$$

Also, the phase retardation Γ due to the electric field E_z can be defined as

$$\Gamma \equiv \frac{\omega}{c}\left(n_x' - n_y'\right) \times 2d = \frac{2\pi}{\lambda} n_0^3 r_{41} E_z \times 2d , \tag{4.15}$$

where d is the thickness of the GaAs. Since Fig. 4.3 shows a reflective measurement scheme, the effective modulation length is twice the thickness of d. Equation 4.15 is derived based on the assumption that the electric field is uniformly distributed inside of the GaAs along the y′ direction (Fig. 4.3). This assumption is reasonable if the thickness of the GaAs is smaller than wavelength of the electric field.

In many occasions, a half-wave voltage V_π is defined as the condition of the bias voltage that satisfies Γ=π. However, since the objective quantity of the electro-optic sensing is electric field, it is more reasonable to define "half-wave electric field E_π" instead of half-wave voltage. The parameters in Eq. 4.15 are determined by optical properties and physical size of the GaAs except the electric field E_z. Thus the retardation Γ can be considered as a function of E_z for a given GaAs crystal. As a result, the half-wave electric field can be defined as

$$\Gamma(E_z=E_\pi)=\pi. \tag{4.16}$$

where E_π is the half-wave electric field.

From Eq. 4.14 and 4.16, the half-wave electric field can be obtained as follows

$$E_z^\pi=\frac{\lambda}{4n_0^3 r_{41} d}=\frac{V_\pi}{2L}. \tag{4.17}$$

where V_π is the traditional half-wave voltage and L is the effective path length of the optical beam in the GaAs crystal. Now, Eq. (4.14) can be expressed as

$$\Gamma=\pi\frac{E_z}{E_\pi}. \tag{4.18}$$

In practical applications, a proper wave plate and polarizer are placed in the path of the output beam modulated by the electro-optic effect of the GaAs in order to convert the retardation signal into the power signal. The wave plate and polarizer combination is often called an analyzer. The intensity (or power) modulation caused by the electro-optic effect can be expressed as

$$I=I_0\cdot\sin^2\left(\frac{\Gamma_0+\Delta\Gamma}{2}\right), \tag{4.19}$$

where I_0 is the intensity without any retardation, Γ_0 is the static phase retardation due to the external wave plate as a part of the analyzer, and $\Delta\Gamma$ is the retardation induced by the electro-optic effect and electric field in the crystal.

By using proper adjustment for the analyzer, it is possible to make the static phase retardation $\Gamma_0 = \pi/2$. This condition is called the quarter-wave bias condition. For actual

application this quarter-wave bias point set of the analyzer is preferable, and the reason will be explained with Fig. 4.4.

Under the quarter-wave bias condition, Eq. 4.19 can be expressed as

$$\begin{aligned} I &= I_0 \cdot \sin^2\left(\frac{\pi}{4}+\frac{\Delta\Gamma}{2}\right) = I_0\left\{\frac{1}{\sqrt{2}}\cos\left(\frac{\Delta\Gamma}{2}\right)+\frac{1}{\sqrt{2}}\sin\left(\frac{\Delta\Gamma}{2}\right)\right\}^2 \\ &= I_0\left\{\frac{1}{2}+\cos\left(\frac{\Delta\Gamma}{2}\right)\sin\left(\frac{\Delta\Gamma}{2}\right)\right\} \\ &= I_0\left\{\frac{1}{2}+\frac{1}{2}\left[\sin\left(\frac{\Delta\Gamma}{2}-\frac{\Delta\Gamma}{2}\right)+\sin\left(\frac{\Delta\Gamma}{2}+\frac{\Delta\Gamma}{2}\right)\right]\right\} \\ &= \frac{I_0}{2}\{1+\sin(\Delta\Gamma)\} = \frac{I_0}{2}\left\{1+\sin\left(\pi\frac{E_z}{E_\pi}\right)\right\} \end{aligned} \tag{4.20}$$

Since, in this thesis, the purpose of the electro-optic field sensing is the measurement of microwave or millimeter wave structures, the electric field E_z in Eq. 4.20 should be expressed as a time varying function. Thus, from Eq. 4.20, the intensity modulation can be expressed as

$$I = \frac{I_0}{2}\left\{1+\sin\left[\pi\frac{E_z^0\sin(\omega_m t)}{E_\pi}\right]\right\} \tag{4.21}$$

where E_z^0 is electric field amplitude and ω_m is the frequency of the electric field.

Figure 4.4 shows the relation between the input RF electric field E_z and output intensity modulation I. The input sinusoidal electric field is converted into the output optical intensity modulation according to the response curve of the GaAs crystal. Now, the reason for the quarter-wave bias setting of the analyzer can be explained. From the Γ_0 axis (static phase retardation), if the static retardation is $\pi/2$, the zero point of the input

electric field is aligned to the center of the response curve. Thus, by setting the Γ_0 to $\pi/2$, the input signal corresponds to the most linear region of the response curve.

Since the input electric field is in the microwave or millimeter frequency range, one can expect only a certain amount of the electric field from the DUT can be penetrate into the GaAs. As a result, the electric field propagation from DUT to the GaAs should be explained to obtain a complete analysis of the GaAs as an electric field sensor.

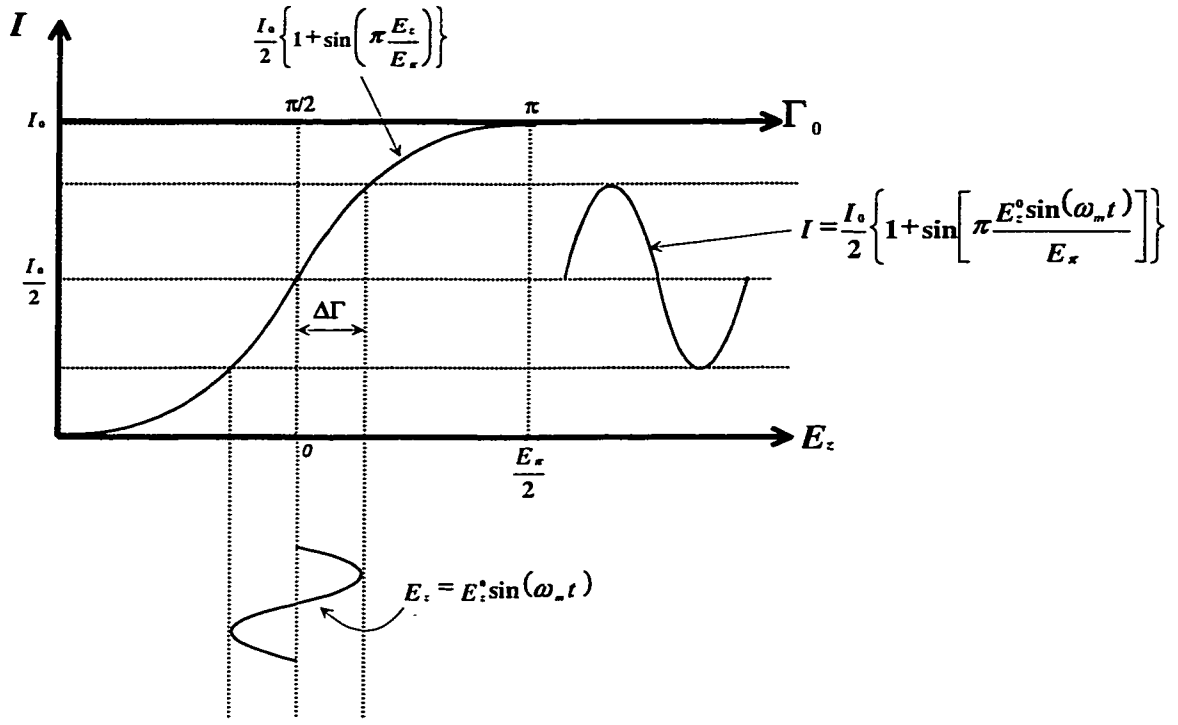

Figure 4.4: Output beam intensity response I with respect to the input RF electric field E_z. The upper x-axis (Γ_0) represents initial quarter-wave bias condition of the analyzer.

Figure 4.5 shows the electric properties between air (medium I) and GaAs (medium II). Since we consider the z-component (or z′-component) electric field, the electric field should be parallel to the air/GaAs interface, and the propagation direction of

the field can be assumed to be perpendicular to the air/GaAs interface. The z-component electric field generated from a DUT propagates via air along the y′ direction to the interface. Since the distance from the GaAs field sensor to the DUT is extremely small (typically several tens ~ hundreds micrometer range) with respect to the wavelength, the electric field in the air just before the interface can be considered as the electric field on the DUT.

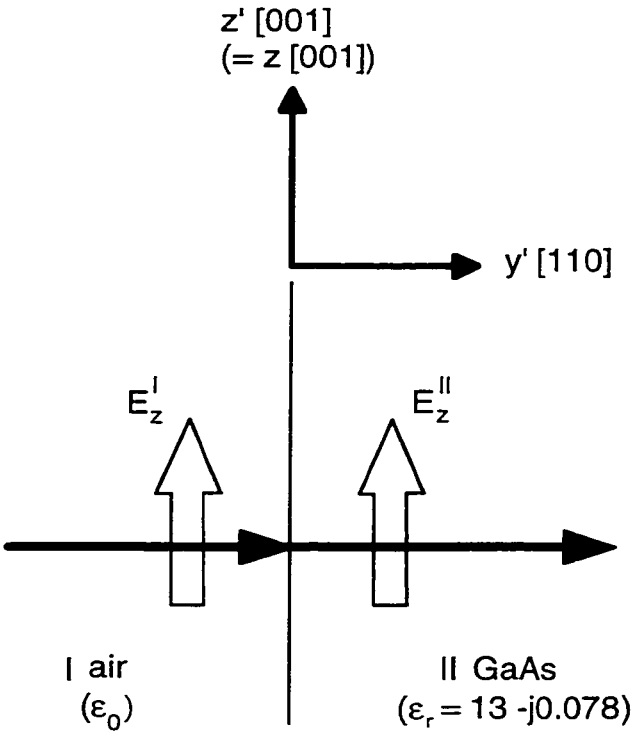

Figure 4.5: Electric field propagation between air (I) and GaAs (II) media. The propagation direction is assumed to be normal to the boundary, and displayed with solid arrows. Also, the incident electric field is assumed to be parallel to z′ axis.

The electric field propagating along the y′ direction in medium I (air) can be expressed as

$$\mathbf{E}^{\mathrm{I}}=\hat{z}'E_z^I e^{-jk_0 y'}, \tag{4.22}$$

where E_z^I is the amplitude of the electric field in the air and k_0 is the propagation constant of air.

The electric field in medium II (GaAs) is determined by the transmission constant $\boldsymbol{T}$ and complex propagation constant γ (based on the assumption that medium II has a certain amount of loss). The electric field in the GaAs can be expressed as

$$\begin{aligned}&\mathbf{E}^{\mathrm{II}}=\hat{z}'\boldsymbol{T}E_z^I e^{-j\gamma y'}\\ &\text{where}\\ &\boldsymbol{T}=\frac{2Z}{Z+Z_0}\\ &\gamma=j\omega\sqrt{\mu\varepsilon}\end{aligned} \tag{4.23}$$

where Z, Z_0 are intrinsic impedance of air and GaAs, and μ, ε are permeability and permittivity of the GaAs. By using the constants shown in Fig. 4.4, equation 4.23 can be written as

$$\mathbf{E}^{\mathrm{II}}=\hat{z}'\left(0.434+j0.001\right)E_z^I e^{-\omega\left(3.61\times10^{-11}+\,j1.20\times10^{-11}\right)y'} \tag{4.24}$$

If we focused only on the amplitude variation in GaAs, Eq. 4.24 can be simplified as

$$\left|\mathbf{E}^{\mathrm{II}}(y')\right|=0.434\left[E_z^I(y'=0)\right]e^{-\omega\,3.61\times10^{-11}y'}. \tag{4.25}$$

Using Eq. 4.25 and a nonuniform electric field distribution in the GaAs along the y′ direction, equation 4.15 can be expressed as

$$\Gamma = \frac{2\pi}{\lambda} n_0^3 r_{41} \times 2 \times \int_0^d E_z(y')dy'$$
$$= \frac{2\pi}{\lambda} n_0^3 r_{41} \times \left[E_z^I(y'=0)\right] \times \frac{0.868}{3.6 \times 10^{-11}} \left(1 - e^{3.6 \times 10^{-11} \omega d}\right) \quad (4.26)$$

Finally, the electro-optic effect of the GaAs due to the electric field on the DUT is expressed in Eq. 4.26. Equation 4.26 can be plugged in to Eq. 4.19 in order to determine the optical intensity modulation due the microwave or millimeter wave electric fields.

4.2 Measurement Results

Based on these characteristics, two different GaAs electro-optic probes are fabricated. Because the main purpose of this experiment is to examine the possibility of using GaAs crystals as electro-optic probes that have sensitivity to three orthogonal field components, simple mechanical cleaving process is used initially to fabricate the GaAs probe tips. For the detection of the field that is perpendicular to the surface of the DUTs (normal component), a GaAs wafer that has (100) orientation with 600 μm thickness is selected and cleaved into a cube that has 1 mm × 1 mm facets on the bottom and top. For the fabrication of the probe that has tangential field sensitivity, a (110) GaAs wafer with 400 μm thickness is selected and also cleaved to a cube that has 1 mm × 1 mm facets.

To demonstrate the performance of the GaAs probes, the 4-GHz microstrip patch antenna that was used in Chapter 3 is used as the DUT. The measurement setup is almost identical to Fig. 3.1, except that the BSO and $LiTaO_3$ electro-optic crystals are replaced with (100) and (110) GaAs probes, respectively. To optimize the sensitivity, it is very important to minimize the laser absorption of GaAs by utilizing longer wavelengths. The laser system is tuned to maintain a wavelength of 900 nm under mode-locking conditions. Figure 4.6 shows the mapping result comparison between BSO/$LiTaO_3$-based and GaAs-based system. Figure 4.6(a) and (b) show normalized amplitude and phase mapping

results respectively for both BSO/$LiTaO_3$ and GaAs system. For the scanning, 250 μm × 200 μm unit step size and 80 × 80 total steps are taken. Total scanning time is about 30 minute.

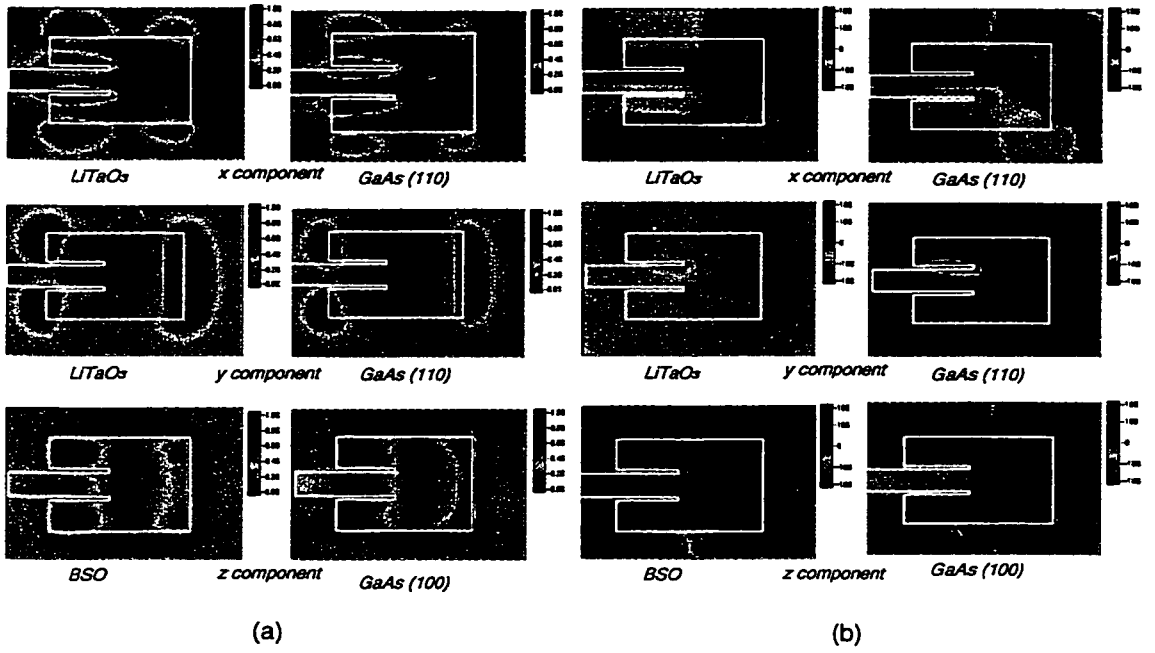

Figure 4.6: Comparison of electro-optic mapping results obtained by BSO/LiTaO3 and (100)/(110) GaAs-based system. (a) normalized amplitude; (b) phase in degrees.

Figure 4.6 shows excellent agreement between the results obtained by the two systems. In the y-component mapping results, both results show very low amplitude on the impedance matching slots. However, the phase measurement results obtained on both systems display identical abnormal phase distributions around the upper slot that are possibly caused by some small defect. This y-component comparison reveals the accuracy and repeatability of both systems. Also, the GaAs (110) probe shows superior results to the BSO crystal probe in terms of high definition for both amplitude and phase

mapping. GaAs electro-optic probes show excellent performance and successfully demonstrate three-orthogonal-component measurement capability.

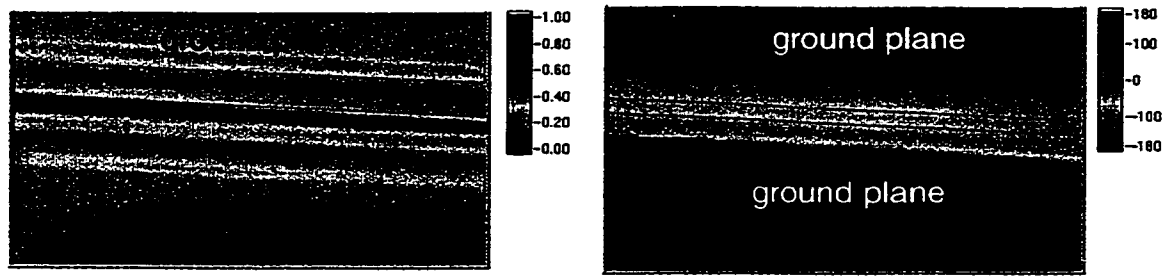

Figure 4.7: Electro-optic mapping result of coplanar waveguide structure for normal component. (a) normalized amplitude; (b) phase in degrees. (110) GaAs probe is used for measurement.

To demonstrate the high-resolution scanning capability, the electric field in a CPW line was mapped by the GaAs probe. Figure 4.7 shows electro-optic measurement results from a CPW structure for the normal component. The widths of the center conductor, gap, ground plane are 16 μm, 35 μm, and 106 μm, respectively. The normalized amplitude mapping result clearly shows that the peak amplitude occurs on the center conductor (Fig. 4.7(a)). Also, a good symmetric amplitude distribution can be observed on the center conductor, which implies that the resolution of the measurement is at least 8 μm (half width of the center conductor). The phase result shows a 180° phase difference on the center conductor and ground plane due to the direction change of the normal field component. A detailed explanation of the CPW structure is discussed in Chapter 2.

The final DUT for the GaAs-based electro-optic measurement is a frequency multiplier that has 6 times multiplication factor. The input frequency for the multiplier is

16.7205 GHz. The resultant output signal has a frequency of 100.323 GHz at the output waveguide opening. This output signal includes a 3 MHz IF signal in it. Figure 4.8 displays a 2-dimensional field mapping result of the output opening of the multiplier for the dominant field component. The actual scanning area is 3 mm × 2 mm, which includes 2.3 mm × 1 mm output waveguide openings. Because the dominant component should be parallel to the opening plane of the waveguide, the (110) GaAs probe is used to detect it. The result shows a reasonable amplitude shape in the output opening. However, the phase distribution is a little bit asymmetric. This asymmetric phase distribution can be explained by the fact that the measurement point is too close to the output source. In spite of an asymmetric distribution of phase, the result shows only a small amount of variation over the whole aperture.

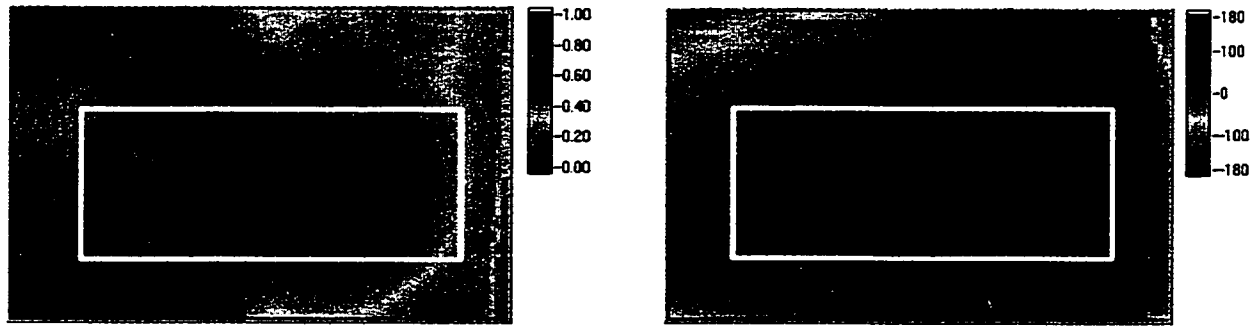

Figure 4.8: Electro-optic field mapping results of 6× frequency multiplier for dominant component. Input frequency: 16.7025 GHz, output frequency: 100.323 GHz. (a) normalized amplitude; (b) phase in degrees.

4.3 Summary

GaAs electro-optic probes are developed as an alternative to BSO and $LiTaO_3$ crystals. To achieve complete three-orthogonal-component measurement capability,

(100) and (110) orientation GaAs probes are developed. A detailed theoretical analysis of the GaAs probe is performed. For the demonstration of the GaAs free-space external field mapping, a microstrip patch antenna is selected and measured to determine its three orthogonal components. Also, the results obtained by GaAs probes are compared with those obtained by BSO/$LiTaO_3$. The comparison shows excellent agreement and consistency between them. Also, a normal-field component measurement was performed on coplanar waveguide structures. The results show an 8-μm resolution of the GaAs-based electro-optic measurement system. Finally, for the high frequency application, a 6× frequency multiplier that has 100-GHz output frequency is used as a DUT and successfully measured.

In conclusion, a new electro-optic crystal that has low permittivity and high flexibility for miniaturization is suggested by extending the application of a GaAs-based electro-optic measurement system into three complete orthogonal-field-component measurement regimes.

The GaAs EO probe can provide many promising applications such as a fiber-based electro-optic measurement system that will be discussed in Chapter 5.

CHAPTER 5

FIBER-BASED ELECTRO-OPTIC FIELD-MAPPING SYSTEM

5.1 Introduction

Accurate electric field distributions have been one of the most important information for the analysis of microwave (or mm-wave) structures since the functionality or performance of those structures are often determined by the field distributions around the structures. In particular, the near-field distributions can reveal a great deal of detailed information about micro/mm-wave structures because the observation point is very close to the device under test (DUT), and thus, undesired effects on the field measurements caused by the long distance between the observation point and DUT can be avoided.

Traditionally, theoretical approaches have been used in order to obtain detailed near-field information [50][51]. However, the experimental method that can provide detail near-field information about microwave structures under actual operating conditions, as a result, it has been considered to be advantageous to the theoretical analysis [52][53]. Furthermore, in numerous cases, conventional theoretical methods have limitations for analyzing complicated modern microwave integrated circuits or antenna arrays.

For conventional near-field measurements, small dipoles or open-ended waveguides have being employed as near-field sensors [25][26]. However, those metal structures introduced in the near-field regime of the microwave structures are often

considered to cause field distortions. Moreover, due to the limitation of the minimum physical dimensions of the sensor structures, the conventional near-field mapping fails to provide sufficient information on complicated structures.

Electro-optic (EO) field mapping has attracted a lot of attentions as a new near-field measurement method that can provide a great deal of information in micro- and mm-wave integrated circuits and radiating structures [4], [17], [19]. The detailed applications of the EO field mapping are covered from Chapter 2 to Chapter 4 of this thesis.

Since the external EO field mapping utilizes miniaturized EO crystals positioned above the DUT to detect the electric field, external EO field mapping has the capability to measure the electric field from the very top surface of the DUT to the certain distance where the field is strong enough to be detected. Because the external EO sampling does not require any metalization around the sensors, the undesired disturbance of the electric field from the presence of metal structures can be eliminated. Since the resolution of the external (or internal) EO mapping is determined by the diameter of the focused detection beam, the resolution can easily be reduced to less than the 10-μm range [54]. In addition, the measurement bandwidth of the EO mapping can cover up to THz range, and the actual measurement of W-band (100 GHz) structure was reported [54].

Based on the initial embodiment of the external EO field-mapping system, known as a "free-space measurement system" since both the detection and signal laser beams traveled in the open air [4], [17], [54], a new field-mapping system has been developed using fiber-mounted, micro-machined GaAs crystals as the electric-field sensors. The EO crystals used as the field sensors are known to have much less invasiveness than conventional metal field sensors. However, most of commonly used EO crystals such as bismuth silicate (BSO, $\varepsilon_r = 50$) and lithium tantalate ($LiTaO_3$, $\varepsilon_r = 43$) have relatively large permittivity with respect to air. Thus, finding a new EO crystal that has low permittivity is one of way to reduce the invasiveness of the field sensor. GaAs crystal has

been known as one EO material that has low permittivity (ε_r =12). Also, in addition to its low permittivity, various semiconductor etching procedures can be used to miniaturize the GaAs to suitable sizes as an electric-field sensor. As a result, the fiber-mounted EO field-mapping system is much less prone to disturb the DUT. Furthermore, since both detection and signal beams travel through the optical fiber, it provides exceptional flexibility to probe many different structures from a variety of perspectives.

5.2 GaAs Probe Tip Fabrication

For the EO field mapping application, the GaAs should have a certain amount of thickness that provides enough interaction path length for the detection beam. At the same time, it is desirable to miniaturize the size (top or bottom facet) of the GaAs EO tip as much as possible in order to reduce the invasiveness of the tip to a DUT. This design rule causes a technical difficulty during the fabrication process. In order words, an etching process with very high aspect ratio (d/g in Fig. 5.1) is required to form a GaAs EO probe tip. Furthermore, this process is even more challenging because the final goal of the processing is not removing the material but defining a geometry by using the etching process. As shown in Fig 5.1, during the etching process, the material is removed from the four sides of the pattern (if the pattern is rectangular shape). In the course of the etching process, the etchant removes the material between the patterns not only in the vertical direction but also in the lateral directions, which is called undercut. This undercut phenomenon is often observed in the etching processes with direction selectivity (anisotropic etching). Since the GaAs tip fabrication requires a very depth etching process, it is very difficult to define the final dimension of the tip (w in Fig. 5.1) precisely.

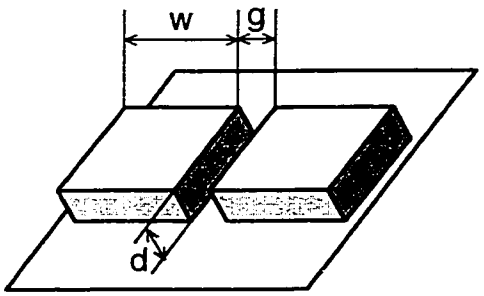

Figure 5.1: Expected GaAs EO probe etching result

In order to find a suitable process, a number of GaAs dry and wet etching processes were explored. In terms of the high aspect ratio and excellent vertical side profile, dry etching techniques such as the reactive ion etching (RIE) process are the best choice. However, the maximum etching depth of the RIE method can reach only several microns. Due to this limit of the etching depth, the dry etching process could not be used for the EO probe fabrication.

Due to the limitation of the dry etching, various wet etching processes were examined for the GaAs probe tip formation. As mentioned before, the etching process should provide high aspect ratio in order to form the GaAs EO probe. For this reason, a number of anisotropic wet-etching processes were considered. Also, another required characteristic of the etching process is high etching rate. Since the etchant has to remove a very thick GaAs wafer, an etchant with high etching rate is definitely preferable than a slow etchant if it can provide similar etching quality. Several GaAs etchants are summarized in table 5.1.

Some etchants in table 5.1 shows reasonable numbers in etching rate. However, a series of tests revealed most etchants are not suitable for the EO probe tip fabrication due to their poor etching selectivity. In other words, those etchants show very high undercut ratio during the etching anisotropic characteristics, and as a result, it is almost impossible to control the shape of the probe tips after the etching process.

Etchants (volume ratio)	Etch rate (Å/sec)			Etch ratio	Ref.
	{111}	{100}	{110}		
$H_3PO_4 : H_2O_2:H_2O$ (1 : 9 : 1)	715	525	785	1 : 0.73 : 1.1	[55]
$NH_4OH : H_2O_2:H_2O$ (20 : 7 : 150)	33	20		1 : 0.6	[56]
$H_2SO_4 : H_2O_2:H_2O$ (1 : 8 : 40)	239	200		1 : 0.84	[57]
$H_2SO_4 : H_2O_2:H_2O$ (1 : 8 : 1)	3015	2433	2295	1: 0.8 : 0.7	[58]

Table 5.1: Anisotropic wet etchants for GaAs crystal

Sulfuric acid (H_2SO_4), hydrogen peroxide (H_2O_2), and de-ionized water (DI-H_2O) with 1:8:1 volume ratio was found to be a appropriate etchant for the process due to its fast etching rate under the anisotropic etching condition. During the etching process, the sample was agitated about 30 second with 30-second interval in order to enhance the uniformity of the etching. With the agitation, etching rate was about 10 ~ 13 μm per minute.

Even though an appropriate etchant had been found, it was still necessary to find the correct alignment between the mask patterns and the orientation of the crystal to obtain a good vertical side profile. A GaAs (100) wafer is usually cleaved along (011) and $(01\bar{1})$ planes normal to the (100)-oriented top surface. These two cleavage surfaces can be used as reference planes unless a full-size wafer is used for the fabrication. Figure 5.2 displays the side profiles of the etched pattern (hatched area represent etched surface) under the case in which the mask patterns are aligned to the cleaved surfaces. Due to the characteristics of GaAs crystal structures, the side wall has positive slope along $[01\bar{1}]$ direction, while it shows negative slope along [011] direction [59].

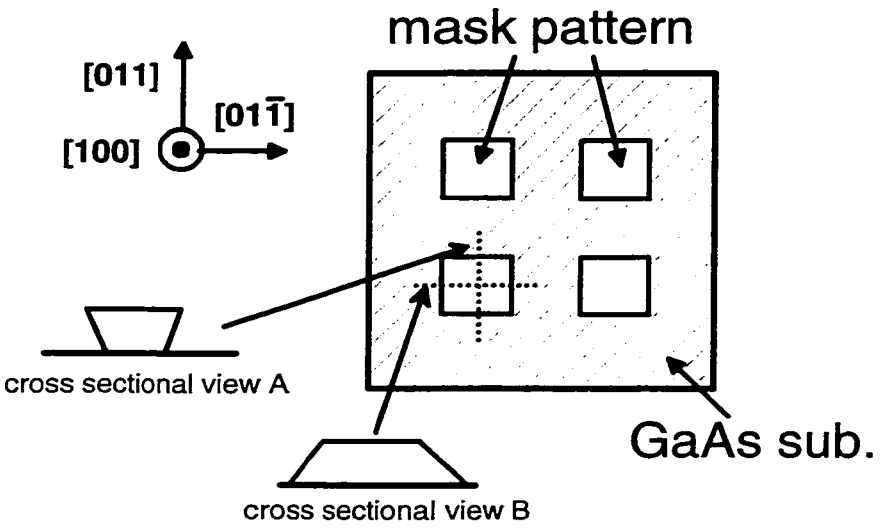

Figure 5.2: Appearances of mesa-type etching result of GaAs when the mask patterns are aligned to the cleaved edges of the substrate.

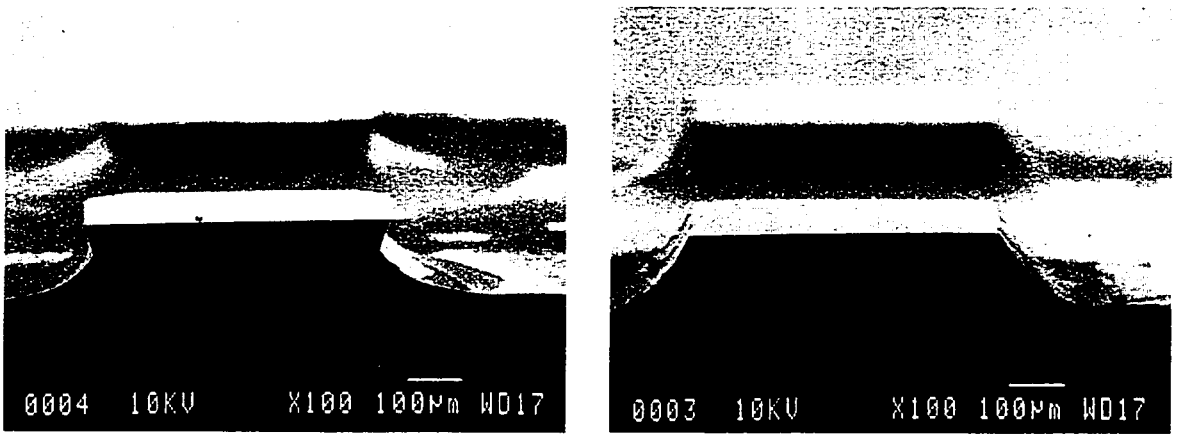

Figure 5.3: Etching results of GaAs. The SEM photo shows cross sectional view along (a) [011] and (b) [01$\bar{1}$] directions when the mask patterns are aligned to the cleaved edges of GaAs (Fig. 5.2).

The SEM photo in Fig. 5.3 clearly displays the positive and negative slope of the side walls after the etching process. Figure 5.3(a) displays a cross sectional view along [011] direction (cross sectional view A in Fig. 5.2), while Fig. 5.3(b) shows a cross sectional view B in Fig. 5.2.

In order to achieve symmetry side wall profiles, the mask patterns were aligned to the GaAs as shown in Fig. 5.4. In this case, the edges of the square mask patterns were aligned to the cleaved plane with a 45° offset angle. As a result, the boundaries of the patterns become parallel to the [100] and [010] direction of GaAs crystal.

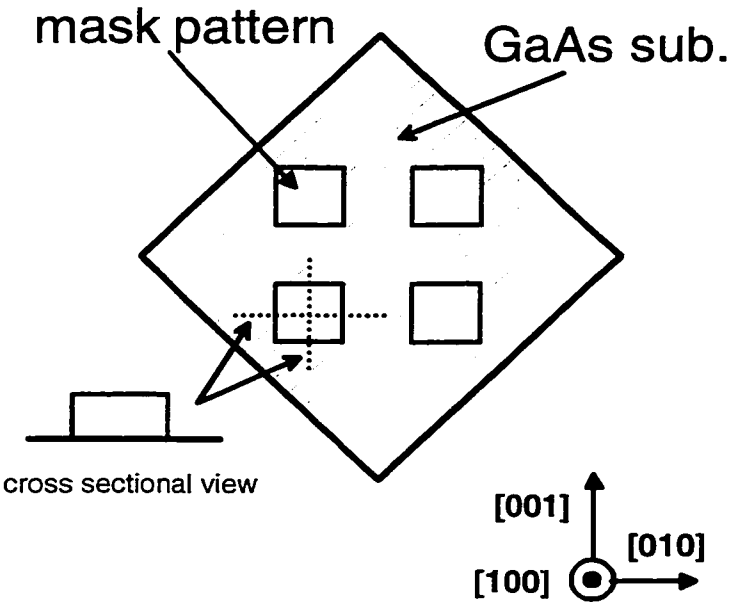

Figure 5.4: Appearances of mesa-type etching result of GaAs when the mask patterns are aligned to the (100) direction.

By using this alignment configuration, good vertical side profiles were obtained because all exposed areas to the etchant had identical crystal structures. However, as a result, the undercut (side direction) ratio became very close to 1. In other words, the

etching rates along the vertical and side directions were almost the same. Thus if this alignment scheme is used, extra margins of the patterns are required during design to compensate for the high undercut rate. In Fig. 5.4, the etched area is depicted with hatches.

Figure 5.5 shows a SEM photo of GaAs sample after the test etching process with the alignment scheme in Fig. 5.4. For the test, square patterns were masked on the top of the 600-μm, (100)-oriented GaAs wafer by using standard photolithography techniques. The SEM photo displays excellent definition between the top and side surfaces. Also it shows good vertical side profiles. Again, in this etching test, a certain amount of the anisotropic etching characteristic is sacrificed in order to obtain good vertical side profiles.

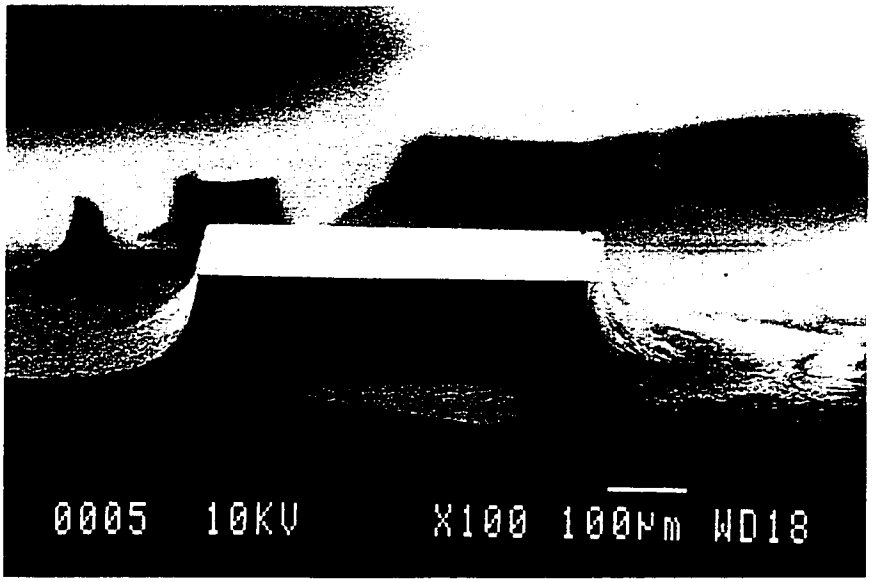

Figure 5.5: Test wet etching result with the pattern alignment in Fig. 5.4. The GaAs ample in the SEM photo was etched about 10 minute, and the etchnat was H_2SO_4:H_2O_2:DI-H_2O solution with 1:8:1 volume ratio.

Based on the etching test results, actual masks for the probe tips were designed. For the actual fabrication, the probe tip patterns were formed on (100) and (110)-oriented GaAs wafers with 200-μm thickness. A positive photo resister PR 1827 was spin coated with thickness of 3.5 μm and patterned by using photolithography technique. Since the PR patterns had to protect the GaAs from the etchant, an additional post hard bake process was added in order to enhance the strength of the PR patterns.

The resultant size of the tip was designed to be a 500 × 500-μm footprint and 200-μm thickness. Thus, additional margins that compensated the undercut during the etching process were introduced to the mask patterns. As a result, the individual tip pattern had 900 × 900-μm area.

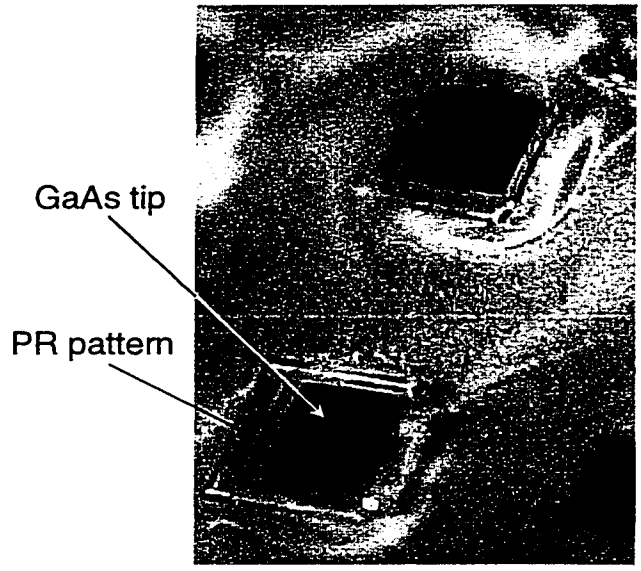

Figure 5.6: Microscope photograph of the GaAs sample during the etching process

After the patterning, the GaAs sample was mounted on the glass substrate using clear wax to protect the backside of the sample during the etching process. In the course of the etching process, the etchant was agitated every 30 second for 30 second to enhance the etching uniformity. Also, the etchant was replace every 10 minute to maintain the

etching condition uniform. Figure 5.6 shows the microscope photograph of the GaAs sample during the etching process. The PR patterns can be observed as semi-transparent membranes on the top of GaAs structures, which eventually become the probe tips. Unlike the top surfaces of the tips, which appear as dark gray squares, the etched area is shown in a bright gray color. Also, a considerable amount of the undercut occurred, and as a result, the edges of the GaAs tips can be found under the PR patterns.

The etching process was continued until the tips were completely isolated from each other. In other words, the etching process was finished when the GaAs between the tips (bright gray area in Fig. 5.6) was completely etched away. The resultant sample after the etching process had isolated hexahedral shape probe tips on the glass substrate. After the etching process, the PR patterns that provided protection were no longer required. In general, a sample is soaked in acetone to remove residue PR patterns. However, the acetone also attacks the clear wax that holds the probe tips on the glass substrate. To remove the PR patterns on the top of the probe tips, a variation of the photolithography technique was used. The sample (with PR pattern on top) was exposed without any mask. Since the PR was positive type, the PR patterns could be removed in the developer after the exposure. Unlike the acetone, the developer did not attack the clear wax.

After removing the PR residue on the top, the sample was ready to move to the next fabrication step. Since the reflected signal from the probe tip contained the EO signal, it was very important to maximize the reflected beam strength to enhance the sensitivity of the EO system. For this purpose, the free-space system utilized a probe tip that had total internal reflection facets as described in Chapter 3. However, in the fiber-based EO system, the probe tip was mounted at the end of the optical fiber. As a result, intentional control of the incident position of the optical beam into the tip was impossible. Thus, instead of using total internal reflection scheme, a high-reflection coating was deposited on the GaAs tip to maximize the reflection of the beam. For the high-reflection coating, four sets of MgF_2 and ZnSe layers were deposited on the GaAs

tips. Since the tips were totally isolated from each other, no additional masking process was required.

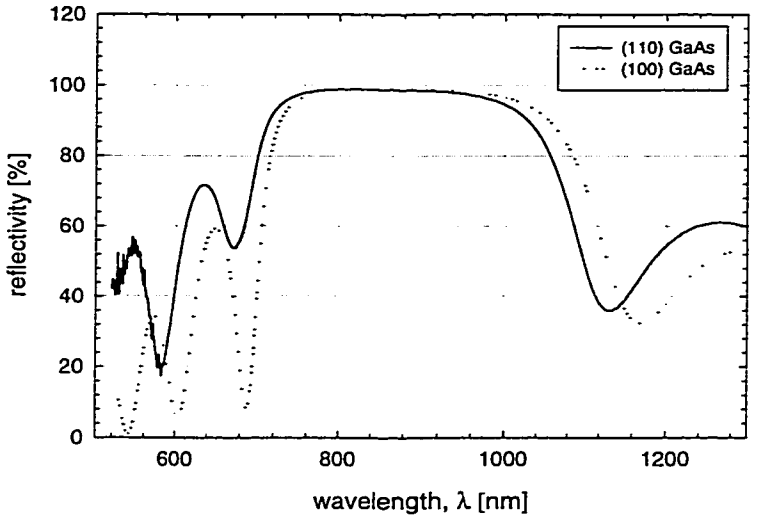

Figure 5.7: Reflectivity of the dielectric high-reflection coating on the (100) and (110) GaAs surface.

The dielectric layers were deposited by using an evaporation method. The reflection coating was designed to have its maximum reflectivity at the wavelength of 900 nm. The thicknesses of the layers are 1406 Å for MgF_2 and 833 Å for ZnSe. Figure 5.7 displays the reflectivity measurement of the high-reflection coating. The result demonstrates that the high-reflection coating provides more than 90 % reflectivity in the wavelength range of 780 nm to 930 nm for both (100) and (110) GaAs.

The fabrication processes explained above was mostly based on the (100)-oriented GaAs, which was used to detect normal (to DUT) field component. For the tangential field detection, (110)-oriented GaAs probe tips were fabricated following the identical processes as the (100) GaAs. However, the (110)-oriented GaAs has a different

crystal orientation than the (100) GaAs, and thus a different mask pattern was required in order to achieve the same etching result.

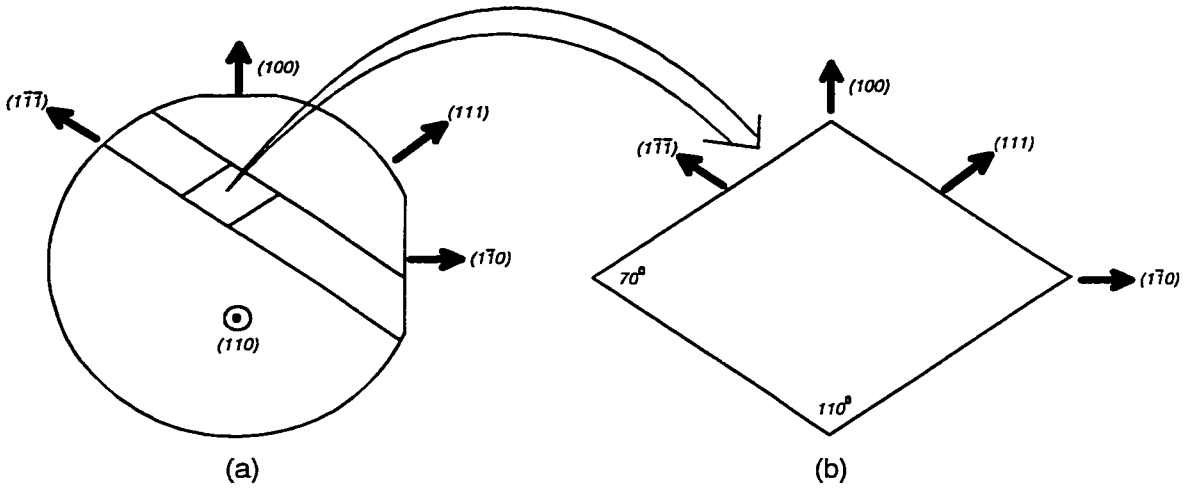

Figure 5.8: Cleavages of (110)-oriented GaAs wafer (solid lines in (a)). The directions of the cleaved planes are shown in (b).

Based on the cleaved planes of the (110)-oriented GaAs wafer, a mask pattern for the EO probe tip was designed. The mask pattern was designed to have identical shape as the cleaved GaAs sample shown in Fig. 5.8(b) in order to achieve a vertical side profile. This pattern also can be found in Fig. 4.2 in Chapter 4. After a series of etching tests, the final the mask pattern was designed as shown in Fig. 5.9.

Figure 5.9 shows the mask pattern with solid lines and the expected GaAs tip pattern with dashed lines. The undercut rates are 5.65 μm/min and 24.78 μm/min for the upper and lower sides of the pattern, respectively. The goal for the etching process was to obtain a probe tip with diagonal length (L_f) of 500 μm. From this condition, the mask was designed as follows

$$L_f = L_i - (d_1 + d_2) \times 2$$
$$= L_i - \left(5.65 \times t \times \cos(35^\circ) + 24.78 \times t \times \sin(55^\circ)\right) \times 2 \quad (5.1)$$

where L_i, L_f represent the initial and final diagonal length of the tip, and t is the total etching time.

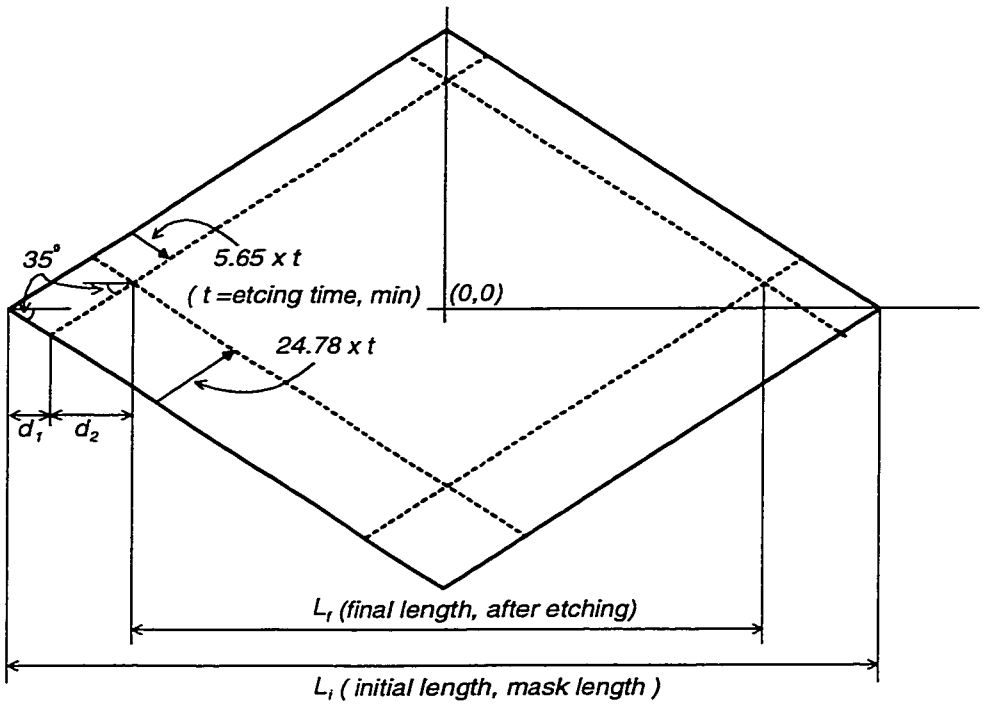

Figure 5.9: Mask pattern design for the (110)-oriented GaAs

Since the etch rate for the (110) GaAs was found to be 18.86 μm/min during the test etch, the total etch time for the 200-μm thick GaAs can be calculated as

$$t = \frac{200}{18.86} = 10.6\ [\text{min}] \quad (5.2)$$

From Eq. 5.1 and 5.2, for the final tip of 500-μm diagonal, the initial length L_i (i.e., mask size) was determined to be

$$\begin{aligned} L_i &= 500 + \left(5.65 \times \cos(35^\circ) + 24.78 \times \sin(55^\circ)\right) \times 2 \times 10.6 \\ &= 1029\ [\mu m] \end{aligned} \tag{5.3}$$

Again, the pattern was formed on (110) GaAs with PR1827 photo resistor, and the etching process was performed. After the etching process, the high-reflection coating was deposited to enhance the reflectivity. Both (100) and (110)-GaAs EO tips with high-reflection coating on them were released in hot acetone for probe assembly.

As mentioned in Chapter 1, the resolution of the EO field mapping is mainly determined by the focusing diameter of the detection beam. This rule also applies to the fiber-based EO field mapping system. Thus, it is advantageous to make the detection beam well focused into the GaAs tips in order to achieve high-resolution. A gradient index (GRIN) lens has almost perfect features for this application. Unlike conventional convex lenses, the GRIN lens has cylindrical shape, and thus, it can be perfectly placed between the end of the optical fiber and the GaAs probe tip. Figure 5.10 displays the GaAs probe tip assembled with the GRIN lens at the end of the single mode optical fiber that has 4 μm core diameter and the cladding of 120-μm diameter. The length of the GRIN lens was selected so that the beam is focused at the surface of the GaAs probe as shown in Fig. 5.10. The diameter of the GRIN lens is 1.0 mm.

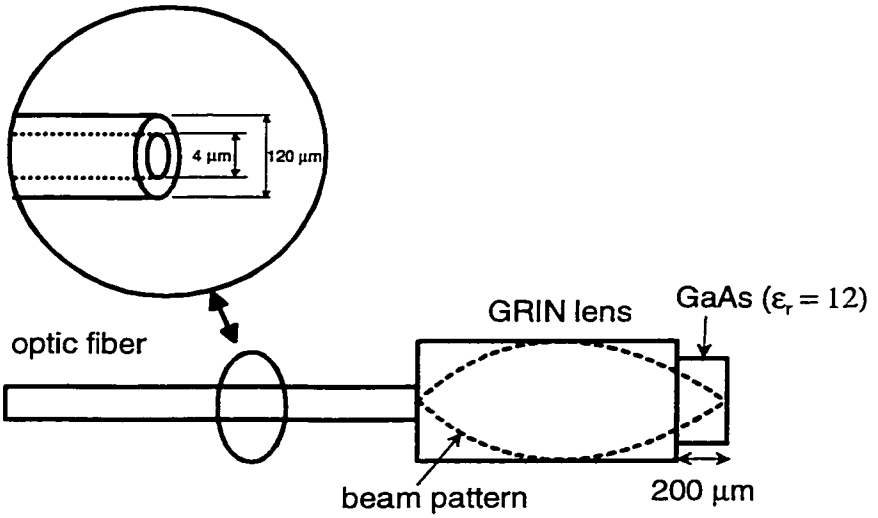

Figure 5.10: GaAs EO probe assembly using a GRIN lens. The core and cladding of the single mode optical fiber is magnified in the circle.

Figure 5.11: Microscope photograph of the GaAs probe mounted at the end of GRIN lens.

5.3 System Configuration

The experimental measurement system used is shown in Fig. 5.12. The optical beam from a phase-stabilized Ti:sapphire laser, which had 100-fs duration pulse output at an 80-MHz pulse repetition rate, was focused into the single-mode optical fiber in order to detect the EO signals. The laser wavelength was tuned to 900 nm and its average power was attenuated to around 15 mW to avoid absorption by the GaAs [49]. The input (detection) beam generated from the laser passed through the optical isolator to suppress any backward reflection that could disturb the phase stability of the laser system from the fiber coupler. Then the polarization of the input beam was manipulated from vertical to horizontal polarization by utilizing the half-wave retardation plate. The input beam focused into the optic fiber through the fiber coupler traveled to the end of the fiber and was focused into the GaAs EO probe tip via GRIN lens. The reflected (signal) beam modulated by the presence of the electric field inside of the GaAs then traveled backward to the polarization dependent beam splitter, and the direction of the signal beam was changed to the photodiode by the beam splitter.

The optical signal from the beam splitter was converted into an electrical signal by the photodiode and detected the by lock-in amplifier. Since all electronic equipment had a common 10 MHz reference signal from the laser, it was possible to measure the amplitude and phase of the electric field simultaneously. The signal frequency from an RF-synthesizer was selected to be an integer multiple of the pulse repetition rate of the laser (80 MHz) plus an IF frequency. By using a harmonic mixing scheme between the RF signal to the DUT and the detection laser pulse repetition rate, the lock-in amplifier was able to detect the IF frequency EO signal from the photodiode. Also, to achieve 2-dimensional field mapping, the sensing end of the fiber was attached to the computer controlled x-y-translation stage.

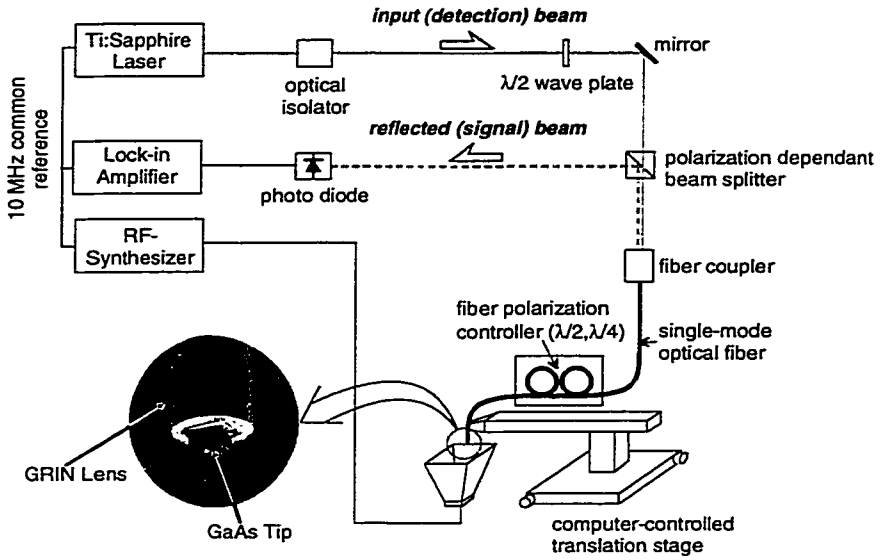

Figure 5.12: Fiber-based electro-optic field mapping system schematic. The input (detection) and reflected (signal) beams are depicted with solid and dotted gray lines. All electrical connections are displayed with solid lines. Also, a magnified photo of the probe tip area is included in the circle.

The resultant EO signal was obtained from the polarization difference between detection (input) and signal (reflection) beams. Since both detection and signal beams traveled exactly the same path, a special polarization manipulation schematic was required to separate one beam from other. The polarization dependent beam splitter has the unique property that it allows a beam to pass that has specific polarization without any change of the propagation direction. In this case, the horizontally-polarized beam traveled through the beam splitter without any propagating direction change. The laser generated a vertically polarized output beam. Thus, the half-wave retardation plate was introduced into the beam path in order to achieve horizontal polarization input to the beam splitter. Figure 5.13 displays the polarization conditions at the critical points in the system. The polarization conditions of the detection beam at various positions are displayed with solid circles and lines while the conditions of the signal beam are shown

with dotted lines. The horizontally polarized detection beam (IN1, Fig. 5.13) propagated through the beam splitter and was focused into the single-mode optical fiber by the fiber coupler. Since the single-mode fiber preserved the polarization, the beam inside of the fiber maintained same horizontal polarization (IN3, Fig. 5.13). From this stage, it as necessary to manipulate the polarization so it was aligned to the optic axis of the GaAs probe in order to detect the EO signal [1]. Also, at the same time, the signal beam should have a certain amount of polarization rotation in order to be separated from the detection beam. For these polarization controls, two in-situ polarization control loops were utilized. The first loop (from the fiber coupler) had the function of quarter-wave retardation and the other served as half-wave retardation. In both cases, the planes of the loops were equivalent to the fast axes of the wave plates. Thus, one could control the polarization by setting the loop planes at certain angle from the horizontal (or vertical) axis.

The fast plane of the quarter-wave loop is set to be 22.5° off from the horizontal axis. Thus, a linearly, horizontally polarized beam was changed into the elliptically polarized beam that was 22.5° off from the horizontal axis (IN4, Fig. 5.13). The half-wave loop provided arbitrary control of the polarization (θ in IN5, Fig. 5.13) of the input beam to the GaAs probe. Thus the polarization axis could be aligned to the optical axis of the GaAs probe tip. Now, the detection beam that traveled through the GaAs was reflected from the high-reflection coating on the bottom surface and reflected backward to the GRIN lens. In the course of travel, the polarization of the beam was slightly altered by the presence of the electric fields due to the EO property of the GaAs crystal. The angle δ shown in OUT1 in Fig. 5.13 represents the electro-optically-modulated polarization angle. The reflected (signal) beam passed the half-wave loop again. Since the beam passed the loop twice, the total retardation became one full wavelength, and thus, the retardation effect was cancelled. As a result, the signal beam after the half-wave loop (OUT2, Fig. 5.13) had identical polarization as the detection beam at position IN4, except that the signal beam included an additional EO signal that is expressed as the polarization

angle δ. Now, the signal beam traveled through the quarter-wave loop again. Since the beam passes the loop twice, the total polarization retardation was equal to a half wavelength with 22.5° offset. Thus the signal beam after the loop (toward the fiber coupler) was linearly polarized at (45 + δ)° off from horizontal axis (OUT3, Fig. 5.13).

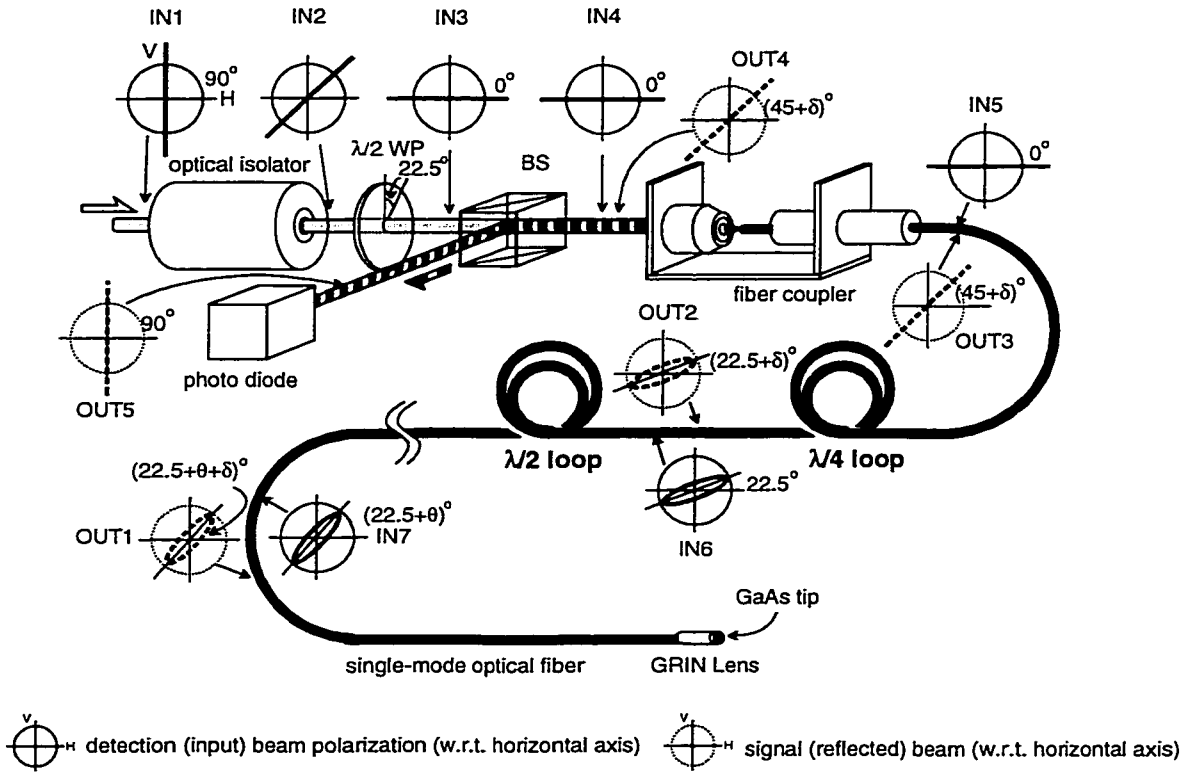

Figure 5.13: Phase control diagram of the fiber-based electro-optic field mapping system. The detection beam is depicted with thick gray line, and dark gray bands are used to indicate the signal beam. The polarization conditions of the detection beam are displayed with solid lines (or ellipses) in the solid circular axes. The dotted circular axes and dotted lines (or ellipses) are used for the signal beam. The horizontal axis is used as reference for the polarization angles.

The polarization dependent beam splitter used in the system allowed a horizontally polarized beam to pass it without change of propagation direction. In other words, if a vertically polarized beam enters the beam splitter, the propagation direction is altered by 90°. As a result, for an incident beam with the polarization between horizontal and normal polarization, the output beam is splitted into two perpendicular directions with different power ratio with respect to the polarization angle. Thus the output beam power from the splitter has the best linearity when the input beam has 45° polarization angle. The signal beam from the probe tip had the polarization angle of $(45 + \delta)°$, and thus, approximately half of the beam was reflected from the beam splitter into the photodiode that is placed perpendicular to the direction of the detection beam. Since the angle δ was much smaller than the fixed 45° angle, the input power variation to the photodiode was linearly proportional to the variation of angle δ. As a result, the photodiode detects the power-modulated EO signal that was originally generated from the GaAs tip as a mean of polarization modulation.

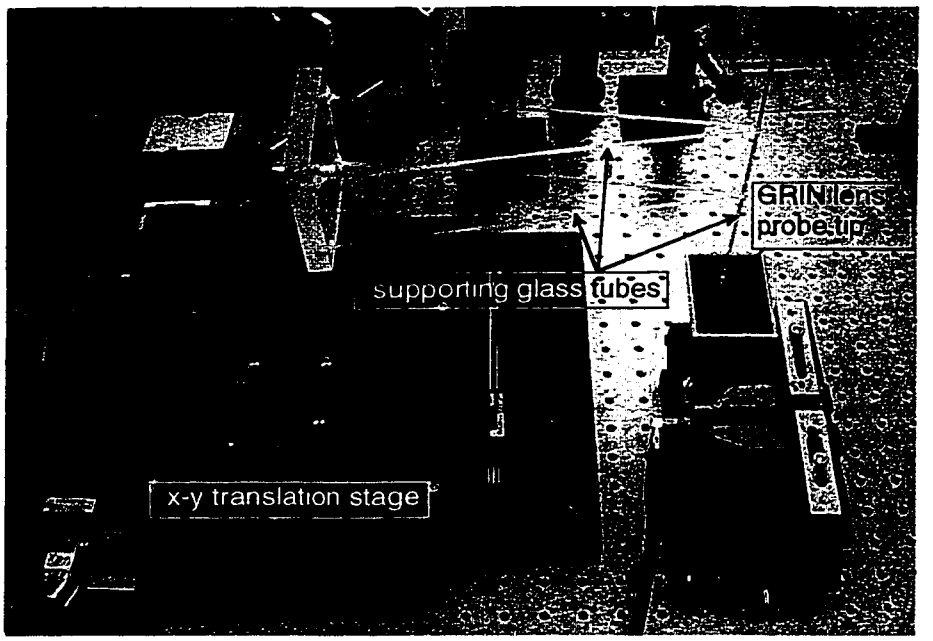

Figure 5.14: Photograph of the fiber-based EO field mapping system

5.4 Measurement Results

5.4.1 Folded Slot Antenna

For the demonstration of the three-orthogonal field measurement capability, a folded slot antenna [60] fabricated on a duroid substrate that had a thickness of 1.524 mm and a dielectric constant of 2.94 was measured by the fiber-based EO mapping system. The operating frequency was 11.203 GHz, which was the sum of the integer multiple of the pulse repetition rate (11.2 GHz) and the IF signal frequency (300 MHz). The width of the radiating slot and the center conductor were 0.35 mm and 0.50 mm, respectively.

A (110) oriented GaAs probe was used to measure the tangential electric field components that were parallel to the surface of the slot antenna. The two tangential components (*i.e.*, x- and y- component) were measured separately by rotating the orientation of the probe or the antenna by 90° after one measurement. Also, the normal field component was measured by utilizing the (100) GaAs probe tip. During the 2-dimensional field mappings, the measurement step size was 265 μm × 98 μm along the x-direction (parallel to the radiating slot) and y-direction, and 50 × 50 steps were taken. The distance between the top surface of the antenna to the probe was 500 μm in all three cases.

Figure 5.15 shows the 2-dimensional mappings of the three electric field components in normalized amplitude and phase. The y-component (dominant field component) of the slot antenna displays its peak amplitudes inside of the horizontal slots (Fig. 5.15(a)) and nulls in the two short vertical slots. Also, the phase mapping of the y-component shows almost uniform phase distribution in both upper and lower slot areas. Since the fields in the upper and lower gaps are in phase, the fields are constructively added each other.

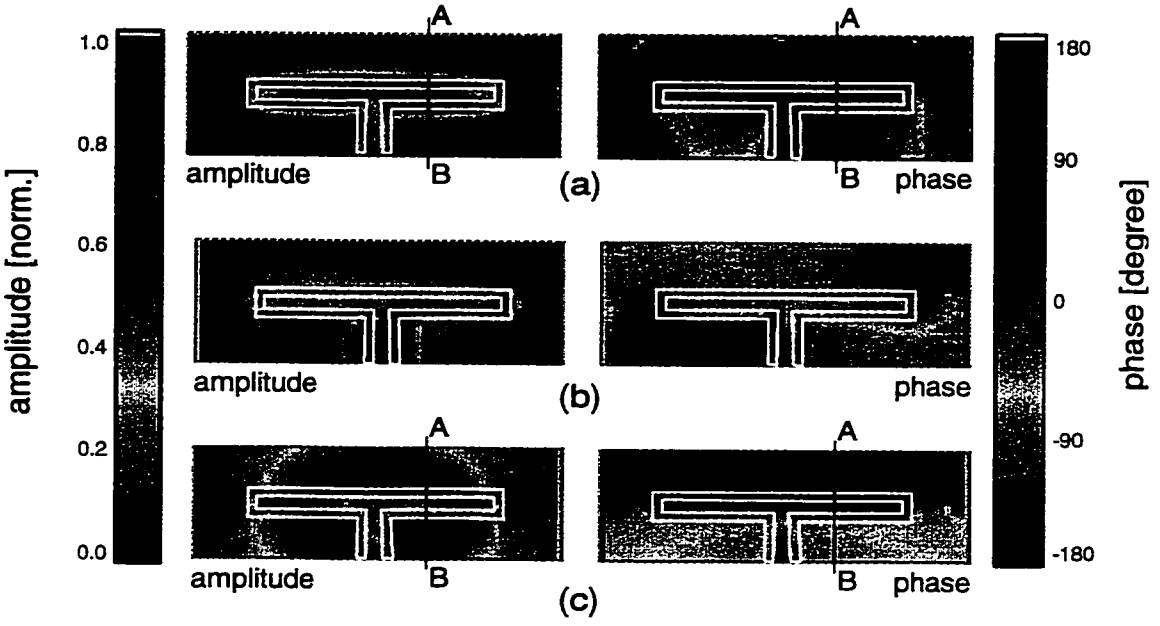

Figure 5.15: Two-dimensional amplitude (left-hand column, normalized) and phase (right-hand column, in degrees) distributions of a folded slot antenna. A (110) oriented GaAs probe is used for (a) y-component and (b) x-component measurements while a (100) oriented GaAs probe used for (c) z-component measurement. The directions of the electric fields are displayed at the left upper corner of the amplitude maps. The cross sectional line $\overline{AB}$ used in Fig. 5.4 is displayed. Also, the outline of the antenna is overlayed with white lines.

Unlike the dominant y-component, the other tangential field component (x-component, Fig. 5.15(b)) displays very low amplitude distribution in the horizontal radiating slots. Actually, the peak x-fields exist in the gaps of the feeding coplanar waveguide (CPW) structure. The amplitude of the x-component in the feeding CPW shows very similar distribution as the y-component in the radiating slots. Both x- and y-component display their peak amplitudes in the gaps between the center conductor and

ground plane. Thus the amplitude distributions show somewhat similar patterns across the radiating slots (y-component) and CPW feed line (x-component). However, it is the phase distributions that provide critical information about the difference between the radiating and guided waves. As pointed out previously, the y-component in the radiating slots are in phase while the x-components in the feed CPW show 180° off phases (Fig. 5.15(b)). As a result, the radiated x-component fields from each gap cancel each other. Also, the two tangential components clearly display that the even mode signal in the CPW feed line is transformed into the odd mode fields in the radiating slots, which is in good agreement with previous studies of the folded slot antenna [61].

The comparison between the two tangential components demonstrates that it is very important to acquire accurate phase information along with the amplitude to analyze micro- or mm-wave structures correctly, and especially, those structures that have both guided and radiating structures. In this sense, the fiber-based EO mapping system can be the most effective measurement means for providing high-resolution amplitude and phase information simultaneously.

Since the electric field should always be perpendicular to the surface of the metal, the peaks of the normal field exist on the metal plane. As a result, unlike the tangential components that have their peak amplitudes in the gaps, the normal field has its peak amplitudes on the two lower ground plane corners, the center of the upper ground plane (Fig. 5.15(c)), and on the center conductor of the slot antenna. The two peaks on the lower ground plane have identical phases while the peak on the upper ground plane has 180° off phase. The peaks on the center conductor have 90° off phase from the peaks on the upper and lower ground planes.

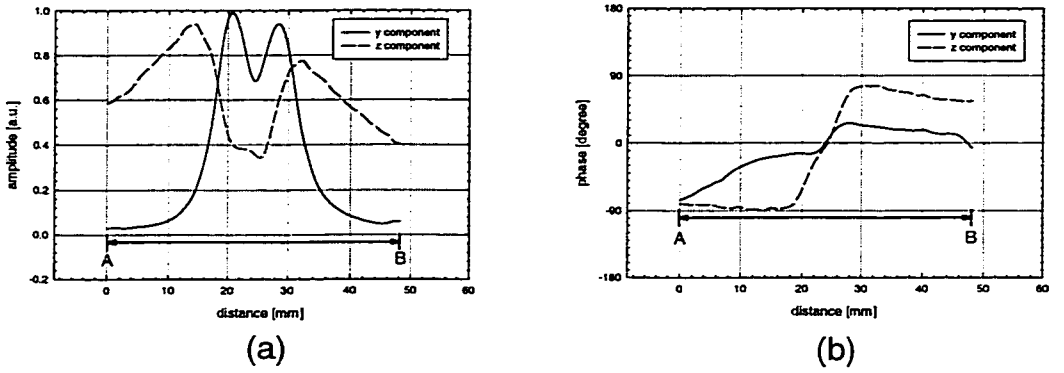

Figure 5.16: One-dimensional y- and z-component (a) amplitude (in a.u.) and (b) phase (in degree) variations along the cross section AB shown in Fig. 5.15.

Figure 5.16 displays 1-dimensional y- and z-component amplitude (Fig. 5.16(a)) and phase (Fig. 5.16(b)) comparisons along the line $\overline{AB}$ shown in Fig. 5.16(a) and (c). The y-component amplitude displays its two peaks where the positions correspond to the slots. Also, the two peaks show around 40° phase difference. Unlike the y component, the z component displays its main peak amplitudes on the upper and lower ground planes and small peak on the center conductor. The phase plot of the z-component (Fig. 5.16(b)) shows the two peaks have 180° off phase with respect to each other.

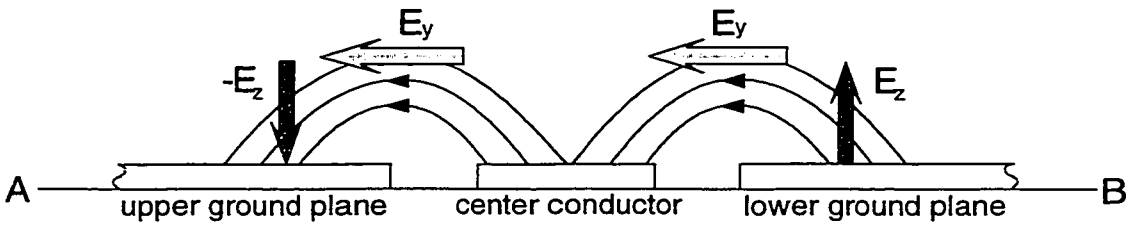

Figure 5.17: Cross sectional field electric field lines along the line $\overline{AB}$ shown in Fig. 5.15.

As a result of the two- and one-dimensional results of both y- and z-component distributions, the electric field line plots can be overlayed with the cross-sectional view of the slot antenna (Fig. 5.17). The electric field lines generated from the lower ground plane have normal direction (z-direction). As the electric field travels toward the center conductor, the magnitude of tangential (y) component increases while the normal component decreases. As a matter of fact, the tangential field reaches its peak just above the gap between the ground plane and the center conductor. While the field generated from the lower ground plane (ground plane on the right side in Fig. 5.17) merges into the center conductor, another field starts its travel from the center conductor to the upper ground plane. The direction of the electric fields can be altered with respect to the phase condition. Finally, the EO field mapping results successfully confirm that the folded slot antenna operates under the "odd-mode" [61].

5.4.2 Ka-Band Horn Antenna

One of outstanding features of the fiber-based EO system is its measurement flexibility. Since the EO crystals are mounted at the end of the flexible optical fiber, the probe can be positioned at any place with arbitrary directions. Due to its incomparable versatility, the fiber-based EO mapping system can possibly provide high-resolution near-field data for micro/mm-wave structures mounted inside of partially closed structures such as waveguide or horn antennas [62][63]. Even for the fully closed structures, the fiber-based EO system requires only a small access hole to obtain accurate near-field information. As a result, the fiber-based EO system makes it possible to extend the range of the near-field measurement.

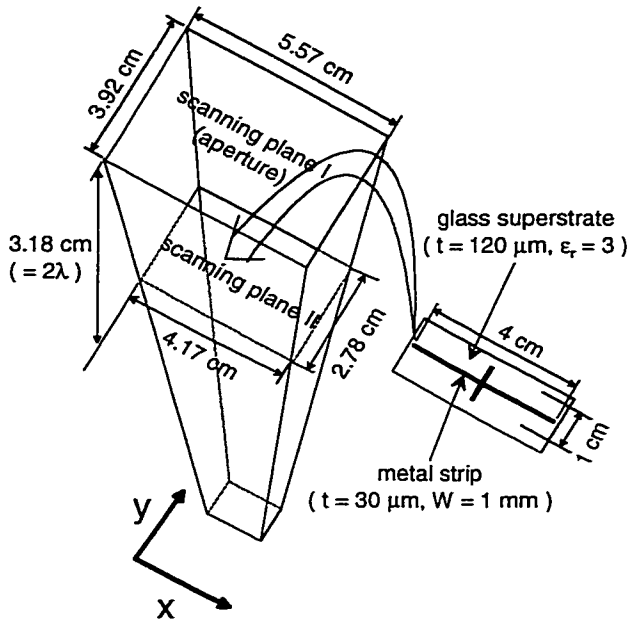

Figure 5.18: The Ka-band horn antenna diagram used as an antenna under test. The scanning plane I (aperture) and plane II (2 wavelength inside of the horn) are displayed their dimensions. Also, the metal insertion structure is depicted separately.

To demonstrate the versatility of the fiber-based EO system, the dominant electric field in a plane that was two wavelengths from the aperture within the interior of the horn of a Ka-band horn antenna was scanned as well as the aperture plane. The step sizes for the scanning were 777 × 1108 μm along x and y direction for the aperture plane (plane I, Fig. 5.18) and 518 × 803 μm for the plane inside of the horn (plane II, Fig. 5.18) with 50 steps for both x and y directions. The operating frequency during the scans was 18.883 GHz and elapse time for one complete scanning was about 30 minute. Also, to measure the effects of the presence of a scattering structure inside of the horn, a copper strip structure shown in Fig. 5.18 was inserted into the horn and the electric fields were scanned on the same planes.

Figure 5.19 displays 2 dimensional amplitude and phase mappings of the dominant field component (y-component, Fig. 5.18) on both plane I and II without (Fig. 5.19(a) and (b)) and with the metal insertion structure (Fig. 5.19(c) and (d)). The mapping results are displayed with the actual scanning area ratio. The inserted metal structure is overlayed on the results in Fig. 5.19(c) and (d). From Fig. 5.19(a) and (b), it is noticeable that the amplitude in the plane II (Fig. 5.19(b)) has a rectangular shape, while it transformed into a more elliptical shape at the aperture plane (plan I, Fig. 5.19(a)). Also, the electric field has about a 90° phase variation from the top (or bottom) edge to the center of the plane. However, the phase variation along the y direction (co-polarization, horizontal direction in Fig. 5.19) is almost uniform. Thus the field distribution in the plane II can be considered as a cylindrical wave that has a curvature along the x direction (cross-polarization, vertical direction in Fig. 5.19). As the electric field travels toward the aperture, the phase distribution becomes more uniform, and the field has almost uniform distribution at the aperture plane. The amplitude and phase transitions explains that a tightly concentrated and curvatured field inside of the horn expandes in both amplitude and phase as it travels through gradually increasing aperture areas in the horn. As a result, the field in the aperture shows a very uniform distribution.

The next experiment was planned to measure the field distortion due to the presence of an alien structure – in this case the metal structure shown Fig. 5.18 – inside of the horn. Since the metal structure overlayed in Fig. 5.19(c) and (d) is mounted beneath the glass superstrate for the mechanical support, it is important to isolate the effects induced by the glass superstrate. Thus, exactly the same glass plate without the metal structure is inserted into the horn, and the field is measured. Since the glass plate is very thin (120 μm) and low dielectric constant ($\varepsilon_r \approx 3$), the effect of the glass was expected to be negligible, which is confirmed by obtaining the identical results shown in Fig. 5.19(a) and (b). The metal structure was fabricated to be a "cross" shape to study the effect of the orientation of the metal strip with respect to the electric field direction. A 1

cm-long and 1 mm-wide short branch is designed to be parallel to the electric field (co-polarization, y-direction in Fig. 5.18), while the 4 mm-long branch is aligned the cross-polarization orientation.

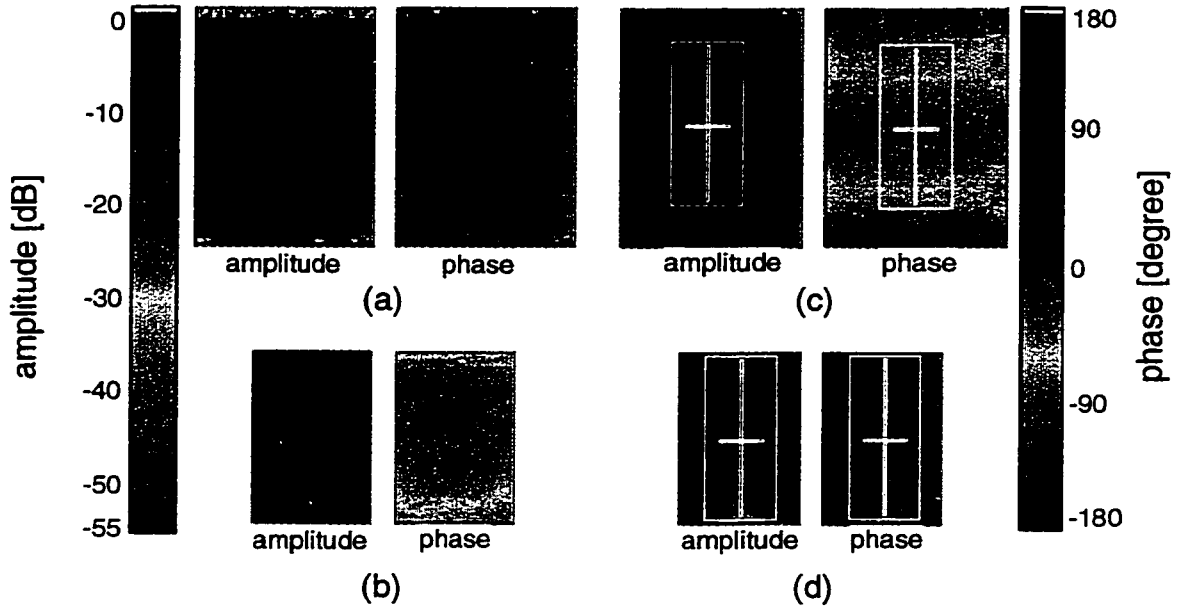

Figure 5.19: Two-dimensional electric-field amplitude (normalized) and phase (in degree) mapping results. The results show the field distributions at (a) the plane I and (b) the plane II without the metal structure while (c) and (d) display the field patterns with the metal structure at the plane I and II. The boundary of the metal structure and glass superstrate is overlayed with white lines in (c) and (d).

The amplitude in plane II (Fig. 5.19(d)) has a similar amplitude distribution without the metal structure (Fig. 5.19(b)). However, it is clearly indicated that the co-pol branch effectively blocks the field. Since the width of the metal strip is about 16 times

narrower that the operating wavelength (λ = 1.59 cm), the cross-pol branch does not show any detectable effects on the electric field distribution.

Another noticeable effect of the structure can be found in the phase disturbance. The phase distribution in plane II without the metal structure shows consistently decreasing phase from the center of the plane toward lower or upper edges (Fig. 5.19(b)). However, with the metal structure, the phase decreases until the mid-point between the center and the upper or lower edge of the plane, and after the mid-point, the phase increases to the edges. In other words, the gradient of the slope changes from negative (decreasing gradient) to a positive value around the mid-point while it has consistently negative value without the metal structure.

Since the electric field is expanded as it travels toward the aperture, the field outside of the co-pol branch expands over the null created by the metal strip. As a result, the null shown in Fig. 5.19(d) cannot be detected at the aperture plane. Thus the amplitude distribution is quite similar to that without the metal structure. However, the phase still maintains the distribution observed in Fig. 5.19(d).

The fiber-based EO system provides much valuable information that may be critical to design and analysis of the horn antenna. Furthermore, due to outstanding versatility, it is possible to obtain high quality near-field amplitude and phase information even inside of the horn.

5.4.3 Shielded Microstrip Line

In the previous section, the fiber-based EO system has successfully extracted the electric field distributions inside of a horn antenna. The results demonstrate a unique feature of the fiber-based EO system that separates the system from other conventional electric field measurement techniques. However, in order to demonstrate the exceptional measurement versatility of the fiber-based EO sampling system, the normal (*w.r.t.* the top

surface of the microstrip) field component inside of a completely-shield misrostrip transmission line was mapped using a (100)-oriented GaAs probe tip at an 8-GHz operating frequency. Also, the results were compared with the field distribution of the identical microstrip without shielding cavity.

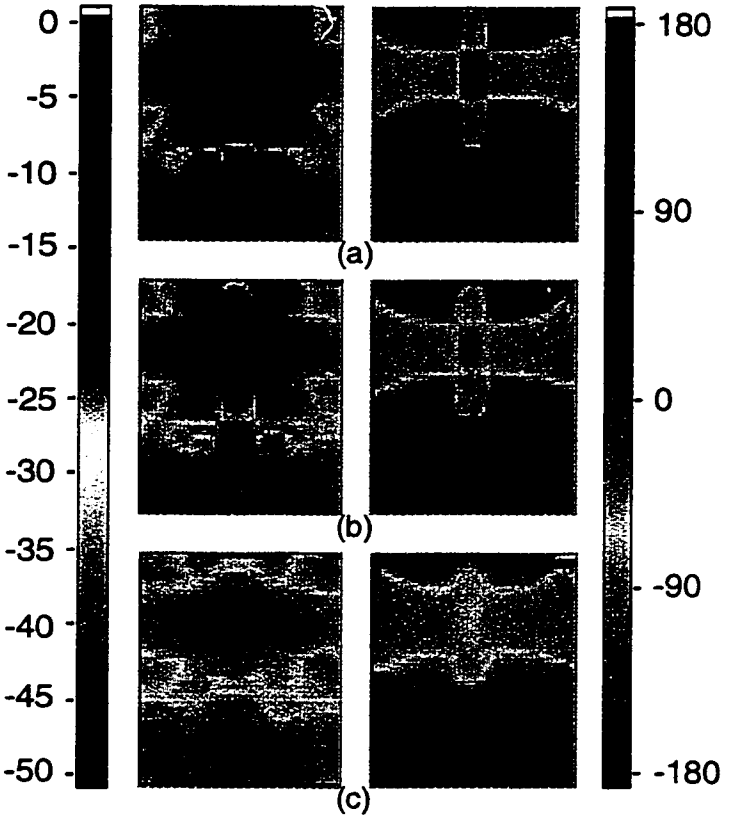

Figure 5.20: Normal electric field component distributions of the exposed microstrip line with a short termination. The amplitude (left-hand side, in dB) and phase (right-hand side, in degrees) are measured at the distances of (a) 1.0 mm, (b) 2.5 mm, and (c) 5.0 mm from the top of the microstrip. All amplitude values are normalized to the peak electric field at 1.0 mm.

For the measurement, a 50-Ω microstrip transmission line was fabricated on a duroid substrate with thickness of 75 mil and dielectric constant (ε_r) of 6.15. The output port of the microstrip was short-terminated in order to measure standing wave pattern.

Before mounting the microstrip in the cavity, the electric field distributions of the exposed microstrip at different heights were mapped. The mapping areas were 2.9 cm × 3.9 cm along the x- and y-directions with 580 μm × 780 μm resolutions. The distances of the probe tip to the top surface of the microstrip (mapping height) were 1.0, 2.5, and 5.0 mm, respectively. Figure 5.20 displays the measured amplitude (left hand side, dB) and phase (degrees) of the fields at the three different heights. All amplitude values are normalized by the peak electric field at 1.0 mm. The results show typical standing wave patterns that have periodic peaks with 180° phase changes. The separation between the peaks on the microstrip is 0.87 mm, and it shows excellent agreement with theoretically expected peak-to-peak distance. The peak amplitude is decreased by 16 dB as the measurement distance increases from 1.0 mm to 5.0 mm.

A metal cavity was fabricated around the microstrip to examine the shielding effects. The height of the side wall was designed to be 6.0 mm above the top surface of the microstrip. Since the purpose of this work was to demonstrate the three-dimensional electric field measurement capability of the fiber-based EO system, the probe tip required freedom of movement in three directions in the closed metal cavity.

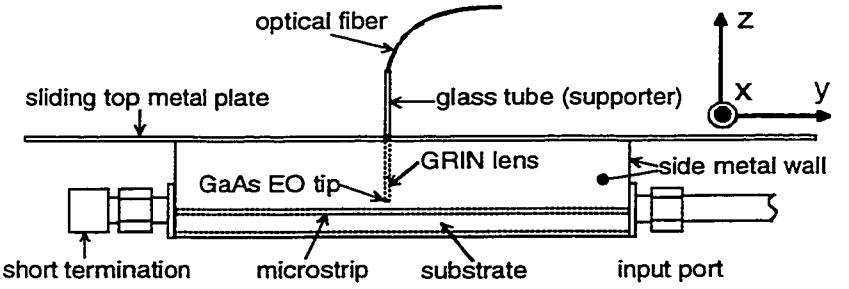

Figure 5.21: Side view of the shielded microstrip line probed with the fiber-based EO probe. The top slide plate is connected to a computer-controlled x-y translation stage in order to achieve two-dimensional movement.

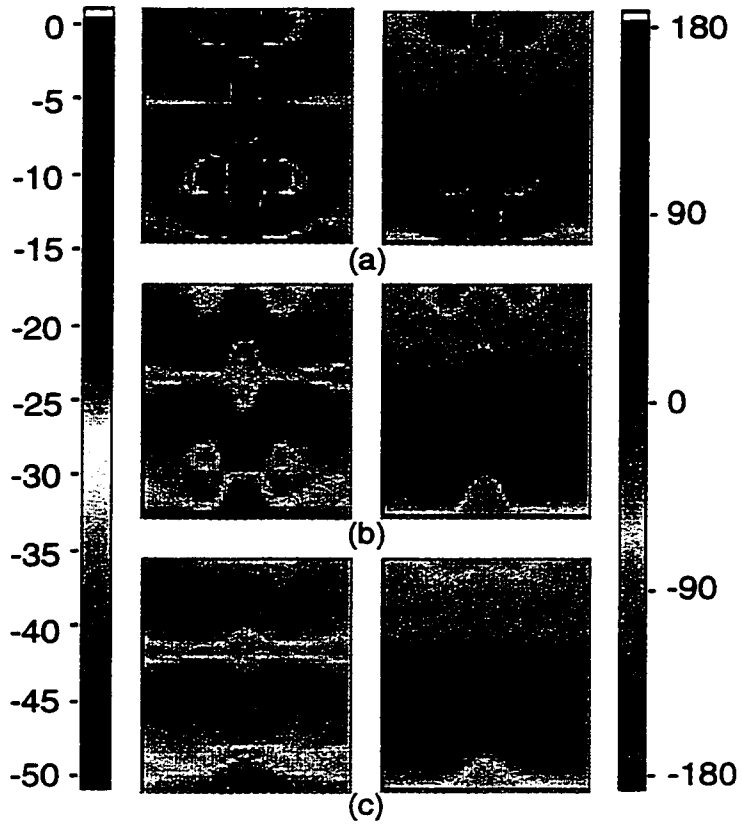

Figure 5.22: Normal electric field component distributions of the shielded microstrip line with a short termination. The amplitude (left-hand side, in dB) and phase (right-hand side, in degrees) are measured at the distances of (a) 1.0 mm, (b) 2.5 mm, and (c) 5.0 mm from the top of the microstrip. All amplitude values are normalized to the peak electric field at 1.0 mm.

In order to achieve the movement of the probe, a sliding top metal plate was employed to complete the closed cavity. The sliding top plate had a small access hole (diameter: 2.0 mm) that allowed the EO probe to be positioned inside of the cavity as shown in Fig. 5.21. Since the top plate and the fiber-based EO probe are mechanically connected to x-y translation stage, the probe could scan a two-dimensional field

distribution from the interior of the cavity while the top plate maintained electrical contact to the side walls. In addition to the two-dimensional (*i.e.*, x-y plane) field mapping capability, the vertical position (z-direction) of the probe could be adjusted externally.

Again, the normal electric fields of the shielded microstrip were measured at the distances of 1.0, 2.5, and 5.0 mm from the top of the microstrip surface. The scanning window area and position were set to be identical to the measurements of exposed microstrip. Figure 5.22 displays the measured amplitude (left hand side, dB) and phase (degrees) of the fields at the three different heights. All amplitude values are normalized by the peak electric field at 1.0 mm. The peak amplitude is decreased by 16 dB as the measurement distance increases from 1.0 mm to 5.0 mm.

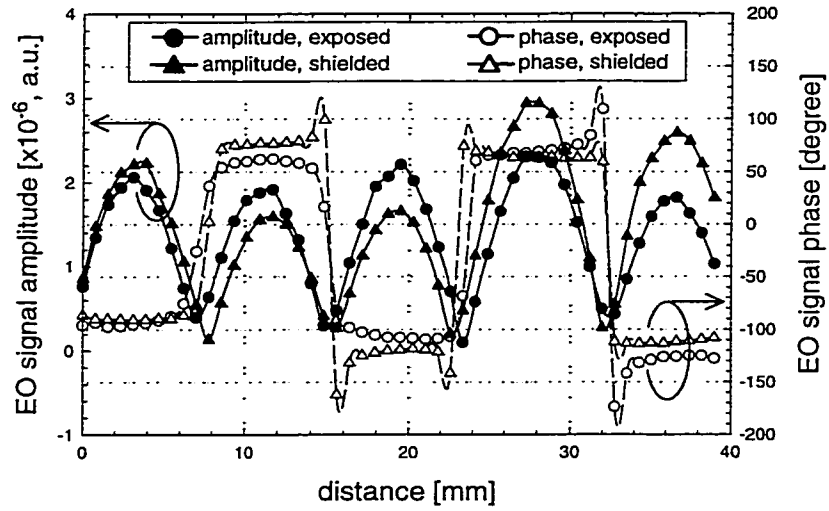

Figure 5.23: One-dimensional field comparison between exposed and shielded microstrips. The line plots are extracted along the centerlines of the microstrips at the measurement height of 1.0 mm.

For an accurate comparison, the one-dimensional amplitude and phase distributions are extracted along the centerlines of the exposed and shielded microstrips. Figure 5.23 shows the one-dimensional amplitude and phase comparison between the exposed and shielded microstrip along the centerlines at 1.0-mm height. In both cases, the phases show almost identical change on each amplitude peak. However, the nonuniform amplitude distribution is observed on the shielded microstrip while the exposed microstrip exhibits fairly uniform amplitude distribution. Since the geometries of the two microstrips (including the size of the substrate) are identical, the most plausible explanation of the amplitude discrepancy can be the existence of the cavity mode wave. The possible cavity mode wave is calculated based on the cavity resonator theory, and the effect of the microstrip substrate was taken into account by using the cavity perturbation theory. The calculated cavity standing wave pattern was then superimposed on the measurement results of the exposed microstrip.

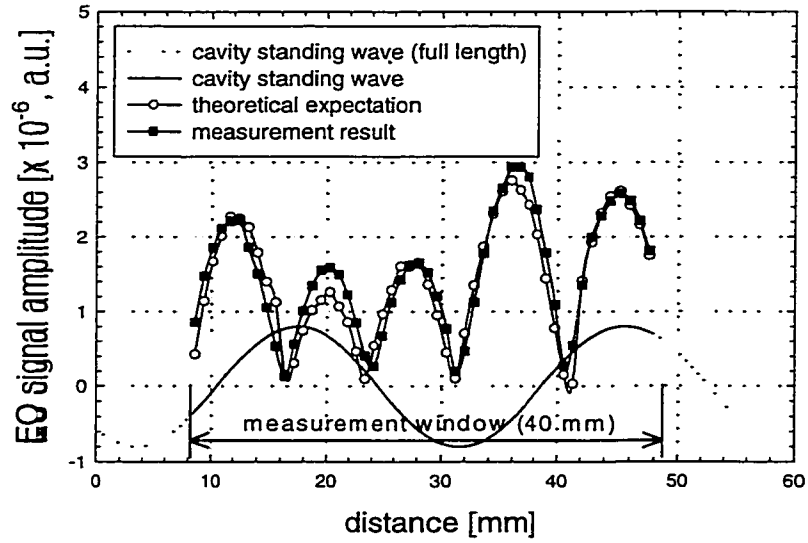

Figure 5.24: Comparison between the measured and theoretically expected electric field standing wave pattern of the shielded microstrip.

Figure 5.24 displays the comparison between the measured amplitude of shielded microstrip and the theoretically expected pattern, and two results show outstanding agreement.

In this work, a (100)-oriented GaAs probe tip was utilized to detect normal field component. However, two orthogonal tangential fields can be easily obtained simply by replacing the (100)-oriented GaAs tip with the (110)-oriented GaAs tip. As a result, complete three-dimensional field distributions of the three-orthogonal components can be mapped from the interior of a cavity by the fiber-based EO system. In particular, the fiber-based EO field mapping system can be directly applied to more complicated shielded microwave circuitry.

5.5 Summary

A fiber-based electro-optic (EO) field mapping system has been developed by utilizing (100) and (110) gallium arsenide (GaAs) probes that were fabricated by micromachining technique. Due to the low dielectric constants of the GaAs and other components near the probe such as a gradient index lens and optical fiber, the invasiveness of the system to the device under the test was significantly reduced. Since the probes were mounted at the end of the flexible optical fiber, the fiber-based EO system provided outstanding flexibility that has not been found in other near-field measurement methods.

For the demonstration of the three-orthogonal-component measurement capability of the fiber-based EO system, a folded slot antenna was scanned. By using the high-resolution near-field amplitude and phase data, it was possible to analyze the folded slot antenna operation accurately.

Also, due to the incomparable versatility of the fiber-based EO system, the electric field distribution inside of a horn antenna was successfully mapped as well as the aperture plane. The comparison between the maps at the two planes clearly displayed the transformation of the field distribution. Furthermore, the disturbed field patterns caused by the presence of an alien metal structure inside of the horn were measured. The results confirmed the dominant effect of the co-polarization oriented metal strip against the cross-polarization oriented strip.

Finally, the electric field distributions inside of closed, shielded microstrip have been successfully extracted by the fiber-based EO system.

The fiber-based system has lower permittivity than other scanning field probes, provides excellent measurement flexibility so that the scanning can be performed at any arbitrary orientation, and allows insertion of the field sensor into microwave enclosures and packages. The fiber-based EO system can be applied to the design, characterization, and failure analysis of guided-wave and radiating-wave systems including quasi-optical power combining arrays, transmit/receive modules, and other microwave and millimeter-wave circuits.

CHAPTER 6

NEAR- TO FAR-FIELD TRANSFORMATION USING HIGH-RESOLUTION ELECTRO-OPTIC NEAR-FIELD MAPPING

6.1. Introduction

Recently, the demands for high-speed, sophisticated radiation systems have been accelerated by the explosive spread of mobile communication systems both in commercial and special application areas. However, it is true that the evolutionary development of radiation systems requires more sophisticated and accurate measurement techniques. Furthermore, as the systems become more complicated and sophisticated, they need information that conventional measurement techniques fail to provide yet are very critical for the analysis and design of those systems.

One of the analysis methods that displays its usefulness for modern complicated radiation systems is the near- to far-field transformation technique [64][65]. This technique can provide profound far-field information by offering the relation between the near-field distribution and far-field formation with a relatively compact measurement range. By the nature of the transformation method, the accuracy and easiness of the method strongly relies on reliable near-field measurement methods. However, conventional near-field methods that utilize small antennas or open-waveguide as electric field sensors have been suffered several limitations. In the application of those methods, it is inevitable to introduce metal structures into the near-field region to sense the electric fields. The presence of metal structures in the near-field region can cause local distortion of electric field distributions, which is known as invasiveness. This invasiveness of the

sensor (or so-called probe) limits accurate measurement of the electric field distribution and, moreover, it can even alter the operating conditions of the devices under test (DUTs), especially when DUTs are sensitive to their environment.

Recently, the electro-optic field-mapping technique has been spotlighted as an accurate near-field measurement method [5]-[7]. Unlike conventional near-field measurement methods in which metal structures are used as field sensors, the electro-optic field mapping method utilizes crystals or dielectric polymers that have properties called Pockles effect as a field sensor. As a result, it can achieve much less invasiveness than conventional antenna-based near field measurement methods. Also, the resolution of electro-optic field mapping is determined by the focus size of detection laser beam inside of electro-optic crystal, which makes it possible to achieve high-resolution field mapping easily. The EO field mapping system proved its capability to measure structures small as 8 μm and frequency up to 100 GHz [54]. Furthermore, by applying common reference signal configuration during the field measurement, it is possible to measure accurate amplitude and phase information simultaneously. Thus, only single-plane near-field scanning is necessary to calculate accurate far-field patterns [66]. In addition to these advantages, the close proximity of the electro-optic crystal to the DUTs makes it possible to measure evanescent mode waves (also known as "invisible waves" in conventional measurements [25]) that may exist in the reactive near-field region [25]. The lower-invasiveness, high spatial-resolution, and accurate phase measurement capability of the electro-optic near-field mapping technique make the method ideal for the near- to far-field transformation application.

In this chapter, theoretical approaches to a simplified near- to far-field transformation utilizing the advantages of electro-optic near-field mapping method are discussed. For actual applications, as an example of near- to far-field transformation based on electro-optically measured near-field data, a 4-GHz microstrip patch antenna was chosen as a device under test (DUT). The electric field in the scanned unit cell can be

transformed to the magnetic current by employing the equivalence principle. Then the far field is calculated by using 2-dimensional array theory. The transformed far field from the measured near field was compared with an analytical cavity model [68] and conventional far-field measurement results. Also, the high spatial-resolution of the electro-optic near-field mapping made it possible to isolate the two main radiating edges of the patch during the transformation. As a result, contributions of those radiating edges to the far-field formation were examined separately.

Also, high-resolution electro-optic near-field mapping has been performed on a Ka-band 2×2 patch antenna array. The far-field patterns for the array have been calculated from simultaneously obtained near-field amplitude and phase data using a near- to far-field transformation process. The transformed field patterns display outstanding agreement with theoretically predicted results and independent far-field measurements. Also, various filtering processes were introduced to investigate the contributions to the far-field formation of individual radiating elements in the array.

Finally, as an example of an active array, the contributions of each radiating structure in the array – including substrate – are analyzed for a 6×6 Ka-band quasi-optical (QO) amplifier array.

6.2 Theory

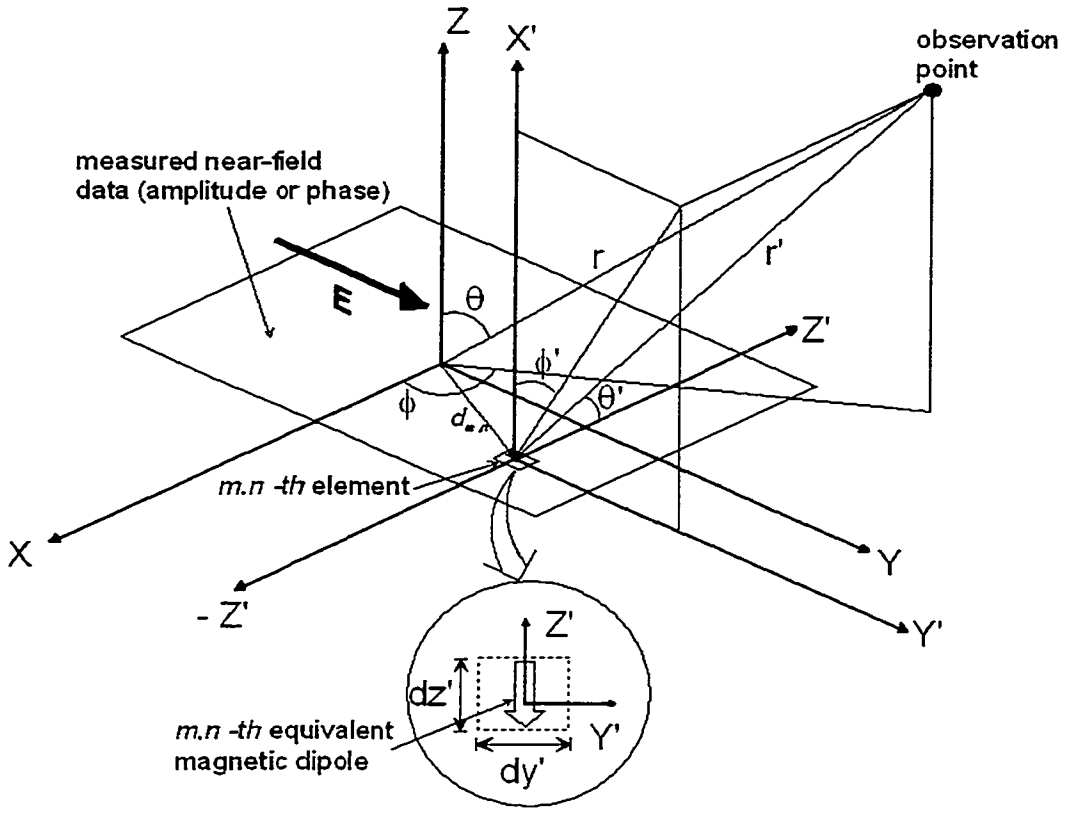

Figure 6.1: Conceptual schematic for the near- to far-field transformation. The near-field data (amplitude or phase) are expressed as a rectangle in space. The global axes (X, Y, and Z) and local axes (X′, Y′, and -Z′) used in the course of the derivation of the near- to far-field transformation formula are depicted. The magnified unit scanning cell (*m,n-th* cell) that has size of dy′ × dz′ is displayed in the circle with its equivalent magnetic dipole.

Figure 6.1 shows a conceptual diagram of the near- to far-field transformation. The global axes (X-Y-Z) and local axes (X′-Y′-Z′) systems are used to derive the relation between the measured near-field data to be transformed to the far-field pattern. For the

convenience of calculation, the relation between global and local coordinate systems is set as

$$\begin{aligned} \hat{\mathbf{x}}' &= \hat{\mathbf{z}}, \\ \hat{\mathbf{y}}' &= \hat{\mathbf{y}}, \text{ and} \\ \hat{\mathbf{z}}' &= -\hat{\mathbf{x}}. \end{aligned} \tag{6.1}$$

The measured near-field data (either amplitude or phase) can be considered as a plane because 2-dimensional scanning has been performed for the measurement. The unit cell in the near-field data (*i.e.*, *m,n-th* cell in Fig. 6.1) has dimensions of $dy' \times dz'$ – which are determined by the EO scanning resolution. The size of the unit cell (*i.e.*, the resolution of EO scanning) is determined by factors such as operating frequency (wavelength) and physical size of the structures in a DUT. Uniform electric field distribution can be assumed in each unit cell. All DUTs used in this work are aligned so that the dominant field component is parallel to $-\hat{\mathbf{y}}$ for convenience during the transformation. The measured electric field in the *m,n-th* cell can be expressed as

$$\begin{aligned} &\mathbf{E}_{m,n} = E_{m,n} e^{-j\psi_{m,n}} (-\hat{\mathbf{y}}) \\ &\text{where} \\ &E_{m,n} : \textit{measured near-field amplitude} \\ &\psi_{m,n} : \textit{measured near-field phase.} \end{aligned} \tag{6.2}$$

The amplitude $E_{m,n}$ and phase $\psi_{m,n}$ are uniform on the *m,n-th* cell.

The far-field pattern induced by the *m,n-th* unit cell can be obtained from the far-field pattern from the field uniformly distributed in the aperture [40] under the given local axes system. To isolate the effect of the *m,n-th* cell exclusively, the aperture is assumed to be mounted on a ground plane and thus the electric field only can exist in the *m,n-th* cell. From Eq. 6.2, the equivalent magnetic current $\mathbf{M}_{m,n}$ can be expressed as

$$\begin{aligned}\mathbf{M}_{m,n} &= 2\mathbf{E}_{m,n}\times\hat{\mathbf{n}} \\ &= 2E_{m,n}e^{-j\psi_{m,n}}(-\hat{\mathbf{y}}')\times\hat{\mathbf{x}}' \\ &= 2E_{m,n}e^{-j\psi_{m,n}}\hat{\mathbf{z}}'.\end{aligned} \tag{6.3}$$

Form Eq. 6.3, the far-field pattern formulation $\mathbf{E}_{m,n}^{ff}$ can be obtained as follows;

$$\mathbf{E}_{m,n}^{ff} = \frac{jk_0}{4\pi r'}e^{-jk_0r'}\hat{\mathbf{r}}'\times\iint_{S_{m,n}}\mathbf{M}_{m,n}e^{jk_0\mathbf{r}''\cdot\hat{\mathbf{r}}'}dy''dz'' \tag{6.4}$$

In Eq. 6.3, $S_{m,n}$ represents the area where the magnetic current $\mathbf{M}_{m,n}$ exists, $\mathbf{r}''$ represents a vector from the local origin (in X′-Y′-Z′ system) to an arbitrary point, and dy″, dz″ are small segments of dy′, dz′ as shown in Fig. 6.1. The integral shown in Eq. 6.3 is well known as Fourier transform. Since the aperture is assumed to be on ground plane, the integration area $S_{m,n}$ is the same as the area of the *m,n-th* cell. Also, the vector $\mathbf{r}''$ can be confined in the *m,n-th* cell. After performing Fourier transform integration and using Eq. 6.3, the resultant far field from the *m,n-th* cell $\mathbf{E}_{m,n}^{ff}$ can be expressed as

$$\begin{aligned}\mathbf{E}_{m,n}^{ff} &= \frac{jk_0}{2\pi r'}e^{-jk_0r'}\hat{\mathbf{r}}'\times\hat{\mathbf{z}}'\left(dy'dz'\,E_{m,n}e^{-j\psi_{m,n}}\frac{\sin(A)}{A}\frac{\sin(B)}{B}\right) \\ &= -\frac{jk_0dy'dz'}{2\pi r'}E_{m,n}e^{-j\psi_{m,n}}\frac{\sin(A)}{A}\frac{\sin(B)}{B}e^{-jk_0r'}\sin(\theta')\hat{\boldsymbol{\phi}}' \\ &\text{where} \\ A &= k_{y'}\frac{dy'}{2} = \frac{1}{2}k_0\sin(\theta')\sin(\phi')dy' = \frac{\pi dy'}{\lambda_0}\sin(\theta')\sin(\phi') \text{ and} \\ B &= k_{z'}\frac{dz'}{2} = \frac{1}{2}k_0\cos(\theta')dz' = \frac{\pi dy'}{\lambda_0}\cos(\theta').\end{aligned} \tag{6.5}$$

As mentioned above, the size of the *m,n-th* unit cell is decided by the scanning resolution. Typical scanning resolutions used in this work are in the 100-μm range, about

100 times smaller than the wavelength in Ka band ($\lambda_0 \approx 1$ cm). Thus, it is a reasonable assumption that the coefficients A and B in Eq. 6.5 are very close to 0. As a result, Eq. 6.5 can be simplified as

$$\mathbf{E}_{m,n}^{ff} = -\frac{j k_0 dy'dz'}{2\pi r'} E_{m,n} e^{-j\psi_{m,n}} e^{-jk_0 r'} \sin(\theta')\hat{\boldsymbol{\phi}}'. \tag{6.6}$$

Equation 6.6 reveals the far-field pattern from the *m,n-th* cell is identical to that of an infinitesimal magnetic dipole that has amplitude of $2E_{m,n}dy'dz'$ and phase delay of $\psi_{m,n}$. The direction of the infinitesimal dipole is aligned to $\hat{\mathbf{z}}'$ as shown in Fig. 6.1.

Using the relationships between the global and local axes systems shown in Eq. 6.1 under far field condition, the local positions can be transformed into global axes as

$$\begin{aligned}
&\mathbf{r}' \approx \mathbf{r}, \\
&\theta' = \operatorname{acos}\left(\hat{\mathbf{r}}' \cdot \hat{\mathbf{z}}'\right) \approx \operatorname{acos}\left(\sin(\theta)\cos(\phi)\right), \\
&\phi' = \operatorname{acos}\left(\frac{1}{\sqrt{1+\tan^2(\theta)\sin^2(\phi)}}\right), \text{ and} \\
&\hat{\boldsymbol{\phi}}' = -\hat{\mathbf{z}}\sin(\phi') + \hat{\mathbf{y}}\cos(\phi').
\end{aligned} \tag{6.7}$$

Now the transformation procedure can be simplified as a far-field calculation of a 2-dimensional infinitesimal magnetic dipole array. In other words, the total far field $\mathbf{E}^{ff}$ can be obtained by the summation of individual far-field $\mathbf{E}_{m,n}^{ff}$ considering the phase delay with respect to the position of the unit cell.

$$\begin{aligned}
&\mathbf{E}^{ff} = \sum_{m,n} \mathbf{E}_{m,n}^{ff} e^{-jk_0 d_{m,n}^{x} \sin(\theta)\cos(\phi)} e^{-jk_0 d_{m,n}^{y} \sin(\theta)\sin(\phi)} \\
&\text{where} \\
&d_{m,n}^{x} = d_{m,n}\cos(\phi) \\
&d_{m,n}^{y} = d_{m,n}\sin(\phi) \\
&d_{m,n} : \textit{distance of } m,n-\textit{th cell from global origin.}
\end{aligned} \tag{6.8}$$

The two exponential functions in Eq. 6.8 represent the phase delay caused by the distance of the *m,n-th* cell from the global origin ($d_{m,n}$, see Fig. 6.1).

For the actual far-field calculation, a Pentium-III personal computer was used, and it took about 30 seconds of computing time (CPU time) to obtain 2,500 far-field data points in θ -ϕ space from the measured near-field amplitude and phase that have 126 × 121 data points.

Equation 6.8 clearly shows that the resultant far field is the summation of the far fields generated from the individual unit cells. This property leads to another unique application of the near- to far-field transformation. The summation procedure shown in Eq. 6.8 can be divided into a number of small sub-summation groups without any mathematical inconsistency because the variables θ and ϕ are only decided by the position of the observation points regardless of the unit cells. Thus the far field $\mathbf{E}^{ff}$ can be considered as a result of the superposition of multiple far fields generated from the small near-field sections that are mathematically expressed as sub-summation groups. Since the distance between the EO crystal to the DUT is usually extremely small during the EO field mapping (several tens ~ hundreds microns), the obtained near-field data can be considered as an actual field distribution right on the DUT. Based on this theory, various filtering (or it could also be called 'windowing') procedures were introduced to isolate certain areas of the DUT, and the contributions of those areas for the far-field formation have been investigated. Due to the high-resolution property of the EO field mapping, the far-field patterns from the two radiating edges of a single patch antenna have been successfully calculated [67] and the transformed patterns demonstrated excellent agreements with theoretical expectations and measured far-field patterns.

For the validation of the near- to far-field transform process, two basic radiating structures — a short dipole antenna and a rectangular aperture — are artificially generated. Most complicated radiating structures can be considered as a composition of

these two elementary radiating structures. Also these two structures have theoretically well defined far-field patterns. Thus, by making comparisons to the far fields obtained from the near- to far-field transform with the theoretically expected far field of three basic radiating structures, one can examine the validity of the transform procedure. Furthermore, once the validity of the process is proven, the near-to far-field process can be applied for actual situations.

6.6.1 Short Dipole Antenna

Figure 6.2 shows the amplitude (Fig. 6.2(a)) and phase (Fig. 6.2 (b)) of the artificially generated ideal short dipole antenna. The length of the dipole is designed to be 0.1λ. Since the length of the dipole is much shorter than the wavelength, it is reasonable to set a uniform amplitude and phase.

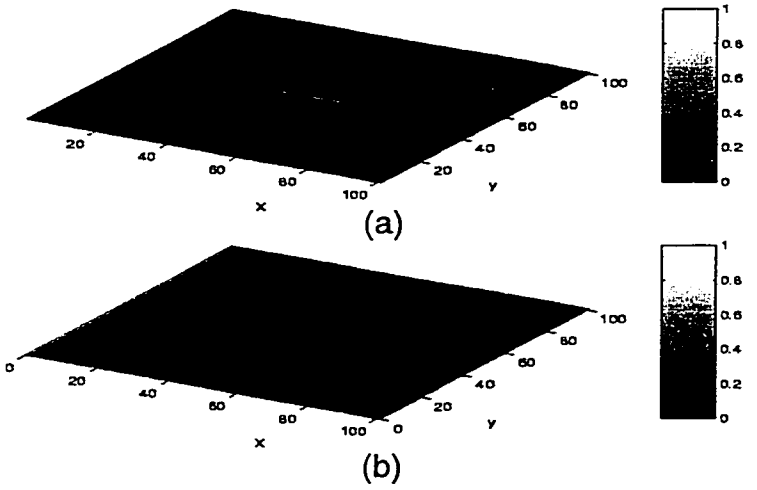

Figure 6.2: Amplitude and phase distribution of ideal short dipole

As shown in Fig. 6.2, the amplitude is 1.0 only on the dipole and 0 for elsewhere, while the phase is 0° for the whole window. In an actual situation, an electro-optically measured near-field amplitude and phase will be used.

The far-field pattern of the short dipole can be expressed as [40]

$$E_\theta \equiv j\eta \frac{k\, I_0 l\, e^{-jkr}}{4\pi r} \sin(\theta), \tag{6.9}$$

where k and η are wave propagation constant and intrinsic impedance of air, and I_0, l are current amplitude and length of the dipole.

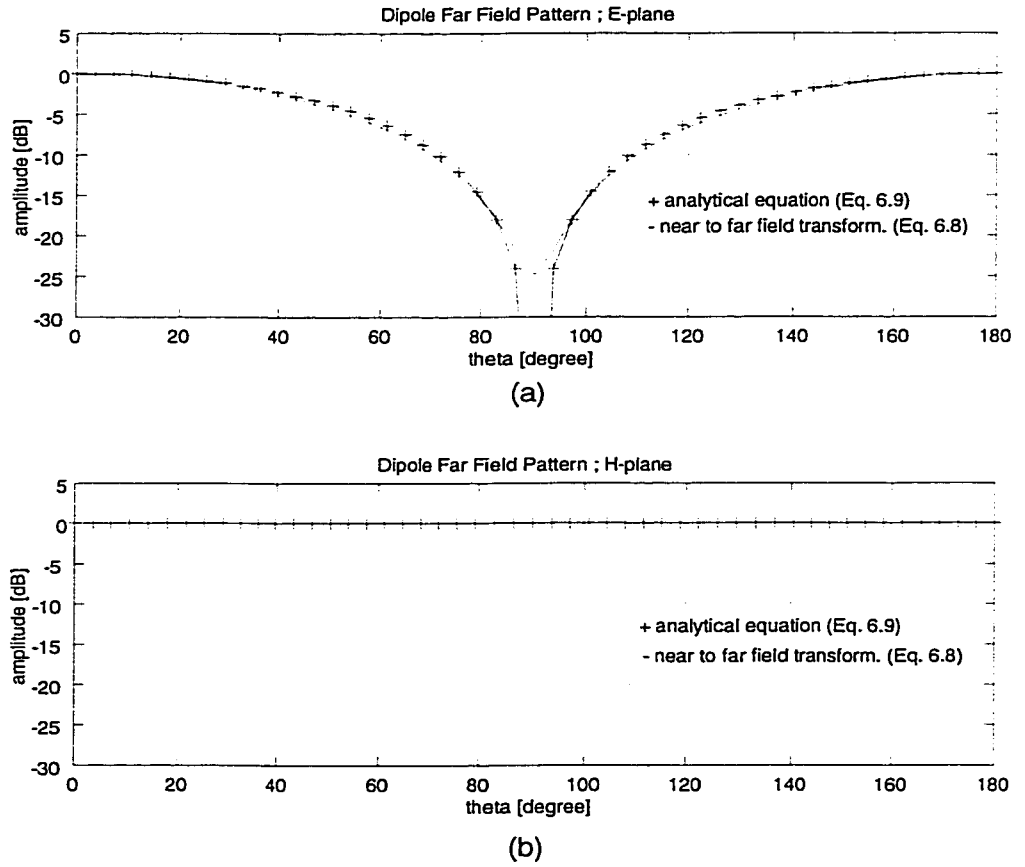

Figure 6.3: Short dipole far-field comparison between analytical approach (cross hair) and transformation (solid line) in (a) E-plane and (b) H-plane.

Figure 6.3 shows the far-fields obtained from Eq. 6.8 and Eq. 6.9. The two far-field patterns display outstanding agreement in both E- and H-plane. The maximum error between the two patterns is about 0.5 dB.

6.2.2 Rectangular Aperture

A rectangular aperture that has uniform field distribution is shown in Fig. 6.4. In order to simplify the theoretical model, the aperture is mounted on a ground plane.

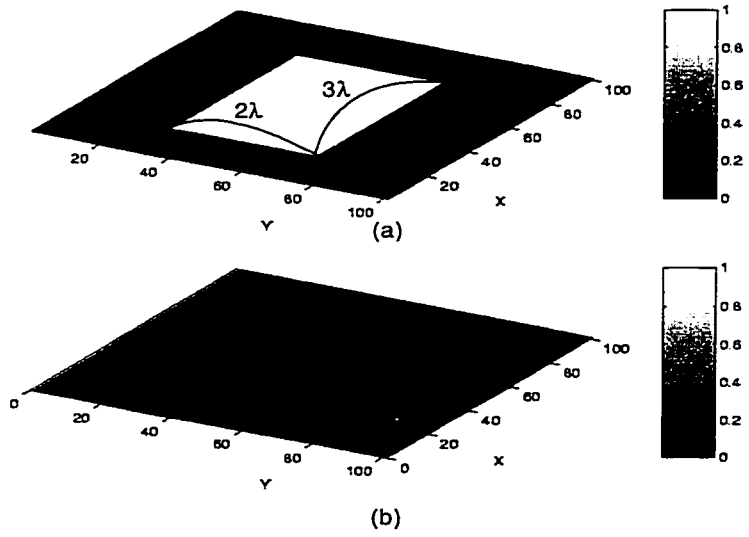

Figure 6.4: Rectangular aperture with uniform electric field. (a) Amplitude and (b) phase. The electric field is parallel to the Y-axis. The step sizes are 0.05λ for both X- and Y-direction.

The aperture has 3λ × 2λ size along the X- and Y-axis. Again, for ideal aperture model, the electric field in the aperture is assumed to be uniform. Also, since the ground plane surrounds the aperture, the electric field should be absent outside of the aperture.

As a result, the amplitude (Fig. 6.4(a)) is 1 in the aperture and 0 elsewhere, while the phase is 0 everywhere. The direction of the electric field is aligned to be parallel to the Y-axis.

The theoretical far-field pattern from the aperture can be expected as [40]

$$
\begin{aligned}
&E_r = 0 \\
&E_\theta \sim \sin(\phi)\frac{\sin(X)}{X}\frac{\sin(Y)}{Y} \\
&E_\phi \sim \cos(\theta)\cos(\phi)\frac{\sin(X)}{X}\frac{\sin(Y)}{Y}
\end{aligned}
\qquad (6.10)
$$

where

$$X = \frac{k \cdot 3\lambda}{2}\sin(\theta)\cos(\phi)$$

$$Y = \frac{k \cdot 2\lambda}{2}\sin(\theta)\sin(\phi)$$

The constant k in the Eq. 6.10 represents the wave propagation constant of air.

Figure 6.5 shows the transformed far field in three-dimensional space. The X-, Y-, and Z-axes represent spatial coordination (a.u.). The aperture is positioned at the origin of the axes (X = Y = Z = 0). Since the aperture is mounted on the ground plane, there is no restriction of the radiation under the aperture as well as above the aperture. In other words, the aperture radiates identical electric field into both upper and lower space at the same time. As a result, the transformed field pattern displays a mirror image in both upper (Z > 0) and lower space (Z < 0) with respect to the plane where the aperture is placed (Z = 0). The field pattern in the lower space is colored gray so that it is easily distinguished from the pattern in the upper space. The pattern shows a very strong main lobe at the center of the aperture (X = Y = 0). Also, four small side lobes that are 90° apart from each other can be observed on the plane where the aperture is placed (Z = 0).

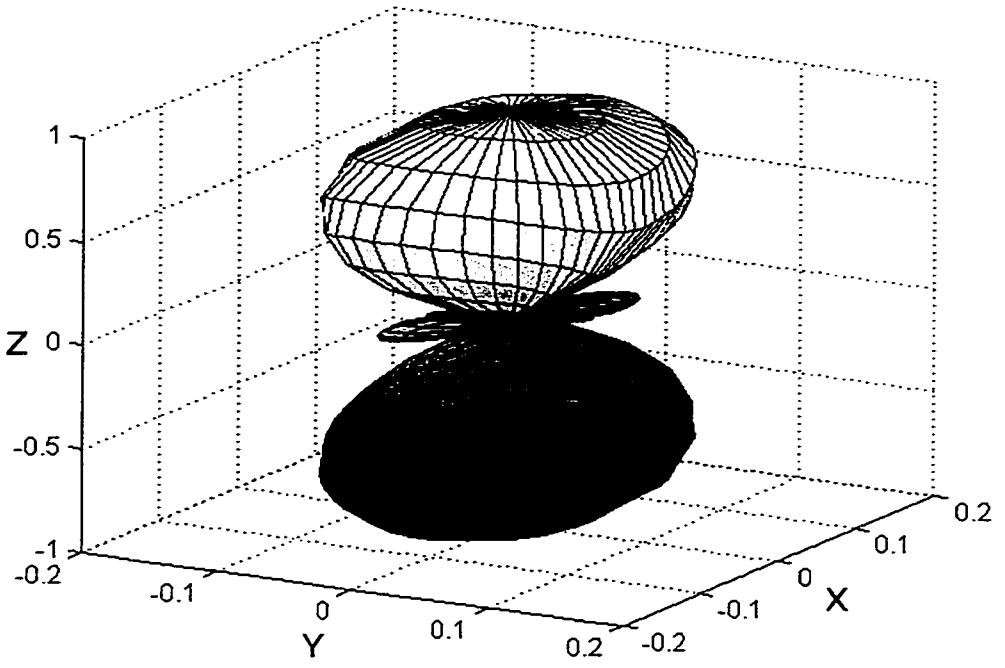

Figure 6.5: Transformed far-field pattern from the aperture in three-dimensional space. The aperture is placed at the origin of the axes (X = Y = Z = 0). The axes only indicate the spatial coordination and are irrelevant to the amplitude.

The one-dimensional far-field patterns obtained from Eq. 6.8 and Eq. 6.10 are compared in Fig. 6.6. Again, the theoretical expectation and transformed results show good agreements in both E- ($\phi = \pi/2$ in Eq. 6.10) and H-plane ($\phi = 0$).

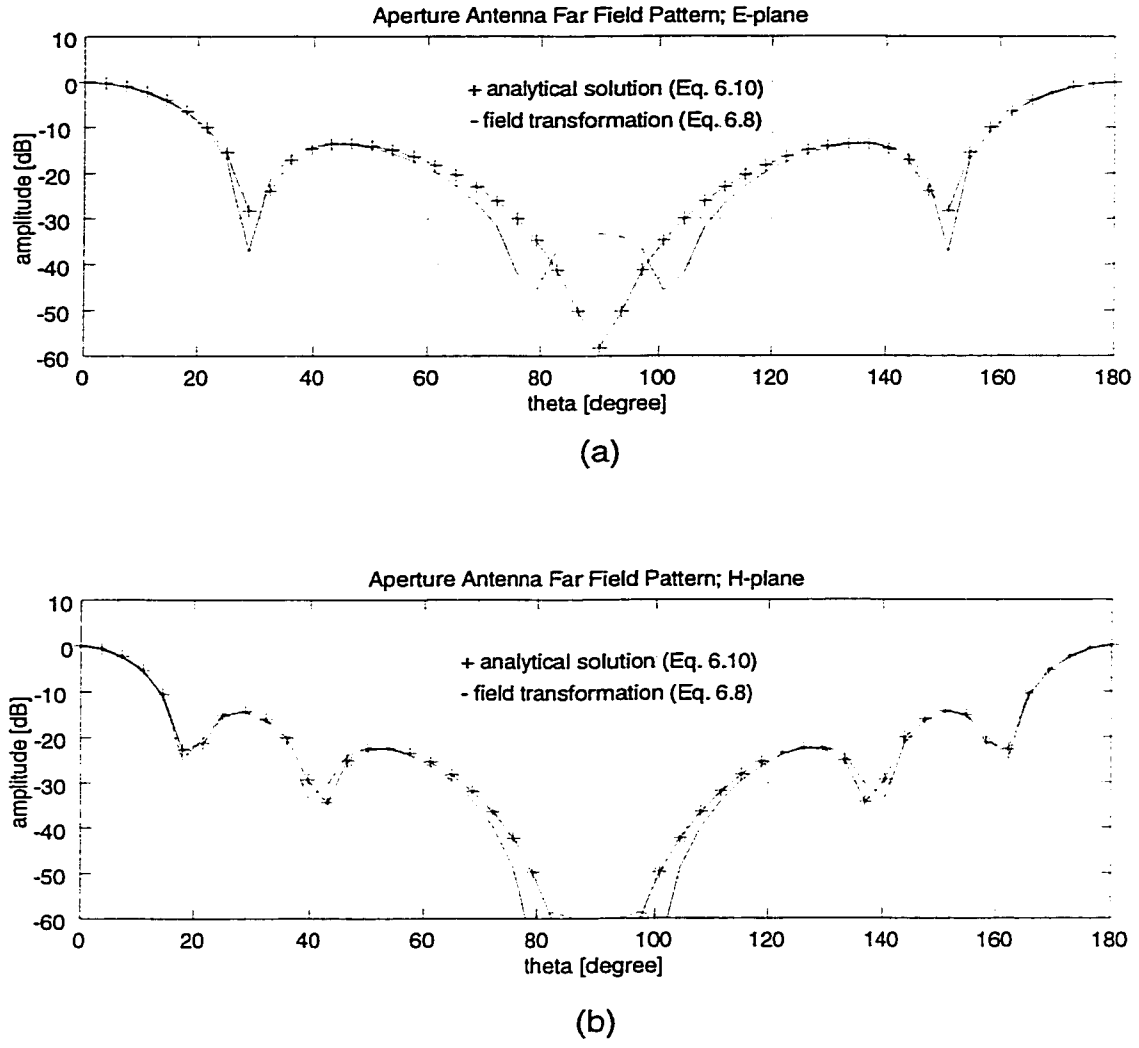

Figure 6.6: Rectangular aperture far-field comparison between analytical approach (cross hair) and transformation (solid line) in (a) E-plane and (b) H-plane.

The comparisons between the transformed and theoretical far fields for the short dipole and rectangular aperture confirm that the near- to far-field transformation procedure provides very accurate far-field patterns. In the following sections, this transformation procedure is applied to actual near-field data obtained by the EO field mapping for the far-field characterization of various radiating structures.

6.3 Microstrip Patch Antenna

Complete details about the electro-optic measurement can be found in Chapter 3 of this thesis. In this case, a $LiTaO_3$ crystal has been used as the sensor to detect the dominant electric field component of the DUT (patch antenna), which is parallel to the Y-axis in Fig. 6.7. The unit step size for the scanning was 200 μm × 250 μm, and 80 steps were taken for both the x- and y-direction.

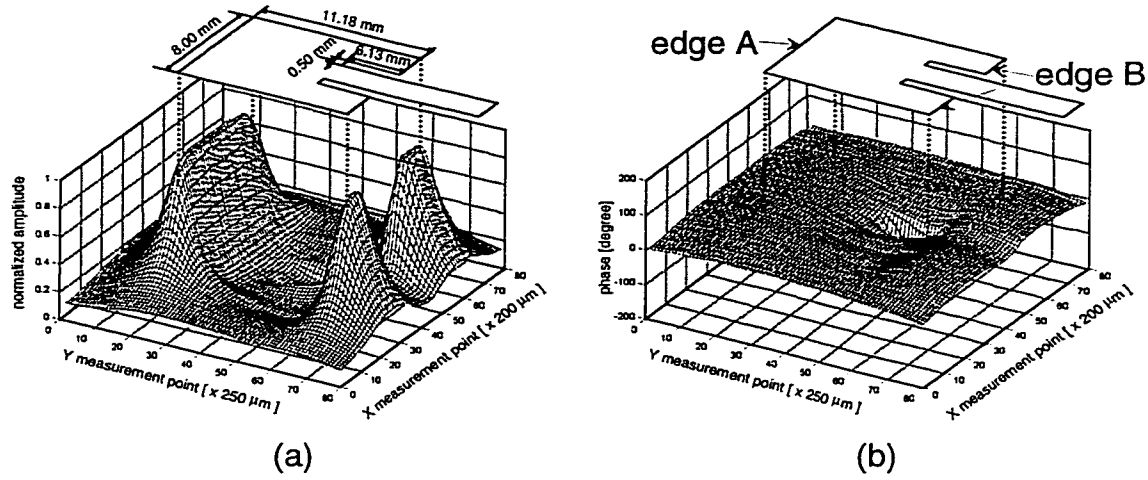

Figure 6.7: Electro-optic near-field measurement results for dominant (y) component of 4-GHz patch antenna: (a) amplitude (normalized by the peak value) and (b) phase in degrees. The two main radiating edges (front side: edge A, feed side: edge B) are labeled in (b).

Based on the near-field data shown in Fig. 6.7, near- to far-field transformation was performed as described in previous section. To verify the accuracy of the transformed far field from Eq. 6.8, a conventional far-field measurement has been performed in an anechoic chamber. Also, the results obtained from theoretical calculations based on the cavity model are compared.

For the theoretical analysis, the effective dielectric constant ε_{eff} of the microstrip structure is defined as [39]

$$\varepsilon_{eff}=\frac{\varepsilon_r+1}{2}+\frac{\varepsilon_r-1}{2\cdot\sqrt{1+12\cdot h/w}} \tag{6.11}$$

where ε_r, h are the dielectric constant and the thickness of the substrate ($\varepsilon_r = 10.3$, $h = 2.55$ mm), and w is the width of the conductor – in this case, w is the width of the patch antenna (8.00 mm).

From Eq. 6.11, the effective length of the patch L_e can be described as [68]

$$\begin{aligned} L_e &= L + 2\,dL, \\ dL &= \frac{h\cdot 0.412\left(\varepsilon_{eff}+0.3\right)\cdot\left(w/h+0.264\right)}{\left(\varepsilon_{eff}-0.258\right)\cdot\left(w/h+0.8\right)} \end{aligned} \tag{6.12}$$

where L is the original length of the patch ($L = 11.18$ mm).

Now the theoretical far field from the patch E_θ can be obtained as

$$E_\theta=\sin(\theta)\frac{\sin\left(\frac{kh}{2\sin(\theta)\cos(\phi)}\right)}{\frac{kh}{2\sin(\theta)\cos(\phi)}}\cdot\frac{\sin\left(\frac{kw}{2\cos(\theta)}\right)}{\frac{kw}{2\cos(\theta)}}\cdot\cos\left(\frac{kL_e}{2\sin(\theta)\sin(\phi)}\right) \tag{6.13}$$

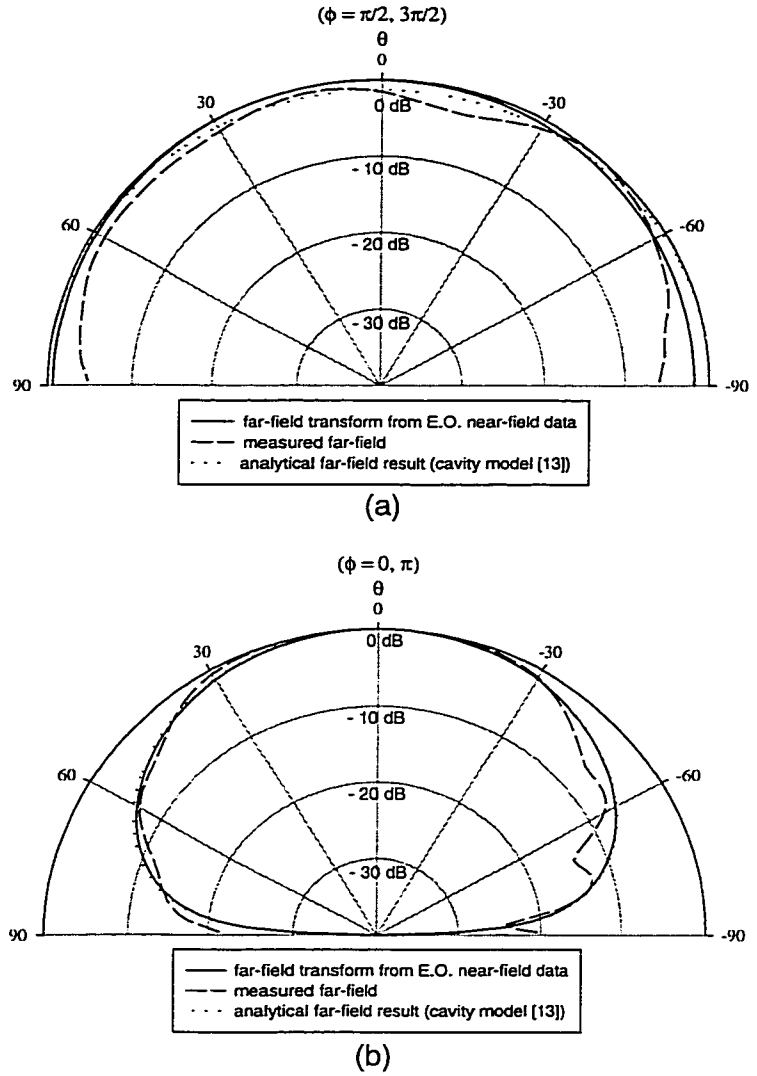

Figure 6.8: Far-field pattern comparison between the transformed result, measured far-field, and cavity model results in (a) E-plane and (b) H-plane.

Figures 6.8(a) and (b) show far-field-pattern comparisons for the E-plane (ϕ = $\pi/2$, $3\pi/2$; $-\pi/2 \leq \theta \leq \pi/2$) and H-plane ($\phi$ = 0, π; $-\pi/2 \leq \theta \leq \pi/2$), respectively. In both cases, the transformed results show excellent agreement with the cavity model and actual far-field measurement. The limited size of the ground plane causes a small but noticeable

deviation of the measured pattern from the cavity model (maximum difference: 6.25 dB) and transformed results (maximum difference: 4.3 dB) around the azimuthal region ($\theta \approx \pm\pi/2$) in the E-plane comparison (Fig. 6.8(a)) [68]. This difference can be ignored in the H-plane comparison because the effect of a finite ground plane is minimized by the small electric field around the azimuthal region (Fig. 6.8(b)).

Another distinct advantage of the transformation based on electro-optic near-field mapping is that it is possible to isolate a certain section of a radiating structure in order to examine its contribution to the far-field pattern. The high-resolution capability of electro-optic probing makes it possible to separate even a small region of a single antenna. For the further radiation pattern analysis, two different filtering procedures were introduced to isolate two main radiating edges – front (edge A in Fig. 6.7(b)) and feed (edge B in Fig. 6.7(b)) – of the patch antenna. A filter 1 is designed to isolate the radiating edge A, and filter 2 is used for edge B. Filter1 and filter 2 are designed to be complementary. In other words, the summation of the resultant far fields generated through application of filter 1 and filter 2 has to be identical to the far field without the filtering procedure. Figure 6.9(a) and (b) show the far-field patterns obtained after applying filter 1 and filter 2 in the E-plane and H-plane, along with the far-field pattern without filtering. In both planes, the fields from edge A show a 2 dB stronger amplitude than the field from edge B. In an ideal situation, both edge A and B have to radiate identical fields. However, as shown in Fig. 6.7, a section of the edge B that is about 40 % of the total length is devoted to the feed microstrip line and impedance matching insets. This reduced radiating edge on the feed side causes the discrepancies between the results obtained from filters 1 and 2. The summation of the fields obtained after applying filter 1 and filter 2 display perfect agreement with the results without filtering, as expected.

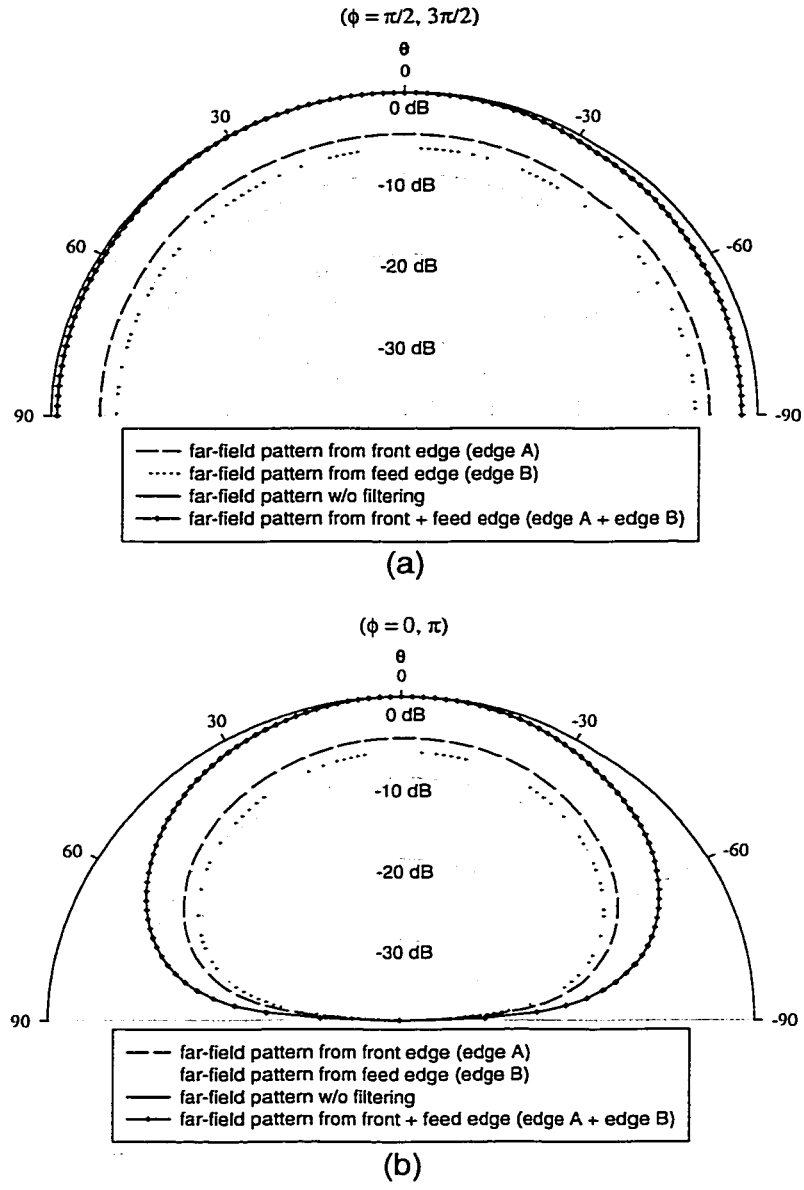

Figure 6.9: Far-fields generated from front (edge A in Fig. 1(b)) and feed edges (edge B in Fig. 1(b)) in (a) E-plane and (b) H-plane. The filters 1 and 2 are used to isolate edges A and B, respectively. The combined results of filter 1 and 2 (crosshair) are displayed along with the far-field pattern without the filtering.

Due to its simplicity and accuracy, this far-field transformation technique can be used where conventional analysis and measurement methods fail to reveal accurate relationships between near-field distributions and far-field patterns.

6.4 Ka-Band 2×2 Patch Antenna Array

The far-field transformation based on the high-resolution near-field data obtained by the EO field mapping has successfully revealed detailed information of a far-field formation of a single antenna. In this section, the transformation procedure is applied to a passive patch array to analyze the contribution of near fields to the far-field formation. For the EO field-mapping of the Ka-band 2×2 patch antenna array, the same phase-stabilized Ti:sapphire laser, which has 100-fs duration pulse output at an 80-MHz pulse repetition rate, was utilized. The laser was focused into a Lithium Tantalate ($LiTaO_3$) crystal sensor to detect the transverse, dominant radiating field component shown in Fig. 6.10.

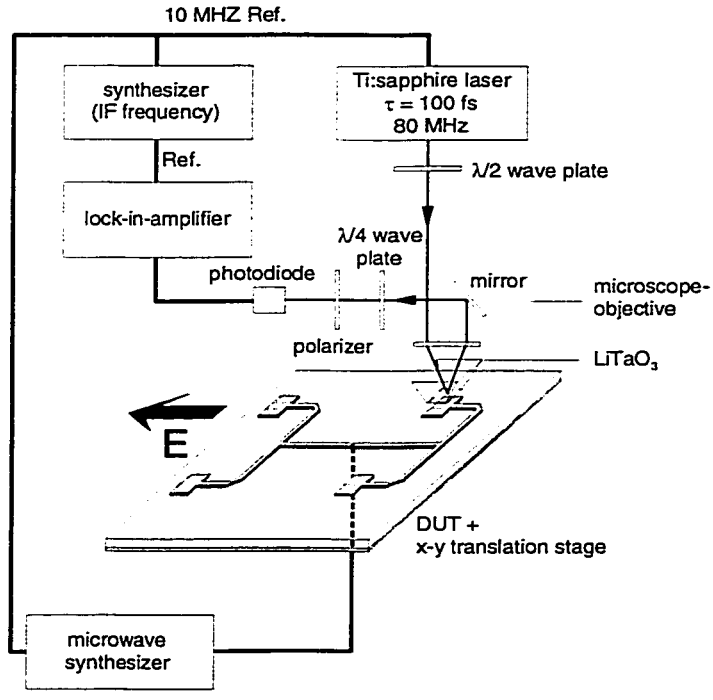

Figure 6.10: Measured system schematic of the patch antenna array.

For the E.O. mapping, the unit scanning step size was 202 μm × 200 μm, and 100 and 146 steps were taken for the cross polarization and co-polarization direction, respectively. The distance from the electro-optic crystal to the array was ~100 μm, and the operating frequency was 34.6 GHz.

Figure 6.11 shows detailed dimensions of the array.

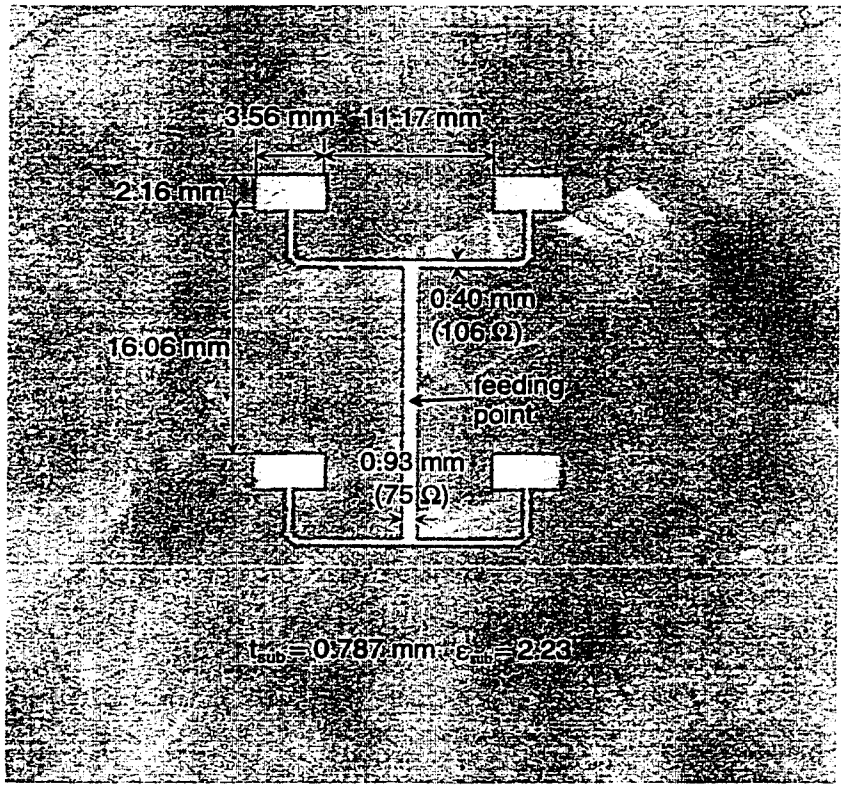

Figure 6.11: Ka-band 2×2 passive patch antenna array

The measured results clearly display the two main radiating edges on the individual patch (Fig. 6.12(a)). Also, the radiated fields at the two edges are found to have identical phase (Fig. 6.12(b)). In addition, the E.O. measurement reveals the electric field distribution of the microstrip network. Unlike the patch antennas, the electric fields around

the microstrip show 180° phase difference with respect to the center of the microstrip line. Thus, one can expect that the fields along the microstrip may cancel each other under the far-field condition. Over all, the measured near-field data display good symmetry distributions on every patch antenna for both amplitude and phase.

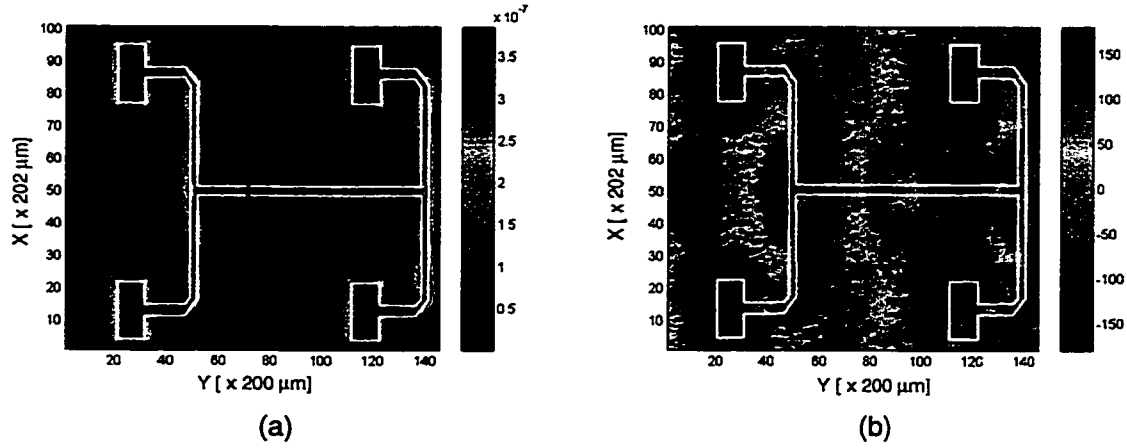

Figure 6.12: Measured near-field amplitude (in a.u., (a)) and phase (in degree, (b)).

Figure 6.13 shows a composite electric field distribution obtained from the amplitude and phase data shown in Fig. 6.12. The composition is performed in the area shown with red box in Fig. 6.12(a). Since the surface plot includes not only the amplitude but also phase, the value of the electric field varies from positive to negative numbers. The positive electric field represents positive y-component while the electric field in negative y-direction has negative value. Theoretically, the patch antenna has two main radiation edges, and thus, it should have two identical peak radiating patterns on each edge. However, a small section of the feed edge is sacrificed for the feed microstrip line. As a result, the patch shows a long radiation peak on the front side edge while the feed side pattern is divided into two. Figure 6.13 clearly demonstrates the difference between the two microstrip patches and microstrip transmission lines. Basically, the electric field generated from the microstrip has almost identical characteristics as the one from the

patch. However, Fig. 6.13 shows that the three positive peaks on the patch while the field around the microstrip displays negative value (blue valley) on the patch side and positive value on the other side. This comparison provides a one of most important information of radiating structures. In general, most of a radiating structure is designed to deliver information to a point spatially remote from it, where the radiation characteristic at this distance is often called the far-field characteristic. Under the far-field condition, the dimensions of the radiating structures are very small compared to the distance between observation point and the structure. As a result, the fields with opposite polarity (or 180° off phase) in close proximity cancel each other.

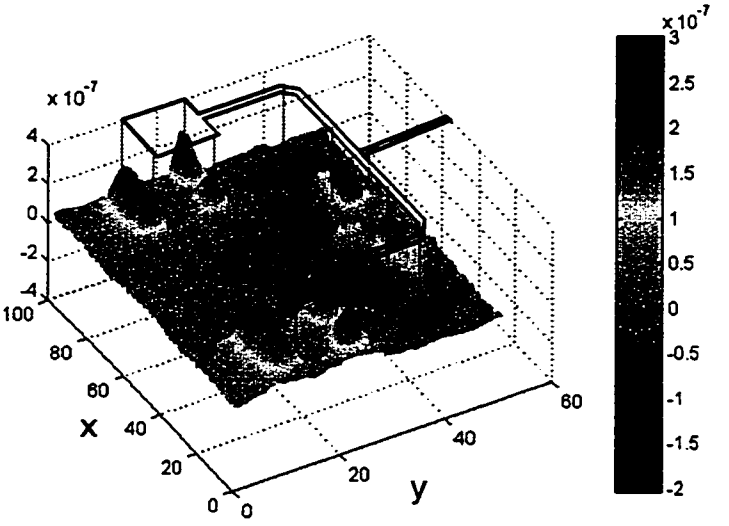

Figure 6.13: Amplitude and phase composite electric field distribution.

Thus, in this case, one can easily notice that the patches with uniform phase electric field are the dominant radiating structures of the array.

This explains the reason why accurate phase measurement is so crucial for the complete near-field analysis, and emphasizes the excellent feature of the EO near-field mapping technique.

Based on this high-resolution near-field data obtained by the EO field mapping, near- to far-field transformations are performed. The detailed transformation procedure can be found in section 6.2 of this chapter. Besides the calculation, the array far-field patterns are measured in an anechoic chamber, and a theoretical analysis of the array is performed for the validation of the transformed far field. For the theoretical analysis, the far-field pattern from the single patch antenna is obtained by Eq. 6.13. After the calculation of the far field from a single patch antenna, an array factor AF is calculated as follows;

$$AF = \frac{1}{M}\frac{1}{N}\frac{\sin\left(\frac{M\varphi_x}{2}\right)\sin\left(\frac{M\varphi_y}{2}\right)}{\sin\left(\frac{\varphi_x}{2}\right)\sin\left(\frac{\varphi_y}{2}\right)}$$

$$\varphi_x = k \cdot dx \cdot \sin(\theta)\cos(\phi) \tag{6.14}$$

$$\varphi_y = k \cdot dy \cdot \sin(\theta)\sin(\phi)$$

where M and N is the number of antenna elements along X- and Y-directions, and dx and dy represent the distances between the antenna elements along the X- and Y-axes. In this case $M = N = 2$, and dx, dy are 14.73 mm and 18.22 mm, respectively.

Finally, the theoretical far-field pattern E_{ff} can be obtained from Eq. 6.13 and 6.14 as follows;

$$E_{ff} = E_\theta \cdot AF \tag{6.15}$$

where E_θ can be found in Eq. 6.13.

Obviously, Eq. 6.15 reveals the radiation pattern only from the four patch antennas in the array.

Figure 6.14 shows the far-field patterns obtained by the near- to far-field transformation procedure (solid line) with the theoretically expected pattern (dash-dotted line) and measured far-field pattern (dashed line). The three results display good agreements in both E- (Fig. 6.14(a)) and H-plane (Fig. 6.14(b)). Especially, almost identical null and lobe positions are obtained.

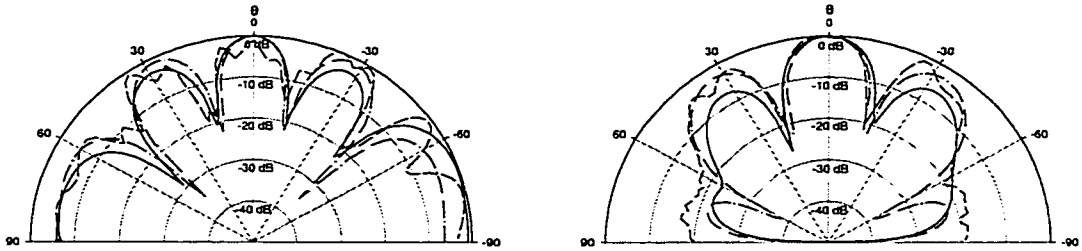

Figure 6.14: Far-field patterns of the patch antenna array. The transformed pattern (solid line), measured pattern (dashed line), and the theoretical calculation result (dash-dotted line) in (a) E- and (b) H-plane.

As mentioned in the previous sections, another distinct advantage of the near- to far-field transform procedure based on the EO near-field mapping is that it is possible to use various filtering procedures to examine the contribution of a small portion of the radiating structures to the total far-field formation.

From Eq. 6.8, it is obvious that the far field can be expressed as a sum of many small subgroups. This means that the total far field can be divided according to their origins. Due to the high-resolution property of the EO near-field mapping, it is possible to isolate a certain section of a radiating structure in order to examine its contribution to the far-field pattern. Since the near-field data can be considered as an array of infinitesimal magnetic dipoles, the scanned near field can be treated as a sum of small subgroup arrays during the transformation procedure. Thus, the contributions of those small subgroups for

the total far-field formation can be examined separately. Also, since the unit step size during the scanning is much smaller than the operating wavelength of the DUT, even a small area of a single radiating structure can be isolated. The isolation of a certain area of interest called a filtering procedure is so accurate that even two radiating edges of a single patch antenna can be isolated and their contribution for the far-field formation examined as shown in the previous section of this chapter.

In many arrays, a substantial amount of the radiation is often found from the structures that were not originally designed as radiating elements. This unexpected parasitic radiation can significantly degrade the performance of the array. Especially, as arrays employ more complicated geometries, the possibility of parasitic radiation increases. However, either traditional numerical analysis techniques or experimental methods have failed to provide sufficient information to understand the parasitic radiation in complicated arrays.

For the 2×2 patch antenna array, the four patch antennas are assumed to be the dominant radiating structures of the array. However, there are a number of different radiating structures in the array beside of the patches. For example, as shown in the near-field mapping (Fig. 6.12), the microstrip network also radiates considerable amount of electric fields. Also, even though it is not noticeable, a surface mode wave can have significant effect on the far field under the certain circumstances.

For the complete far-field analysis, two different filtering procedures were applied to the near-field data of the array to examine the contributions of the radiating elements in the array for the far field. A filter 1 is designed to isolate just the four patch antennas to study their dominance in the far-field pattern formation. Also, a filter 2 is introduced to examine the effect from areas of the array excluding the patch antennas. Thus, the filter 2 isolates the electric field on the microstrip feeding network and substrate. The filters 1 and 2 are designed to be complementary to each other. In other words, the combined

results from filter 1 and 2 are identical to the field pattern without the filtering procedure (Fig. 6.14, solid line).

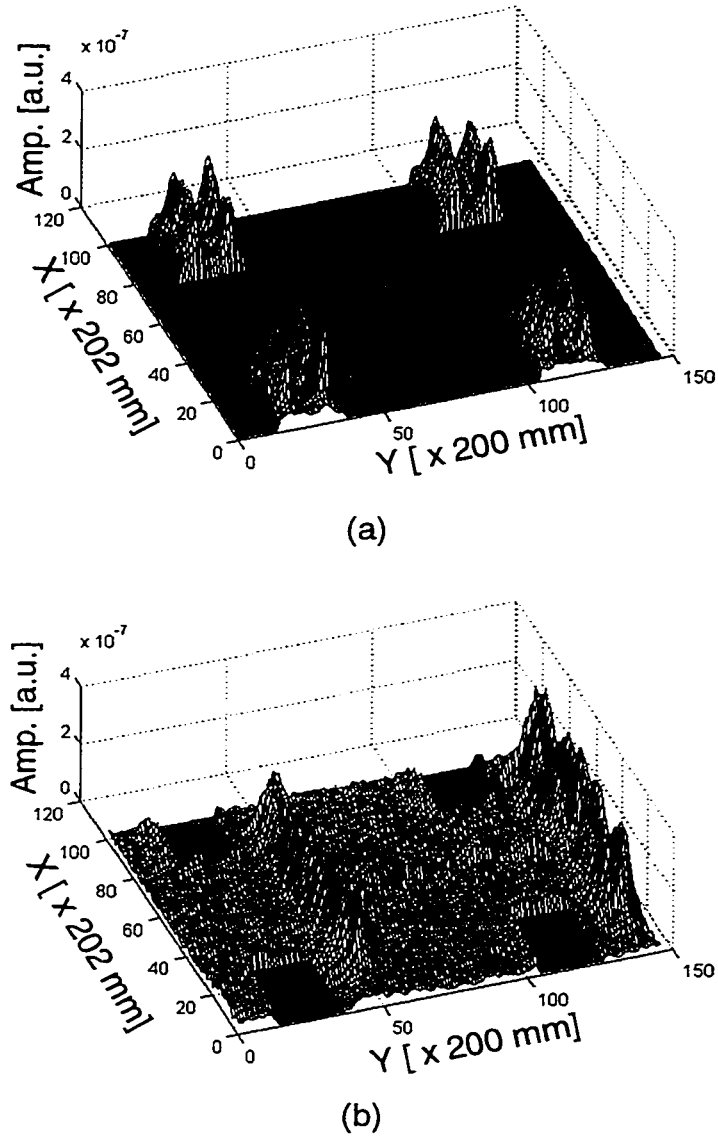

Figure 6.15: Near-field amplitude after applying the (a) filter 1 and (b) filter2.

The filter can be realized by introducing the additional filter matrix that has identical dimensions as the measured near field data. The elements of the filter matrix

have value "1" for the area of interest (open window), and "0" is assigned to the rest of the matrix (closed window). The product of the filter matrix and the near-field-amplitude-data matrix yields a filtered amplitude matrix that has identical values as the original near-field data for the open window and 0 for closed window. Figure 6.15 displays the near-field amplitude data after applying the two filters. Figure 6.15(a) shows four isolated patches with three amplitude peaks in each of them after applying the filter 1. However, the four patches are perfectly excluded from the amplitude data after applying the filter 2 (Fig. 6.15(b)).

Based on these amplitude data, the near- to far-field transformations were performed. Figure 6.16 displays the far-field patterns without filtering (solid line), after applying the filter 1 (dashed line) and the filter 2 (dash-dotted line).

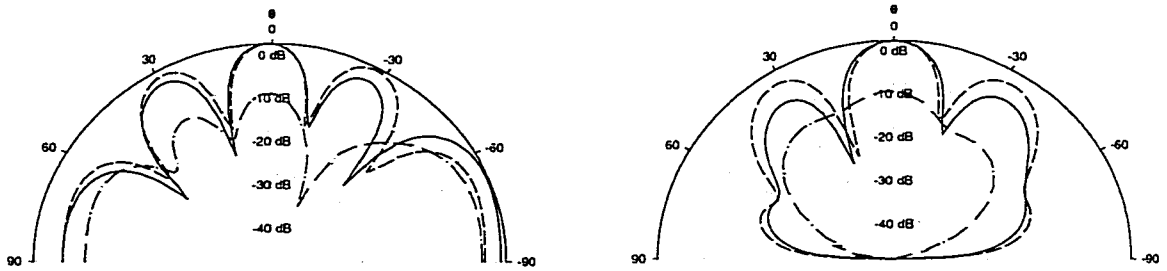

Figure 6.16: Comparison between transformed far field after applying the filter 1 (patches, dashed line) and the filter 2 (microstrip + surface, dash-dotted line) with the pattern without filtering (solid line) in (a) E-plane and (b) H-plane.

The results show the dominant role of the patches for the main lobe formations ($\theta \cong 0$) in both the E-plane (Fig. 6.16(a)) and H-plane (Fig. 6.16(b)). However, for the side lobes, the amplitudes obtained after applying the filter 1 are slightly bigger than the

results without the filtering procedure at certain position. This implies that the fields from the patches are partially compensated by the fields from the microstrip lines around the side-lobe regions. Overall, the results in Fig. 6.16 display the dominant role of the patches for the far-field formation.

Since the filter 1 isolates four patches in the array, the far-field pattern after applying the filter 1 should be identical to the theoretically expected field pattern, which is calculated from the patches. Thus, based on the assumption that the theoretical expectation reveals true pattern, the comparison between these two patterns can be used for the validation of the filtering process. Figure 6.17 displays the theoretical far-field pattern obtained from Eq. 6.15 (dashed line) and the pattern after applying the filter 1 (solid line).

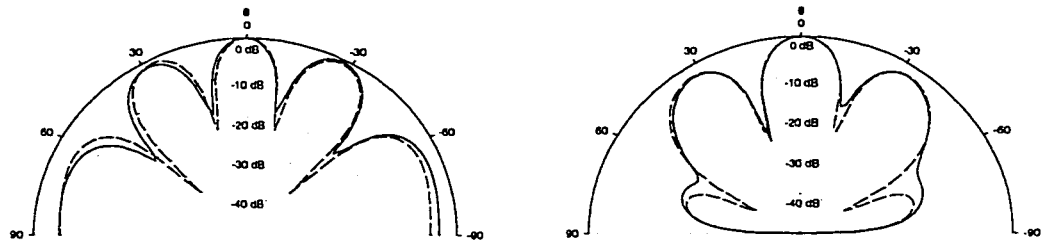

Figure 6.17: Comparison between transformed far field after applying the filter 1 (patches, solid line) and the theoretical pattern (Eq. 6.15, dashed line) in E-plane (a) and H-plane (b).

The comparison displays outstanding agreement between the far-field pattern after applying the filter 1 and theoretical expectation, and as a result, it validate the accuracy of the transformation procedure including the filtering procedure.

This near- to far-field transformation that was developed based on the high-resolution EO near-field mapping can be one of most powerful diagnostic tools available

for arrays because of its accuracy, and efficiency. Moreover, the transformation procedure associated with various filtering procedures can reveal remarkably detailed phenomena of the far-field formation that cannot obtained from any other measurement methods.

6.5 Ka-Band Quasi-Optical Amplifier Array

In the previous section, a Ka-band passive 2×2 patch antenna array was measured by the EO field mapping system, and the near-field data were transformed into the far-field. In the course of the transformation, various filtering procedures were introduced to examine the contribution of the antennas and microstrip lines to the far-field formation.

In this section, high-resolution electro-optic near-field mappings have been performed for a Ka-band 6×6 quasi-optical amplifier array under a number of different operating conditions. Due to the high sensitivity and outstanding measurement proximity of the electro-optic field mapping system, the surface waves were measured successfully, and their contributions for the far-field formation were analyzed.

6.5.1 Near-Field Measurement

For the completeness of the far-field transformation process of the array, a brief description of the array and the measurement setup are mentioned afterwards.

A Ka-band slot antenna amplifier array with 36 elements fabricated on aluminum nitride substrates utilizing commercial low-power MMIC amplifiers in a CPW geometry is measured by the electro-optic field mapping system. The normal operation of the quasi-optical array is shown in Fig. 3.19. A feed antenna radiates a wave that illuminates the feed (input) slot antennas of the active array. Ideally, each element should receive the same amplitude and phase input, amplify it, and radiate it in phase throughout the radiating slot antennas. The feed slot antennas and radiating slot antennas have identical

geometry except they are arranged to be 90° off angle to achieve input and output signal isolation. The saturated output powers at 31 GHz were 0.3 W and 0.5 W, with each MMIC contributing on average between 8.3 and 14 mW — this is 7 dB lower than the power specified by the manufacturer for a higher bias point. No liquid cooling was needed, and the AlN substrate reached a peak temperature of 40 $^{\circ}$C. The average small signal gain contributed by the MMICs was 10 and 14 dB, respectively, and was measured relative to a passive array.

The measurement setup schematic was shown in Fig. 3.20. For the measurements under the normal operation, a specially designed hard horn [41] was used as feed antenna to achieve plane wave feeding within a compact distance from the array. Also, to analyze near- and far-field relations under the nonuniform operation conditions – such as uneven input wave or nonuniform operation of active elements, single element activation measurements have been performed using WR-28 open-end waveguide as a feed antenna on the center and corner of the array.

For both single-element activation and normal-operation measurements, a miniaturized $LiTaO_3$ crystal was used as an EO sensor to detect the dominant output field component (Y-component, Fig. 3.20). The scanning resolution was 450 μm × 500 μm, and 121 × 126 points were taken along X and Y directions.

Figure 6.18 displays the measured amplitude (Fig. 6.18(a)) and phase (Fig. 6.18(b)) distribution on the QO array with waveguide feeding of a unit cell at the center of the array. The outlines of the array structures including input and output slots and bias network are overlayed with white lines, and the position of the open waveguide is displayed with a blue rectangle.

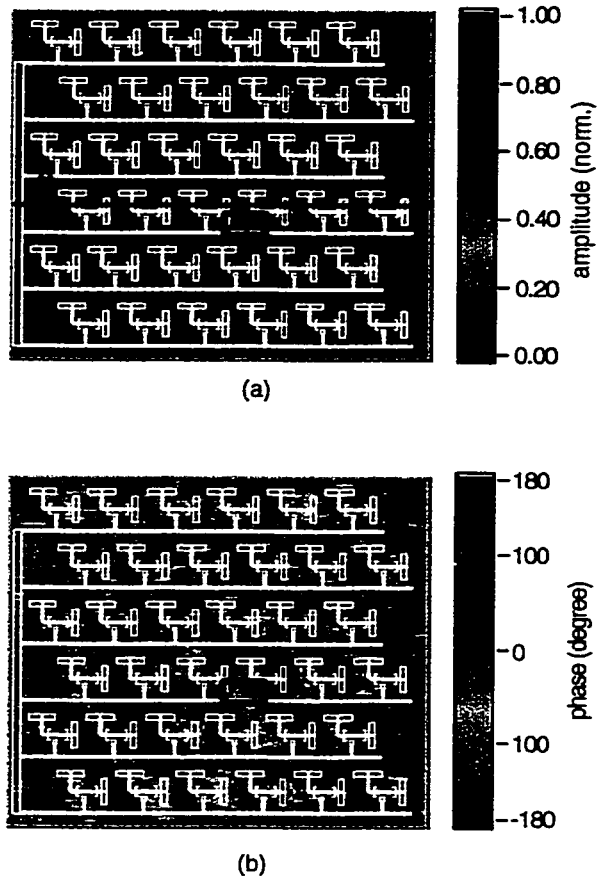

Figure 6.18: Measured electric field (a) amplitude (normalized) and (b) phase (degree) of the array under the single element activation condition. The outline of the array is overlayed with white line, and the position of the feed waveguide aperture is marked with a blue rectangle.

The amplitude distribution shown in Fig. 6.18(a) clearly displays the peak amplitude on the output slot placed nearest from the feed waveguide aperture. Also, relatively weak peaks can be found in the neighboring output slots on the same row. Under ideal circumstance, the peaks in the neighboring slots around the direct fed cell should not exist. However, in an actual situation, the surface wave [69] and propagation wave though the dc bias line serve as input signals to the neighboring cells.

Another remarkable result obtained by the EO near-field mapping system used in this work is the successful measurement of surface waves [70]. The outstanding sensitivity and measurement proximity of the EO system to the DUT makes it possible to measure the wave propagating through the substrate under the actual operating condition.

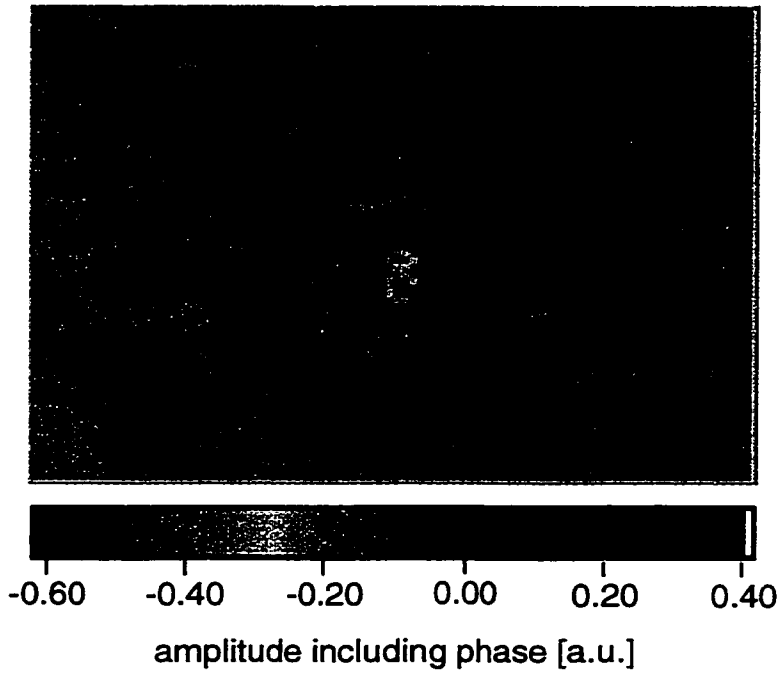

Figure 6.19: Measured surface wave under the single cell activation condition. The amplitude and phase data are combined according to Eq. 6.16 for display. The output slot of the direct fed cell is enclosed with dotted box.

Figure 6.19 shows the electric field distribution around the direct fed element (enclosed with dotted box) under the single element activation condition (Fig. 6.18). To display the surface wave effectively, the amplitude and phase data are combined as

$$E_{m,n}\sin(t_0+\psi_{m,n})$$
where
$E_{m,n}$: *measured near−field amplitude*
$\psi_{m,n}$: *measured near−field phase, and*
t_0 : *time argument.* (6.16)

Thus Fig. 6.19 displays the amplitude and phase conditions on the individual measurement point with a constant time argument t_0. As a result, the wave fronts in the substrate are displayed by alternating blue and green arcs in Fig. 6.19.

The measured electric field amplitude and phase distributions under the normal operation are shown in Fig. 6.20. For the near-field measurement under the normal operation, a hard horn was used as a feeding antenna to obtain uniform amplitude and phase incident wave to the array. The outlines of the array including the input/output slot antennas and bias lines are overlayed by solid white lines on both amplitude (Fig. 6.20(a)) and phase (Fig. 6.20(b)) results.

Unlike the unit cell activation condition (Fig. 6.18), most of the cells are activated as shown in Fig. 6.20(a). Also Fig. 6.20(b) displays almost uniform phase distribution in the output slots. However, even under the normal operation condition, the amplitude distribution shows somewhat nonuniform magnitudes between each cell.

The possible explanations can be found both in the feed antenna and the array itself. The hard horn used in the measurements has much better uniformity than conventional horn antenna in amplitude and phase distributions. However, still it has certain amount of amplitude and phase variations across the aperture [19]. Also, the uniformity of the amplifier MMICs mounted on the array can be another issue for the nonuniform amplitude distribution. More detailed analysis of the near-field distribution can be found in the ref. [19].

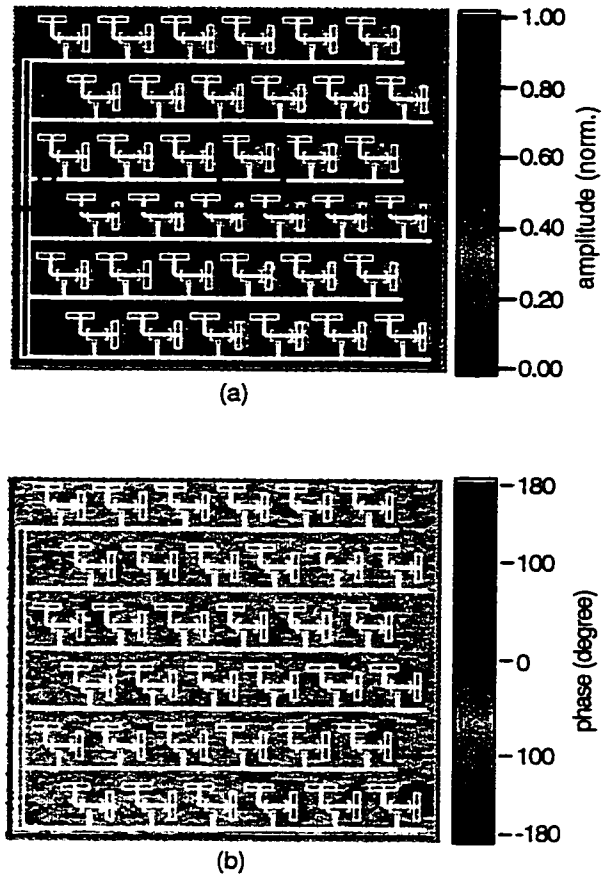

Figure 6.20: Measured electric field (a) amplitude (normalized) and (b) phase (degree) of the array under the normal operation condition with hard horn antenna feed. The outline of the array is overlayed with white line. The unit cell structure of the array is enclosed with the black square.

6.5.2 Near- to Far-Field Transformation

As mentioned in section 6.2, the high-resolution near-field data obtained from the EO field mapping system make it possible to divide the array into small sections. Thus, the contributions of those small sections can be examined separately. In this section, various isolation procedures (filtering) are used for the characterization of the far field pattern using certain areas of the array. The filter can be realized by introducing an

additional filter matrix that has identical dimension as the measured near field data. The elements of the filter matrix have value "1" for the area of interest (open window), and "0" is assigned to rest of the matrix (closed window). The product of the filter matrix and the near field amplitude data matrix yields a filtered amplitude matrix that has identical values as the original near-field data for the open window and 0 for the closed window. Thus the far fields generated from the elements in the closed area are nullified because $E_{m,n}$ equals 0 in Eq. 6.5 for those elements. As a result, only those elements in the open window can contribute to the total far field after applying the filtering procedure. The two filtering procedures – filter 2 and 3, which will be discussed later in this section – are designed to be complementary to each other. In other words, the summation of the far fields obtained from each filtering procedure has to be identical to the far field pattern without the filtering procedure. In this work, three different filters – filter 1, 2 and 3 – are used for the far field analysis, and detailed discussions of those filters and results follow.

Since the EO probe is aligned with the direction of output electric field component (Y-direction in Fig. 3.20), the measured electric field exists only in the output slot. Thus, if the measurement and far field transformation procedure are correct, the resultant far-field pattern from the unit cell (the element enclosed by solid black line in Fig. 6.20(a)) should be identical to the far field of the slot antenna. The filter 1 is designed to isolate the unit cell shown in Fig. 6.20(a).

For the verification of the transformed results, theoretical far field pattern of the slot antenna [71] is displayed together in Fig. 6.22. Both theoretical expectation (solid line) and transformed pattern show good agreements in E- (Fig. 6.22(a)) and H-plane (Fig. 6.22(b)).

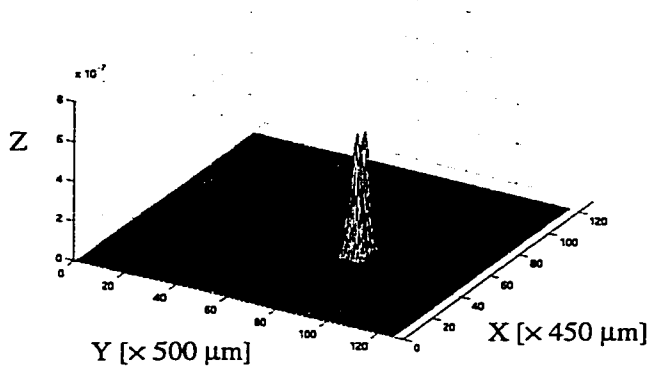

Figure 6.21: Near-field amplitude of the quasi-optical amplifier array after applying the filter1. The array is under unit cell activation condition (waveguide feed). The amplitude (Z) unit is a.u.

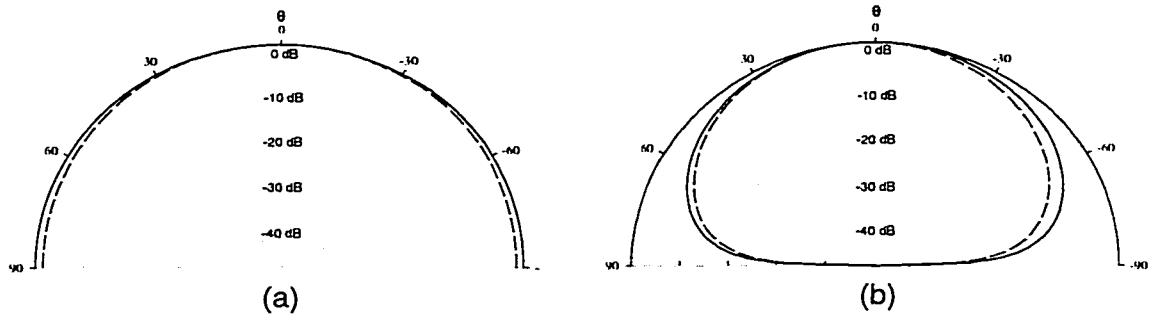

Figure 6.22: Transformed far field patterns in (a) E-plane and (b) H-plane for the unit cell shown in Fig. 6.20(a). To isolate the unit cell, filter 1 is applied. Theoretically predicted patterns (solid line) are shown along with the transformed pattern (dashed line).

As shown in Fig. 6.19, the EO field mapping system provides the surface wave information under the actual operation condition. Based on the advantage of the EO

system, filter 2 and filter 3 are designed to isolate electric fields in the main radiating slots and in the substrate. The amplitudes after applying filter 2 and 3 are displayed in Fig. 6.23(a) and (b) for the single element activation case.

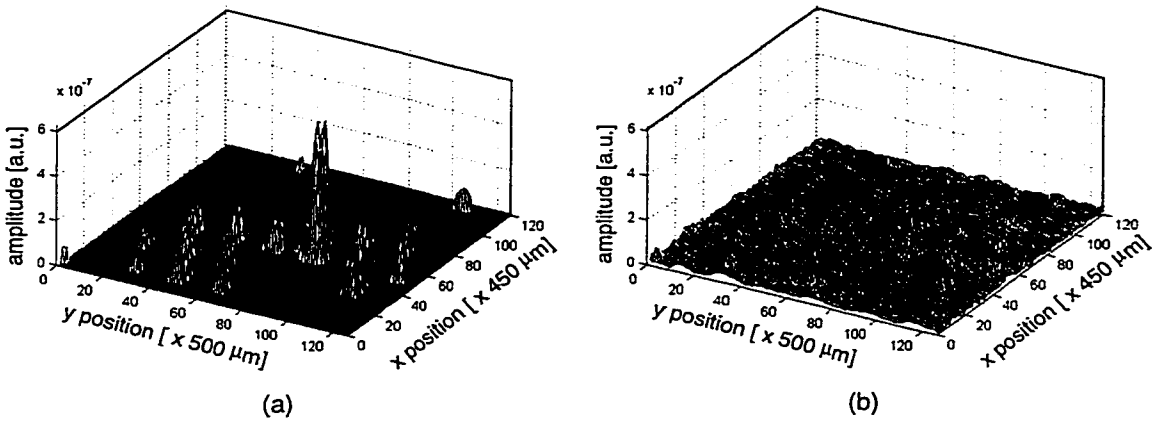

Figure 6.23: Amplitude data after applying (a) filter 2 and (b) filter 3 for single cell activation (Fig. 6.18). The highest peak in (a) corresponds to the output slot of the direct fed cell.

For the purpose of verification, the two filters are designed to be complementary. Thus, if the two filters are correctly designed, the superposition of the two far fields obtained from each filter should have identical patterns as those without any filtering procedure. From the measured near field amplitudes for both single element activation (Fig. 6.18(a)) and normal operation (Fig. 6.20(a)) conditions, it is noticeable that the fields inside of the slots have much stronger signal than the fields in the substrate. Thus, by applying filter 2 and 3, the contributions to the far field formation from the well confined strong fields in the slots and the fields in the substrate that have much lower amplitude but spread widely over the whole array can be examined under the actual operation conditions. The filter 2 has open windows for those elements that have amplitudes stronger than -20 dB with respect to the peak amplitude. The filter 3 that is

complementary to the filter 2 has an open window for the amplitudes lower than -20 dB with respect to the peak amplitude. As a result, the filter 2 isolates the electric fields in the slots, and only the electric field in the substrate is displayed after applying the filter 2.

Since the hard horn is used as a feed antenna under the normal operation condition, the individual elements are expected to have almost identical input signals. On the contrary, under the single cell activation, individual elements in the array receive the input signal from the output slot of the direct-fed element in the form of surface mode wave or transmitted wave via the bias networks. Thus, one can expect that the behaviors of the surface wave may be different in each case, and as a result, the contributions of the surface wave to the far field are also expected to be different.

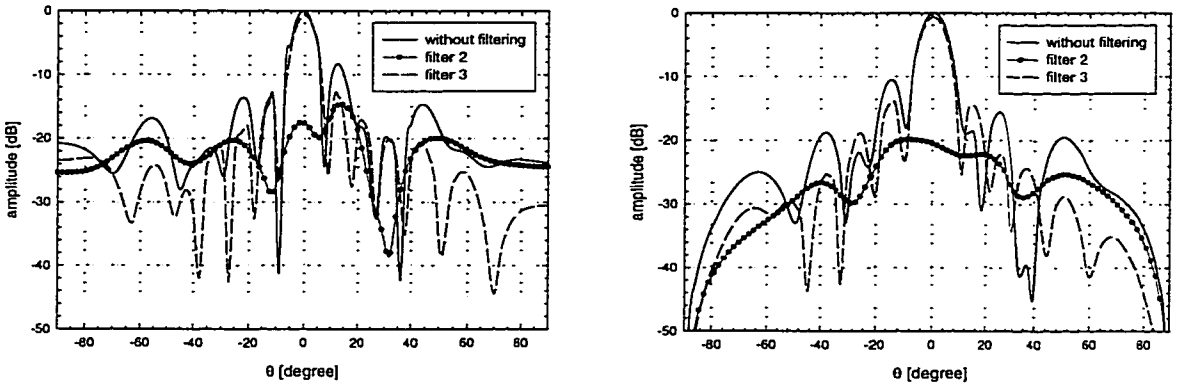

Figure 6.24: Transformed far-field patterns under the unit cell activation condition. The total far field pattern obtained from original near field data without filtering is plotted with the far field pattern generated by the main output slots (filter 2) and surface wave (filter 3) of the array in (a) E- and (b) H-plane.

Figure 6.24 and 6.25 show the resultant far field patterns obtained from the near-to far-field transformation procedures for single activation (Fig. 6.24(a): E-plane and (b):

H-plane) and normal operation (Fig. 6.25(a): E-plane and (b): H-plane), respectively. In both cases, the superposition of the results after applying filter 2 and 3 is confirmed to be identical to the far field pattern without filtering procedure.

From Fig. 6.24, it is quite noticeable that most of the far field pattern (without filtering, solid line) is the result of the surface wave (filter 2, dashed line) in both E- (Fig. 6.24(a)) and H-plane (Fig. 6.24(b)). The peak of the far field pattern from the main output slots obtained by applying the filter 2 is about 15 dB and 20 dB lower than the peak of the pattern obtained by the filter 3 in E- and H-planes, respectively.

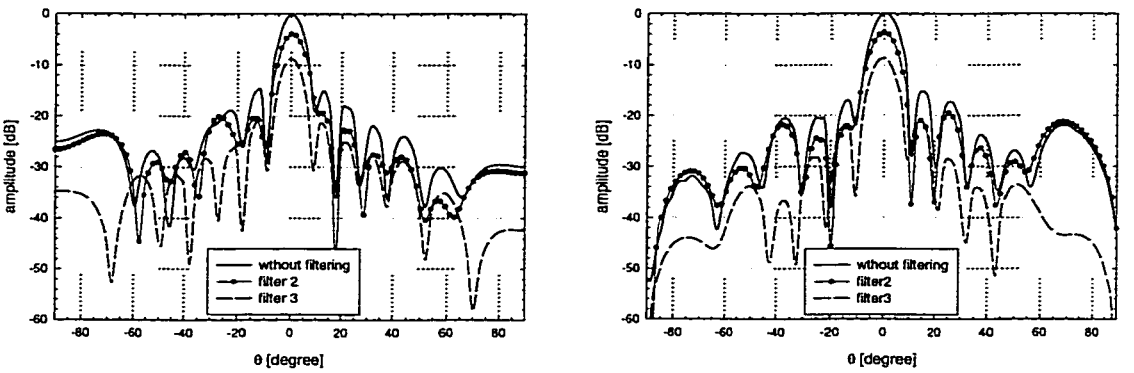

Figure 6.25: Transformed far-field patterns under the normal operation condition. The total far field pattern obtained from original near field data without filtering is plotted with the far field pattern generated by main output slots (filter 2) and surface wave (filter 3) of the array in (a) E- and (b) H-plane.

For the normal operation condition, the cells in the array are operated in a more balanced fashion than the single mode activation. As a result, the effect of the surface wave is reduced while the contributions of the main slots increase for the far field pattern as displayed in Fig. 6.25. As a result, the surface wave generates about 5dB lower far field than the field from the slots at the main lobe position in both E- (Fig. 6.25(a)) and

H-plane (Fig. 6.25(b)). Also, the shape of the total far-field pattern (without filtering) is determined by the pattern from the slots, while it is almost identical with the pattern generated from the surface wave under the single cell activation (Fig. 6.24(a) and (b)).

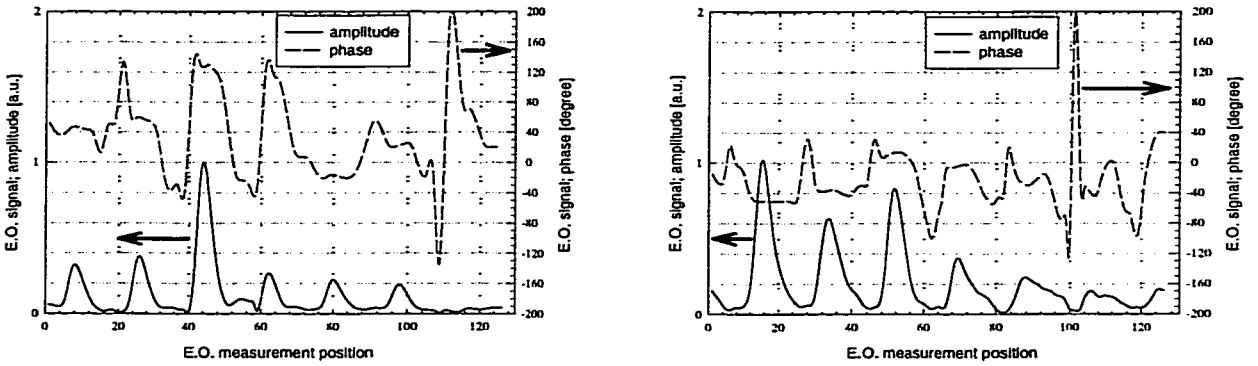

Figure 6.26: One-dimensional amplitude and phase plot for (a) single activation (along the line AA′ in Fig. 6.18(a)) and (b) normal operation (line BB′ in Fig. 6.20(b)).

To explain the far field results, the 1-dimensional amplitude and phase of the near field data are examined. Figure 6.26 shows the amplitude (solid line) and phase (dashed line) plots under the single cell activation (Fig. 6.26(a)) and normal operation conditions (Fig. 6.26(b)) along the black solid line AA′ and BB′ shown in Fig. 6.18(a) and Fig. 6.20(a), respectively. For the single cell activation case, the amplitude peaks in the slots show large phase variations to each other while the phase variation of the surface wave is relatively small. On the contrary, the amplitude peaks display quite uniform phase distribution under the normal operation condition. Thus, the electric fields in the slots are constructively added to each other under the normal operation condition, and as a result, the fields in the slots dominantly determine the far field pattern.

However, from the near field amplitude data in Fig. 6.20(a), the array does not operate in a perfectly balanced way even under the normal operation condition. The contribution of the surface wave under the normal operation (Fig. 6.25) can be explained as a result of this unbalanced operation of the array.

6.6 Verification of Near- to Far-Field Transformation and Filtering Process

The near- to far-field formation based on the EO near-field data demonstrates its usefulness for various radiating structures. The transformation technique provides accurate far-field patterns in very short computing time by employing a simple mathematical algorithm. Furthermore, by combining with various filtering procedures, the near- to far-field transformation makes it possible to isolate the parasitic radiating elements in a complicated system and examine their effect on the far-field formation. This is a truly unique advantage of the transformation procedure and cannot be found from other analysis methods. However, since the transformation and filtering procedures are so unique, questions about the validity of those procedures can be raised.

The verification of the transform technique can be achieved by answering a series of possible questions about the procedure. First of all, as the most fundamental question, one can ask about the mathematical completeness of the deriving procedure. If the mathematical steps are correct, then the far-field results obtained from the transformation have to be carefully compared with other independent results such as actual far-field measurements or theoretically expected fields.

Once the transform procedure is proven to be correct in mathematics, and it reveals true far-field patterns, similar verification procedures have to be applied to the filtering process that truly separate the near- to far-field transformation from other methods.

In this section, the verification of the near- to far-field transformation technique and the associated filtering process were performed by using mathematical proofs and actual result comparisons. In most cases, the results from the quasi-optical amplifier array (previous section) are used for the verification process and the results from other structures are utilized on some occasions. Thus, the filters mentioned during the verification process are consistent with the filters in section 6.5.

Figure 6.27 shows the verification flow charts for the validation of the transformation and filtering procedures.

I. Verification of the Transformation

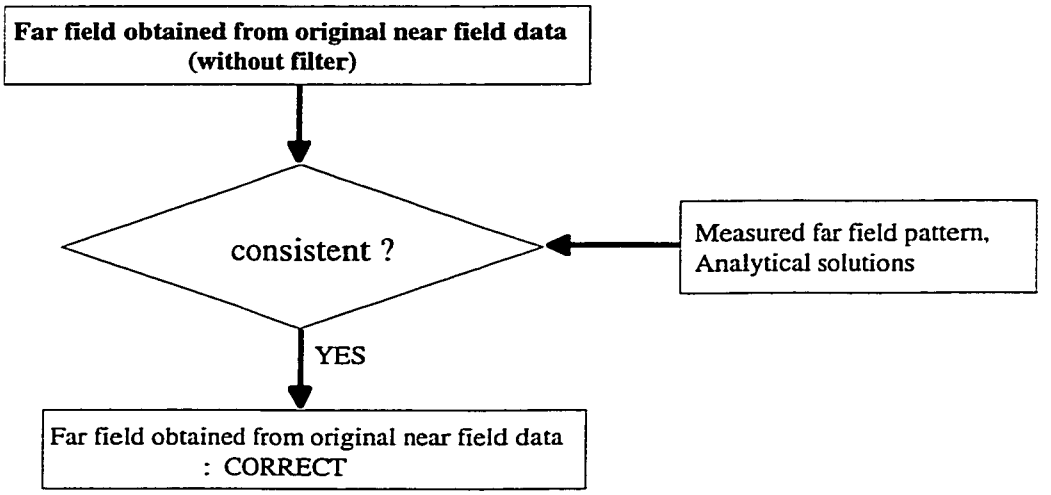

II. Verification of Filter 1

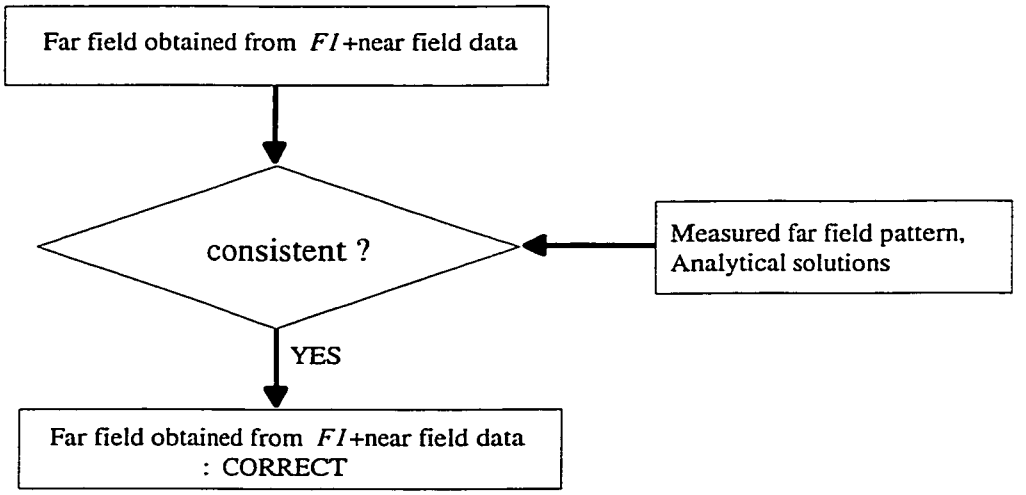

Figure 6.27: Flow charts of the verification procedure for the near- to far-field transformation and filtering process.

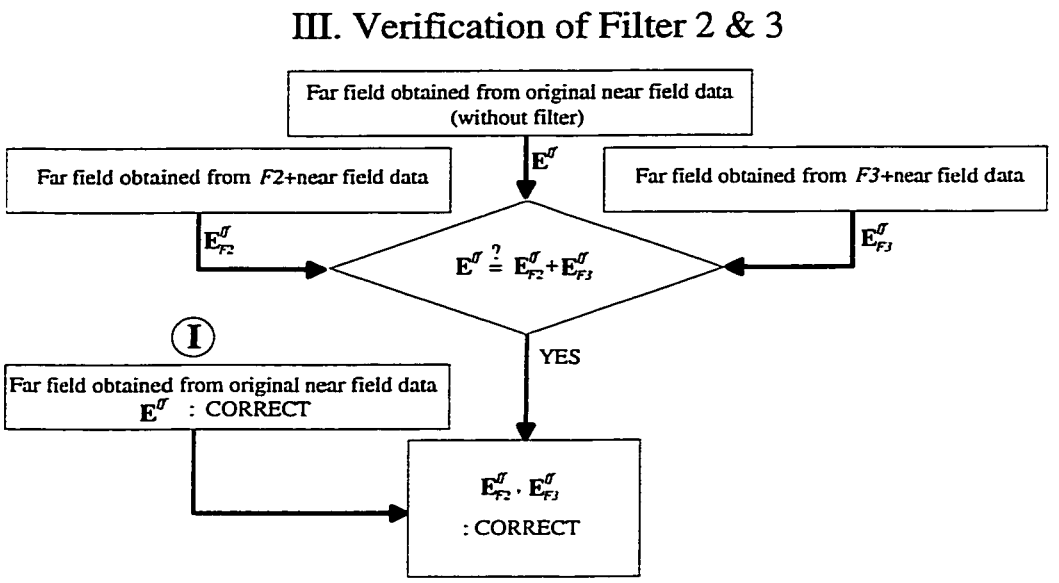

Figure 6.27: Flow charts of the verification procedure for the near- to far-field transformation and filtering process (*cont.*).

6.6.1 Verification of Near- to Far-Field Transformation

The most important step of the near- to far-field transformation is that the individual near-field data point is considered as an infinitesimal magnetic dipole due to the high-resolution property of the EO field mapping. This assumption can be proven by using the far-field pattern of an aperture structure.

The near-field unit cell can be considered as a rectangle that has size of $dx \times dy$. The size of the unit cell is determined by the scanning resolution of the EO field mapping, and the electric field has uniform value in one unit cell. Also, the electric field in one unit cell is totally irrelevant to the electric fields in adjacent cells during the measurement. As a result, one can easily find a similarity between the unit cell in the EO near-field map and aperture structure. As a matter of fact, the unit cell has the identical properties of an aperture mounted on a ground plane with a uniform field distribution in

it. The ground plane keeps the electric field confined only in the aperture. Thus the electric field in one aperture cannot have any interference from the fields in other apertures, which is the identical behavior of the near-field data. The only major difference between the actual aperture and the near-field unit cell is the size. In most cases, the size of a near-field unit cell is about $0.01\lambda \times 0.01\lambda$ range. However, this EO field-mapping resolution can be reduced to $4 \times 10^{-4}\ \lambda$ or less, if it is necessary. This extremely small size of the unit cell – or, high-resolution of the EO field mapping – makes it possible to use infinitesimal magnetic dipole approximation.

Figure 6.28 displays the aperture mounted on a ground plane with a uniform field distribution.

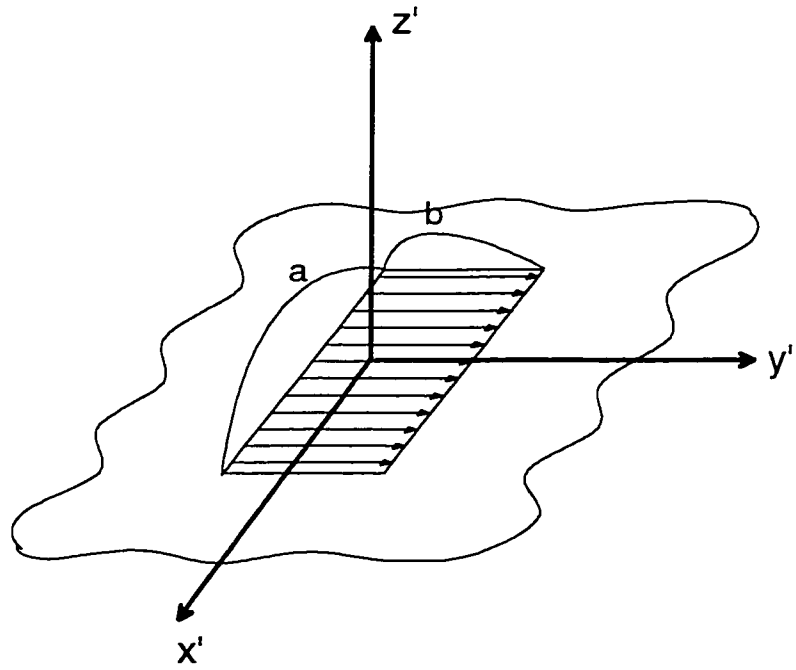

Figure 6.28: Rectangular aperture on ground plane.

The size of the aperture is a × b along the x′- and y′-direction.

The far field from the aperture shown in Fig. 6.28 can be expressed as [39]

$$E_{r'}=0$$

$$E_{\theta'}=C\sin(\phi')\frac{\sin(X)}{X}\frac{\sin(Y)}{Y}$$

$$E_{\phi'}=C\cos(\theta')\cos(\phi')\frac{\sin(X)}{X}\frac{\sin(Y)}{Y}$$

where (6.17)

$$X=\frac{k\cdot a}{2}\sin(\theta')\cos(\phi')$$

$$Y=\frac{k\cdot b}{2}\sin(\theta')\sin(\phi'), \text{ and}$$

$$C=j\frac{a\cdot b\cdot k E_0 e^{-jkr'}}{2\pi r'}$$

where E_0 is the amplitude of the electric field in the aperture, and θ', ϕ', and r' are spherical coordinate values corresponding to the x′-y′-z′ axes.

If the size of the aperture (a and b) is sufficiently small with respect to the wavelength (*i.e.*, ka and kb $\rightarrow$ 0), the normalized form of Eq. 6.17 can be approximated as

$$X\approx 0$$

$$Y\approx 0, \text{ and}$$

$$E_{r'}=0 \qquad (6.18)$$

$$E_{\theta'}\approx\sin(\phi')$$

$$E_{\phi'}\approx\cos(\theta')\cos(\phi')$$

Now, we introduce new axes system x-y-z that is related to the x′-y′-z′ axes as follows

$$\begin{aligned} x &= y' \\ y &= z' \\ z &= x' \end{aligned} \tag{6.19}$$

For the convenience of the axis transformation, Eq. 6.18 is converted into cartesian coordinate vector components as follows

$$\begin{aligned} E_{x'} &= -E_{\phi'}\sin(\phi') + E_{\theta'}\cos(\theta')\cos(\phi') \\ E_{y'} &= E_{\phi'}\cos(\phi') + E_{\theta'}\cos(\theta')\sin(\phi') \\ E_{z'} &= -E_{\theta'}\sin(\theta') \end{aligned} \tag{6.20}$$

From Eq. 6.19 and 6.20, the cartesian field components can be transformed into the x-y-z axes system.

$$\begin{aligned} E_x &= E_{y'} \\ E_y &= E_{z'} \\ E_z &= E_{x'} \end{aligned} \tag{6.21}$$

From Eq. 6.18, 6.20, and the vector relations between θ'-ϕ'-r' and θ-ϕ-r, equation 6.21 can be obtained as

$$\begin{aligned} E_x &= \sin(\theta)\cos(\theta)\cos(\phi) \\ E_y &= \sin(\theta)\cos(\theta)\sin(\phi) \\ E_z &= -\sin^2(\theta) \end{aligned} \tag{6.22}$$

Now, these cartesian components can be expressed as spherical coordinate components as

$$E_\theta = 0$$
$$E_\phi = \sin(\theta) \qquad (6.23)$$
$$E_r = 0$$

Equation 6.23 shows that the far-field pattern from the aperture with infinitesimal size (with respect to the wavelength) is identical to the pattern of infinitesimal magnetic dipoles that is aligned in the z-axis direction. Figure 6.29 graphically summarizes the results in order to help understanding.

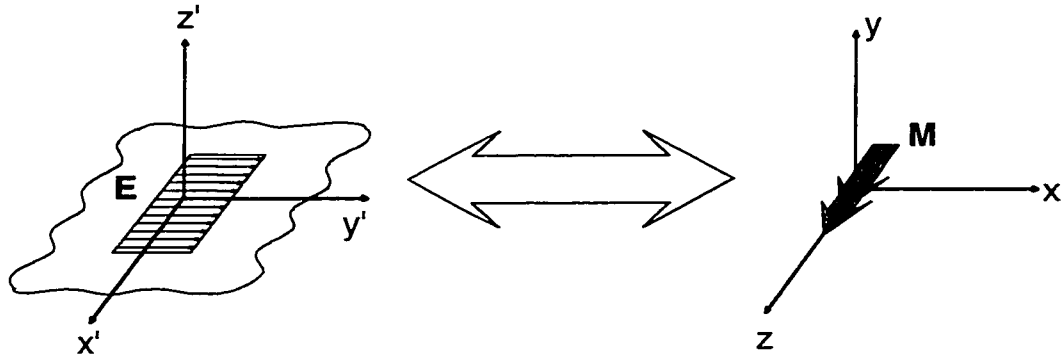

Figure 6.29: Infinitesimal magnetic dipole approximation of small aperture.

Figure 6.29 displays the small aperture that is identical to the unit cell of EO near-field map and its equivalent magnetic dipole **M**. The electric field in the aperture points in the y′-direction, and the equivalent magnetic dipole is aligned to z (x′)-direction.

Since the magnetic dipole approximation has been proven, the near- to far-field transformation is nothing else but the far-field calculation of a two-dimensional array. Thus, no further mathematical verification is necessary for the rest of the near- to far-field transformation procedure shown in Eq. 6.1 ~ Eq. 6.8.

In order to demonstrate the accuracy of the near- to far-field transform technique, various ideal radiating structures are artificially generated, and the theoretically expected patterns are compared with the results obtained from the transformation process. Those ideal structures include a short dipole and rectangular aperture. The comparisons are detailed in section 6.2 of this chapter. The transformed far-field patterns display excellent agreements with theoretically expected patterns in both the dipole (Fig. 6.3) and the aperture (Fig. 6.6). Also, for the actual application, the near-field data of a patch antenna obtained by the EO field mapping are transformed into the far-field pattern through the transformation process. The comparison between the transformed pattern and theoretically obtained pattern show good agreement (Fig. 6.8).

Now, the near- to far-field transformation technique has been verified to be mathematically correct and to reveal true far-field patterns.

6.6.2 Verification of Filtering Process

Another distinct advantage of the transformation based on the EO near field mapping is its capability to isolate certain parts of the near field and transform them to far fields. Using this method, it is possible to examine the contribution of each section of the DUT for the far field formation. For the systematic approach for the sectional isolation of the near field data, the filtering (windowing) processes are used to isolate a certain section of the radiating structure.

In this section, a mathematical verification of the filtering process is discussed. Also, based on the three filters used for the Ka-band quasi-optical amplifier array under the single cell activation condition (section 6.5.2), the validity of the results obtained from the filtering process is examined.

From the transformation formula shown in Eq. 6.8, it is obvious that the equation can be expressed as a summation of small subgroups because the expression is nothing more than a simple summation procedure.

For the concise expression, new functions $P^x_{m,n}$ and $P^y_{m,n}$ are introduced such as

$$P^x_{m,n} \equiv e^{-jk_0 d^x_{m,n}\sin(\theta)\cos(\phi)} \text{ and}$$
$$P^y_{m,n} \equiv e^{-jk_0 d^y_{m,n}\sin(\theta)\sin(\phi)}. \tag{6.24}$$

By using Eq. 6.24, Eq. 6.8 can be expressed as

$$\begin{aligned}\mathbf{E}^{ff} &= \sum_{m,n} \mathbf{E}^{ff}_{m,n} e^{-jk_0 d^x_{m,n}\sin(\theta)\cos(\phi)} e^{-jk_0 d^y_{m,n}\sin(\theta)\sin(\phi)} \\ &= \sum_{m,n} \mathbf{E}^{ff}_{m,n} P^x_{m,n} P^y_{m,n} \\ &= \sum_{G1} \mathbf{E}^{ff}_{x1,y1} P^x_{x1,y1} P^y_{x1,y1} + \sum_{G2} \mathbf{E}^{ff}_{x2,y2} P^x_{x2,y2} P^y_{x2,y2} + \cdots\cdots + \sum_{Gi} \mathbf{E}^{ff}_{xi,yi} P^x_{xi,yi} P^y_{xi,yi}\end{aligned} \tag{6.25}$$

where

G1,G2, ...,Gi : subgroups

xk,yk : data point in group Gk

Thus, the total far field can be considered as a sum of small far field groups. Since each sub-far-field is corresponding to the certain sectional group of near-field data (Eq. 6.6), we can examine the contribution of a specific section of DUT for the far field formation. For example, if we are interested in the specific section of DUT that corresponds to the far-field formation of the group *Gi* in Eq. 6.25, we can easily extract the contribution of the section using the condition such as

$$\mathbf{E}^{ff}_{x1,y1} = \mathbf{E}^{ff}_{x2,y2} = \cdots\cdots = 0 \text{ except } \mathbf{E}^{ff}_{xi,yi}. \tag{6.26}$$

If the condition shown in Eq. 6.26 is true for an arbitrary observation point, equation 6.26 is identical to the condition such as

$$E_{x1,y1}=E_{x2,y2}=\cdots\cdots=0 \text{ except } E_{xi,yi}$$

where (6.27)

$E_{xk,yk}$: *near−field amplitude data in the group Gk.*

In other words, Eq. 6.26 is true if and only if Eq. 6.27 is true. By introducing filter function F to the near-field amplitude data that satisfies Eq. 6.27, we can extract the contribution of a certain section (*e.g.*, the group *Gi*) for the far field formation. The filter F can be expressed in a matrix form that has the same dimensions as the near field data. The filter F can be expressed mathematically as

$$F=\left[f_{m,n}\right]$$

where

$f_{m,n}=1$ *if* $m, n \in G_i$ (6.28)

otherwise,

$f_{m,n}=0$.

Since, the size and position of the group *Gi* can be chosen arbitrarily, the filter F can be applied to an arbitrary section in the near field amplitude data. Thus the filtering procedures have been verified mathematically. The next step is to decide appropriate filter(s) to examine the role of microwave structures in a DUT (including substrate) for the far-field formation. Especially, these three filters are very useful for array structures.

As mentioned earlier, 3 types of filters used for the far-field characterization of the Ka-band quasi-optical amplifier array will be used. Filter 1 (*F1*) is designed to isolate a unit cell in the DUT. Once the size of *F1* is decided, it can be placed anywhere on the near field data. The second filter (*F2*) is designed to isolate certain sections in the near-field data where the amplitudes are stronger than other areas. Usually, *F2* isolates the main radiating structures in the arrays. Specifically, *F2* isolates sections where the amplitude is equal or higher than 10 % of the global maximum value (or ≥ -20 dB in power). The last filter (*F3*) has the property to isolate certain sections in the near-field data where the amplitudes are lower than other areas. Typically, the near field data applied by *F3* include structures that radiate very low electric fields such as feeding lines and substrate. The criterion of *F3* is equal or lower than 10 % of the global maximum value (or ≤ -20 dB in power). Actually *F3* is designed to be the complementary filter to *F2*. By using this approach, it is very convenient to prove the validity of the filter design. The characteristics of the three filters are summarized in table 6.1.

Filter type	Specification	Function
F1	Decided by DUT geometry	Isolate unit cell in the DUT
F2	Isolate areas where Amplitude ≥ 0.1×global Max (≥-20 dB in Power)	Isolate areas where the radiating field is stronger than other areas. Usually, *F2* isolate main radiating structures in DUT.
*F3**	Isolate areas where Amplitude ≤ 0.1×global Max (≤-20 dB in Power)	Isolate areas where the radiating field is lower than other areas such as feeding lines or substrate.

**F3* is designed to be complementary filter of *F2*.

Table 6.1: Summary of filters used in the verification process.

To verify the filter *F1*, the transformed results are compared with analytical solutions. Since most of the unit elements in arrays are well defined analytically, the comparisons with analytical solutions are the most efficient way to verify filter *F1*. For example, *F1* is applied to the near-field pattern obtained from the Ka-band 6×6 quasi-

optical amplifier array that has slot antennas as unit radiating structures. Then the transformed far field is compared with the analytical solution for a slot antenna. Figure 6.22 shows excellent agreements between the transformed far field (after applying *F1*) and analytical solution in both E- and H-plane. Thus we can conclude that filter *F1* is reasonably designed and successfully reveals a true far-field pattern.

For the verification of the filter 2 (*F2*) and filter 3 (*F3*), a slightly different approach is taken than the verification of *F1*. Since *F2* and *F3* are designed mathematically, it is very difficult to perform actual measurements under the same condition of filter *F2* or *F3*. Thus, mathematical verification is more appropriate for *F2* and *F3* by using the property that *F2* and *F3* are complementary to each other.

The transformation (without filtering) has been verified in section 6.6.1. Thus we can assume that the transform itself reveals true far-field patterns. Based on this assumption, we can derive logical proof procedure based on variables such as

$$\begin{aligned} \mathbf{E}^{ff} &: \textit{transformed far-field without filtering} \\ \mathbf{E}^{ff}_{F2} &: \textit{transformed far-field with fliter2} \\ \mathbf{E}^{ff}_{F3} &: \textit{transformed far-field with fliter3.} \end{aligned} \tag{6.29}$$

The far fields $\mathbf{E}^{ff}_{F2}$ and $\mathbf{E}^{ff}_{F3}$ are complementary to each other since they are obtained from complementary filters *F2* and *F3*. In other words, the relationship between three far field groups in Eq. 14 can be expressed as

$$\mathbf{E}^{ff} = \mathbf{E}^{ff}_{F2} + \mathbf{E}^{ff}_{F3}. \tag{6.30}$$

Since the left side of Eq. 6.30 is true (from section 6.6.1), the two terms in the right side have to be true if the equation itself is true.

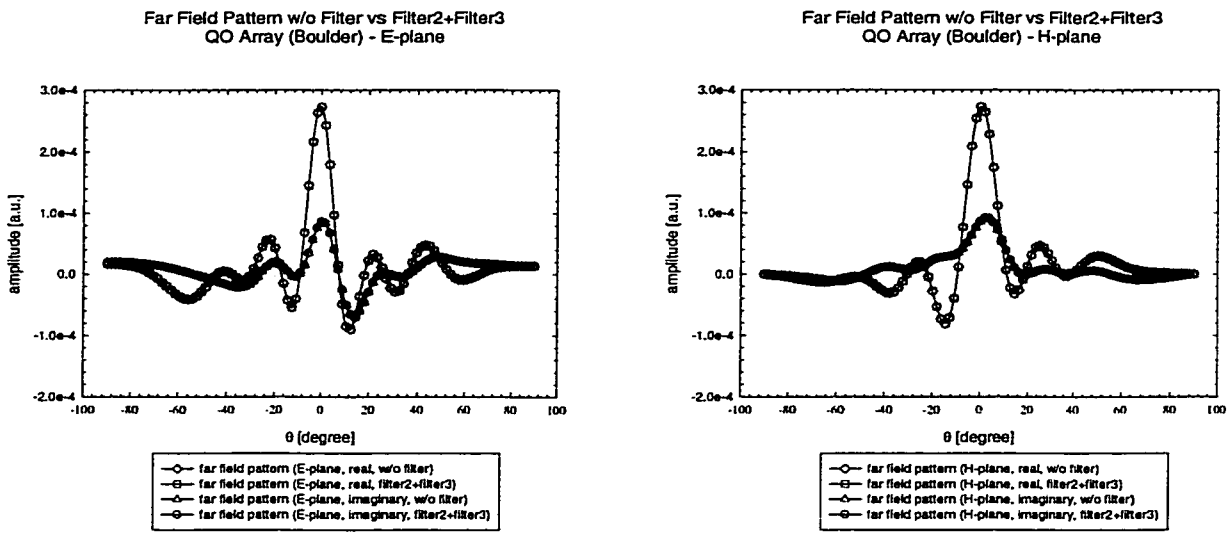

(a) (b)

Figure 6.30: Comparison between far fields $\mathbf{E}^{ff}$ and $\mathbf{E}^{ff}_{F2}+\mathbf{E}^{ff}_{F3}$ (Eq. 6.30) in complex field form. (a) E-plane and (b) H-plane.

Figure 6.30 displays perfect agreement between the far field transformed from the original near-field data (without filtering procedure) and composite far fields that are obtained from the transformation after applying *F2* and *F3* on the original near field data.

Based on the facts that Eq. 6.30 is true and the left side of the equation ($\mathbf{E}^{ff}$) is true, the two terms in the right side of the equation ($\mathbf{E}^{ff}_{F2}$, $\mathbf{E}^{ff}_{F3}$) have to be true. Thus the validity of filter *F2* and filter *F3* are successfully proven.

6.7 Summary

Based on the high-resolution near-field amplitude and phase data obtained from the electro-optic field mapping system, a new near- to far-field transformation procedure was developed. In the course of the transformation procedure, the unit element in the near-field data was able to be considered as an infinitesimal magnetic dipole due to the small size of the unit cell with respect to the operation wave length. As a result, the near-

field data was treated as two-dimensional magnetic-dipole arrays for the far-field calculation. The transformed far-field displayed excellent agreements with the theoretically obtained patterns for an ideal short dipole and rectangular aperture.

For the actual applications, a near- to far-field transition technique has been applied to the amplitude and phase near-field data that were obtained by electro-optic field mapping for a 4-GHz microstrip patch antenna. In the course of the transformation, two filters were introduced to isolate the effects of the two radiating edges of the patch antenna.

Also, the transformation technique has been applied to a Ka-band passive microstrip patch antenna array and quasi-optical amplifier array. The transformation technique provided accurate far-field patterns. Furthermore, by introducing various filtering procedures, the effects of the parasitic radiation structures were examined.

At the end of the chapter, the transformation procedure and filtering processes have been verified by using mathematical and experimental methods.

In conclusion, the near- to far-field transformation based on the near field data obtained by the electro-optic field mapping system can be one of the most comprehensive far-field analysis techniques that can provide a lot of important information by revealing the relationship between near-fields and their contributions to far-field formation. Especially, by introducing appropriate filtering procedures, the contributions from certain areas of interest to the far-field formation can be accurately examined.

CHAPTER 7

NEAR-FIELD WAVE-FRONT RECONSTRUCTION (WFRC)

7.1 Introduction

The near-field amplitude and phase information obtained by the fiber-based EO mapping system may play an important role in a variety of areas such as design, fault isolation, and overall performance verification of the micro/mm-wave structures including particular ones inside of the closed space.

However, since the fiber-based EO system is able to provide incomparably accurate, high-resolution near-field data, it is also possible to expand the application area of the system to the next level based on the first-hand raw amplitude and phase information. The accurate near- to far-field transformation [72] can be one of the typical secondary applications of the fiber-based EO system.

On many occasions, an accurate radiating wave front may provide important information about the properties of the radiating wave by visualizing the actual shape of the radiation wave. Furthermore, in particular areas such as designing quasi-optical amplifier arrays [73][74], it is crucial to take into account the incident (input) wave shape. By using the high-resolution 2-dimensional amplitude and phase data obtained from fiber-based EO system, accurate wave fronts can be successfully reconstructed (wave front reconstruction-WFRC procedure).

7.2 Mathematical Derivation of WFRC Process

Figure 7.1 displays the 1-dimensional schematic used in the theoretical formula development. The series of parallel arcs represent discretized wave fronts. Also, the straight line marked as x_1 and x_m at each end represents an experimental 1-dimensional scanning path. A small portion of the path is magnified in the circle.

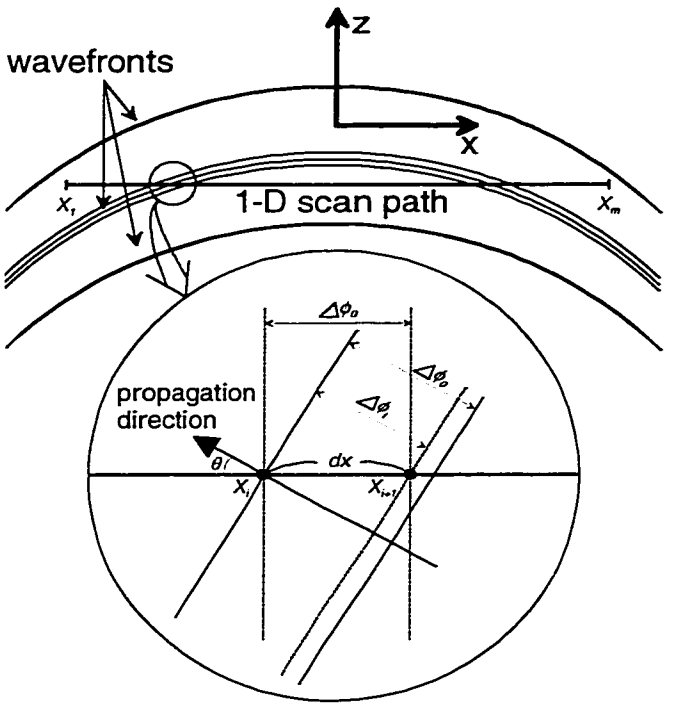

Figure 7.1: Diagram used for the development of the 1-dimensional wave front reconstruction (WFRC) formula. The series of arcs represent wave fronts that have different phase conditions. A scan path is displayed by the straight line marked with X_1 and X_m at both ends. The close up figure at certain positions of the scan path is detailed in the circle.

Two adjacent measurement points x_i and x_{i+1} separated by distance dx are marked with thick dots on the scanning path in the magnified circle. Because of its curvature shape, the angle between the wave front and the scanning path can have values from 0° to

90°. These two values mean either the wave front is parallel (0°) or perpendicular (90°) to the scanning path. The two vertical dash-dotted lines that pass the two measurement points represent the wave fronts in one of these two extreme conditions that the wave fronts have perfect vertical alignment with respect to the scanning path.

If the wave fronts are vertically aligned to the scanning path, the expected phase difference between the two measurement points $\Delta\phi_0$ can be expressed as

$$\Delta\phi_0 = 2\pi\frac{dx}{\lambda} \tag{7.1}$$

where λ is the operating wavelength.

The actual measurement situations can be found between the two extreme conditions. Thus, the generalized wave fronts alignment can be displayed as Fig. 7.1. The propagation direction of the wave (arrow in Fig. 7.1) is assumed to be at an arbitrary angle θ_i degree off from the measurement path. Since the wave fronts are not perpendicular to the scanning path any more, the expected phase different between the two measurement points is changed as follows.

$$\Delta\phi_i = \Delta\phi_0\cos(\theta_i) \tag{7.2}$$

It is obvious that Eq. 7.2 becomes identical to Eq. 7.1 if the angle θ_i is 0° (wave front $\perp$ scanning path). In the opposite case, if the wave front is parallel to the scanning path (θ_I = 90°), the phase difference between two measurement point should disappear.

From Eq. 7.1 and 7.2, the angle θ_i can be expressed as

$$\theta_i = \text{acos}\left(\frac{\Delta\phi_i}{\Delta\phi_o}\right)$$
$$= \text{acos}\left(\frac{\lambda\ \Delta\phi_i}{dx\ 2\pi}\right) \tag{7.3}$$
$$\text{where } \Delta\phi_i = \phi_{i+1} - \phi_i$$

where $\Delta\phi_i$ represents the phase difference obtained from the actual measurement phase data ϕ_i and ϕ_{i+1}.

Since the 1-dimensional scanning model is used for this derivation, the resultant wave front shape can be expressed in the x-z coordinate systems. The two dimensional coordination can be expressed as

$$x_i = \lambda\frac{\phi_i}{2\pi}\cos(\theta_i), \text{ and}$$
$$z_i = \lambda\frac{\phi_i}{2\pi}\sin(\theta_i) \tag{7.4}$$

The identical procedure can be applied for the y-direction 1-dimensional scanning model. Finally, the two orthogonal 1-dimensional results are combined to obtain a complete wave front expressed in 3-dimensional space as follows

$$x_{i,j} = \left(\frac{\lambda}{2\pi}\right)^2 \frac{\phi_{i,j}\cdot\left(\phi_{i+1,j} - \phi_{i,j}\right)}{dx}$$
$$y_{i,j} = \left(\frac{\lambda}{2\pi}\right)^2 \frac{\phi_{i,j}\cdot\left(\phi_{i,j+1} - \phi_{i,j}\right)}{dy} \tag{7.5}$$
$$z_{i,j} = \lambda\frac{\phi_{i,j}}{2\pi}\sin\left(\text{acos}\left(\frac{\lambda}{2\pi\cdot dx}\cdot\frac{\phi_{i+1,j} + \phi_{i,j+1} - 2\cdot\phi_{i,j}}{2}\right)\right)$$

6.3 WFRC Application

The WFRC procedures are applied to the horn antenna results obtained by utilizing the fiber-based EO system. Detailed information about the measurement can be found in Chapter 5 of this thesis. However, for convenience of reading, the near-field results are briefly repeated herein.

Figure 7.2 shows the Ka-band horn antenna used as a DUT during the measurement. Due to the excellent measurement flexibility of the fiber-based EO field mapping system, the near-field in a plane that was two wavelengths from the aperture within the interior of the Ka-band horn antenna (plane II) was scanned, as well as the aperture plane (plane I).

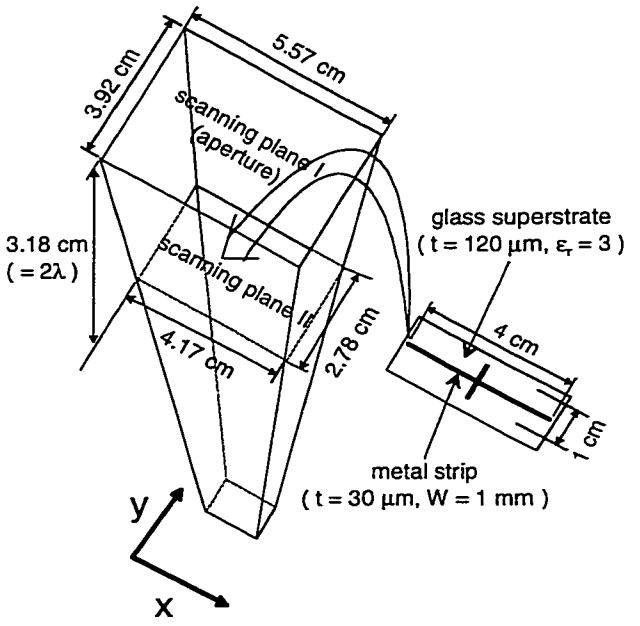

Figure 7.2: Ka-band horn antenna with the field scanning planes. The metal field scattering structure is also displayed.

Also, a field scattering metal structure fabricated on a thin glass substrate is displayed at the side of the horn. Further information on the metal structure is mentioned in Chapter 5.

Figure 7.3 displays measured electric field amplitude and phase distributions in the plane I and II.

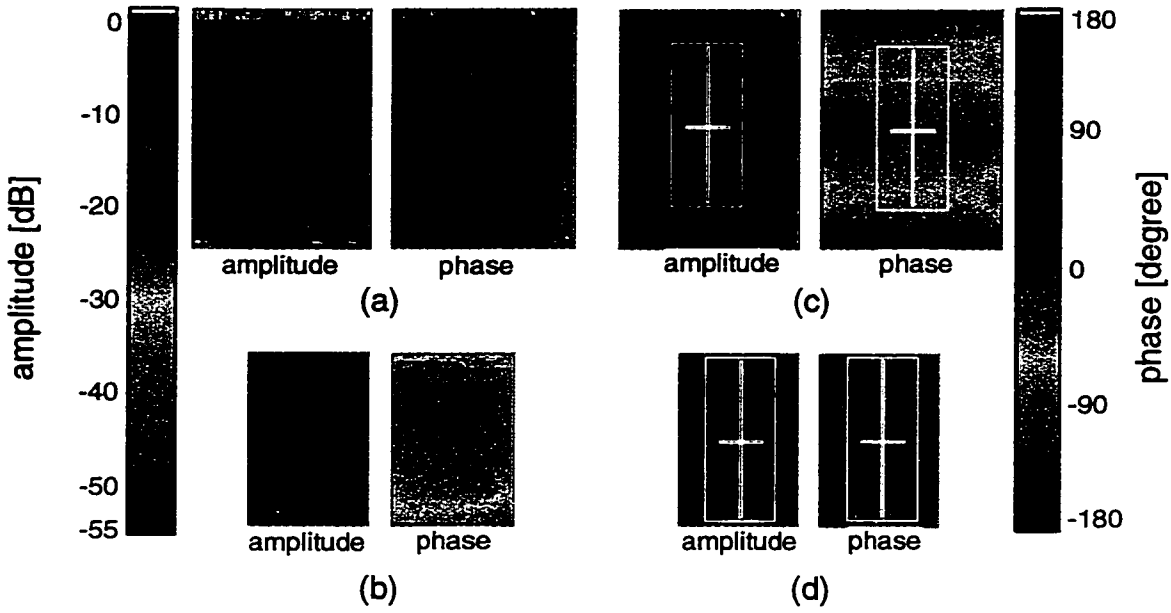

Figure 7.3: Two-dimensional electric-field amplitude (normalized) and phase (in degree) mapping results. The results show the field distributions at (a) the plane I and (b) the plane II without the metal structure while (c) and (d) display the field patterns with the metal structure at the plane I and II. The boundary of the metal structure and glass superstrate is overlayed with white lines in (c) and (d).

The step sizes for the scanning were 777 × 1108 μm along x and y directions for the aperture plane (plane I, Fig. 5.18) and 518 × 803 μm for the plane inside of the horn (plane II, Fig. 5.18) with 50 steps for both x and y directions. The operating frequency

during the scans was 18.883 GHz, and the elapsed time for one complete scanning was about 30 minutes.

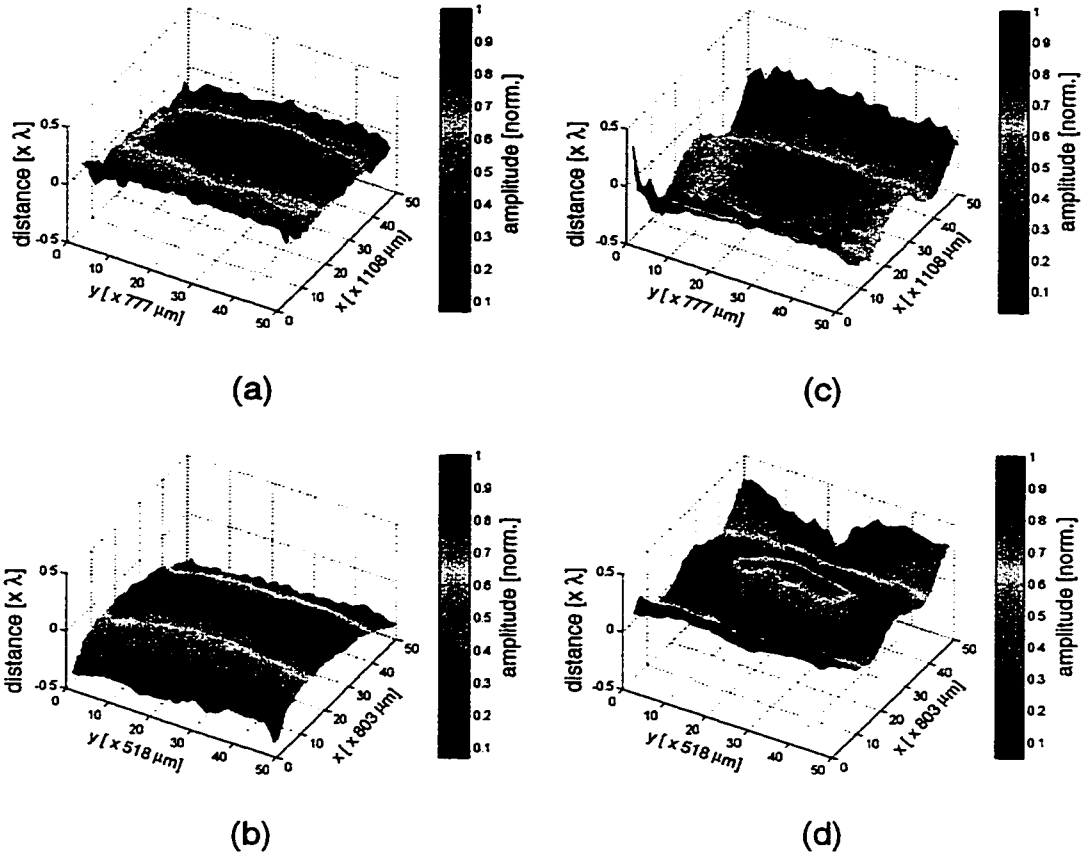

Figure 7.4: The reconstructed wave fronts for the horn antenna shown in Fig. 7.2 at (a) the plane I and (b) the plane II without the metal structure. The calculated wave fronts with the metal structure at the plane I and plane II are displayed in (c) and (d), respectively. The x- and y-axes correspond to the actual 2-dimensional scanning positions, and the z-axis represents the distance of the wave front from the scanning plane with respect to the operating wavelength λ (1.59 cm). Also, the normalized amplitude in a color scale is mapped on each wave front.

Based on the near-field data, the WFRC has been performed according to Eq. 7.5. Figure 7.4 displays the WFRC results at the aperture (plane I in Fig. 7.2) and the plane 2 wavelengths inside of the horn (plane II in Fig. 7.2) without and with the metal insertion structure. The wave front shapes are displayed by x- and y-scanning position versus the relative distance with respect to the wavelength λ (1.59 cm) in z-axis. Also, the normalized amplitude information is overlapped on the wave front surface in color scale. The electric field in the plane II displays (Fig. 7.4(b)) a cylindrical shape wave front, and the peak amplitude exists at the center of the wave front along the y direction. However, the wave front in the aperture (Fig. 7.4(a)) displays very flat shape with respect to the wave front in the plane II. The results demonstrate that the electric field is transformed from the cylindrical wave to the plane wave as it travels along the horn, and it corresponds very well with the principle of the horn antenna [40].

The wave fronts display severe distortion of the shape by the presence of the metal structures as shown in Fig. 7.4(c) and (d). Unlike the arc shape wave front in Fig. 7.4(b), the wave front in the plane II is distorted into a "W" shape along the x direction by the metal structure (Fig. 7.4(d)). Also, the amplitude null created by the co-pol metal strip is observed at the center of the wave front. At the aperture plane (plane I), the null at the center is no longer detected while the overall wave front shape is maintained. The WFRC results reveal the effects of the co-pol metal strip on both amplitude and phase. The field blocking by the co-pol metal strip was expected before the experiments, and clearly confirmed by the amplitude distribution. However, considering the narrow width of the metal strip (1.0 mm, 0.062λ), the effect on the phase distribution is much more significant than the expectation. However, the amplitude disturbance is no longer detectable in the electric field at the aperture. The results reveal that only near-field mapping can correctly identify the field disturbance source, and it demonstrate the importance of the near-field mapping. Also, as expected, the effect of the cross-pol metal branch is not observed on both planes.

The unique WFRC technique based on the high-resolution near-field data can be a very useful to design and analyze various radiating structures by providing an accurate wave radiation characteristics. Furthermore, by utilizing the fiber-based EO field mapping system, the coverage of the WFRC technique can be extended to the structures inside of the closed space.

6.4 Summary

A unique wave front reconstruction (WFRC) technique based on the electro-optically obtained near-field data was introduced. The WFRC technique made it possible to observe accurate wave front shape in 3-dimensional space. Furthermore, by combining with the fiber-based EO system, the wave front inside of the horn was successfully obtained.

By using the WFRC procedure based on the fiber-based EO field mapping system, the electric field transition at the interior of a Ka-band horn antenna was examined. Also, an extrinsic metal structure was inserted into the horn, and the distorted field distributions were measured in the aperture and inside of the horn.

In conclusion, the WFRC technique can be very useful analysis tool for various radiating structures by providing accurate wave front information in the near-field range. As a result, the WFRC is expected to contribute for analysis of closely placed radiating structures. Especially, associated with the fiber-based EO field mapping system, the WFRC technique can be applied to micro- and millimeter wave structures in enclosures.

CHAPTER 8

PHOTOCONDUCTIVE PROBING OF MICROWAVE POTENTIALS INSIDE A SiGe MMIC

8.1 Introduction

A number of different techniques for the measurement of the high-speed or high-frequency performance internal to integrated circuits have been developed in the past. In particular, the use of picosecond and femtosecond pulsed lasers has lead to electro-optic and photoconductive [75]-[77] measurement systems with high bandwidth, low invasiveness and high spatial resolution. Recently, the capabilities of the photoconductive technique have been significantly extended by the use of external, high-impedance sampling probes [78]-[82]. Among these, a micromachined photoconductive probe (PC probe) consisting of a low-temperature-grown-GaAs (LT-GaAs) active optoelectronic sampling head has been demonstrated to have excellent performance in conducting time-domain measurements in digital integrated circuits [23][24]. In this chapter, the photoconductive probe technique is applied for the first time, using the micromachined LT-GaAs PC probe, for frequency-domain measurements of potentials internal to an analog MMIC. It is also the first time that electrical characteristics at internal nodes of a SiGe circuit have been probed. The circuit investigated is a three-stage amplifier. The network analyzer measurements initially performed after fabrication showed amplification in good agreement with the predictions of the CAD software used to design the circuit. The actual photoconductive measurements were carried out later after degradation of the circuit became obvious. One goal of this work was then to provide

results of the circuit performance at internal nodes (*e.g.*, before and after each amplifier stage) to investigate the origins of this degradation.

8.2 Electro-optic and Photoconductive Measurements

The electro-optic (EO) and photoconductive (PC) sampling methods share same common ground in terms of utilizing short pulse laser to detect high frequency electrical signal. The EO technique relies on the optical property modulation due to the presence of electric field in electro-optic material, while the PC method utilizes electrical resistance variation of a photoconductive material due to the optical illumination. Basic principles of these two methods are explained in Chapter 1 of this thesis.

The two techniques can perform similar measurements, however, at the same time, the two methods have their own unique advantages with respect to the application. For example, both techniques have a time-domain short-pulse measurement capability due to their extremely fast responses. Also, both techniques can measure high-frequency signal at internal points of micro- or millimeter wave circuitry in frequency domain. The EO probe basically responds to the electric field near the radiating structures – including guided waves, and the resultant lead out signal from the EO probe is in the form of optical beam power modulated by the electric field. Eventually this optical signal is converted to voltage signal by a photodiode. As a result, the EO technique does not require direct contact on a DUT structure.

Since the PC probe detects potential variation of the DUT, it requires direct contact on a DUT. The contact can be made directly on exposed metal structure where the signal propagates or on the dielectric passivation layer on the metal. However, for the absolute potential measurement, it is necessary to make direct contact on the metal structure.

In special application, the EO probe can also detect absolute potential with an additional metal tip that can make direct contact on exposed metal in a DUT and appropriate calibration procedure. Also, the PC technique can be associated small antenna structure to measure an electric field distribution rather than potential measurement [83]. However, these applications are preferred only special applications since the extra metal tip (for EO method) and antennas (for PC method) can limit the original capability of the EO and PC techniques.

The EO technique is more preferred for the measurement of radiating structures such as antennas or arrays where the electric field distribution is more important than potential variation in DUTs. Also, the EO method can be used for the diagnosis of integrated circuitry. On the contrary, the PC technique has its advantages to the EO method for the highly integrated circuitry where the absolute potentials at certain points are crucial for the circuit performance. In general, the overall field distributions of a DUT can be easily obtained by the EO method, while it is more advantageous to use the PC technique to obtain point to point absolute potential values.

8.3 Fabrication of Photoconductive Probe

For the explanation of the basis of the photoconductive (PC) probe, it is very important to discuss the properties of the semiconductor material used as a substrate of the PC probe, because the performance of the probe is mainly determined by the carrier life time of the substrate. In this work, a low-temperature-grown GaAs (LT-GaAs) epitaxial layer is utilized as a substrate of the PC probe.

The LT-GaAs layer is grown by the molecular beam epitaxial (MBE) process at a temperature around 200 °C, and a post-annealing procedure follows at an temperature of 600 °C under arsenic overpressure conditions. As an additional process, an $Al_xGa_{1-x}As$ layer of several thousands-Å is often deposited prior to the LT-GaAs growth, and this

serves as an etch-stop layer during the PC probe fabrication. The most attractive feature of the LT-GaAs as a substrate of the PC probe is its extremely short carrier lifetime. The short carrier lifetime is due to a high density of defects that serve as carrier trapping centers in the band gap. Once free carriers (in the conduction band) are generated in the LT-GaAs crystal, the majority of the carriers are trapped in the recombination centers caused by defects, and transferred into the valance band via electron-hole recombination process. As a result, the lifetime of the free carriers in the LT-GaAs is much shorter than that of normal GaAs, and the carrier lifetime can be less than 1 ps [22].

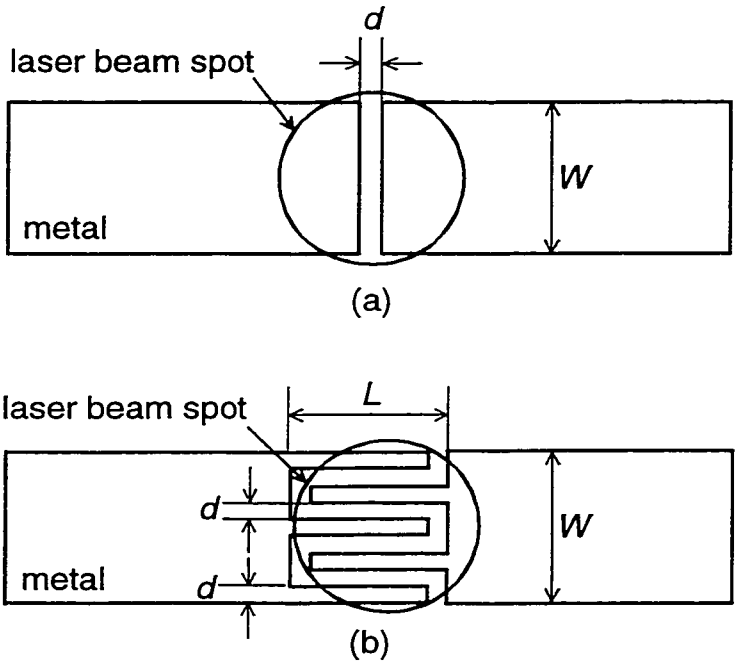

Figure 8.1: Comparison between (a) a straight gap gate and (b) interdigited gate. The beam spot is displayed with circle.

Another important factor that has an effect on the PC probe performance is the geometry of the metal-semiconductor-metal (MSM) gate. Since the PC probe is turned on and off by the laser pulses, an interdigited finger structure is the preferred geometry for

the MSM gate because the effective interaction area to the laser beam can be significantly increased in those structures. Figure 8.1 demonstrate the effectiveness of the interdigited structure with respect to the simple, straight gap-type gate with an identical laser beam spot.

From Fig. 8.1, the effective gate area where the laser interacts with the semiconductor (i.e., LT-GaAs) can be obtained as

$$\begin{aligned} &A_g = d \cdot W \text{ : straight gap} \\ &A_g = d \cdot W \cdot (N-1) \text{ : interdigited gap} \\ &\text{where} \\ &N\text{: number of interdigited fingers} \end{aligned} \tag{8.1}$$

In Eq. 8.1, the width of the finger is assumed to be same as the size of the gap (d).

LT-GaAs (200℃)	1.1 μm
$Al_{0.7}Ga_{0.3}As$ (580℃)	5000 Å
GaAs (580℃)	5000 Å
GaAs substrate	600 μm

Figure 8.2: Cross sectional view of the LT-GaAs sample used in the PC probe fabrication. The growth temperatures are shown in the brackets.

For the actual fabrication of the PC probe, an LT-GaAs sample with a 5000-Å thick $Al_{0.7}Ga_{0.3}As$ etch-stop layer was used as the PC probe substrate. The cross sectional

view of the material including the thickness and growth temperature of each layer is displayed in Fig. 8.2.

The PC fabrication starts with the top LT-GaAs layer patterning. To form a teardrop shape pattern, a positive photoresist PR 1813 is spin coated on the top surface. Then the PR is exposed and developed by using a standard photolithography process. After the PR patterning, the LT-GaAs is etched in the etchant composed of H_3PO_4:H_2O_2:H_2O with 3:1:25 volume ratio. The elapsed time for the etching process is about 3 minute for the 1-μm thick LT-GaAs layer. After the etching process, the PR 1813 is spin coated on the top for the metalization mask patterning. Again, photolithography techniques are utilized for the patterning. After the patterning, Ti/Au layers are deposited on the sample by using an evaporation method, and the metalized sample is soaked in acetone to remove metals deposited on the PR layer (metal lift-off process). Now, the processes for defining the PC probe are finished. However, at this stage, the PC probes are still on the $Al_{0.7}Ga_{0.3}As$/GaAs layers.

After the topside processes, the backside of the sample is mechanically lapped in order to reduce the thickness of the substrate. After the lapping process, the final thickness of the sample is reduced to 300 μm. Since the GaAs substrate has most of the thickness of the sample, the lapping is exclusively applied on only the GaAs substrate. This additional lapping process really contributes to a reduction in the backside etching time.

After the lapping, the sample is mounted facedown on a glass substrate using a small amount of black wax, and soaked in the etchant composed of NH_4OH:H_2O_2 with 1:24 volume ratio. For the uniformity of the etching process, a magnetic stirrer is used during the backside etch. Since there is a 5000-Å thick $Al_{0.7}Ga_{0.3}As$ etch-stop layer between the LT-GaAs and GaAs layer, the etching process is automatically stopped at the $Al_{0.7}Ga_{0.3}As$ layer. The backside-etching rate is about 167 μm/hour.

Now, the sample has exposed $Al_{0.7}Ga_{0.3}As$ layer on the top, while the actual PC probes are protected by black wax between the $Al_{0.7}Ga_{0.3}As$ and glass substrate. The $Al_{0.7}Ga_{0.3}As$ layer is then removed in an HF solution ($HF:H_2O$ = 1:5). Finally, the PC probes are released from the glass substrate in the hot acetone.

8.4 Measurement System and Device under Test

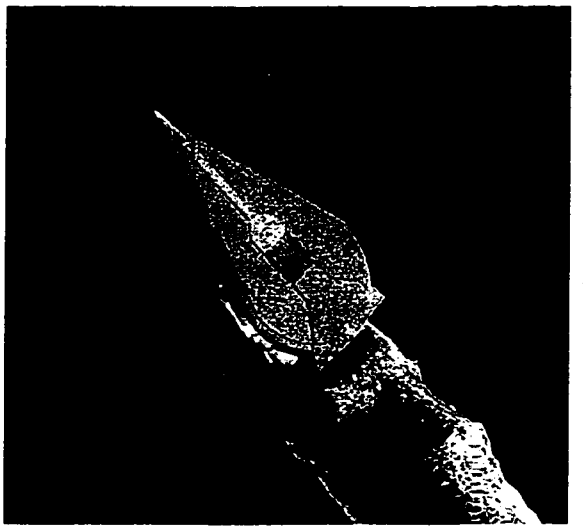

Figure 8.3: Photoconductive sampling probe, SEM image. The probe is 130 μm × 230 μm (at its widest points) by 1 μm, The finger size of the interdigital MSM switch is 1.5 μm.

The PC probe employed in this work is shown in Fig. 8.3. It consists of an epitaxial layer of micromachined, low-temperature-grown GaAs attached to a single-mode optical fiber. The fiber is beveled at 45 ° where it meets the probe so that 100-fs laser pulses from a Ti:Sapphire laser may be coupled, after total-internal reflection, to a 30 × 30 μm^2 interdigitated photoconductive sampling gate on the probe [80]. A 3.5-ps time response, resulting in a bandwidth exceeding 100 GHz, and a sensitivity of 1

$\mu V/(Hz)^{1/2}$ [24] have been demonstrated for this probe. The width of a metal tip extending out past the end of the probe is 7 μm, which is sufficient to measure the interconnects within typical microwave circuits.

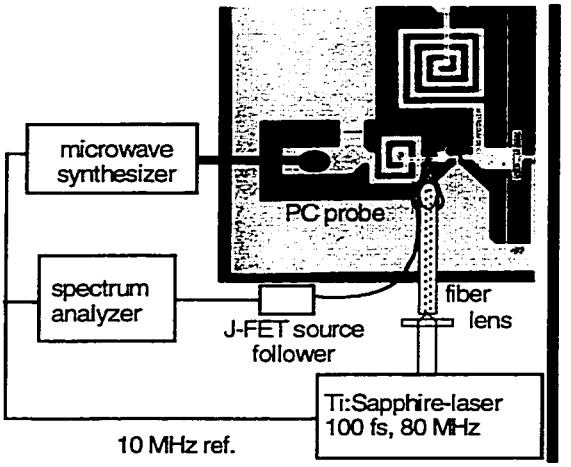

Figure 8.4: Schematic of the photoconductive probing setup, (the probe and circuit are drawn to scale).

The principal experimental layout is sketched in Fig. 8.4. A heterodyne-mixing scheme is applied for the frequency-domain measurements, similar to the EO probing technique. This method requires that the signal to be measured has a frequency f_m of:

$$f_m = n \cdot f_{rep} \pm f_{IF}, \tag{8.2}$$

where f_{IF} is an intermediate frequency, n an integer, and f_{rep} the laser pulse repetition frequency. The circuit rf signal is downconverted to the intermediate frequency and can then be measured using low-frequency electronic instrumentation, *e.g.*, a spectrum analyzer or a lock-in amplifier for low noise detection. It is also worth noting that this IF is the only signal that needs to appear at the PC probe output, and thus high-speed

connections from the probe to the post-processing electronics are not required. In addition, the Ti:Sapphire laser used in our setup allows phase locking of the laser pulse repetition rate and the microwave source, so that the in-circuit electrical signal can be determined in amplitude and phase.

The photoconductive probe has an off-state resistance of 100 MΩ, which is comparable to the input impedance of commonly used readout instruments (*e.g.*, 10-100 MΩ for a lock-in amplifier). Since this embodiment would lead to a current flow and to charge draining from the test point, the probe is instead integrated with a JFET source follower having an input impedance of 1 TΩ and an input capacitance of 3 pF. This then acts as a readout circuit. The circuit avoids charge drainage from the DUT (currents are reduced to about 3 pA), so that measurement with minimal invasiveness is achieved. Moreover, the current measurement is converted to a voltage measurement. Due to the small amount of charge necessary to load the source follower input, the actual voltage level is built up in a short time, allowing a higher modulation bandwidth and the ability to measure absolute voltage levels. Additionally, the high input resistance of the source follower allows the instantaneous dc voltage at the probe node to be determined at the output of the source follower, and thus both ac and dc signals can be measured simultaneously.

The circuit examined (Fig. 8.5) using the PC probe is a three-stage amplifier based on Si/SiGe HBTs and micromachined lumped elements as matching devices. The circuit is found by conventional network analysis to have a maximum gain of 12.6 dB at 11.1 GHz [84], as measured through an on-wafer probe at the end of the third stage.

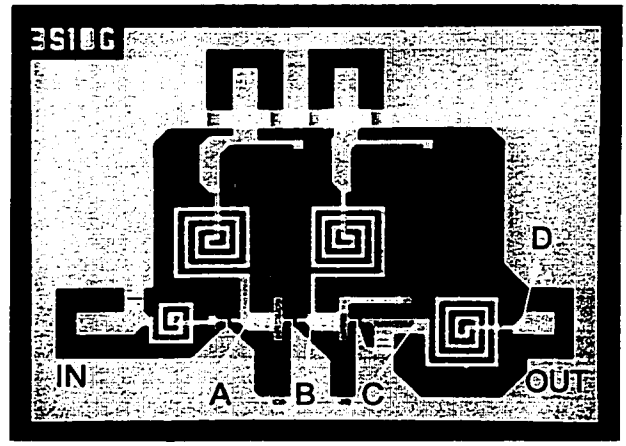

Figure 8.5: Three-stage SiGe amplifier, chip size: 1.15 x 0.84 mm; measured nodes are marked A-D.

As mentioned in Chapter 1 of this thesis, the EO field mapping method can be utilized for this type of internal measurement due to its high-resolution measurement capability. However, for the EO measurement, a certain amount of space is required to move the EO prove over a DUT because of the size of EO probe. As shown in Fig. 8.5, the input, output and dc bias ports are placed in very small distances. As a result, in this case, the PC probe is more advantageous than the EO probe.

Figure 8.6 displays this result, as well as a simulation result obtained using HP EEsof's LIBRA 5.0. A good agreement is observed between the network analyzer and LIBRA results. A second measurement of the circuit performed approximately 6 months after the processing revealed a degradation of the circuit performance. At this time, the amplification was determined to be only 7 dB. Probably, the degradation occurred because of excessive bias applied (by mistake) to the circuit during additional measurements.

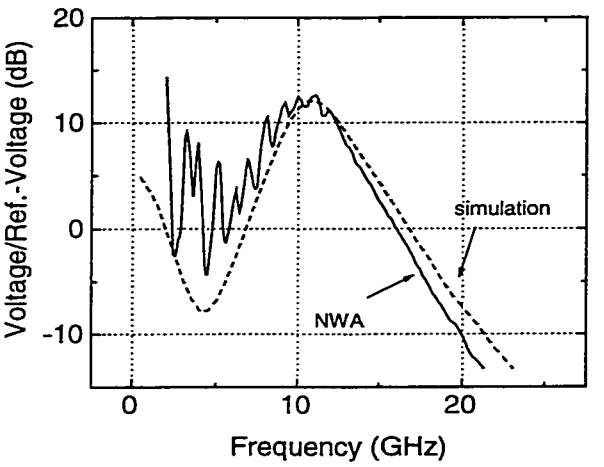

Figure 8.6: Network analyzer measurement and simulation of the functioning circuit.

8.5 Simulation Procedure

The potentials at the circuits interior were also determined using HP EEsof's LIBRA 5.0. In order to accomplish this, test points were inserted at the circuit nodes, and the potentials were calculated using the harmonic balance method. The calculated voltages were normalized with respect to the input voltage of 0.225 mV (0 dBm at 50 Ω). Figure 8.7 shows the schematic of the circuit with the test points.

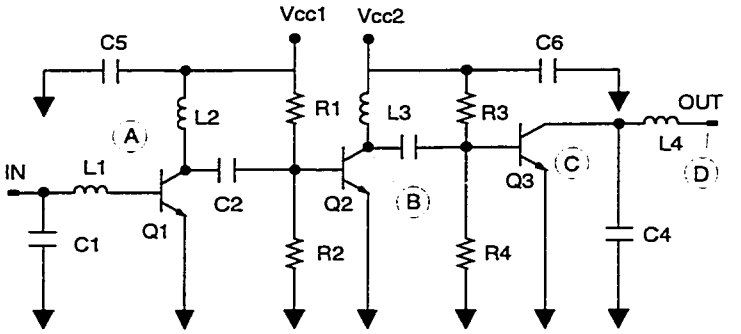

Figure 8.7: Circuit diagram including locations of the test points A, B, C, and D.

8.6 PC Probe Measurement Calibration

Potentials were measured using the PC probe at the circuit nodes shown in Fig. 8.7 (output of each of the three stages, plus output of the whole circuit) while an RF input of 0 dBm was applied. To remove the effects of a resonance in the frequency response of the probe, which appears around 10 GHz, as well as the frequency-dependent transmission properties of the microwave cables and connectors used, a calibration measurement was performed. The calibration standard used was a coplanar waveguide with a characteristic impedance of 50 Ω and a 50-Ω thin film resistor matching termination. A 0 dBm RF input was applied in this instance also. All in-circuit measurements presented are normalized to the values of this reference measurement. The calibration is in fact not perfect, as the ripple pattern in the measurements reveals, because the source and load mismatches are not corrected. However, for the measurements inside the circuit, the errors induced by these mismatches are not significant due to the high isolation provided by the active devices. A full vector error correction is possible with additional measurements of other calibration standards. Figure 8.8 shows the gain of the circuit as determined both by the second network analyzer measurement (of the circuit after degradation) and by the photoconductive measurement. A very good agreement is observed in this comparison, providing strong evidence of the high degree of accuracy that can be expected from the photoconductive probe measurements.

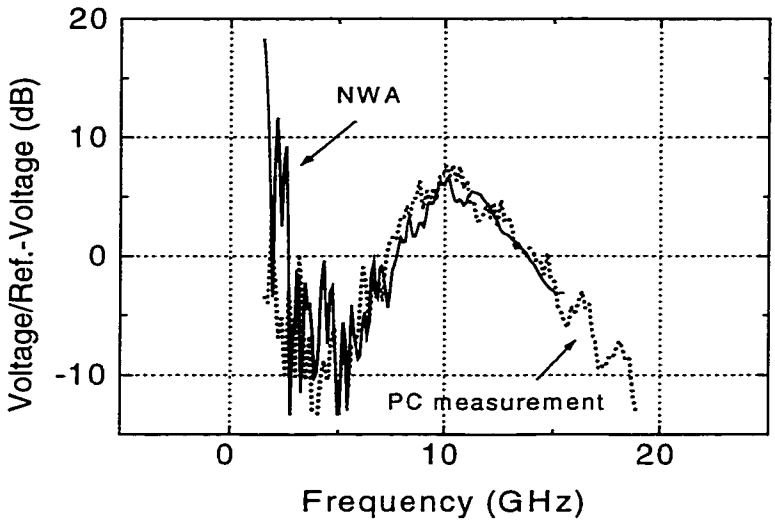

Figure 8.8: Results of NWA measurement (S_{21}) and photoconductive probe measurement of the output of the circuit at pos. D.

8.7 Results

Since LIBRA accurately simulates the output of the circuit as it operated originally, we can reasonably assume that it also simulated the correct response at the circuit internal test points when the circuit was initially fabricated. Thus we can use comparisons between the PC probe in-situ measurements and the LIBRA simulations to determine how the internal circuit characteristics have changed. These measurements can then also reveal which amplifier stages are responsible for the degraded performance.

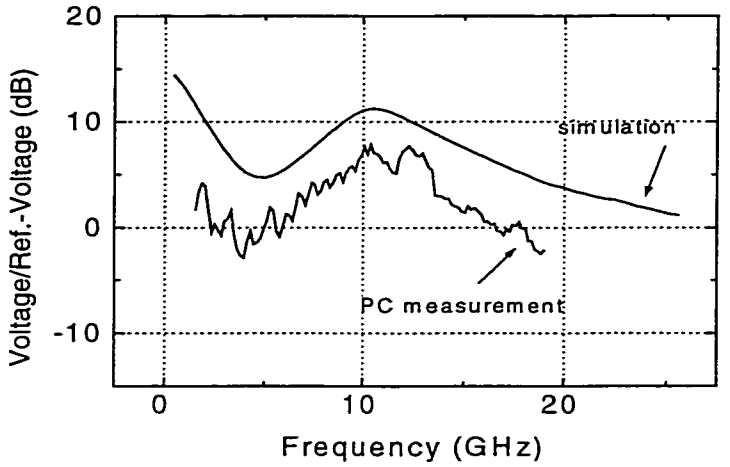

Figure 8.9: Measured and simulated voltage at node A (output of the first stage).

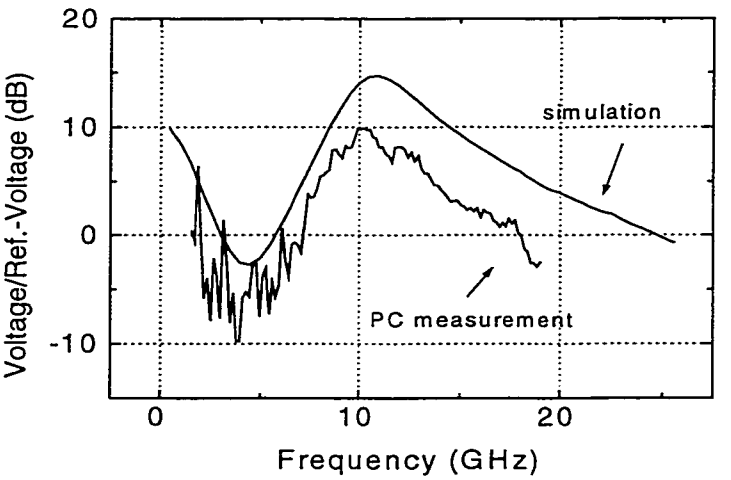

Figure 8.10: Measured and simulated voltage at node B (output of the second stage).

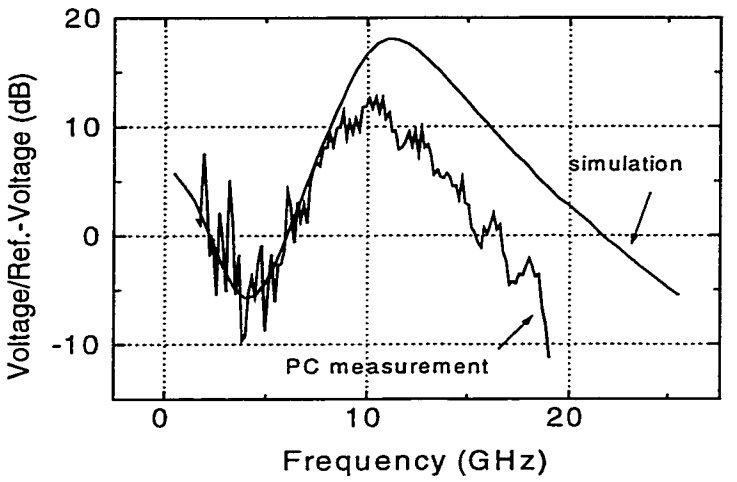

Figure 8.11: Measured and simulated voltage at node C (output of the third stage).

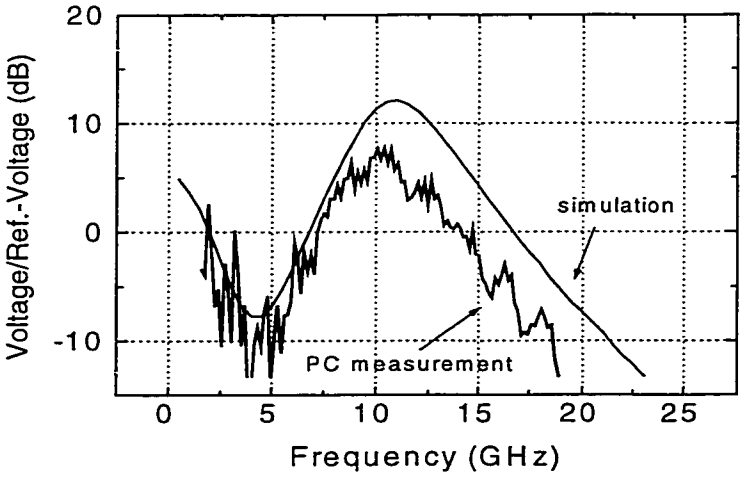

Figure 8.12: Measured and simulated voltage at output of the circuit at node D.

Figure 8.9 through Fig. 8.12 show voltages both measured via the PC probe and calculated with LIBRA for nodes A, B, C, and D (from Fig. 8.7). The obtained values for

both the simulations and measurements correspond to the sum of the potentials of the forward and backward propagating waves at the nodes. Thus, their values can be significantly larger for nodes inside the circuit than for the potential at the output. The shapes of the curves agree very well, showing the maximum amplification at 10.5 GHz for the photoconductive measurement results and 10.8 GHz for the simulation. The discrepancy in the absolute value is around 5 dB for all of the measurements across the frequency range where maximum gain is obtained. This is again illustrated in Fig. 8.13, where a difference of 5 dB is obvious at the output of the first stage, and this difference does not significantly increase as the signal passes through the second and third stages. This result implies that the first stage has the greatest impact on the inferior performance of the circuit.

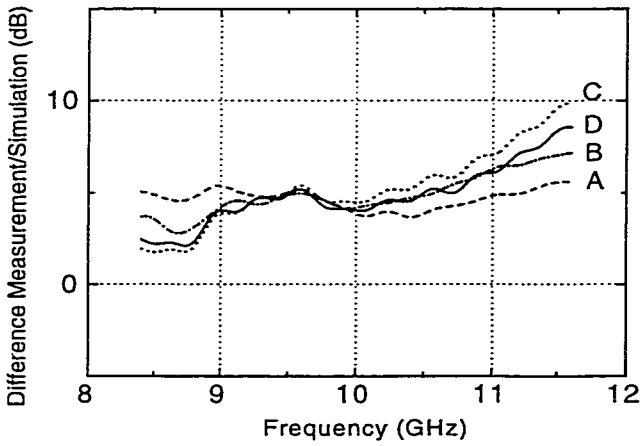

Figure 8.13: Difference between PC measurement and simulation.

Another indication that malfunctioning may take place in the first stage is that at normal DC bias values for V_{CC1} for the first stage, the collector current for both the first stage and the second stage show abnormally high values. This indicates that probably

both stages have considerable leakage current at the base-collector junction, thus leading to the reduced gain. With the additional information from the PC measurements, it is evident that the first stage degraded more seriously than the second. In fact, both the second and third stage exhibit the expected performance.

8.8 Summary

A photoconductive probing method that can measure absolute potentials at internal nodes of integrated micro- and millimeter wave circuitry was compared with the electro-optic field probing method, which has its advantages for radiating structure measurements.

As an actual application of the photoconductive probing, absolute potentials at a several critical nodes of a three-stage SiGe amplifier MMIC were measured. In summary, the comparison of calculated potentials and the results of circuit internal photoconductive probing in a Si-MMIC amplifier have allowed a detailed analysis of the circuit performance. It is demonstrated that deviations exist between the performance of a circuit as it was designed and as it was fabricated, with aging or stress degradation in the circuit proving problematic. The performance of single amplifier stages is investigated individually, and a malfunction of the first stage is isolated. The combination of photoconductive measurements and computer simulation provides the capability of MMIC internal-node RF characterization.

CHAPTER 9

CONCLUSIONS

9.1 Summary of Achievement

The main goal of this dissertation was the development of the high-speed, high-resolution, near-field electro-optic (EO) measurement methods for the full characterization of various microwave and millimeter guide and radiating structures. For this purpose, the second-generation free-space external EO field mapping system has been successfully developed and applied to various integrated circuits and antennas. Also, the third-generation fiber-based EO field mapping system has been developed as the most advanced near-field measurement tool that can provide great detail of the device under test with incomparable measurement flexibility.

The free-space external EO field mapping method, in which various EO crystals were utilized as electric field sensors to measure the three separate field components, has demonstrated its excellent capability to isolate malfunctioning sections of microwave integrated circuits. Also, the free-space external EO field mapping has provided profound information on antennas and arrays, which were crucial for both fundamental understanding and advanced diagnosis of those radiating structures. Furthermore, due to its high sensitivity and extreme proximity of the measurement, the external EO system was able to map surface mode waves in active arrays under normal operating condition. This valuable information led to new approached in array design.

To enhance certain aspect of the measurement technique, such as flexibility and stability, the fiber-based EO sampling system has been developed by utilizing

micromachined GaAs as the EO crystal. The fiber-based EO field-mapping system has provided the same high-quality near-field measurement results as the free-space external EO system. However, due to the small size and low dielectric constant of the GaAs tip, the fiber-based EO system has a much smaller invasiveness than any other near-field measurement method. The exceptional measurement versatility of fiber-based EO field mapping allows the probe to access the inside of enclosures and measure the complete field.

The high-resolution near-field data obtained by EO field mapping has led to the development of new analysis techniques for the characterization of various radiating structures. By using the advantages of the EO near-field mapping, the near- to far-field transformation has extended its capability to beyond its original purpose, which was a simple transformation of the near field into the far field. Due to the high-resolution of the EO field mapping, small areas of interest in antennas or arrays can be isolated by introducing a proper filtering procedure, and as a result, the contribution of any structure in the antenna or array, including substrate, to the far-field formation can be separately examined. Also, accurate near-field wave fronts have been successfully recovered from the EO near-field data.

In addition, as a contact, absolute potential measurement technique, a phtoconductive (PC) probe has been applied to a SiGe amplifier integrated circuit for full internal characterizations, and the results were compared and verified with LIBRA circuit simulations.

In conclusion, high-resolution near-fields obtained by the EO field mapping technique in broad bandwidth make it possible to open a new era of the characterization of various microwave and millimeter wave devices. In particular, by utilizing the fiber-based system, the EO field mapping technique overcomes virtually any possible measurement limitations that may be caused by the geometry of a device under test. Also, the PC probe provides accurate internal signals of high-frequency integrated circuits. The

results obtained from the EO field mapping and PC absolute voltage measurement can be the most powerful tools for fault isolation, performance verification of guided or radiating wave structures. Furthermore, the profound information from the EO field mapping and PC measurement allows a thorough understanding of those high frequency structures, and, as a result, the results can be fed back to the design procedure and easily lead to more improved, efficient designs.

9.2 Suggested Future Work

The EO field mapping method clearly is one of the most advanced near-field measurement methods. However, it is true that there is a margin for improvement. First of all, developing a reliable calibration method will significantly enhance the capability of the EO field mapping system. By developing an absolute field-strength measurement capability, it will be possible to make cross comparison between various micro and millimeter wave structures. Also, in addition to the calibration of the probe for the absolute field measurement, the effects of environment such as temperature and humidity variations to the probe should be studied to improve the measurement accuracy.

The next issue will be some improvements of the system itself. As mentioned previously, the fiber-based EO field mapping system is the most advanced method and it provides detailed electric field information from the structures that can not be characterized from any other methods. However, it is also possible to employ new electro-optic materials that have extremely low permittivities and much higher electro-optic coefficients instead of electro-optic crystals. Especially, the research of electro-optic polymers has been actively pursued, and the results demonstrate promising possibilities.

In addition to the performance enhancement, the EO field mapping method – especially, the fiber-based EO field mapping – has a lot of application possibilities in

various research fields. For instance, due to its high-sensitivity and versatility, the fiber-based EO field mapping system can be directly applied to electro-magnetic coupling (EMC) diagnostics, which are very difficult to perform by conventional measurement methods. Also, after proper modification, the fiber-based EO field mapping may be applicable for medical applications such as medical imaging and high-resolution diagnostics.

APPENDICES

APPENDIX A

1×4 DISTRIBUTION NETWORK FABRICATION PROCESS

In this appendix, detailed fabrication processes for the 1×4 power distribution network that is used as device under test in chapter 2 is presented.

1. Cleave a high-resistivity 4-inch Si wafer into 4 pieces.
2. Choose one of the quarter wafer piece and cleaning as follows
   (a) Soak in acetone for 10 minutes.
   (b) Soak in methanol for 10 minutes.
   (c) Soak in isopropyl alcohol (IPA) for 10 minutes.
   (d) Dry excess IPA with nitrogen (N_2) air gun.
   (e) Cleaning in plasma asher for 3 minutes at 150 W, 250 mT.
3. Mask cleaning
   (a) Soak in the EKS mask cleaner for 5minutes. Rube the surface of the mask with Q-tips very gently.
   (b) Soak in the acetone for 5minutes. Rube the surface of the mask with Q-tips very gently.
   (c) Stir mask in IPA for 5 minutes.
   (d) Dry excess IPA with nitrogen (N_2) air gun.
4. Thin film resistor – photolithography
   (a) Dehydrate sample for 1minute at 105 °C.
   (b) Spincoat adhesion promoter HMDS for 30 seconds at 3.5 Krpm.
   (c) Spincoat positive photoresist AZ 1813 for 30 seconds at 3.5 Krmp.
   (d) Softbake for 1 minute at 105 °C.

(e) Align to thin film mask (MASK #1) and expose for 7 seconds at 20 mW/cm^2.

(f) Develop in MF 351:H_2O (1:5) for 20 seconds.

(g) Rinse in DI-H_2O and Dry excess water with nitrogen (N_2) air gun.

(h) Descum in plasma asher for 1 minute at 80 W, 250 mT.

(i) Examine the pattern under microscope.

5. Thin film resistor – metallization

(a) Evaporate thin film resistor layer: NiCr (340 Å).

(b) Soak in hot PRS-2000 for metal lift-off.

(c) Once patterns are formed, stir the sample in IPA for 3 minutes for rinsing.

(d) Dry excess IPA with nitrogen (N_2) air gun.

(e) Examine the thickness of NiCr pattern with DekTek thickness monitor.

6. CPW lines – photolithography

(a) Dehydrate sample for 1minute at 105 °C.

(b) Spincoat adhesion promoter HMDS for 30 seconds at 3.5 Krpm.

(c) Spincoat positive photoresist AZ 1827 for 30 seconds at 3.5 Krmp.

(d) Softbake for 1 minute 30 seconds at 80 °C.

(e) Soak in chlorobenzen for 5 minutes and gently dry excess chlorobenzen with nitrogen (N_2) air gun.

(f) Align to CPW line mask (MASK #2) and expose for 15 seconds at 20 mW/cm^2.

(g) Develop in MF 351:H_2O (1:5) for 50 seconds.

(h) Rinse in DI-H_2O and Dry excess water with nitrogen (N_2) air gun.

(i) Descum in plasma asher for 1 minute at 80 W, 250 mT.

(j) Examine the pattern under microscope.

7. CPW lines – metallization

(a) Evaporate CPW line layer: Ti/Al/Ti/Au (500/11000/500/5000 Å).

(b) Soak in acetone for metal lift-off.

(c) Once patterns are formed, stir the sample in IPA for 3 minutes for rinsing.

(d) Dry excess IPA with nitrogen (N_2) air gun.

(e) Examine the thickness of NiCr pattern with DekTek thickness monitor.

8. Airbridge – Pillar

(a) Dehydrate sample for 1minute at 105 °C.

(b) Spincoat adhesion promoter HMDS for 30 seconds at 3.5 Krpm.

(c) Spincoat positive photoresist AZ 1827 for 30 seconds at 3.5 Krmp.

(d) Softbake for 1 minute 30 seconds at 80 °C.

(e) Align to pillar mask (MASK #3) and expose for 15 seconds at 20 mW/cm^2.

(f) Develop in MF 351:H_2O (1:5) for 50 seconds.

(g) Rinse in DI-H_2O and Dry excess water with nitrogen (N_2) air gun.

(h) Descum in plasma asher for 2 minute at 80 W, 250 mT.

(i) Examine the pattern under microscope.

(j) Bake on 150 °C hot plate for 1 minute.

(k) Evaporate exposure blocking layer: Ti (500 Å).

9. Airbridge – Span

(a) Spincoat adhesion promoter HMDS for 30 seconds at 3.5 Krpm.

(b) Spincoat positive photoresist AZ 1827 for 30 seconds at 3.5 Krmp.

(c) Softbake for 20 minutes in 80 °C oven.

(d) Soak in chlorobenzen for 6 minutes and gently dry excess chlorobenzen with nitrogen (N_2) air gun.

(e) Align to span mask (MASK #4) and expose for 15 seconds at 20 mW/cm^2.

(f) Develop in MF 351:H_2O (1:5) for 110 seconds.

(g) Rinse in DI-H_2O and dry excess water with nitrogen (N_2) air gun.

(h) Descum in plasma asher for 1 minute at 80 W, 250 mT.

(i) Examine the pattern under microscope.

(j) Etch exposed Ti in buffered HF (BHF) for 50 seconds.

(k) Evaporate CPW line layer: Ti/Al/Ti/Au (500/11000/500/5000 Å).

(l) Soak in acetone for metal lift-off.

(m) Once patterns are formed, stir the sample in IPA for 3 minutes for rinsing.

(n) Dry excess IPA with nitrogen (N_2) air gun.

(o) Examine under microscope.

APPENDIX B

FIBER-BASED ELECTRO-OPTIC PROBE FABRICATION

In this appendix, detailed fabrication processes for the fiber-based electro-optic probe with (100)-oriented GaAs tip introduced in chapter 5 is presented.

1. Cleave a 200-μm thick GaAs wafer into 1 cm × 1 cm pieces.
2. Choose one of the square wafer piece and cleaning as follows
   (a) Soak in acetone for 10 minutes.
   (b) Soak in methanol for 10 minutes.
   (c) Soak in isopropyl alcohol (IPA) for 10 minutes.
   (d) Dry excess IPA with nitrogen (N_2) air gun.
   (e) Cleaning in plasma asher for 3 minutes at 150 W, 250 mT.
3. Mask cleaning
   (a) Soak in the EKS mask cleaner for 5minutes. Rube the surface of the mask with Q-tips very gently.
   (b) Soak in the acetone for 5minutes. Rube the surface of the mask with Q-tips very gently.
   (c) Stir mask in IPA for 5 minutes.
   (d) Dry excess IPA with nitrogen (N_2) air gun.
4. Photolithography
   (a) Dehydrate sample for 1minute at 105 °C.
   (b) Spincoat adhesion promoter HMDS for 30 seconds at 3.5 Krpm.
   (c) Spincoat positive photoresist AZ 1827 for 30 seconds at 3.5 Krmp.
   (d) Softbake for 1 minute at 105 °C.

(e) Align to mask and expose for 15 seconds at 20 mW/cm^2.

(f) Develop in MF 351:H_2O (1:5) for 50 seconds.

(g) Rinse in DI-H_2O and Dry excess water with nitrogen (N_2) air gun.

(h) Descum in plasma asher for 1 minute at 80 W, 250 mT.

(i) Hardbake for 1 minute at 105 °C.

(j) Examine the pattern under microscope.

(k) Mount the sample on glass substrate with clear wax on 150 °C hot plate.

(l) Cool down the assembled sample in room temperature.

5. Etching process

(a) Prepare ethcant: H_2SO_4:H_2O_2:H_2O (1:8:1) + a few drops of NH_4OH.

(b) Soak the sample in the etchant. During the etching process, agitate the etchant every 30 seconds for 30 seconds. Change etchant every 10 minutes.

(c) Once etching is finished, examine the sample under microscope.

(d) Expose the sample (without mask) for 20 seconds at 20 mW/cm^2.

(e) Develop in MF 351:H_2O (1:5) for 50 seconds.

(f) Rinse in DI-H_2O and Dry excess water with nitrogen (N_2) air gun.

(g) Examine the sample under microscope.

6. High reflection coating

(a) Evaporate 4 sets of MgF_2/ZnSe layers (1406/833 Å) directly on the sample. No lithography is required.

7. Releasing probe

(a) Release the GaAs probes from the glass substrate in hot acetone.

(b) During the releasing process, change acetone several times.

(c) Strain the tips with filter paper. Pour IPA on the tips (on the filter paper).

(d) Dry tips in room temperature.

8. Probe assembly

(a) Prepare single mode optical fiber with desired length.

(b) Sock the two ends of the fiber in acetone for 20 minutes and remove protective jacket.

(c) Insert one end of the fiber into guiding quartz ferrule, and mount GRIN lense with UV optical glue.

(d) Mount a GaAs tip at the top of GRIN lens with UV optical glue. The high-reflection coating should points opposite direction from GRIN lens.

APPENDIX C

PHOTOCONDUCTIVE PROBE FABRICATION

In this appendix, detailed fabrication processes for the photoconductive probe introduced in chapter 9 is presented.

1. Cleave an LT-GaAs wafer into 1 cm × 1 cm pieces.
2. Choose one of the square wafer piece and cleaning as follows
   (a) Soak in acetone for 10 minutes.
   (b) Soak in methanol for 10 minutes.
   (c) Soak in isopropyl alcohol (IPA) for 10 minutes.
   (d) Dry excess IPA with nitrogen (N_2) air gun.
   (e) Cleaning in plasma asher for 3 minutes at 150 W, 250 mT.
3. Mask cleaning
   (a) Soak in the EKS mask cleaner for 5minutes. Rube the surface of the mask with Q-tips very gently.
   (b) Soak in the acetone for 5minutes. Rube the surface of the mask with Q-tips very gently.
   (c) Stir mask in IPA for 5 minutes.
   (d) Dry excess IPA with nitrogen (N_2) air gun.
4. Photolithography
   (a) Remove top oxidation layer in HCl:H_2O (1:15) solution.
   (b) Rinse in DI-H_2O and dry excess water with nitrogen (N_2) air gun.
   (c) Dehydrate sample for 1minute at 105 °C.
   (d) Spincoat adhesion promoter HMDS for 30 seconds at 3.5 Krpm.

(e) Spincoat positive photoresist AZ 1813 for 30 seconds at 3.5 Krmp.

(f) Softbake for 1 minute at 105 °C.

(g) Align to etching mask (MASK #1) and expose for 4.7 seconds at 20 mW/cm^2.

(h) Develop in MF 351:H_2O (1:5) for 10 seconds.

(i) Rinse in DI-H_2O and dry excess water with nitrogen (N_2) air gun.

(j) Measure the thickness of photoresist with DexTek depth monitor and record the value.

(k) Descum in plasma asher for 1 minute at 80 W, 250 mT.

(l) Examine the pattern under microscope.

5. Topside etching process

(a) Prepare ethcant: H_3PO_4:H_2O_2:H_2O (3:1:25).

(b) Soak the sample in the etchant for 3 minutes. During the etching process, agitate the etchant.

(c) Once etching is finished, examine the depth of the pattern.

(d) Soak the sample in acetone to remove the PR patterns.

(e) Rinse in IPA and dry excess IPA with nitrogen (N_2) air gun.

6. Metallization

(a) Dehydrate sample for 1minute at 105 °C.

(b) Spincoat adhesion promoter HMDS for 30 seconds at 3.5 Krpm.

(c) Spincoat positive photoresist AZ 1813 for 30 seconds at 3.5 Krmp.

(d) Softbake for 1 minute at 105 °C.

(e) Soak in chlorobenzen for 5 minutes and gently dry excess chlorobenzen with nitrogen (N_2) air gun.

(f) Align to thin metal mask (MASK #2) and expose for 6 seconds at 15 mW/cm^2.

(g) Develop in MF 351:H_2O (1:5) for 20 seconds.

(h) Rinse in DI-H_2O and Dry excess water with nitrogen (N_2) air gun.

(i) Descum in plasma asher for 1 minute at 80 W, 250 mT.

(j) Examine the pattern under microscope.

(k) Evaporate CPW line layer: Ti/Au (500/5000 Å).

(l) Soak in acetone for metal lift-off.

(m) Once patterns are formed, stir the sample in IPA for 3 minutes for rinsing.

(n) Dry excess IPA with nitrogen (N_2) air gun.

(o) Examine the metal pattern under microscope.

7. Backside etching I

(a) Mount the sample (facedown) on the glass chuck of lapping machine with melted paraffin wax.

(b) Lap 300 μm of the substrate.

(c) Remove the sample from the chuck.

(d) Soak in acetone for 10 minutes.

(e) Soak in methanol for 10 minutes.

(f) Soak in isopropyl alcohol (IPA) for 10 minutes.

(g) Dry excess IPA with nitrogen (N_2) air gun.

(h) Cleaning in plasma asher for 3 minutes at 150 W, 250 mT.

(i) Mount the sample on glass substrate with clear wax on 150 °C hot plate. The metal patterns should facedown to the glass substrate.

(j) Cool down the assembled sample in room temperature.

(k) Prepare ethcant: NH_4OH:H_2O_2 (1:24).

(l) Soak the sample in the etchant. During the etching process, agitate the etchant using magnetic stirer.

(m) Rinse in DI-H_2O and Dry excess water with nitrogen (N_2) air gun.

(n) Examine the sample under microscope.

8. Backside etching II

(a) Prepare ethcant: HF:H_2O (1:5).

(b) Soak the sample in the etchant. During the etching process, agitate the etchant.

(c) Rinse in DI-H_2O and Dry excess water with nitrogen (N_2) air gun.

(d) Examine the sample under microscope.

9. Releasing probe

(a) Release the PC probes from the glass substrate in hot xylen.

(b) During the releasing process, change xylen several times.

(c) Pour acetone in the beaker to dilute the xylen. Repeat this process 3 ~ 4 times.

(d) Pour IPA in the beaker to dilute the xylen. Repeat this process 3 ~ 4 times.

(e) The probes should be stored in the IPA.

10. Probe assembly

(a) Prepare single mode optical fiber with desired length.

(b) Sock the two ends of the fiber in acetone for 20 minutes and remove protective jacket.

(c) Polish one end of the fiber to make 45° facet.

(d) Mount a PC probe at the fiber.

BIBLIOGRAPHY

BIBLIOGRAPHY

[1] A. Yariv and P. Yeh, *Optical Waves in Crystals-Propagation and Control of Laser Radiation*, Wiley-Interscience, New York, USA, 1984.

[2] J. A. Valdmanis and G. A. Mourou, "Subpicosecond electro-optic sampling: Principles and applications," *IEEE J. Quantum Electronics.*, vol. 22, pp. 69-78, 1986.

[3] J. A. Valdmanis, "1 THz-bandwidth prober for high speed devices and integrated circuits," *Electron. Lett.*, vol. 23, pp. 1308-1310, Nov. 1987.

[4] K. Yang, G. David, S. Robertson, J. F. Whitaker and L. P. B. Katehi, "Electro-Optic mapping of near-field distributions in integrated microwave circuits," *IEEE Trans. On Microwave Theory and Techniques*, Vol. 46, No. 12, pp. 2338-2343, December, 1998.

[5] G. David, R. Tempel, I. Wolff, and D. Jäger, "Analysis of microwave propagation effects using 2D electro-optic field mapping techniques," *Opt. Quantum Electron.*, vol. 28, pp. 919-931, July 1996.

[6] B. H. Kolner and D. M. Bloom, "Electrooptic sampling in GaAs integrated circuits," *IEEE J. Quantum Electron.*, vol. QE-22, pp. 79-93, Jan. 1986.

[7] M. G. Li, E. A. Chauchard, C. H. Lee, and H.-L. A. Hung: "Two-dimensional field mapping of GaAs microstrip circuit by electrooptic sensing," *OSA Proc. Picosecond Electronics and Optoelectronics*, , Salt Lake City, USA, pp. 54-58, March 1991.

[8] G. David, S. Redlich, W. Mertin, R. M. Bertenburg, S. Koßlowski, F. J. Tegude, and D. Jäger, "Two-dimensional direct electro-optic field mapping in a monolithic integrated GaAs amplifier," *Proc. 23rd EuMC* 1993, Madrid, pp. 497-499, Sept. 1993.

[9] M. S. Hutmaker, T. B. Cook, B. Bosacchi, J. M. Wiesenfeld, and R. S. Tucker, "Electrooptic sampling of a high-speed GaAs integrated circuit," *IEEE J. Quantum Electron.*, vol. 24, pp. 226-233, Jan. 1988.

[10] J. A. Valdmanis, G. A. Mourou, and C. W. Gable, "Picosecond electro-optic sampling system," *Appl. Phys. Lett.*, vol. 41, pp. 211-212, 1986.

[11] K. E. Meyer, D. R. Dykaar, and G. A. Mourou, "Characterization of TEGFETs and MESFETs using the electrooptic sampling technique," *Picosecond Electronics and Optoelectronics, Springer Series*, vol. 21, pp. 54-57, 1985.

[12] M. Y. Frankel, J. F. Whitaker, G. A. Mourou, and J. A. Valdmanis, "Experimental characterization of external electro-optic probes," *IEEE Microwave Guided Wave Lett.*, vol. 1, pp. 60-62, 1991.

[13] J. M. Wiesenfeld, "Electro-optic sampling of high-speed devices and integrated circuits," *IBM J. Res. Develop.*, vol. 34, pp. 141-161, 1990.

[14] M. Y. Frankel, J. F. Whitaker, G. A. Mourou, and J. A. Valdmanis, "Ultra-high bandwidth vector network analyzer based on external electro-optic sampling," *Solid State Electron.*, vol. 35, pp. 325-332, 1993.

[15] J. F. Whitaker, J. . Valdmanis, T. A. Jackson, K. B. Bhasin, R. Romanofsky, and G. A. Mourou, "External electro-optic probing of millimeter-wave integrated circuits," *IEEE MTT-S Dig.*, pp. 211-224, 1989.

[16] M. Shinagawa, T. nagatsuma, "A picosecond external electro-optic prober using laser diodes," *Pro. Int. Test Conf.*, vol. 45-1, pp.1035-1039, 1990.

[17] K. Yang, G. David, J.-G. Yook, I. Papapolymerou, L. P. B. Katehi, and J. F. Whitaker, "Electrooptic mapping and finite-element modeling of the near-field pattern of a microstrip patch antenna," *IEEE Trans. Microwave Theory Tech.*, 2000, 48, pp.288-294.

[18] K. Yang, J. Morsey, L. W. Pearson, J. F. Whitaker, and L. P. B. Katehi, "Far-field analysis of a Ka-band patch antenna array using high-resolution electro-optic near-field mapping," *to be published in European Microwave Conference*, Paris, France, 2000.

[19] K. Yang, T. Marshall, M. Forman, J. Hubert, L. Mirth, Z. Popović, L.P.B. Katehi, and J.F. Whitaker, "Active-Amplifier-Array Diagnostics Using High-Resolution Electro-Optic Field Mapping," Submitted to *IEEE Trans. Microwave Theory and Tech.*

[20] K. Yang, K. Yang, L. P. B. Katehi, and J. F. Whitaker, "Optical-Fiber-Based Electro-Optic Field-Mapping System," submitted to *Appl. Phys. Lett.*

[21] K. Yang, L. P. B. Katehi, and J. F. Whitaker, "Micro/Millimeter-wave Antenna Measurements by Utilizing Fiber-Based Electro-Optic Field-Mapping System and Radiating Wave Front Recovery," submitted to *IEEE Trans. Microwave Theory and Tech.*

[22] H.-J. Cheng, "Highs speed signal generation, guidance and detection in the millimeter-wave regime by ultrafast optical techniques," Ph. D. dissertation, U. of Michgan, 1995.

[23] G. David, J. Whitaker, E. Ledbetter, T. Weatherford, D. Fouts, W. Goyette, K. Jobe, and K. Elliott, "A picosecond-response photoconductive-sampling probe for digital circuit testing," *IEEE LEOS '97 Conference Digest*, San Francisco, USA, pp. 236-237, Nov.1997.

[24] G. David, J. F. Whitaker, T. R. Weatherford, K. Jobe, S. Meyer, M. Bustamante, W. Goyette , S. Thomas III, and K. Elliott, "DC-to-mm-Wave Absolute Potential Measurements Inside Digital Microwave ICs Using a Micromachined Photoconductive Sampling Probe," 1998 *IEEE MTT International Microwave Symp. Digest.*

[25] A. D. Yaghijian, "An overview of near-field antenna measurements," *IEEE Trans. Antenna Prop.*, vol. 34, pp 30-45, Jan. 1986.

[26] T. Budka, S. D. Waclawik, and G. Rebeiz, "A coaxial 0.5-18 GHz near electric field measurement system for planar microwave circuits using integrated probes," *IEEE Trans. on Microwave Theory Tech.*, vol. 44, pp. 2174-2183, Dec. 1996.

[27] M. Kanda, "Standard probes for electromagnetic field measurements," *IEEE Trans. Antenna Prop.*, vol. 41, pp. 1349-1364, 1993.

[28] T. Pfeifer, H.-M. Heiliger, T. Loeffler, C. Ohlhoff, C. Meyer, G. Luepke, G. Roskos, and H. Kurz, "Optoelectronic on-chip characterization of ultrafast electric devices: Measurement techniques and applications," *IEEE J. Sel. Topics in Quantum Electron.* vol. 2, pp. 586-604, Sept. 1996.

[29] J. M. Weisenfeld, R. S. Tucker, A. Antreasyan, C. A. Burrus, A. J. Taylor, V. D. Mattera, Jr., and P. A. Garbinski, "Electro-optic sampling measurements of high-speed InP integrated circuits," *Appl. Phys. Lett.*, vol. 50, pp. 1310-1312, 1987.

[30] J. L. Freeman, S. K. Diamond, H. Fong, and D. M. Bloom, "electro-optic sampling of planar digital GaAs integrated circuits," *Appl. Phys. Lett.*, vol. 47, pp. 1083-1084, 1985.

[31] B. H. Kolner and D. M. Bloom, "Direct electro-optic sampling of tranamission line signals propagating on a GaAs substrate," *Electron. Lett.*, vol.. 20, pp. 818-819, 1984.

[32] D. R. Dykaar, R. F. Kopf, U. D. Keil, E. J. Laskowski, and G. J. Zydzik, "Electro-optic sampling using an aluminum gallium arsenide probe," *Appl. Phys. Lett.*, vol. 62, pp. 1733-1735, 1993.

[33] T. Pfeifer, T. Loeffler, H. G. Roskos, H. Kurz, M. Singer, and E. M. Bieble, "Electrooptic measurement of the electric near field distribution of a 7 GHz planar resonator," *Electron. Lett.*, vol. 32, pp. 1305-1307, 1996.

[34] J. A. Valdmanis and S. S. Pei, "A non-contact electro-optic prober for high speed integrated circuits," in *Picosecond Electronics and Optoelectronics II.*, New York: Springer-Verlag, New York, 1987.

[35] T. Nagatsuma, T. Shibata, E. Sano, and A. Iwata, "Subpicosecond sampling using a noncontact electro-optic probe," *J. Appl. Phys.*, vol. 66, pp 4001-4009, Nov. 1989.

[36] K. Kamogawa, I. Toyoda, K. Nishikawa, and T. Tokumitsu, "Characterization of a monolithic slot antenna using an electro-optic sampling technique," *IEEE Microwave and Guided Wave Lett.*, vol. 4, pp. 414-416, Dec. 1994.

[37] T. Pfeifer, T. Loeffler, H. G. Roskos, H. Kurz, M. Singer, and E. M. Bieble, "Electro-optic near-field mapping of planar resonators," *IEEE Trans. Antenna Prop.*, vol. 46, pp. 284-291, Feb. 1998.

[38] K. Yang, G. David, W. Wang, T. Marshall, L. W. Pearson, Z. Popovic, L.P.B. Katehi, and J.F. Whitaker, "Electro-Optic Field Mapping of Quasi-Optic Power-combining Arrays," in *Ultrafast Electronics and Optoelectronics Conference*, Technical Digest Series (Optical Society of America, Washington DC, 1999), pp. 30-32.

[39] D.M. Pozar, *Microwave Engineering*, Addison-Wesley, USA, 1990.

[40] C. A. Balanis, *Antenna Theory*, John Wiley & Sons, USA, 1982.

[41] M. A. Ali, S. Ortiz, T. Ivanov, and A. Mortazawi, "Analysis and measurement of hard horn feeds for the excitation of quasi-optical amplifiers," *IEEE Trans. Microwave Theory and Tech.*, vol. 46, no. 10, pp. 1469-1473, Oct. 1998.

[42] S. Hollung, A. E. Cox, and Z. Popović, "A bi-directional quasi-optical amplifier," *IEEE Trans. Microwave Theory and Tech.*, vol. 45, no. 12, pp. 2352-2357, Dec. 1997.

[43] T. Marshall, M. Forman, and Z. Popović, "Two Ka-band quasi-optical amplifier arrays," to appear in the Special Symposium Issue of the *IEEE Trans. on Microwave Theory and Tech.* Dec. 1999.

[44] J. Hubert, J. L. Mirth, S. Ortiz, and A. Mortazawi, "A 4 Watt Ka-band quasi-optical amplifier," *IEEE MTT-S International Microwave Symposium Digest 1999,* New York: IEEE, pp. 551-554.

[45] R. E. Williams, *Gallium Arsenide Processing Techniques*, Arten House, Dedham, USA, 1984.

[46] K. J. Weingarten, M. J. W. Rodwell, D. M. Bloom, "Picosecond Optical Sampling of GaAs Integrated Circuits," *IEEE J. of Quantum Electronics*, vol. 2, no. 2, pp.198-220, Feb. 1988.

[47] M. Shinagawa, T. nagatsuma, "Electro-optic sampling using an exteranl GaAs probe tips," *Electron. Lette.*, vol. 26, pp.1341-1343, 1990.

[48] M. S. Heutmaker, G. T. Harvey, D. G. Cruickshank, P. E. Bechtold, "Electrooptic sampling of silicon integrated circuits using a GaAs probe tips," *Dig. 17 int. Conf. Quantum Electron IQEC 90*, p. 50 and pp. 52-53.

[49] S. M. Sze, *Semiconductor Devices physics and Technology*, John Wiley & Sons, USA, 1985.

[50] R. F. Harrington, *Field Computation by Moment Methods*, New York: Macmillan, 1968.

[51] J.-G. Yook, and L. Katehi, "Characterization of CPW to microstrip transitions using the finite element method," *IEEE Ant. Propagat. Soc. Int.Symp. Dig.*, vol. 17, pp. 1206-1209, May, 1994.

[52] J. H. Richmond and T. E. Tice, "Probes for microwave near-field measurements," *IRE Trans. Microwave Theory Tech.*, vol. MTT-3, pp. 32-34, Apr. 1955.

[53] J. J. Lee, E. M. Ferren, D. P. Woolen and K. M. Lee, "Near-field prove used as a diagnostic tool to locate defective elements in an array antenna," *IEEE Trans. Antenna Prop.*, vol. 36, pp. 884-889, 1988.

[54] K. Yang, L. P. B. Katehi, and J. F. Whitaker, "Electro-Optic Field Mapping System utilizing External Gallium Arsenide Probes," *Appl. Phys. Lett.*, vol. 77, no. 4, pp. 486-488, 2000.

[55] Y. Mori and N. Watanabe, "A new etching solution system, H_3PO_4-H_2O_2-H_2O for GaAs and its kinetics," *J. Electrochem. Soc.*, vol. 125, pp. 1510-1514, 1978.

[56] J. J. Cannon and C. J. Nuese, "A chemical etchant for the selective removal of GaAs through SiO_2 mask," *J. Electrochem. Soc.*, vol. 121, pp. 1215-1219, 1974.

[57] D. W. Shaw, "Localized GaAs etching with acidic peroxide solutions," *J. Electrochem. Soc.*, vol. 128, pp. 874-880, 1981.

[58] S. Iida and K. Ito, "Selective etching of GaAs crystals in H_2SO_4-H_2O_2-H_2O system," *J. Electrochem. Soc.*, vol. 118, pp. 768-771, 1971.

[59] J. C. Phillips, *Bonds and Bands in Semiconductors*, New York, Academic Press, 1973.

[60] D. H. Evans, P. J. Gibson, "A coplanar waveguide antenna for MMICs," *European Microwave Conference proceedings*, 1989.

[61] S. V. Robertson, N. I. Dib, G. Yang, and L. P. B. Katehi, "A folded slot antenna for planar quasi-optical mixer applications," *IEEE Ant. Propagat. Soc. Int.Symp. Dig.*, pp. 600-603, 1994.

[62] R. A. York, and Z. Popović, *Active and Quasi-Optical Arrays for Solid-State Power Combining*, New York, Wiley, 1997.

[63] N.-S. Cheng, T.-P. Dao, M. G. Case, D. B. Rensch, and R. A. York, "A 60-Watt X-band spatially combined solid-state amplifier," *IEEE MTT-S International Microwave Symposium Digest 1999,* New York: IEEE, pp. 539-542.

[64] J. Brown, and E. V. Jull, "The prediction of aerial radiation patterns from near-field measurements," *Proc. Inst. Elec. Eng. Monograph 169R*, pp. 307-312, Mar, 1956.

[65] R. C. Johnson, H. A. Ecker, and J. S. Hollis, "Determination of far-field antenna patterns from near-field measurements," *Proc. IEEE*, vol. 61, pp. 1668-1694, Dec. 1973.

[66] O. M. Bucci, G. D'elia, G. Leon, and R. Pierri, "Far-field pattern determination from the near-field amplitude on two surface," *IEEE Trans. Antennas Propagat.*, vol. 38, pp. 1772-1779, Nov. 1990.

[67] K. Yang, L. P. B. Katehi, and J. F. Whitaker, "Far-field transformation using high-resolution near-field data obtained by electro-optic field mapping," submitted to *IEEE Trans. Antennas Propagat.*

[68] C. A. Balanis, *Antenna Theory: Analysis and design,* 2nd ed., John Wiley & Sons, 1997.

[69] N. G. Alexopoulos, P. B. Katehi, and D. B. Rutledge, "Substrate optimization for integrated circuit antenna," *IEEE Trans. Microwave Theory and Tech.*, vol. MTT-31, pp. 550-557, July 1983.

[70] R. M. Reano, J. F. Whitaker, L. P. B. Katehi "Near-field characterization of parasitic and slotline mode coupling in a quasi-optical unit cell via electro-optic sampling," to be appear in *IEEE Ant. Propagat. Soc. Int.Symp. Dig.*, 2000.

[71] R. E. Collin, *Antennas and Radiowave Propagation*, McGraw-Hill, USA, 1985.

[72] K. Yang, L. P. B. Katehi, and J. F. Whitaker, "Far-Field Analysis of a Ka-Band Quasi-Optical Amplifier Array Using High-Resolution Electro-Optic Near-Field Mapping," to be submitted to *IEEE Trans. Microwave Theory and Tech.*

[73] Z. Popovići and A. Mortazawi, "Quasi-optical transmit/receive front ends," *IEEE Trans. on Microwave Theory Tech.*, vol. 46, pp. 1964-1975, Aug. 1989.

[74] H. S. Tsai, M. J. Rodwell, and R. A. York, "Planar amplifier array with improved bandwidth using folded-slots," *IEEE Microwave Guided Wave Lett.*, vol. 4, pp. 112-114, Apr. 1994.

[75] D. E. Cooper, and S. C. Moss, "Picosecond optoelectronic measurement of the high frequency scattering parameters of a GaAs FET," *IEEE J. Quantum Electron.*, vol. 22, pp. 94-100, Jan. 1986.

[76] H. L. A. Hung, P. Polak-Dingels, K. J. Webb, T. Smith, H. C. Huang, and C. H. Lee, "Millimeter-wave monolithic integrated circuit characterization by a picosecond optoelectronic technique," *IEEE Trans. on Microwave Theory Tech.*, vol. 37, pp. 1223-1231, Aug. 1989.

[77] J. Kim, S. Williamson, J. Nees, S. Wakana, and J. F. Whitaker, "Photoconductive sampling probe with 2.3 ps temporal resolution and 4 μV sensitivity," *Appl. Phys. Lett.*, vol. 62, pp. 2268-2270, May 1993.

[78] T. Pfeifer, H.-M. Heiliger, E. Stein von Kaminski, H. G. Roskos, and H. Kurz, "Fabrication and characterization of freely positionable silicon-on-sapphire photo-conductive probes," *J. Opt. Soc. Am. B*, vol. 11, pp. 2547-52, Dec. 1994.

[79] J.-R. Hwang, H.-J. Cheng, J. F. Whitaker, and J. V. Rudd, "Photoconductive sampling with an integrated source follower/amplifier," *Appl. Phys. Lett.*, vol. 68, pp. 1464-1466, Aug. 1996.

[80] R. K. Lai, J.-R. Hwang, J. Nees, T.B. Norris, and J.F. Whitaker, "A fiber-mounted, micromachined photoconductive probe with 15nV/ Hz^{-} sensitivity," *Appl. Phys. Lett.*, vol. 69, pp. 1843-1845, Sept. 1996.

[81] K. Takeuchi, A. Mizuhara, "Potential image observation with ultra-high space-time resolution," *Ultrafast Electronics and Optoelectronics, Technical Digest*, (Optical Society of America, Washington, D.C., 1997), pp. 151-153.

[82] G. David, K. Yang, M. Crites, J. -S. Rieh, L. -H. Lu, P. K. Bhattacharya, L. P. B. Katehi, and J. F. Whitaker, "Photoconductive Probing and Computer Simulation of Microwave Potentials inside a SiGe MMIC," *Topical meeting on Silicon Monolithic Integrated Circuits in RF Systems*, Ann Arbor, MI, U.S.A.1998.

[83] A. Ruffin, J. F. Whitaker, and T. Norris, "Time-reversal and object reconstruction using single-cycle terahertz pulses," to be published in *LEOS 2000 Technical Digest*, Rio Grande, Puerto Rico.

[84] J. -S. Rieh, L. -H. Lu, L. P. B. Katehi, P. Bhattacharya, E. T. Croke, G. E. Ponchak, and S. A. Alterovitz, "*X*- and *Ku*-Band Amplifiers Based on Si/SiGe HBT's and Micromachined Lumped Components," *IEEE Trans. on Microwave Theory and Tech.*, Vol. 46, pp. 685-694, May 1998.